TECHNISCHE UNIVERSITÄT DARMSTADT

MAX-PLANCK-INSTITUT FÜR FESTKÖRPERFORSCHUNG

Advanced Transmission Electron Microscopy of Transition Metal Oxides with Unconventional Growth Mechanisms

Dissertation by Anna Scheid

Submitted to the *Department of Materials and Geosciences* at the *Technical University of Darmstadt* in fulfillment of the requirements for the degree of

Doctor rerum naturalium (Dr. rer. nat.)

Referee:

Prof. Dr. Christian Kübel

Co-referee:

Prof. Dr. Peter Antonie van Aken

Darmstadt 2025

This work was conducted at the

Max Planck Institute for Solid State Research

Scheid, Anna: Advanced Transmission Electron Microscopy of Transition Metal Oxides with Unconventional Growth Mechanisms

Darmstadt, Technische Universität Darmstadt
Publication year of dissertation at TUprints: 2025
URN: urn:nbn:de:tuda-tuprints-306661
Date of Oral Examination: 03.06.2025
Date of Submission: 15.04.2025
Publication under CC BY 4.0 International
https://creativecommons.org/licenses/

Declaration

I, Anna Scheid, hereby declare that I have independently prepared and written this thesis entitled "Advanced Transmission Electron Microscopy of Transition Metal Oxides with Unconventional Growth Mechanisms" at the Max Planck Institute for Solid State Research. This work satisfies the requirements for the Doctor of Natural Science (Dr. rer. nat.) degree in the Department of Materials- and Geosciences at the Technical University of Darmstadt. Only the indicated auxiliary means were used. All information taken verbatim or in spirit from other works is marked with the source, as are contributions by other persons. This also includes drawings, sketches as well as pictorial and graphical representations that were not made by my own hand. The work has not yet been published or presented in any other form as an examination performance.

Stuttgart: _____ Signature:_____

Acknowledgement

First and foremost, I would like to express my deepest gratitude to **Prof. Dr. Peter A. van Aken** for allowing me to conduct my research at the Stuttgart Center for Electron Microscopy (StEM), for his excellent supervision, and for providing me with the opportunity to attend numerous conferences and workshops. His support enabled me to present my research to and connect with colleagues in the field of electron microscopy all over the world.

I would also like to thank **Prof. Dr. Christian Kübel**, **Prof. Dr. Lambert Alff**, and **Prof. Dr. Andreas Rosenauer** for having agreed to serve on my thesis defense committee at TU Darmstadt.

A heartfelt thank you goes to **Dr. Tobias Heil**, my day-to-day supervisor, for his invaluable advice, friendship, and encouragement. His support, both in work and as an office mate, has been essential throughout the easy and hard days. I am especially grateful for his patience in reading and correcting endless pages of documents and manuscripts.

I deeply appreciate **Kersten Hahn** and **Peter Kopold** for their invaluable support with TEM, and **Marion Kelsch**, **Ute Salzberger,** and **Birgit Bußmann** for their exceptional sample preparation work—without their contributions, none of my results would have been possible.

Special thanks go to **Dr. Julia Deuschle** for being a fantastic office mate, for our relaxing morning chats, all the enjoyable lunch breaks, and for always being there to listen.

I am grateful to **Caroline Heer** for her administrative assistance and guidance through the countless challenges of German bureaucracy.

Many thanks also to my PhD colleagues, especially **Dr. Nicolas Bonmassar**, for many fun evenings with our friend, the beer vending machine in the canteen.

I also extend my thanks to **Dr. Qi Song** and **Prof. Dr. Darrell G. Schlom** from Cornell University for providing us with fascinating thin-film samples, and to **Dr. Arvind Kumar Yogi** for his collaboration on oxide crystal samples. I am especially grateful for the support of **Dr. Stephanie Ribet** and **Dr. Colin Ophus** from the National Center of Electron Microscopy (NCEM) at the Lawrence Berkeley National Laboratory (LBNL) for teaching me a significant part of the data analysis procedures. Without their help, many of the results would not have been achieved.

I sincerely appreciate the external supervision of my PhD work by **Dr. Rotraut Merkle**.

I would like to thank the **Deutsche Gesellschaft für Elektronenmikroskopie (DGE)** for the financial support, which allowed me to present my work at numerous conferences and enabled a trip

to the LBNL, without which many of the results of this work would not have been possible. I am grateful to the **European Microscopy Society (EMS)** for their financial support, which allowed me to attend the 17th European Microscopy Congress in Copenhagen, Denmark.

I am deeply grateful to my family **Evi**, **Volker** and **Alex** for their constant support, encouragement and for always believing in me.

A special thank you to my wonderful boyfriend, **Adrian**, for his endless support and companionship. Your presence fills my life with joy and has been a steady source of strength, for which I am truly grateful.

Finally, I wish to thank the entire **StEM group** for creating a positive work atmosphere and engaging in lively discussions. Working with you all has been a pleasure, and I enjoyed every day of my time at the StEM.

Table of contents

Declaration I
Acknowledgement II
List of published manuscripts VII
List of conference contributions and research trips IX
List of Abbreviations X
List of Figures XII
List of Tables XX
Abstract XXI
Zusammenfassung XXIII
1 Introduction 1
1.1 Transmission electron microscopy 1
1.1.1 Fundamentals and limitations 1
1.1.2 Lens aberrations and aberration correction 2
1.1.3 Imaging 4
1.1.3.1 CTEM - Conventional transmission electron microscopy 5
1.1.3.2 STEM - Scanning transmission electron microscopy 6
1.1.4 Spectroscopy 7
1.1.4.1 EELS - Electron energy-loss spectroscopy 7
1.1.4.2 XEDS - X-ray energy-dispersive spectroscopy 8
1.2 Electron ptychography 8
1.2.1 4D STEM detectors 9
1.2.2 The phase problem 11
1.2.3 Non-iterative phase reconstructions 13
1.2.3.1 Single-Sideband (SSB) reconstruction 15
1.2.3.2 Wigner distribution deconvolution (WDD) 16
1.2.4 Iterative phase reconstructions 17
1.2.4.1 Mixed-state electron ptychography 20
1.2.4.2 Multi-slice electron ptychography 21
1.2.5 What makes a good 4D STEM dataset for electron ptychography? 22
1.2.5.1 Probe step size 23

1.2.5.2 Detector sampling considerations 24
1.2.5.3 Finding the optimum (de)focus 26
1.2.5.4 Hyper-parameter tuning for iterative phase reconstructions 27
1.2.6 Center-of-mass imaging 29
1.3 Oxides, oxide heterostructures, and interfaces 30
1.3.1 Fabrication of oxide heterostructures *via* PVD 33
1.3.2 Coherent, semi-coherent, and incoherent interfaces 35
1.3.3 Analysis of misfit dislocations and strain in TEM: GPA and phase lock-in technique 37
2 Direct evidence of anomalous Peierls transition induced charge density wave order at room temperature in metallic $NaRu_2O_4$ 38
2.1 Introduction 39
2.2 Materials and methods 41
2.2.1 Sample preparation 41
2.2.2 TEM investigations 42
2.3 Results and discussion 43
2.3.1 Microscopic structural investigation of $NaRu_2O_4$ along the *b*-axis 43
2.3.2 Electronic transport measurements 45
2.3.3 *In-situ* heating experiments 47
2.3.4 Periodic lattice displacement mapping 54
2.4 Conclusions 59
3 Unveiling the interfacial reconstruction mechanism enabling stable growth of the delafossite $PdCoO_2$ on Al_2O_3 and $LaAlO_3$ 60
3.1 Introduction 62
3.2 Materials and methods 63
3.2.1 Sample preparation 63
3.2.2 STEM specimen preparation 64
3.2.3 STEM investigations 64
3.2.4 Density functional theory calculations 65
3.3 Results and discussion 65

3.3.1 Structural characterization of the $PdCoO_2$ thin films 65

3.3.2 Structural characterization of the $PdCoO_2/Al_2O_3$ and $PdCoO_2/LaAlO_3$ interfaces . 68

3.3.3 Chemical analysis of the $PdCoO_2/Al_2O_3$ and $PdCoO_2/LaAlO_3$ interfaces 73

3.3.4 Electron ptychography of the $PdCoO_2/Al_2O_3$ and $PdCoO_2/LaAlO_3$ interfaces 76

3.4 Conclusions 84

4 Atomic-scale mechanisms of nucleation and stabilization in $CuCrO_2$ and $CuFeO_2$ delafossite thin films on Al_2O_3 85

4.1 Introduction 86

4.2 Materials and methods 88

4.2.1 Sample preparation 88

4.2.2 STEM specimen preparation 88

4.2.3 STEM investigations 88

4.3 Results and discussion 89

4.3.1 Structural characterization of the $CuCrO_2$ and $CuFeO_2$ thin films 89

4.3.2 Lattice modulation analysis of the $CuCrO_2$ and $CuFeO_2$ thin films 94

4.3.3 Electron ptychography of the $CuFeO_2/Al_2O_3$ and $CuFeO_2/Al_2O_3$ interfaces 96

4.3.4 Chemical analysis of the $CuFeO_2/Al_2O_3$ and the $CuFeO_2/Al_2O_3$ interfaces 102

4.4 Conclusions 105

5 Summary 106

6 References 109

List of published manuscripts

(1) **Scheid, A.**, Isha, Yogi, A.K., Isobe, M., Bußmann, B., Heil, T., van Aken, P. A.*:* Direct evidence of anomalous Peierls transition-induced charge density wave order at room temperature in metallic $NaRu_2O_4$. *Microscopy and Microanalysis* **31**, ozae129 (2025), https://doi.org/10.1093/mam/ozae129.

(2) **Scheid, A.**, Heil, T., Suyolcu, Y. E., Song, Q., Enderlein, N., Nono Tchiomo, A. P., Ngabonziza, P., Hansmann, P., Schlom, D. G. & van Aken, P. A. Unveiling the interfacial reconstruction mechanism enabling stable growth of the delafossite $PdCoO_2$ on Al_2O_3 and $LaAlO_3$. *ACS Applied Materials & Interfaces* **7**, 14795–14802 (2025), 10.1021/acsami.5c03536.

(3) **Scheid, A.**, Song, Q., Ribet, S. M., Ophus, C., Suyolcu, Y. E., Schlom, D. G., Heil, T., van Aken, P. A.: Atomic-scale mechanisms of nucleation and stabilization in $CuCrO_2$ and $CuFeO_2$ delafossite thin films on Al_2O_3. *Advanced Materials Interfaces* **12**, 2500218 (2025), 10.1002/admi.202500218.

(4) Nono Tchiomo, A. P., Sharma, A., Sajeev, S., **Scheid, A.**, van Aken, P. A., Harada, T., Ngabonziza, P.: Magnetotransport properties in epitaxial films of metallic delafossite $PdCoO_2$: Effects of thickness and width variations in Hall bar devices. *Physical Review Materials* **9**, 055001 (2025), 10.1103/PhysRevMaterials.9.055001.

(5) Song, Q., He, Z., Faeth, B. D., Parzyck, C. T., **Scheid, A.**, Mowers, C. J., Feng, Y., Xu, Q., Hasko, S., Park, J., Barone, M., Suyolcu, Y. E., van Aken, P. A., Pamuk, B., Fennie, C. J., King, P. D. C., Shen, K. M., Schlom, D. G.: Surface reconstructions and electronic structure of metallic delafossite thin films. *APL Materials* **12**, 081117 (2024), https://doi.org/10.1063/5.0217540.

(6) **Scheid, A.**, Song, Q., Pokhrel, H., Heil, T., Ribet, S.M., Ophus, C., Enderlein, N., Suyolcu, Y. E., Hansmann, P., Schlom, D. G., van Aken, P. A.: Unraveling atomic-scale reconstruction at the interface: A novel insight into epitaxial growth mechanism of metallic delafossite thin films. *Microscopy and Microanalysis* **30**, Issue Supplement_1, ozae044.914 (2024), https://doi.org/10.1093/mam/ozae044.914.

(7) **Scheid, A.**, Isha, Yogi, A.K., Isobe, M., Bußmann, B., Heil, T., van Aken, P. A.*:* Unlocking orbital-driven Peierls dimerization: Atomic-scale insights into the unconventional metal-to-metal phase transition in $NaRu_2O_4$. *Microscopy and Microanalysis* **30**, Issue Supplement_1, ozae044.745 (2024), https://doi.org/10.1093/mam/ozae044.745.

(8) Ngabonziza, P., Sharma, A., **Scheid, A.**, Sajeev, S., van Aken, P. A., Mannhart, J.: Magnetotransport properties of epitaxial films and Hall bar devices of the correlated layered ruthenate $Sr_3Ru_2O_7$. *Physical Review Materials* **8**, 044401 (2024), https://doi.org/10.1103/PhysRevMaterials.8.044401.

List of conference contributions and research trips

MC 2023 Darmstadt, Germany	Poster presentation: Electron ptychographic phase imaging of beam-sensitive all-inorganic halide perovskites using 4D-STEM
IMC 2023 Busan, South Korea	Oral presentation: Atomic-resolution imaging of room-temperature bond order in metallic $NaRu_2O_4$
M&M 2024 Cleveland, USA	Oral presentation: Unraveling atomic-scale reconstruction at the interface: A novel insight into epitaxial growth mechanism of metallic delafossite thin films
	Oral presentation: Unlocking orbital-driven Peierls dimerization: Atomic-scale insights into the unconventional metal-to-metal phase transition in $NaRu_2O_4$
EMC 2024 Copenhagen, Denmark	Oral presentation: Novel insights into atomic-scale interface reconstruction during epitaxial growth of metallic delafossite thin films
	Poster presentation: Picometer-accurate mapping of lattice displacements from unconventional room-temperature bond order in metallic $NaRu_2O_4$
QEM 2022, Port-Barcarès, France	8th–20th May 2022
MerlinEM User Meeting, Oxford, United Kingdom	21st November 2023
PARADIM, Cornell, Ithaca, USA	05th–12th January 2024
NCEM, LBNL, Berkeley, USA	13th January–05th February 2024
NordTEMHub workshop, Trondheim, Norway	11th–13th June 2024

List of Abbreviations

1D	One-Dimensional
2D	Two-Dimensional
3D	Three-Dimensional
4D	Four-Dimensional
ABF	Annular Bright Field
ADF	Annular Dark Field
ARPES	Angle Resolved Photoemission Spectroscopy
BF	Bright Field
BO	Bayesian Optimization
CBED	Convergent Beam Electron Diffraction
CCD	Charge-Coupled Device
CDW	Charge Density Wave
CMOS	Complementary Metal Oxide Semiconductor
CoM	Center of Mass
CO	Charge Order
CTEM	Conventional Transmission Electron Microscopy
CTF	Contrast Transfer Function
DEC	Direct Electron Camera
DF	Dark Field
DGE	Deutsche Gesellschaft für Elektronenmikroskopie
DFT	Density Functional Theory
DQE	Detective Quantum Efficiency
DPC	Differential Phase Contrast
EELS	Electron Energy-Loss Spectroscopy
EFTEM	Energy Filtered Transmission Electron Microscopy
ELNES	Electron Energy-Loss Near-Edge Structure
EMS	European Microscopy Society
FT	Fourier Transform
GP	Gaussian Process
GPA	Geometric Phase Analysis
HAADF	High Angle Annular Dark Field
HRTEM	High-Resolution Transmission Electron Microscopy
HT	High Temperature
IABF	Inverted Annular Bright Field
LSDA	Local Spin Density Approximation

LT	Low Temperature
MAPS	Monolithic Active Pixel Sensor
MBE	Molecular Beam Epitaxy
MSE	Mean Squared Error
NCEM	National Center for Electron Microscopy
PACBED	Position Averaged Convergent Beam Electron Diffraction
PAD	Pixel Array Detector
PBE	Perdew-Burke-Ernzerhof
PCA	Principal Component Analysis
PCM	Phase Contrast Microscopy
PLD	Pulsed Laser Deposition / Periodic Lattice Displacement
PLE	Pulsed Laser Epitaxy
POA	Phase Object Approximation
PVD	Physical Vapor Deposition
RHEED	Reflection High Energy Electron Diffraction
RT	Room Temperature
RTEM	Raster Transmissions Elektronen Mikroskopie
SAED	Selected Area Electron Diffraction
SCF	Self Consistent Field
SC-XRD	Single Crystal X-ray Diffraction
SNR	Signal-to-Noise Ratio
SOC	Spin-Orbit Coupling
SSB	Single-Sideband
STEM	Scanning Transmission Electron Microscopy
SQUID	Superconducting Quantum Interference Device
TCO	Transparent Conducting Oxide
TEM	Transmission Electron Microscopy
TLE	Thermal Laser Epitaxy
TMC	Transition Metal Compound
WDD	Wigner-distribution deconvolution
WPOA	Weak Phase Object Approximation
XEDS	X-Ray Energy-Dispersive Spectroscopy
XRR	X-Ray Reflectivity

List of Figures

Figure 1. (a) Signals generated by electrons interacting with a sample material. (b) Two basic conditions under which a TEM is operated: conventional transmission electron microscopy (CTEM) with parallel beam illumination, and scanning transmission electron microscopy (STEM) with a convergent electron beam scanned over the sample surface. Adopted and modified with permission, © Springer-Verlag US 2009[15]. 5

Figure 2. Schematics of different STEM detecting modes. (a) Conventional detectors collecting single intensity values for each probe position. (b) Segmented detectors that collect multiple intensity values (4–32 or more channel readouts) for each beam position in the raster scan, and (c) pixelated detectors that record full diffraction patterns at each scan position, resulting in 4D datasets. 10

Figure 3. Schematic of the electron-beam propagation in a 4D STEM experiment with binary data acquisition using a focused convergent electron beam. 13

Figure 4. The flowchart illustrates the iteration of the gradient-descent iterative ptychographic phase reconstruction. One iteration of the algorithm involves processing individual diffraction patterns utilized to refine the estimates of the object and the probe. Typically, iterations are carried out until the error between the measured and calculated diffraction patterns falls below a predefined threshold. 20

Figure 5. (a) Real-space intensity distribution of the electron probe used for typical 4D STEM data acquisition in this study. (b) Example diffraction pattern resulting from the interaction between the sample and the slightly defocused probe shown in (a). (c) Simulated probe with large overfocus, leading to wrap-around artifacts in the reconstruction. (d) Example diffraction pattern from a dataset acquired with a more defocused probe, showing reduced resolution of sample features in the ronchigram, compared to (b). 27

Figure 6. Schematic of degrees of freedom in oxides to tune material properties for the application as functional materials in various fields. 31

Figure 7. (a) Coherent interface with elastic mismatch strain stabilizing the heterostructure interface. (b) Semi-coherent interface with misfit dislocations relieving strain and stabilizing the heterostructure. (c) Incoherent interface. Adopted with permission[177], © 2009 by Taylor & Francis Group, LLC. 36

Figure 8. Representation of the hollow channel geometry of RT $NaRu_2O_4$ along the crystallographic *b*-axis. (a) Simultaneously acquired HAADF and ABF STEM images showing the tunnel structure. The inset shows the atomic arrangement, with the structural model superimposed. The ABF image shows the presence of Na^+ ions in the central cavity of the edge- and corner-sharing RuO_6 octahedra. (b) EELS elemental mapping over the identical sample area confirms the elemental distribution, as the atomic positions match their corresponding positions in the structural model (shown with white overlay). Due to the projection of alternating Ru^{3+} and Ru^{4+} atomic columns along the *b*-axis, they cannot be distinguished from the EELS signal. Reprinted under the terms of a CC-BY license. © 2025 The authors[186]. 44

Figure 9. HAADF STEM images of RT $NaRu_2O_4$ along various zone axes. The HAADF images show contrast only for the heavy Ru atomic columns, while the Na and O columns are not visible. Each image is overlaid with the structural model along the respective zone axis, including only the Ru columns. The structural models, showing all atomic species, are displayed on the right of each STEM image. Reprinted under the terms of a CC-BY license. © 2025 The authors[186]. 45

Figure 10. Temperature-dependent resistivity for $NaRu_2O_4$ in both heating and cooling modes between 590 K and 300 K[141]. The resistivity hysteresis, associated with a first-order phase transition, is indicated by the dotted line, the critical transition temperature of T_C = 535 K is highlighted by the vertical, black dashed line. (b) One-dimensional (1D) Ru chain along the *b*-axis tunnel structure. Above T_C, all atoms are equally spaced with the lattice constant b = 2.82(15) Å and the space group *Pnma*. Below T_C, the periodicity doubles to $2b$ = 5.643(3) Å with a symmetry-breaking transition to the $P112_1/a$ space group and the Ru-Ru bonds are shortened, as shown in the lower chain. This process leads to Ru^{4+}-Ru^{3+} dimerization along the *b*-axis. The physical consequence of such 1D electronic behavior is well defined as a Peierls-type phase transition in condensed-matter physics and leads to the formation of Ru dimers, highlighted in gray at the bottom. Reprinted under the terms of a CC-BY license. © 2025 The authors[186]. 46

Figure 11. *In-situ* atomic-resolution HAADF STEM images of $NaRu_2O_4$ along the crystallographic [100] zone axis. The insets show the Fourier transform of each image. For temperatures below the critical temperature of 535 K, the (0, ½, 0) superlattice peaks are clearly visible (the regions with first-order superlattice peaks are outlined in green). Above the critical temperature, the structure transforms to the HT-*Pnma* phase and the superlattice peaks disappear. Upon cooling to room temperature, the peaks reappear and the structure transforms back to the LT-$P112_1/a$ phase. Adopted under the terms of a CC-BY license. © 2025 The authors[186]. 48

Figure 12. *In-situ* SAED of $NaRu_2O_4$, oriented along the [100] zone axis. (a) Temperature profile of the heating cycle. (b) TEM image of the [100] oriented crystal before the start of the heating

experiment. (c) TEM image of the [100] oriented crystal after cooling back to RT. (d)-(l) SAED patterns taken at different temperatures (the areas with first-order superlattice peaks are outlined in green). Above the critical temperature, the superlattice peaks disappear and reappear when the sample is cooled below T_C. The insets in (d), (h), and (l) show simulated SAED patterns for the respective phases (LT-$P112_1/a$ phase for (d) and (b) and HT-*Pnma* phase for (h)). In addition, the TEM image in (c) and irregular spots in the SAED patterns indicate some degree of structural damage. Reprinted under the terms of a CC-BY license. © 2025 The authors[186]. 50

Figure 13. (a) Schematic of a Peierls transition from the HT phase (left) to the LT phase (right), accompanied by the opening of a gap in the electronic spectrum *E(K)*. The distance between lattice sites in the uniform chain is *b*. (b) Unique molecular orbitals formed by Ru^{4+}-Ru^{3+} dimerization in the Z-type charge and bond order system. Reprinted under the terms of a CC-BY license. © 2025 The authors[186]. 52

Figure 14. (a) *In-situ* atomic-resolution HAADF STEM images of $NaRu_2O_4$ along the crystallographic [100] zone axis with the structural model superimposed for each temperature. (b) Display of the structural models for the LT-$P112_1/a$ phase (RT to 523 K), which shows four independent Ru sites (dimer $Ru_{1A,B}$ and dimer $Ru_{2A,B}$), and the HT-*Pnma* phase (573 K), which shows two distinct Ru sites (Ru_1 and Ru_2). The dashed black boxes indicate the respective unit cells. The dimer bond length and interdimer bond length, elucidated as a function of temperature, were derived from the full field-of-view HAADF images in Figure 11. The solid arrows in the structural model indicate the corresponding lattice spacings for the $Ru_{1A,B}$ dimer, while the dashed arrows indicate the lattice spacings within and between the $Ru_{2A,B}$ dimers. The dotted lines in the plots represent the theoretical values derived from the structural models. Reprinted under the terms of a CC-BY license. © 2025 The authors[186]. 54

Figure 15. Visualization of picometer-scale periodic lattice displacements of Ru sites in $NaRu_2O_4$ oriented along the (a) [100] and (b) [101] zone axes. At the top, the HAADF images show the original LT-$P112_1/a$ phase. In the middle are the synthetic HT-*Pnma* images derived from the original LT phase *via* Fourier processing. At the bottom, the arrows in the PLD maps indicate the ionic displacement, calculated as the difference in atomic positions between the (synthetic) HT and LT phases. The arrows indicate the displacement at each atomic lattice site, with their length representing the displacement amplitude and their color representing the polarization vector angle (the direction of the displacement). Adopted under the terms of a CC-BY license. © 2025 The authors[186]. 56

Figure 16. Gaussian peak fitting of Ru atomic columns along the (a) [100] and (b) [101] zone axis. The HAADF images at the top show the original LT-$P112_1/a$ phase from which the synthetic HT-

Pnma images shown in the middle were derived by Fourier processing. The insets demonstrate the accurate peak positioning of the Atomap algorithm[49]. The difference images at the bottom were calculated from the synthetic HT and the original LT phases and thus represent relevant lattice modulations for the two zone axes. Adopted under the terms of a CC-BY license. © 2025 The authors[186]. 57

Figure 17. (a) Virtual ABF image, created by integrating the diffraction patterns from a 400x400 probe positions 4D STEM scan over an annular mask with inner- and outer radius of 10 and 20.4 mrad. (b) Virtual low-angle annular dark-field (LAADF) image, created by integrating the diffraction patterns over an annular mask with an inner- and outer radius of 30 and 81 mrad. (c) SSB ptychographic phase reconstruction showing high contrast for both light and heavy elements. Reprinted under the terms of a CC-BY license. © 2025 The authors[186]. 58

Figure 18. (a) STEM HAADF images, X-ray diffraction, and *in-situ* RHEED patterns, of two $PdCoO_2$ thin films grown on an Al_2O_3 substrate. The Laue oscillations observed for the $PdCoO_2$ peaks indicate an abrupt and smooth film-substrate interface, which is also visible in the STEM images. (b) STEM HAADF, X-ray diffraction, and *in-situ* RHEED patterns of a $PdCoO_2$ thin film grown on $LaAlO_3$. Asterisks (∗) denote substrate reflections. Adopted under the terms of a CC-BY license. © 2025 The authors[229]. 66

Figure 19. HAADF STEM images of $PdCoO_2$ thin films (right) on (a) Al_2O_3 and (b) $LaAlO_3$ for two structural orientations of the films. For stable growth, the growth is always initiated with a $[CoO]^-$-layer. The insets in the [010] images reveal domains with opposing orientations of the CoO_6 octahedra in subsequent $[CoO]^-$-layers, and highlight stacking faults (0° swap) and twin domains (180° swap) in the films. Adopted under the terms of a CC-BY license. © 2025 The authors[229]... 68

Figure 20. Simultaneously acquired HAADF STEM and ABF STEM images of the $Al_2O_3/PdCoO_2$ interface for the (a) [210] and (b) [010] zone axes and the $LaAlO_3/PdCoO_2$ interface for the (c) [210] and (d) [010] zone axes. While the HAADF STEM images show strong contrast primarily for the heavy elements Pd, Co, and La, the ABF images clearly reveal the O and Al atoms. The insets in the ABF images show an overlay with the structural models of the substrates and thin films with unmatched atomic contrast at the interface within the substrates. Adopted under the terms of a CC-BY license. © 2025 The authors[229]. 69

Figure 21. (a) Oxygen layers exhibiting a triangular (highlighted) in-plane arrangement, a shared structural feature between $PdCoO_2$ and Al_2O_3. The top panel displays the primitive hexagonal unit cells of the two interfaced compounds, while the bottom panel shows the specific rectangular supercells utilized for the interface simulations. (b) Top panel: Side views of the Pd- and Co-interface simulation geometries. The interface region separating the two compounds is highlighted

with transparent blue. Co-substituted Al-sites are highlighted as 'Higher Al' and 'Lower Al' depending on their *c*-axis position. The interface binding energy is calculated as the difference between the total energy of the (optimized) interface and that of its two constituents. (c) Differences in calculated interface energies (per unit cell area of ~40 $Å^2$) between the (in order) Pd-, Co-, 50% Co-substituted, and 100% Co-substituted interfaces. For 50% Co-substitution, various substitution patterns were tested and averaged in the table for simplicity, as all were energetically positioned between the extreme cases of 0% and 100%. The differences are represented as an antisymmetric matrix, where a negative matrix element (i, j) indicates that the i-interface (row index) is more stable than the j-interface (column index). Matrix elements are color-coded: negative values are shown in blue, positive values in red, with a smooth interpolation between the extreme values. Zero values (on the diagonal) are represented in white. The table on the left corresponds to the calculation of interface energies with the shared oxygen layer attributed to the Al_2O_3, and the table on the right to the delafossite ($PdCoO_2$) constituent of the simulation cell, respectively. Adopted under the terms of a CC-BY license. © 2025 The authors[229]. 72

Figure 22. Simulated (SIM) and experimental (EXP) PACBEDs for the [010] orientations of $PdCoO_2$ from 4D STEM scans across the (a) $PdCoO_2/Al_2O_3$ and (b) $PdCoO_2/LaAlO_3$ interface. Adopted under the terms of a CC-BY license. © 2025 The authors[229]. 73

Figure 23. EELS elemental mapping of the (a) $PdCoO_2/Al_2O_3$ and (c) $PdCoO_2/LaAlO_3$ interface, obtained by extracting the indicated edge signals from a 2D spectrum image along the [010] zone axis. The films are initiated with a layer of $[CoO]^-$ and the elemental maps indicate chemical intermixing at the interface between the substrate and the film, while the sharp Pd signal shows that the Pd layer is not involved in the interfacial reconstruction. The O K edge elemental maps include a minor Pd signal due to overlapping of the respective edges in the EELS spectrum. The white arrows indicate the physical interface between substrate and film. (b) and (d) show the Co $L_{3,2}$ and O K edge signals, extracted along the numbered arrows indicated in (a) and (c). A strong Co signal is detectable up to two layers deep in both substrates, and a shift of the edge towards lower energy loss is observed, in combination with a change in the L_3/L_2 edge ratio. The O K edge shows features of the bulk materials far away from the interface and a mixed signal at the interface. Adopted under the terms of a CC-BY license. © 2025 The authors[229]. 75

Figure 24. (a) SSB ptychographic phase reconstruction from a 4D STEM dataset with 800×90 probe positions acquired across the $PdCoO_2/Al_2O_3$ interface. Repeating features in the substrate surface are indicated by white ticks. (b) High-magnification SSB phase reconstruction of the interface revealing the presence of subdomains, indicated by black boxes, with two opposing octahedral orientations of the CoO phase. (c) SSB phase reconstruction from a 4D STEM dataset with 600×100 probe positions acquired across the $PdCoO_2/LaAlO_3$ interface. The insets reveal subdomains with

two opposing octahedral orientations of the CoO phase. Adopted under the terms of a CC-BY license. © 2025 The authors[229]. 77

Figure 25. Orientation relationship between the (a) Al_2O_3, (b) $LaAlO_3$, and (c) $SrTiO_3$ substrates and the $PdCoO_2$ thin film with a 30° rotated growth of the film on the substrate. Lattice parameters are given for the indicated solid unit cells. Adopted under the terms of a CC-BY license. © 2025 The authors[229]. 78

Figure 26. Phase lock-in lattice-modulation analysis from SSB phase reconstructions along the [210] orientation of $PdCoO_2$ on (a) Al_2O_3 and (b) $LaAlO_3$. Extracted modulation amplitude and phase from the fast Fourier-transformed image reveal the presence of defects in the interfacial phase. Adopted under the terms of a CC-BY license. © 2025 The authors[229]. 79

Figure 27. HAADF STEM image of a decomposed $PdCoO_2$ thin film grown on a (111) $SrTiO_3$ substrate. The blue inset highlights an area without decomposition, revealing a $PdCoO_2$ thin film grown with 60° rotation instead of 30° rotation on the substrate in the inverted ABF (IABF) image. The green frame shows the film orientation relative to the (111) $SrTiO_3$ substrate for stable growth and the blue frame shows the actually observed orientation along the *c*-axis of the film. Adopted under the terms of a CC-BY license. © 2025 The authors[229]. 82

Figure 28. SSB ptychographic phase reconstruction from a 4D STEM dataset acquired across the $PdCoO_2/Al_2O_3$ interface of a PLD grown thin film along the [010] film orientation. The black arrows indicate the physical interface between the substrate and film. The insets show structural model overlays with the film and substrate models and the interfacial phase along the respective [010] zone axes. Adopted under the terms of a CC-BY license. © 2025 The authors[229]. 83

Figure 29. SSB ptychographic phase reconstruction from a 4D STEM dataset acquired across the $PdCoO_2/Al_2O_3$ interface of a PLD grown thin film along the [210] film orientation. The black arrows indicate the physical interface between the substrate and film. The insets show structural model overlays with the film and substrate models and the interfacial phase along the respective [210] zone axes. Adopted under the terms of a CC-BY license. © 2025 The authors[229]. 83

Figure 30. Low-magnification HAADF STEM images, *in-situ* RHEED patterns, and X-ray diffraction data of (a) $CuCrO_2/Al_2O_3$ and (b) $CuFeO_2/Al_2O_3$ along different zone axes of the films. For $CuCrO_2$, twin domains are observed in the [010] zone axis image, as indicated by the ticks in the magnified inset, whereas a single domain is present for $CuFeO_2$. Minor surface damage from sample preparation is visible on the $CuFeO_2$ sample. Asterisks (∗) in the X-ray diffraction patterns denote substrate reflections. Adopted under the terms of a CC-BY license. © 2025 The authors[277]. 90

Figure 31. HAADF and ABF STEM images of the $CuCrO_2/Al_2O_3$ interface along the (a) [210] and (b) [010] zone axes. The cutouts of the ABF images show an overlay of the structural model of the film, indicating the orientation of the oxygen octahedra along the (a) [210] and (b) [010] zone axes. Black and white ticks indicate the physical interface in each image. Adopted under the terms of a CC-BY license. © 2025 The authors[277]. 92

Figure 32. HAADF and ABF STEM images of the $CuFeO_2/Al_2O_3$ interface along the (a) [210] and (b) [010] zone axes. The cutouts of the ABF images show an overlay of the structural model of the film, indicating the orientation of the oxygen octahedra along the (a) [210] and (b) [010] zone axes. Black and white ticks indicate the physical interface in each image. Adopted under the terms of a CC-BY license. © 2025 The authors[277]. 93

Figure 33. Phase lock-in analysis of the $CuCrO_2/Al_2O_3$ interface along the [210] orientation. (a) IABF image of the interface and the Fourier transform of the entire field of view. The yellow points in the FFT indicate the lattice modulation selected for analysis. The extracted amplitude (b) and phase (c) of the lattice modulation highlight defects at the interface corresponding to misfit dislocations, characterized by a discontinuity in amplitude modulation and a 2π phase wrap-around. The strain analysis in (d) and (e) highlights the strain distribution around the dislocations. Adopted under the terms of a CC-BY license. © 2025 The authors[277]. 95

Figure 34. Phase lock-in analysis of the $CuFeO_2/Al_2O_3$ interface along the [210] orientation. (a) IABF image of the interface and the Fourier transform of the entire field of view. The yellow points in the FFT indicate the lattice modulation selected for analysis. The extracted amplitude (b) and phase (c) of the lattice modulation highlight defects at the interface corresponding to misfit dislocations, characterized by a discontinuity in amplitude modulation and a 2π phase wrap-around. The strain analysis in (d) and (e) highlights the strain distribution around the dislocations. Adopted under the terms of a CC-BY license. © 2025 The authors[277]. 96

Figure 35. Atomic-resolution multi-slice 4D STEM phase reconstructions of the $CuCrO_2/Al_2O_3$ interface along the (a) [210] and (b) [010] zone axes of the film. The misfit dislocations at the interface, one of which is highlighted by the solid box, alleviate the mismatch strain between substrate and film and cause an in-plane rotational distortion of the CrO_6 octahedra around the misfit dislocation cores (b). The interfacial layer involving the atomic reconstruction at the interface is indicated by black arrows. Adopted under the terms of a CC-BY license. © 2025 The authors[277]. 99

Figure 36. Atomic-resolution multi-slice 4D STEM phase reconstructions of the $CuFeO_2/Al_2O_3$ interface along the (a) [210] and (b) [010] zone axes of the film. The misfit dislocations at the interface, one of which is highlighted by the solid box, alleviate the mismatch strain between substrate and film and cause an in-plane rotational distortion of the FeO_6 octahedra around the misfit

dislocation cores (b). The interfacial layer involving the atomic reconstruction at the interface is indicated by black arrows. Adopted under the terms of a CC-BY license. © 2025 The authors[277]. 100

Figure 37. Full field of view images of the 4D STEM phase reconstructions along two different zone axes for $CuCrO_2$ and $CuFeO_2$ with the Al_2O_3 substrate on the left and the films on the right. The interfacial layer involving the atomic reconstruction at the interface is indicated by black arrows. Adopted under the terms of a CC-BY license. © 2025 The authors[277]. 101

Figure 38. Simulated (SIM) and experimental (EXP) PACBEDs for the [210] and [010]/[010] zone axes of (a) $CuCrO_2$ and (b) $CuFeO_2$. Adopted under the terms of a CC-BY license. © 2025 The authors[277]. 102

Figure 39. EELS elemental mapping and extracted edge spectra of (a) the $CuCrO_2/Al_2O_3$ and (b) the $CuFeO_2/Al_2O_3$ interfaces. A 2D spectrum image was acquired across the interfaces, as shown in the insets on the left. The elemental maps in (a) and (b) show extracted signals from the characteristic energy-loss edges of O (O K edge), Al (Al K edge), Cr (Cr $L_{3,2}$ edge), Fe (Fe $L_{3,2}$ edge), and Cu (Cu $L_{3,2}$). The white ticks indicate the physical interface between the substrate and film. For $CuCrO_2$ (a) and $CuFeO_2$ (b), the $L_{3,2}$ edge signals and the O K edges are shown on the right. Each numbered signal was extracted along the numbered arrows shown in the Cr/Fe elemental maps on the left. Adopted under the terms of a CC-BY license. © 2025 The authors[277]. 104

List of Tables

Table 1. Lattice mismatch calculations for the $PdCoO_2/Al_2O_3$, $PdCoO_2/LaAlO_3$, and $PdCoO_2/SrTiO_3$ interfaces using Equation (42)[173]. Adopted under the terms of a CC-BY license. © 2025 The authors[229]……...78

Table 2. Reconstruction parameters for iterative ptychographic reconstructions. Adopted under the terms of a CC-BY license. © 2025 The authors[277]…….98

Abstract

Complex functional oxides exhibit a wide range of emergent electronic and structural properties, arising from the intrinsic competition between charge, spin, lattice, and orbital degrees of freedom. The interplay between these interactions continuously leads to the discoveries of novel functional oxides, deepening the understanding of correlated materials and expanding their potential applications in electronic and quantum devices. This thesis highlights the critical role of (scanning) transmission electron microscopy ((S)TEM) in exploring such interatomic structure-property correlations in oxides and oxide heterostructures.

Before diving into their practical application, the introductory chapter provides an overview of key methodologies within the broad spectrum of TEM techniques relevant to this work, with particular emphasis on four-dimensional STEM (4D STEM). Electron ptychographic phase reconstructions play a central role in the third and fourth chapters of this thesis, enabling high-resolution imaging with strong contrast not only for heavy elements, but also for light ones, especially oxygen, which is understandably a crucial capability for studying oxide materials.

The second chapter of this thesis underscores the capabilities of TEM in observing rare phenomena in 4*d* transition metal compounds, exemplified by the atomic-scale investigation of an unconventional structural transition in the mixed-valence ruthenate, $NaRu_2O_4$, at elevated temperatures. While retaining metallicity, the material undergoes an atypical Peierls-type transition with emergent charge order at a transition temperature of approximately 535 K. *In-situ* TEM diffraction and STEM imaging, combined with atomic displacement analysis, provide direct microscopic evidence of the reversible Peierls-type transition, characterized by a pronounced dimerization of the quasi-one-dimensional ruthenium chains along the crystallographic *b*-axis. As the coexistence of metallic conductivity, dimerization, and charge ordering is highly unusual, investigating such transitions in detail is essential for developing robust phenomenological models and deepening our understanding of correlated electron systems, which is a necessary step toward harnessing their exceptional properties in functional oxide devices.

The third and fourth chapters of this thesis demonstrate how STEM can contribute to the early stages of translating a material system with unique properties into functional oxide heterostructure devices by applying its techniques to investigate stable growth phenomena of functional ABO_2 delafossites on various substrates. The successful integration of these materials into devices depends on achieving high-quality thin films, yet their unique lattice geometry poses significant challenges, often resulting in inconsistent growth behavior of different delafossites even when using the same substrate. While lattice mismatch alone does not fully account for these variations, unidentified

stabilization mechanisms appear to facilitate epitaxial growth in certain cases, and it is a central objective of this work to investigate these on the atomic scale.

The work presented in the third chapter of this thesis employs advanced STEM techniques— especially 4D STEM electron ptychography (non-iterative phase reconstructions), combined with spectroscopy and conventional imaging— to identify a secondary interfacial phase that stabilizes $PdCoO_2$ delafossite films grown *via* molecular beam epitaxy (MBE) on Al_2O_3 and $LaAlO_3$ substrates. The discovery of this secondary phase provides novel insights into the interfacial stabilization mechanism of $PdCoO_2$, which significantly differs from conventionally observed strain relief mechanisms in oxide heterostructures. Understanding these stabilization mechanisms represents a major step toward the reliable integration of delafossite thin films into functional electronic devices with improved growth strategies.

Building on these findings, the fourth chapter examines the interfacial reconstruction of delafossites with different *A* and *B* cations on the same Al_2O_3 substrates to investigate whether the unconventional film stabilization mechanism previously identified for Pd-based delafossites is a material-specific phenomenon or represents a general stabilization mechanism for delafossite thin films. Here, the combination of 4D STEM electron ptychography (iterative phase reconstructions), spectroscopy, and conventional imaging reveals that a misfit dislocation network at the $CuCrO_2/Al_2O_3$ and the $CuFeO_2/Al_2O_3$ interface, along with monolayer-deep chemical intermixing, plays a crucial role in strain relaxation. This mechanism differs significantly from the one observed in the Pd-based delafossites of the third chapter, as the stabilization involves a reconstruction of the film itself, rather than the formation of a secondary phase at the interface.

These material-specific interfacial stabilization mechanisms, highlight the critical role of the interface structure in the stabilization of delafossite thin films. They must be carefully considered when designing oxide heterostructures for electronic applications, as it is reasonable to assume that they will influence the functional properties of the film during device operation.

Zusammenfassung

Komplexe funktionelle Oxide weisen ein breites Spektrum an elektronischen und strukturellen Eigenschaften auf, die aus dem intrinsischen Austausch zwischen Ladungs-, Spin-, Gitter- und orbitalen Freiheitsgraden entstehen. Das komplexe Zusammenspiel dieser Wechselwirkungen führt zur kontinuierlichen Entdeckung neuartiger funktioneller Oxide, vertieft das Verständnis über korrelierte Materialien und erweitert deren Anwendungsmöglichkeiten in elektronischen und quantenmechanischen Bauelementen. Die entscheidende Rolle, welche die (Raster-) Transmissionselektronenmikroskopie ((R)TEM) bei der Erforschung der Struktur-Eigenschafts-Korrelationen auf atomarer Ebene in Oxiden und Oxid-Heterostrukturen einnimmt, wird in dieser Arbeit dargestellt.

Bevor auf deren praktische Anwendung eingegangen wird, gibt das einleitende Kapitel dieser Arbeit einen Überblick über die wichtigsten, im Rahmen dieser Arbeit relevanten Methoden innerhalb des breiten Spektrums der TEM-Techniken, mit besonderem Fokus auf die vierdimensionale RTEM (4D RTEM). Insbesondere die elektronenptychographischen Phasenrekonstruktionen spielen im dritten und vierten Kapitel dieser Arbeit eine bedeutende Rolle, da durch sie eine hochauflösende Bildgebung mit starkem Kontrast nicht nur für schwere Elemente ermöglicht wird, sondern auch für leichte—insbesondere für Sauerstoff—was nachvollziehbare Vorteile für die Untersuchung von Oxidmaterialien bietet.

Das zweite Kapitel dieser Arbeit unterstreicht die Möglichkeiten der TEM zur Beobachtung seltener Phänomene auf atomarer Ebene in 4*d*-Übergangsmetalloxiden, beispielhaft dargestellt anhand eines unkonventionellen Phasenübergangs, der bei der Erhitzung von gemischt-valentem $NaRu_2O_4$ Ruthenat auftritt. Ohne seine metallische Leitfähigkeit zu verlieren, durchläuft dieses Material bei einer Übergangstemperatur von etwa 535 K eine untypische Phasenumwandlung, die einer Peierls-Umwandlung mit Ladungsordnung ähnelt. *In-situ* TEM-Beugung und RTEM-Bildgebung, in Kombination mit der Analyse der atomaren Verschiebungen, liefern direkte mikroskopische Nachweise zu dieser reversiblen Umwandlung, der eine ausgeprägte Dimerisierung der quasi-eindimensionalen Rutheniumketten entlang der kristallographischen *b*-Achse zu eigen ist. Da die Koexistenz von metallischer Leitfähigkeit, Dimerisierung und Ladungsordnung äußerst ungewöhnlich ist, ist die detaillierte Untersuchung solcher Übergänge essenziell, um fundierte phänomenologische Modelle zu entwickeln und unser Verständnis korrelierter Elektronensysteme zu vertiefen—ein notwendiger Schritt, um die außergewöhnlichen Eigenschaften dieser Materialien in Bauteilen aus funktionalen Oxiden nutzbar zu machen.

Das dritte und vierte Kapitel dieser Arbeit veranschaulichen, wie RTEM zum Verständnis beitragen kann, wie ein Materialsystem mit einzigartigen Eigenschaften in funktionelle Oxid-Heterostrukturen

überführt werden kann, indem mit ihr das Auftreten von stabilem Wachstum von funktionalen ABO_2-Delafossiten auf verschiedenen Substraten untersucht wird. Die erfolgreiche Integration dieser Materialien in elektronische Bauelemente ist auf die Herstellung qualitativ hochwertiger Dünnschichten angewiesen. Die einzigartige Gittergeometrie der Delafossite stellt allerdings eine große Herausforderung dar, da diese oft zu uneinheitlichem Wachstumsverhalten verschiedener Delafossite selbst auf dem gleichen Substrat führt. Während das Missverhältnis zwischen den Gitterkonstanten von Substrat und Filmen allein dieses Verhalten nicht vollständig erklären kann, scheinen bisher unbekannte Stabilisierungsmechanismen das epitaktische Wachstum in bestimmten Fällen zu ermöglichen, und ein zentrales Ziel dieser Arbeit ist es, diese Mechanismen auf atomarer Ebene zu untersuchen.

Konkret werden für die Untersuchungen des dritten Kapitels fortschrittliche RTEM-Techniken—insbesondere die 4D RTEM-Elektronenptychographie (nichtiterative Phasenrekonstruktionen) in Kombination mit Spektroskopie und konventioneller Bildgebung—eingesetzt, um eine sekundäre Grenzflächenphase zu identifizieren, die die $PdCoO_2$-Delafossitfilme stabilisiert, welche mittels Molekularstrahlepitaxie auf Al_2O_3- und $LaAlO_3$-Substraten gewachsen wurden. Die Entdeckung dieser sekundären Phase liefert neue Einblicke in den Grenzflächen-Stabilisierungsmechanismus von $PdCoO_2$, der sich deutlich von den konventionell beobachteten Mechanismen zur Spannungsrelaxation in Oxid-Heterostrukturen unterscheidet. Das Verständnis dieser Stabilisierungsmechanismen stellt einen entscheidenden Schritt für die zuverlässige Integration von Delafossitdünnfilmen in funktionale elektronische Bauelemente und die Entwicklung verbesserter Synthesestrategien dar.

Aufbauend auf diesen Ergebnissen wird im vierten Kapitel die Grenzflächenrekonstruktion von Delafossiten mit anderen *A*- und *B*-Kationen auf den gleichen Al_2O_3-Substraten untersucht, um zu ermitteln, ob es sich bei dem vorherig identifizierten unkonventionellen Stabilisierungsmechanismus um ein materialspezifisches Phänomen oder um einen allgemeinen Mechanismus für die Stabilisierung von Delafossitdünnfilmen handelt. Hier offenbart die Kombination von 4D RTEM-Elektronenptychographie (iterative Phasenrekonstruktionen), Spektroskopie und konventioneller Bildgebung, dass die Verknüpfung eines Versetzungsnetzwerks an der $CuCrO_2/Al_2O_3$- und der $CuFeO_2/Al_2O_3$-Grenzfläche mit einer monomolekularen Vermischungsschicht („monolayer intermixing“) eine entscheidende Rolle bei der Spannungsrelaxation spielt. Dieser Mechanismus unterscheidet sich deutlich von dem, der in den auf Pd-basierenden Delafossiten des dritten Kapitels beobachtet wird, da hier die Stabilisierung über eine Rekonstruktion des Films selbst erfolgt und nicht über die Ausbildung einer sekundären Phase an der Grenzfläche.

Die im dritten und vierten Kapitel identifizierten materialspezifischen Stabilisierungsmechanismen, unterstreichen die entscheidende Rolle der Grenzflächenstruktur bei der Stabilisierung von Delafossitdünnfilmen. Sie müssen bei der Entwicklung von Oxid-Heterostrukturen für elektronische Anwendungen sorgfältig berücksichtigt werden, da anzunehmen ist, dass sie die funktionalen Eigenschaften der Filme im Bauelement beeinflussen können.

1 Introduction

1.1 Transmission electron microscopy

1.1.1 Fundamentals and limitations

Since the first transmission electron microscope (TEM) was constructed in 1931 by Max Knoll and Ernst Ruska, it has become an essential instrument for the structural and compositional characterization of materials across length scales ranging from the micrometer to the angstrom level[1]. Advancements in sample preparation, aberration correction, detector performance, and computational capabilities have opened the door to a wide range of imaging and analytical techniques that are continuously optimized and improved[1-3]. Nowadays, many natural sciences like physics, chemistry, and biology benefit daily from contribution by TEM and it plays a particularly crucial role in advancing research areas like nanotechnology, renewable energy, and medicine[4-6].

Electron microscopy was originally developed to address the resolution limits of light microscopes, which are constrained by the wavelength of visible light (approximately 380–750 nm). According to the Rayleigh criterion for light microscopy, the shortest resolvable distance r_d can be estimated as follows:

$$r_d = 0.61 \cdot \frac{\lambda}{n \cdot \sin(\alpha)} \tag{1}$$

Here, λ is the wavelength of the light used, n denotes the refractive index of the medium between the lens and the specimen, and α is the semi-collection angle of the magnifying lens. The term $n \cdot \sin(\alpha)$ is commonly referred to as the numerical aperture of the system[7]. With an electron wavelength of 2.5079 pm for a 200 kV electron beam, a transmission electron microscope can, in theory, achieve a magnification of 200,000 times better than a perfect light microscope, easily reaching atomic or even sub-atomic resolution. Thus, in principle, TEMs are capable of resolving structures at the picometer scale due to the extremely small de Broglie wavelength of electrons. In practice, however, this high level of resolution is unattainable, and the achievable resolution was limited to approximately 0.2 nm for a long time, depending on the acceleration voltage and on the manner in which electrons are manipulated and guided through the microscope, as explained in the following sections[8,9].

In principle, TEMs consist of the same basic components as light microscopes, namely an illumination source, a condenser system before and an objective system after the investigated sample, plus various apertures and filters to alter the characteristics of the beam to improve the resulting signal in one's favor, only that all these components need to work with electrons instead

of photons[1,10]. In a conventional TEM, electrons are emitted from the electron source through thermionic, Schottky, or field emission. The electron beam must be coherent, stable, and bright, with a narrow energy spread to enable precise imaging and spectroscopic analysis[11]. Thermionic emission involves heating a metal filament, usually tungsten, to release electrons, which are then accelerated by an electric field. This method is relatively simple, affordable, and stable, but produces a rather broad energy distribution with lower brightness and coherence compared to other sources[12]. Field emission, on the other hand, employs a strong electric field to pull electrons from a sharp metal tip. Since this emission depends on Fowler-Nordheim tunneling of the electrons, the resulting beam is highly coherent with a narrow energy spread[13]. This makes it ideal for high-resolution applications, however, it is a rather expensive and sensitive technique[14]. Finally, Schottky emission is a hybrid method between the former two, which enhances thermionic emission by applying a voltage to reduce the work function of the emitter, thereby allowing for improved brightness and stability compared to pure thermionic sources[10,15]. The combination of source and emission field is generally called an electron gun, and regardless of the method chosen for the emission, once the electrons exit the gun system, a linear accelerator is used to speed them up to their final energy, after which a system of condenser lenses and apertures allows the manipulation of the high-energy beam to result in the desired kind of illumination of the sample area[15].

This manipulation of the electron beam is achieved through two physical effects. First, the interaction between electrons and a magnetic field causes the electrons to experience a Lorentz force, thus, electromagnets can precisely control the electron trajectory[16]. Additionally, electrostatic fields can deflect electrons at a constant angle. By coupling two deflections in opposite directions with a small intermediate gap, a shift in the beam path can be created, facilitating beam shifting. Unlike glass lenses, the focusing power of magnetic lenses can easily be adjusted by varying the electric current in their coils. Unfortunately, also unlike (modern) glass lenses, electromagnetic lenses are far from perfect due to intrinsic lens aberrations. The primary limiting factor is the spherical aberration, which is caused by lens fields acting inhomogeneously on off-axis rays. This results in a probe that deviates from the ideal Airy disk, which is the 2D Fourier transform of the illuminated aperture in the back focal plane. Consequently, even though electron wavelengths at high voltages can theoretically provide atomic-scale resolution, aberrations prevent uncorrected microscopes from achieving such limits[10,15,17].

1.1.2 Lens aberrations and aberration correction

The primary factors limiting a TEM's resolution include spherical aberration, chromatic aberration, and astigmatism of the electromagnetic lenses[18,19]. Spherical aberration occurs when the lens field behaves unevenly for off-axis rays, meaning that the farther an electron deviates from the optical axis, the more strongly it is bent toward the center as it passes through the lens. For the first

operation principle of a TEM, in high-resolution TEM (HRTEM), spherical aberration is particularly problematic in the objective lens, as it limits the level of detail that can be resolved in images, with all subsequent lenses amplifying any introduced error. Similarly, in the second operation mode, scanning TEM (STEM), spherical aberration is detrimental in the condenser lenses, which are responsible for forming the smallest and highest-current beam probe on the sample.

The deviation from the ideal trajectory, caused by spherical aberrations (C_S), manifests in the phase of the electron wave. To limit the angular range of aberration effects, apertures are used[2,8,20]. Mathematically, the electron wave passing through the lens and the aperture system is described as a complex function called the aperture function $A(\boldsymbol{K})$[15,21-23].

$$A(\boldsymbol{K}) = T(\boldsymbol{K})\, exp\big(i\chi(\boldsymbol{K})\big) \tag{2}$$

with the wave amplitude $T(\boldsymbol{K})$ representing the aperture in the focal plane of the probe forming lens in terms of a top-hat function:

$$\begin{aligned} T(\boldsymbol{K}) &= 1 \quad \text{if } |\boldsymbol{K}| < K_{max} \\ T(\boldsymbol{K}) &= 0 \quad \text{if } |\boldsymbol{K}| \geq K_{max} \end{aligned} \tag{3}$$

Thus, for reciprocal-space vectors $\boldsymbol{K}$, which are not allowed to pass through the aperture, the amplitude of the wave function is zero. $\chi(\boldsymbol{K})$ describes the geometrical aberration function, *i.e.,* the phase of the electron wave affected by lens imperfections[21]. The breakthrough for the construction of C_S correctors, with the purpose of compensating for spherical aberration in magnetic lenses, occurred with the introduction of non-round lenses, a concept first proposed by Scherzer in 1947[24]. These multipole lenses are capable of generating a negative value of spherical aberrations, effectively canceling the positive spherical aberrations induced by the round lenses. Aberration correction is nowadays achieved through a complex, computer-controlled system of quadrupoles/octupoles or hexapoles[8,20,25]. Currently, there are two main approaches: the CEOS system, developed by Rose and colleagues in Germany, used for both STEM probe correction and TEM image correction, and the system developed by Krivanek *et al*., used in Nion STEMs and retrofitted to VG STEMs[26,27]. The CEOS systems mounted in the transmission electron microscopes at the Stuttgart Center for Electron Microscopy, used for the experiments in this thesis (JEOL ARM200F microscope with a CETCOR - C_S corrector for HRTEM and a JEOL ARM200F microscope with a DCOR - C_S corrector for STEM), are advanced hexapole-type C_S correctors. The correctors have proven to be capable of improving the resolution up to ~50 pm[28,29].

In addition to spherical aberration, other factors—including chromatic aberration, axial coma, astigmatism, and defocus—contribute to image degradation in TEM and STEM. Chromatic aberration originates from the finite energy spread of the electron source. Electrons with slightly

different kinetic energies are focused at different planes along the optical axis. Higher-energy electrons exhibit longer focal lengths in comparison to electrons with lower kinetic energies[18,19]. For high acceleration voltages and microscopes equipped with field emission sources, resulting in a narrow energy spread of the beam, chromatic aberration is not the limiting factor compared to the effects of spherical aberration[8]. However, the implementation of an additional chromatic aberration corrector (C_C corrector) can improve spatial resolution[30,31].

Astigmatism occurs when the electron lens exhibits different focal lengths along orthogonal azimuthal directions, commonly 90°, leading to elliptically shaped beam profiles rather than circular ones. Astigmatism arises due to asymmetries in the electromagnetic lens fields—specifically, when the lens does not produce a perfectly rotationally symmetric magnetic field due to imperfections in the lens design, mechanical misalignments, material inhomogeneities in the pole pieces, *etc*. Astigmatism is routinely corrected using stigmators, which are small electromagnetic or electrostatic coils that apply a controlled distortion to the lens field to counteract the asymmetry and to restore circular symmetry to the probe or image[15].

Axial coma is an aberration in (S)TEM that occurs when the electron beam is tilted with respect to the optical axis of the microscope and causes electrons entering the lens system at different angles to focus at different lateral positions and with different focal lengths. This leads to asymmetric distortions in the image, which can be minimized by aligning the electron beam along the coma-free axis of the microscope[15].

Defocus is the simplest form of aberration and is easily adjusted manually during imaging[15].

1.1.3 Imaging

In the TEM, the illumination of a material with the high-voltage electron beam, usually 60–300 kV, causes the electrons to interact with the sample, producing a variety of signals, as shown in Figure 1(a). Elastically scattered electrons are used for HRTEM, STEM, or diffraction imaging. Inelastically scattered electrons and their secondary effects are useful for analytical spectroscopy, such as X-ray energy-dispersive spectroscopy (XEDS) or electron energy-loss spectroscopy (EELS)[15].

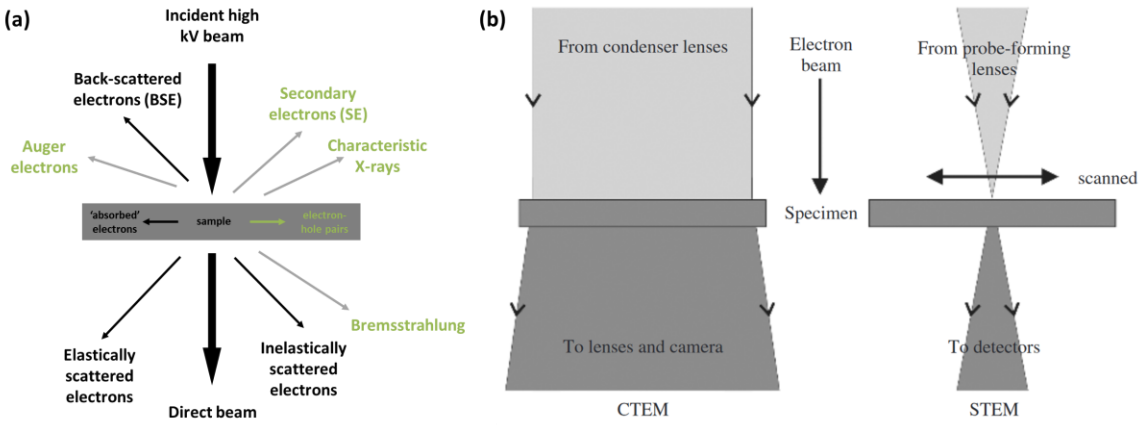

Figure 1. (a) Signals generated by electrons interacting with a sample material. (b) Two basic conditions under which a TEM is operated: conventional transmission electron microscopy (CTEM) with parallel beam illumination, and scanning transmission electron microscopy (STEM) with a convergent electron beam scanned over the sample surface. Adopted and modified with permission, © Springer-Verlag US 2009[15].

Generally, two configurations of TEM offer distinct advantages for material characterization. By adjusting the arrangement of electromagnetic lenses and apertures, the microscope can be operated either as a conventional transmission electron microscope (CTEM) or as a scanning transmission electron microscope (STEM) (Figure 1(b)). The operational mode and the consequential interaction between the sample and the electron beam dictate the application of various contrast mechanisms in TEM. Contrast may arise from differences in thickness or density of the sample, commonly referred to as "mass-thickness contrast", as well as from variations in atomic number ("Z contrast"), crystal structure or orientation ("diffraction contrast"), and the quantum-mechanical phase shifts induced by individual atoms as electrons traverse them ("phase contrast")[10,15]. The following paragraphs provide a more detailed explanation of the contrast mechanisms that prove particularly useful for the analysis of data acquired within the framework of this PhD thesis.

1.1.3.1 CTEM - Conventional transmission electron microscopy

In CTEM, the specimen is illuminated with a plane electron wave, a broad, almost parallel electron beam. After interacting with the sample, unscattered and scattered electrons exit the bottom surface of the specimen, having undergone trajectory deviations due to their interaction with the material. CTEM offers two methods of specimen observation by projecting either the image plane (imaging mode) or the back-focal plane (diffraction mode) of the objective lens onto the viewing screen or the detector. Switching between the two modes is usually accomplished by adjusting the intermediate lens system accordingly. In imaging mode, an image of the illuminated sample area can be obtained with contrast arising from amplitude contrast (mass-thickness contrast, diffraction contrast) or phase contrast[15,32]. When the objective aperture is used to allow only the central diffraction spot electrons to pass (*i.e.,* unscattered and forward-scattered electrons), while all other

electrons are blocked by the aperture, a bright-field (BF) image is obtained, and conversely, if the aperture allows only the signal from diffracted beams to pass, a dark-field (DF) image is formed[15]. Not employing the objective aperture leads to an overlay of both images, which normally resembles the BF image with less overall image contrast. In diffraction mode, the acquired signal resembles a pattern of dots in the case of a single crystal, a series of rings in the case of a polycrystalline material, and diffuse rings in the case of an amorphous material. A selected area electron diffraction (SAED) aperture may be used to define a specific region of the illuminated specimen area from which the signal will be recorded. The diffraction mode is especially useful for providing the experimentalist with knowledge about structural symmetries and long- and short-range order or disorder, as highlighted in the course of this thesis[15,33]. When the parallel beam is converged, the range of incidence angles increases, resulting in the broadening of the diffraction spots into disks in the back-focal plane, and one obtains a convergent beam electron diffraction (CBED) pattern. In CTEM, CBED patterns provide additional information about the sample that is not obtainable through parallel-beam diffraction, including crystal symmetry, structure factors, and lattice strain[34,35]. Moreover, CBED patterns are essential for image formation in STEM, of which the following section outlines the fundamental principles.

1.1.3.2 STEM - Scanning transmission electron microscopy

In the scanning configuration, a convergent electron beam with a tunable diameter is scanned across the sample using scanning coils[36]. As the beam interacts with the material, it generates a CBED pattern at each probe position. These patterns result from the interference of unscattered, forward-scattered, and diffracted electrons and can be detected by various detector configurations. The final image is formed by integrating the detected signal across all probe positions, with each position corresponding to a pixel in the constructed image. The observed contrast in these images depends on the illumination conditions and the specific detector setup, where different detectors selectively capture electrons based on their scattering angles. BF detectors selectively collect a portion of electrons from the direct beam, while annular BF (ABF) detectors detect electrons scattered within a defined annular region inside the BF disk. In BF imaging, contrast arises from the interference between direct and scattered electrons. Conversely, annular DF (ADF) detectors exclusively collect scattered electrons by encircling the direct beam but allowing the BF disk to pass through a central hole. Opposite to BF, the resulting ADF image contrast is primarily not dependent on interference effects, but on sample composition and thickness. Recent advances in STEM aim to collect additional information by segmenting annular detectors into multiple quadrants or by using a direct electron camera (DEC) to record the entire CBED pattern at each probe position[37].

The latter enables the acquisition of four-dimensional STEM (4D STEM) datasets, consisting of a 2D CBED pattern for each point in a 2D raster scan. This approach enables a more comprehensive

analysis, including virtual imaging, orientation mapping, strain mapping, phase contrast imaging, *etc*., though it requires greater data storage and results in slower acquisition speeds[38].

1.1.4 Spectroscopy

1.1.4.1 EELS - Electron energy-loss spectroscopy

Electron energy-loss spectroscopy (EELS) is the investigation of the energy distribution of electrons transmitted through a specimen. During scattering, electrons may lose (inelastic scattering) or not lose (elastic scattering) energy. The energy loss of inelastically scattered electrons can be related to the sample's chemistry and electronic structure (*e.g.*, valence states, dielectric properties, band gaps, thickness, *etc*.)[39,40]. In a spectrometer for electrons, generally called an energy filter in TEM, transmitted electrons pass through a magnetic prism and are deflected by a magnetic field through an angle of ≥ 90°. Electrons that have undergone a high energy loss are deflected further than electrons with low loss, as they travel through the spectrometer at the end of the microscope column. A detector located behind the energy filter thus captures a spectrum in which the intensity distribution is a function of the energy loss the individual electrons suffered during their transmission through the sample[15].

In general, an EEL spectrum is divided into two parts: the low-loss spectrum (energy loss < ~50 eV) and the high-loss spectrum (energy loss > ~50 eV). The low-loss spectrum includes the zero-loss and plasmonic peaks, providing information about dielectric properties and band structure. The high-loss spectrum contains element-specific ionization edges from inner-shell ionization, offering information about the sample chemistry[39]. Element-specific electron energy losses are utilized in the field of energy-filtered TEM (EFTEM), where instead of a spectrum, an image is acquired. To select the specific energy range of electrons that should contribute to the EFTEM image, a slit aperture within the energy filter is inserted into the energy-dispersed beam before the filter lens system transforms it back to be spatially-resolved[41]. Using the energy filter in this way to let only the zero-loss peak pass is called zero-loss filtering, which can help to increase the contrast and resolution of the resulting image, the latter due to the reduction of the influence of the lenses' chromatic aberration[42].

In this thesis, the primary emphasis is directed toward the investigation of high-loss regions through the acquisition of 2D spectrum images, *i.e.,* the acquisition of a full EELS spectrum for each probe position during a 2D STEM scan. The high-loss spectra can be directly correlated with the unoccupied density of states of correlated oxide materials, as element-specific edges represent intra- and interatomic excitations from core states to states above the Fermi level[39]. Using state-of-the-art instrumentation, such energy-loss near-edge structure (ELNES) investigations can be conducted at

the atomic scale, facilitating unprecedented characterization of electronic reconstructions at interfaces[43-45]. Focusing on transition metal oxides and interfaces, the ELNES provides valuable insights into the local electronic structure and chemical composition of materials, particularly when examining transition metal $L_{3,2}$-edges and the oxygen K-edge across an oxide heterostructure interface[46-48]. The $L_{3,2}$-edges, which correspond to transitions from $2p_{1/2}$ and $2p_{3/2}$ core levels to unoccupied 3*d* states near the Fermi level, are sensitive to the oxidation state, crystal field effects, and hybridization. Shifts in the $L_{3,2}$-edge indicate changes in oxidation state, while variations in the fine structure reflect modifications in the local coordination environment or symmetry[49]. Similarly, the oxygen K-edge, arising from transitions from 1*s* core levels to unoccupied 2*p* states, provides information about the oxygen coordination environment and hybridization with transition metal 3*d* states[48]. Changes in the pre-peak intensity of the K-edge reveal variations in bonding or may indicate the presence of oxygen vacancies[43-45]. Compared to other spectroscopic techniques like X-ray absorption spectroscopy or neutron scattering, this ability to differentiate between different electronic states at the atomic scale is unique to EELS[48].

1.1.4.2 XEDS - X-ray energy-dispersive spectroscopy

When an electron undergoes inelastic scattering, it can transfer energy to an electron within the sample, causing it to be ejected from an inner shell and creating an electron hole. This hole is subsequently filled by an electron from an outer shell with higher energy, during which the released energy may form an element-specific characteristic X-ray. The amount and energy of characteristic X-rays are detected by an energy-dispersive spectrometer positioned above the specimen plane in the TEM. X-ray energy-dispersive spectroscopy (XEDS) allows for quantitative and qualitative elemental analysis[50]. It is particularly advantageous for analyzing heavy elements, as the probability of X-ray emission increases with the atomic weight, whereas the emission probability of Auger electrons decreases. In Auger electron events, the excess energy is not emitted as an X-ray, but rather transferred to another electron in the sample, causing it to escape the material[51-53].

1.2 Electron ptychography

Since 4D STEM, particularly electron ptychography, plays a key role in this study on investigating oxide heterostructure interfaces, all considerations essential to the analysis are presented in the following sections. Following a fundamental explanation of the methodology relevant to this work, the final section provides a practical guide to acquiring 4D STEM datasets. This guide is based on my personal experience with the MerlinEM Medipix3 detector installed on the probe-C_S-corrected JEOL ARM200F microscope.

1.2.1 4D STEM detectors

The development of STEM has seen substantial progress since its inception, marked by significant improvements in imaging modes and detector technologies. Early STEM imaging primarily focused on BF and ADF modes, which provide contrast based on transmitted and scattered electrons within specific angular ranges. The detectors usually consist of a scintillator and photomultiplier tube, and for each probe position, a single intensity value is returned by integrating over all electrons registered, as illustrated in Figure 2(a). Contrast arises from variations in the signal as a function of probe position, with each raster scan producing a 2D image[54,55].

Over time, detector technology and their usage evolved, enabling more advanced imaging methods. For instance, ABF imaging[56,57] was introduced to visualize lighter elements, and segmented detectors, as illustrated in Figure 2(b), allow for differential phase contrast (DPC) imaging, as for each scan position 4–32 or more intensity values are acquired from electrons scattered to different detector segments. Image contrast arises from the signal difference between detector segments for each probe position, caused by sample-induced beam shifts or intensity fluctuations in the BF disk, which may, for instance, hold information on electrostatic fields in the sample[58,59].

Historically, the acquisition of whole diffraction patterns for advanced STEM analysis was limited by the acquisition characteristics of CCDs (charge-coupled devices), which were developed in the 1990s and have since been widely used in TEM. While a substantial step forward from photo plates, they feature relatively slow acquisition speeds and a low dynamic range, and their use of scintillators to convert electrons to photons reduces the detective quantum efficiency (DQE) of the detectors[38,60]. The situation for 4D STEM has changed with the most recent development of pixelated direct electron detectors (Figure 2(c)), which now allow for capturing full diffraction patterns at each scan position with sufficient acquisition speeds. This enables the acquisition of 4D STEM datasets consisting of two real-space scan dimensions and two reciprocal-space detector coordinates.

To meet the diverse needs of STEM imaging and spectroscopy, different detector technologies with distinct features have been developed. For example, so-called pnCCDs are modified CCD detectors without a scintillator, offering an exceptionally high frame rate, but a limited dynamic range due to a small pixel depth[61]. Hybrid pixel array detectors (PADs), like the EMPAD[62] and MerlinEM Medipix3[63] detectors, consist of an array of photodiodes bump bonded to an application-specific integrated circuit and detect electrons directly *via* electron-hole pair formation in the active layer[64-66]. These detectors, with large and deep pixels, offer high dynamic range at the expense of angular resolution, as only a limited number of pixels can be employed within the fixed array size. Such detectors are particularly advantageous for high-dose imaging. Monolithic active pixel sensors

(MAPS), such as the Gatan K2 and K3 detectors[67], use CMOS (complementary metal-oxide semiconductor) chips with a sensitive doped epitaxial layer and feature a large number of thin pixels[68]. These detectors provide significant benefits for spectroscopic imaging with minimal beam spreading; however, they have a limited dynamic range, making them again less suitable for high-dose imaging[38,60].

Direct electron detectors are not only advantageous for STEM, but also for CTEM imaging, since they feature enhanced sensitivity, improved resolution, and reduced detector noise. They enable faster acquisition with lower electron doses and, by utilizing their enhanced dynamic range, improve contrast for weakly scattering objects. Thus, these detectors can be used in CTEM to reduce radiation damage to delicate samples, and their enhanced contrast and wider dynamic range further allow to capture fine structural details, making them particularly useful in applications like cryo-EM[60].

For STEM experiments, the choice of an appropriate 4D STEM detector should be based on the specific application. Since the experiments in this work focus on recording CBEDs—simultaneously capturing strong signals in the BF disk and sparse scattering in the DF region—a MerlinEM Medipix3 camera from Quantum Detectors was used. The detector's high dynamic range enables the simultaneous recording of both BF and DF signals with sufficient readout speed for fast scanning.

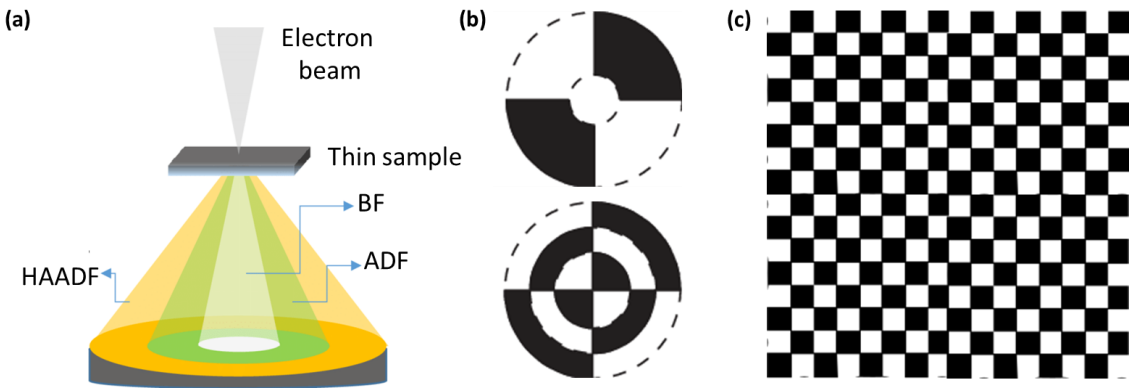

Figure 2. Schematics of different STEM detecting modes. (a) Conventional detectors collecting single intensity values for each probe position. (b) Segmented detectors that collect multiple intensity values (4–32 or more channel readouts) for each beam position in the raster scan, and (c) pixelated detectors that record full diffraction patterns at each scan position, resulting in 4D datasets.

In principle, all standard imaging methods shown in Figure 2 can be derived from a single 4D dataset. By using so-called virtual detectors, 2D images can be calculated from the dataset through masking with various detector geometries. Advanced detector geometries, such as virtually segmented detectors, can also be derived[69,70]. This approach not only allows traditional STEM

imaging techniques to be applied, but also facilitates the direct acquisition of the far-field intensity distribution, enabling advanced data analyses, such as phase reconstructions *via* electron ptychography, which are described in detail in the following paragraphs.

1.2.2 The phase problem

If a thin specimen were illuminated by a convergent electron beam without the use of apertures and lenses, any changes in the electron wave would arise solely from the sample and depend exclusively on the atomic potential of the material. However, to converge the electrons into a small probe, they are directed through a system of apertures and electromagnetic lenses as they travel down the microscope column. Because electromagnetic lenses are inherently imperfect, aberration correctors and apertures are employed to reduce lens aberration effects and limit their angular range, but conveniently, a particular objective (de)focus can be set just by changing the electric current of the lenses. This probe-forming system alters the electron wave incident on the sample[15,21-23].

Figure 3 provides a schematic representation of the beam path during a 4D STEM experiment. A convergent electron probe is scanned over the sample, and at each probe position, a CBED is recorded. In the aperture plane, the electron wave that passes through the lens and aperture system is described by a complex function, referred to as the aperture function, as shown in Equation (2)[15,71,72]. For a perfectly coherent electron beam unaffected by lens imperfections, the phase $\chi(\boldsymbol{K})$ would be constant at constant convergence angles. Unfortunately, in reality, it is strongly affected by axial aberrations of the system[22,73]. Mathematically, the formation of a convergent probe by the lens system is equivalent to the inverse Fourier transform of the aperture function $A(\boldsymbol{K})$ in reciprocal space, resulting in the probe function $P(\boldsymbol{R})$ in real space[21]. For simplicity, researchers in the field of ptychography have adopted a standardized convention for performing forward (4) and backward (5) Fourier transformations, as described below[74]:

$$F(\boldsymbol{y}) = \mathrm{FT}_{\boldsymbol{x}}[f(\boldsymbol{x})] = \int f(\boldsymbol{x}) \exp(2\pi i \boldsymbol{x} \cdot \boldsymbol{y})\, d\boldsymbol{x} \tag{4}$$

$$f(\boldsymbol{x}) = \mathrm{IFT}_{\boldsymbol{y}}[F(\boldsymbol{y})] = \int F(\boldsymbol{y}) \exp(-2\pi i \boldsymbol{y} \cdot \boldsymbol{x})\, d\boldsymbol{y} \tag{5}$$

Therefore, the probe function is given in this case as

$$P(\boldsymbol{R}) = IFT_{\boldsymbol{K}}[A(\boldsymbol{K})] = \int A(\boldsymbol{K}) \exp(-2\pi i \boldsymbol{K} \cdot \boldsymbol{R})\, d\boldsymbol{K} \tag{6}$$

and a shift term is introduced in Equation (7) to express the probe scanning over the sample[21]:

$$P(\boldsymbol{R}-\boldsymbol{R_0}) = \int A(\boldsymbol{K}) \exp(-2\pi i \boldsymbol{K}\cdot\boldsymbol{R}) \exp(2\pi i \boldsymbol{K}\cdot\boldsymbol{R_0})\, d\boldsymbol{K} \tag{7}$$

where $\boldsymbol{R_0}$ refers to the spatial probe position.

Under the assumption that the sample is sufficiently thin to adhere to the phase-object approximation, the interaction of electrons with the sample results solely in a phase change of the electron wave without altering its amplitude, making the scattering-induced phase shift additive along the propagation axis. Consequently, a multiplicative approximation is applied to describe the exit wave $\psi(\boldsymbol{R},\boldsymbol{R_0})$ as the product of the scanned real-space probe function $P(\boldsymbol{R}-\boldsymbol{R_0})$ and the real-space specimen transmission function $\varphi(\boldsymbol{R})$[15,21].

$$\psi(\boldsymbol{R},\boldsymbol{R_0}) \;=\; P(\boldsymbol{R}-\boldsymbol{R_0})\varphi(\boldsymbol{R}) \tag{8}$$

The specimen transmission function $\varphi(\boldsymbol{R})$ is defined for each probe position by

$$\varphi(\boldsymbol{R}) = \exp\big(i\sigma\mu(\boldsymbol{R})\big) \tag{9}$$

where $\mu(\boldsymbol{R})$ is the projected electrostatic potential of the sample, *i.e.,* the summed three-dimensional (3D) potential along the electron wave propagation axis, representing the induced phase shift of the electron wave function by the sample[75]. σ is the interaction parameter and is given by

$$\sigma = \frac{2\pi m e \lambda}{h^2} = \frac{2\pi\, e}{h\, c}\cdot\frac{mc^2+eU}{\sqrt{eU\cdot(2mc^2+eU)}} \tag{10}$$

with e as the elemental charge, m as the electron mass, λ as the relativistically corrected wavelength, c as the velocity of light, h as the Planck constant, and U as the acceleration voltage[21]. As the interaction parameter depends on the acceleration voltage, the electron wave phase shift is in turn dependent on the acceleration voltage regardless of the nature of the sample. For simplicity, a coherent and elastic interaction model is adopted to describe the sample-beam interaction[76].

Electrons exiting the sample are directed through the image-forming intermediate and projector lens system until they reach the detector as a diffraction pattern. In the detector plane, the electron wave is described as the Fourier transform of the exit wave $\psi(\boldsymbol{R},\boldsymbol{R_0})$. Using the convolution and Fourier-shift theorems, the exit wave can be written as a convolution of two functions[77,78]:

$$\psi(\boldsymbol{K_f},\boldsymbol{R_0}) \;=\; [A(\boldsymbol{K_f})\exp(2\pi i \boldsymbol{K_f}\cdot\boldsymbol{R_0})] \;\otimes\; \phi(\boldsymbol{K_f}) \tag{11}$$

where $\boldsymbol{K_f}$ refers to a position in the reciprocal diffraction plane, which corresponds to a position in the detector plane.

In the detector plane, only the squared modulus of the electron wave $\left|\psi\left(\boldsymbol{K_f}, \boldsymbol{R_0}\right)\right|^2 = I(\boldsymbol{K_f}, \boldsymbol{R_0})$ is recorded since it is impossible with the available detectors to directly register the phase of the electron wave, which contains the specimen-induced phase shift information. The inability to measure this phase directly is referred to as the phase problem. However, the phase information can be reconstructed *via in-silico* processing of 4D STEM datasets. If the aperture function is known or reconstructed, the influences of the microscope on the electron wave can be extracted.

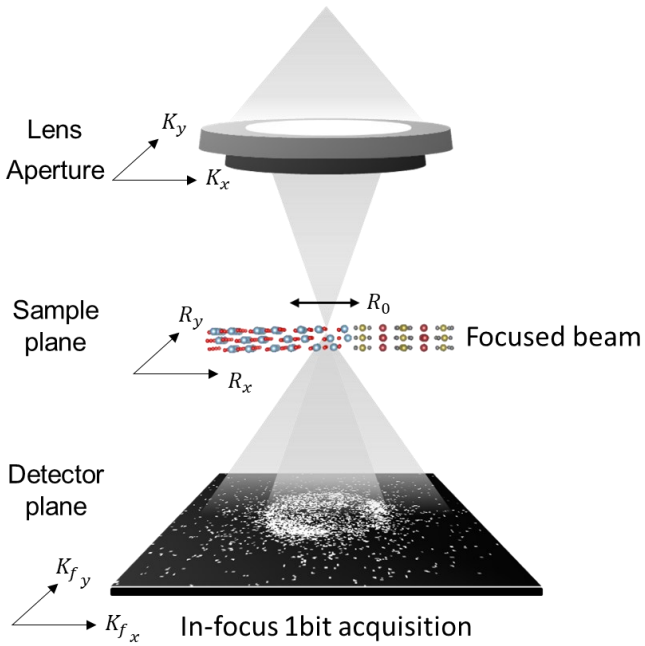

Figure 3. Schematic of the electron-beam propagation in a 4D STEM experiment with binary data acquisition using a focused convergent electron beam.

1.2.3 Non-iterative phase reconstructions

The concept of ptychography as a technique for solving the phase problem using a coherent source was first proposed by Walter Hoppe in 1969[77]. Based on this initial idea, Rodenburg and co-workers developed the Wigner distribution deconvolution (WDD) and Single-Sideband (SSB) reconstruction algorithms during the 1990s. However, due to the limited computational capabilities for handling large datasets and poor detector quality at that time, ptychography gained little attention[22,79]. The introduction of DECs, suitable for TEM, and the constant advancement of computer processing power have made ptychography increasingly accessible, which proves to be a powerful high-resolution, high-contrast, and dose-efficient imaging method by mapping the projected electrostatic potential of the illuminated object as a phase shift map[80].

To retrieve the specimen transmission function, the initial step in both non-iterative algorithms involves performing a Fourier transform of the entire dataset with respect to the spatial probe position $\boldsymbol{R_0}$. This Fourier transform generates a new complex 4D dataset $G(\boldsymbol{K_f}, \boldsymbol{Q_0})$[22]:

$$\begin{aligned} G(\boldsymbol{K_f}, \boldsymbol{Q_0}) &= \mathrm{FT}_{R_0}\left[\left|\psi(\boldsymbol{K_f}, \boldsymbol{R_0})\right|^2\right] \\ &= \mathrm{FT}_{R_0}\left[\left|\left[A(\boldsymbol{K_f})\ \exp(2\pi i \boldsymbol{K_f} \cdot \boldsymbol{R_0})\right] \otimes \phi(\boldsymbol{K_f})\right|^2\right] \end{aligned} \tag{12}$$

with $\boldsymbol{Q_0}$ being the spatial frequency**.** Since the product of a complex number with its complex conjugate is defined as the square of the number's modulus, $\left|\psi(\boldsymbol{K_f}, \boldsymbol{R_0})\right|^2$ can be written as

$$\begin{aligned} \left|\psi(\boldsymbol{K_f}, \boldsymbol{R_0})\right|^2 &= \{[A(\boldsymbol{K_f})\ \exp(2\pi i \boldsymbol{K_f} \cdot \boldsymbol{R_0})] \otimes \phi(\boldsymbol{K_f})\} \\ &\quad \cdot \{[A^*(\boldsymbol{K_f})\ \exp(-2\pi i \boldsymbol{K_f} \cdot \boldsymbol{R_0})] \otimes \phi^*(\boldsymbol{K_f})\} \end{aligned} \tag{13}$$

To simplify Equation (13), the convolution theorem is applied as the first step[78]:

$$\begin{aligned} \left|\psi(\boldsymbol{K_f}, \boldsymbol{R_0})\right|^2 &= \int A(\boldsymbol{a}) \exp(2\pi i \cdot \boldsymbol{a} \cdot \boldsymbol{R_0}) \cdot \phi(\boldsymbol{K_f} - \boldsymbol{a}) d\boldsymbol{a} \\ &\quad \cdot \int A^*(\boldsymbol{b}) \exp(-2\pi i \cdot \boldsymbol{b} \cdot \boldsymbol{R_0}) \cdot \phi^*(\boldsymbol{K_f} - \boldsymbol{b}) d\boldsymbol{b} \\ &= \iint A(\boldsymbol{a}) A^*(\boldsymbol{b}) \phi(\boldsymbol{K_f} - \boldsymbol{a}) \phi^*(\boldsymbol{K_f} - \boldsymbol{b}) \exp(2\pi i \\ &\quad \cdot \boldsymbol{R_0}(\boldsymbol{a} - \boldsymbol{b})) \, d\boldsymbol{a}\, d\boldsymbol{b} \end{aligned} \tag{14}$$

with $\boldsymbol{a}$ and $\boldsymbol{b}$ as dummy variables. Thus, going by Equation (12), for $G(\boldsymbol{K_f}, \boldsymbol{Q_0})$ follows:

$$\begin{aligned} G(\boldsymbol{K_f}, \boldsymbol{Q_0}) &= \iiint A(\boldsymbol{a}) A^*(\boldsymbol{b}) \phi(\boldsymbol{K_f} - \boldsymbol{a}) \phi^*(\boldsymbol{K_f} - \boldsymbol{b}) \\ &\quad \cdot \exp(2\pi i \cdot \boldsymbol{R_0}(\boldsymbol{a} - \boldsymbol{b} + \boldsymbol{Q_0})) d\boldsymbol{a}\, d\boldsymbol{b} d\boldsymbol{R_0} \end{aligned} \tag{15}$$

The first integral is solved as

$$\int \exp(2\pi i \cdot \boldsymbol{R_0}(\boldsymbol{a} - \boldsymbol{b} + \boldsymbol{Q_0}))\, d\boldsymbol{R_0} = \delta(\boldsymbol{a} - \boldsymbol{b} + \boldsymbol{Q_0}) \tag{16}$$

with δ as the Dirac delta function. With a substitution of $\boldsymbol{b} = \boldsymbol{c} + \boldsymbol{Q_0}$ it follows:

$$\begin{aligned} G(\boldsymbol{K_f}, \boldsymbol{Q_0}) &= \iint A(\boldsymbol{a}) A^*(\boldsymbol{c} + \boldsymbol{Q_0}) \phi(\boldsymbol{K_f} - \boldsymbol{a}) \phi^*(\boldsymbol{K_f} - \boldsymbol{c} - \boldsymbol{Q_0}) \delta(\boldsymbol{a} - \boldsymbol{c})\, d\boldsymbol{a}\, d\boldsymbol{c} \\ &= \int A(\boldsymbol{c}) A^*(\boldsymbol{c} + \boldsymbol{Q_0})\, \phi(\boldsymbol{K_f} - \boldsymbol{c}) \phi^*(\boldsymbol{K_f} - \boldsymbol{c} - \boldsymbol{Q_0}) \end{aligned} \tag{17}$$

By applying the convolution theorem to Equation (17), $G(\boldsymbol{K_f}, \boldsymbol{Q_0})$ is brought to the final form[78].

$$G(\boldsymbol{K_f}, \boldsymbol{Q_0}) = \mathrm{FT}_{R_0}\left[\left|\psi(\boldsymbol{K_f}, \boldsymbol{R_0})\right|^2\right]$$
$$= A(\boldsymbol{K_f})A^*(\boldsymbol{K_f} + \boldsymbol{Q_0}) \otimes \phi(\boldsymbol{K_f})\phi^*(\boldsymbol{K_f} - \boldsymbol{Q_0}) \tag{18}$$

$G(\boldsymbol{K_f}, \boldsymbol{Q_0})$ is a function of detector coordinate $\boldsymbol{K_f}$ and probe spatial frequency $\boldsymbol{Q_0}$. It can be interpreted as the Fourier transform of all STEM images generated from the intensities of individual detector pixels during the scan. It essentially represents a map of the specimen-dependent spatial-frequency responses corresponding to the detector pixels[80]. At a particular spatial frequency in the image, $\boldsymbol{Q_0}$, the $G(\boldsymbol{K_f}, \boldsymbol{Q_0})$ dataset contains the amplitude and the phase of the variation of the intensity in the overlap function in relation to the probe position for all diffracted beams separated by $\boldsymbol{Q_0}$[81].

The non-iterative phase reconstructions rely on approximations of the sample-electron beam interaction. WDD assumes that the sample is sufficiently thin to satisfy the phase-object approximation (POA)[22,82]. The POA suggests that the presence of a sample, *i.e.,* the atomic potentials, will only cause a change in the phase of the electron wave function, but not in the amplitude. In SSB, the weak-phase-object approximation (WPOA) is used for the phase reconstruction: If the material is thin enough, such that $\sigma\mu(\boldsymbol{R}) \ll 1$, the specimen transmission function $\varphi(\boldsymbol{R})$ of a phase-object given in Equation (9) can be simplified as a linear approximation using the first-degree Taylor polynomial[79,83,84].

$$\varphi_{\mathrm{WPOA}}(\boldsymbol{R}) \approx 1 + i\sigma\mu(\boldsymbol{R}) = 1 + i\varphi'(\boldsymbol{R}) \tag{19}$$

1.2.3.1 Single-Sideband (SSB) reconstruction

Applying the WPOA, $G(\boldsymbol{K_f}, \boldsymbol{Q_0})$ can be expressed in the following form:

$$G(\boldsymbol{K_f}, \boldsymbol{Q_0}) = \left|A(\boldsymbol{K_f})\right|^2\delta(\boldsymbol{Q_0}) + A(\boldsymbol{K_f})A^*(\boldsymbol{K_f} + \boldsymbol{Q_0})\phi'^*(-\boldsymbol{Q_0})$$
$$+ A^*(\boldsymbol{K_f})A(\boldsymbol{K_f} - \boldsymbol{Q_0})\phi'(\boldsymbol{Q_0}) \tag{20}$$

using an approximation of the transfer function calculated from the Fourier transform of Equation (19), as

$$\phi_{WPOA}(\boldsymbol{K_f}) = \delta(\boldsymbol{K_f}) + \phi'(\boldsymbol{K_f})$$
$$\phi'(\boldsymbol{K_f}) = i\mathrm{FT}_{\mathrm{R}}[\varphi'(\boldsymbol{R})] \tag{21}$$

Equation (20) consists of three parts. The first part corresponds to the direct beam, and the other two represent two scattered beams located at $\pm\,\boldsymbol{Q_0}$. The scattered beams interfere with the central disk and also with each other, depending on the spatial frequency. Due to the constraints imposed

by the aperture function, a transfer theoretically occurs only in the regions of double overlap, *i.e.*, in areas where the direct beam overlaps with a scattered beam. Moreover, since $\phi'(\boldsymbol{Q_0}) = -\phi'^*(-\boldsymbol{Q_0})$, $\phi'(\boldsymbol{Q_0})$ and $\phi'^*(-\boldsymbol{Q_0})$ have the same amplitude, but are π radians out of phase. Therefore, in a region of triple overlap, no transfer will take place due to destructive interference. If no geometrical aberrations are present, the parts of the distribution found outside of the double overlap regions are expected to carry no useful information on the sample. Therefore, the double overlap regions are extracted for each spatial frequency. In a subsequent processing step, adding π to the phase of one of the double overlaps and summing over all $\boldsymbol{K_f}$ for any given $\boldsymbol{Q_0}$ yields $\phi'(\boldsymbol{Q_0})$, which is reverted to the real-space transmission function $\varphi'(\boldsymbol{R})$ *via* Fourier transform. Alternatively, one side (Single-Sideband) of the masked overlap regions is integrated for any given $\boldsymbol{Q_0}$. As such, the contrast transfer in the SSB is equal to the surface of the double overlap regions across the detector space. The contrast transfer function peaks at intermediate frequencies while decaying for higher and lower frequencies[84,85].

In summary, the computational workflow of SSB ptychography includes loading the 4D STEM dataset, followed by performing an FFT with respect to the probe position $\boldsymbol{R_0}$, to obtain $G(\boldsymbol{K_f}, \boldsymbol{Q_0})$. Then, for each spatial frequency $\boldsymbol{Q_0}$, the $\boldsymbol{K_f}$ domain is masked to retain only the double overlap regions. One side of the masked overlap regions is integrated at each spatial frequency to obtain the object function $\phi'(\boldsymbol{Q_0})$ in reciprocal space, and an inverse Fourier transform results in the real space object function $\varphi'(\boldsymbol{R})$.

1.2.3.2 Wigner distribution deconvolution (WDD)

Without applying the WPOA, the function $G(\boldsymbol{K_f}, \boldsymbol{Q_0})$ cannot be simplified any further. Therefore, the separation of the object function from the aperture function through a deconvolution process with a known probe function is required. An inverse Fourier transform of $G(\boldsymbol{K_f}, \boldsymbol{Q_0})$ with respect to the detector coordinate $\boldsymbol{K_f}$ returns a new 4D dataset $H(\boldsymbol{R}, \boldsymbol{Q_0})$, which is mathematically free of convolution and exhibits distinct characteristics[22].

$$\begin{aligned} H(\boldsymbol{R}, \boldsymbol{Q_0}) &= \mathrm{IFT}_{\boldsymbol{K_f}}\left[G(\boldsymbol{K_f}, \boldsymbol{Q_0})\right] \\ &= \int P^*(\boldsymbol{a}) P(\boldsymbol{a} + \boldsymbol{R}) \exp(-2\pi i \boldsymbol{Q_0} \cdot \boldsymbol{a})\, d\boldsymbol{a} \\ &\quad \cdot \int \varphi^*(\boldsymbol{b}) \varphi(\boldsymbol{b} + \boldsymbol{R}) \exp(2\pi i \boldsymbol{Q_0} \cdot \boldsymbol{b})\, d\boldsymbol{b} \end{aligned} \tag{22}$$

with probe and transmission functions with respect to the real-space coordinate $\boldsymbol{R}$.

$H(\boldsymbol{R}, \boldsymbol{Q_0})$ can be written as the product of two Wigner distribution functions of probe and object with

$$\xi_q(x, y) = \int q^*(z) q(z + x) \exp(2\pi i y \cdot z)\, dz \tag{23}$$

as

$$H(\boldsymbol{R}, \boldsymbol{Q_0}) = \xi_P(\boldsymbol{R}, -\boldsymbol{Q_0}) \cdot \xi_\varphi(\boldsymbol{R}, \boldsymbol{Q_0}) \tag{24}$$

At this stage, the purpose of calculating $H(\boldsymbol{R}, \boldsymbol{Q_0})$ becomes clear as it enables the removal of all influences of the microscope transfer function from the dataset by dividing out the probe part. To mitigate noise amplification and to prevent potential division by zero, a Wiener filter is applied, thus the dataset is transformed to:

$$\xi_\varphi(\boldsymbol{R}, \boldsymbol{Q_0}) = \frac{\xi_P^*(\boldsymbol{R}, -\boldsymbol{Q_0}) H(\boldsymbol{R}, \boldsymbol{Q_0})}{|\xi_P(\boldsymbol{R}, -\boldsymbol{Q_0})|^2 + \epsilon} \tag{25}$$

where ϵ is a small constant that should be set as the signal-to-noise ratio (SNR) at each point, but is conventionally chosen as a small fraction of $|\xi_P\ (\boldsymbol{R}, -\boldsymbol{Q_0})|^2$[82]. An ϵ-ratio can be defined as

$$\epsilon_{\text{rat}} = \frac{\epsilon}{|\xi_P(\boldsymbol{R}, -\boldsymbol{Q_0})|^2} \tag{26}$$

and ϵ_{rat} is usually set between 0.01 and 0.1[82,85].

Subsequently, to retrieve the object information, another Fourier transform is performed:

$$D(\boldsymbol{K_f}, \boldsymbol{Q_0}) = FT_{\boldsymbol{K_f}}[\xi_\varphi(\boldsymbol{R}, \boldsymbol{Q_0})] = \phi(\boldsymbol{K_f}) \phi^*(\boldsymbol{K_f} - \boldsymbol{Q_0}) \tag{27}$$

Slicing through this dataset at a spatial frequency of $\boldsymbol{K_f} = 0$ leads to a simple solution of $\phi(\boldsymbol{Q_0})$ as

$$\phi(\boldsymbol{Q_0}) = \frac{D^*(\boldsymbol{0}, \boldsymbol{Q_0})}{\sqrt{D(\boldsymbol{0}, \boldsymbol{0})}} \tag{28}$$

and an inverse Fourier transform returns the specimen transmission function $\varphi(\boldsymbol{R})$.[22]

1.2.4 Iterative phase reconstructions

Due to the inherent complexity of the phase problem, most phase-retrieval algorithms, regardless of the illumination source utilized, rely on iterative optimization rather than directly determining explicit solutions. As previously mentioned, if both the object and the probe are well-defined, the forward calculation from the known specimen to its diffraction plane is straightforward. However, the reverse calculation from the diffraction plane to an unknown object is significantly more

challenging, as the phase information of the exit wave is lost during the measurement. The relationship between the specimen and the resulting measurements is intricate and nonlinear, necessitating advanced algorithms for accurate interpretation. Such methods typically require substantial computational resources, including large amounts of processing power and memory, particularly for handling big datasets. Most algorithms address this inverse problem by starting with an initial estimate of the unknown object and probe functions, then gradually refining their approach to the solution by iteratively adjusting the unknowns based on measured data, to repeatedly update the multiplicative specimen transmission function (Equation (8))[86,87]. For this approach to work properly, a certain level of redundancy within the 4D dataset is necessary. In the experiment, this redundancy can be ensured by overlapping the illuminated regions of adjacent probe positions.

The reconstruction algorithms can be categorized into two main types based on their optimization methodologies: set-projection methods and steepest descent methods[88-96]. In electron ptychography, gradient descent methods have proven their effectiveness, and since the Python package py4DSTEM, utilized for phase reconstructions in this study, operates on this approach, the following discussion focuses on these algorithms[69].

Gradient descent algorithms evaluate the gradient at the current estimate using a well-defined error metric, then proceed in the direction of the negative gradient with a specified step size. These steps are iteratively repeated until the error metric reaches its minimum value, which is then considered the solution. A loss function, ε, is essential for the gradient descent method, typically serving as an error metric to quantify the discrepancy between modeled values and experimental data. As the algorithm converges toward a solution, the value of the loss function decreases, ideally approaching zero at the final solution[97]. Various loss function models, such as mean squared error (MSE), amplitude loss, and Poisson loss, are described in the literature[90,98-101]. All of these models are suitable for iterative phase reconstructions and can significantly influence the reconstruction outcome based on the applied illumination dose[102].

The py4DSTEM iterative algorithm used in this thesis minimizes the discrepancy between modeled and measured diffraction intensities using the following error metric:

$$\varepsilon = \frac{\sum_{\boldsymbol{R_0},\boldsymbol{K_f}} \left| \sqrt{I(\boldsymbol{R_0},\boldsymbol{K_f})} - \sqrt{J(\boldsymbol{R_0},\boldsymbol{K_f})} \right|^2}{\sum_{\boldsymbol{R_0},\boldsymbol{K_f}} I(\boldsymbol{R_0},\boldsymbol{K_f})} \tag{29}$$

i.e., a normalized amplitude loss function, where $I(\boldsymbol{R_0},\boldsymbol{K_f})$ represents the measured diffraction intensities at probe position $\boldsymbol{R_0}$ and $J(\boldsymbol{R_0},\boldsymbol{K_f})$ the modelled diffraction intensities per probe position $\boldsymbol{R_0}$[69].

During each iteration, the minimal adjustment to the current estimate of the exit wave in the detector plane $\psi(\boldsymbol{K_f}, \boldsymbol{R_0})$ involves replacing the calculated intensities (Fourier amplitude of the calculated wave) by the square root of the measured intensity while the phase is kept the same:

$$\psi'(\boldsymbol{K_f}, \boldsymbol{R_0}) = \psi(\boldsymbol{K_f}, \boldsymbol{R_0}) \cdot \frac{\sqrt{I(\boldsymbol{R_0}, \boldsymbol{K_f})}}{\sqrt{J(\boldsymbol{R_0}, \boldsymbol{K_f})}} \tag{30}$$

where $\psi'(\boldsymbol{K_f}, \boldsymbol{R_0})$ represents the revised exit wave. The updated exit wave is Fourier projected to the real space, resulting in

$$\psi'(\boldsymbol{R}, \boldsymbol{R_0}) = IFT_{\boldsymbol{Kf}} \left[\psi(\boldsymbol{K_f}, \boldsymbol{R_0}) \cdot \frac{\sqrt{I(\boldsymbol{R_0}, \boldsymbol{K_f})}}{\sqrt{J(\boldsymbol{R_0}, \boldsymbol{K_f})}} \right] \tag{31}$$

This allows an update of object and probe function using stochastic gradient descent methods:

$$\Delta\psi_{GD}(\boldsymbol{R}, \boldsymbol{R_0}) = \psi'(\boldsymbol{R}, \boldsymbol{R_0}) - \psi(\boldsymbol{R}, \boldsymbol{R_0}) \tag{32}$$

$$\varphi'(\boldsymbol{R}) = \varphi(\boldsymbol{R}) + \alpha \cdot \frac{\sum_{R_0 \in \mathrm{B}} P^*(\boldsymbol{R} - \boldsymbol{R_0}) \cdot \Delta\psi_{GD}(\boldsymbol{R}, \boldsymbol{R_0})}{\|P(\boldsymbol{R} - \boldsymbol{R_0})\|_\beta} \tag{33}$$

$$P'(\boldsymbol{R} - \boldsymbol{R_0}) = P(\boldsymbol{R} - \boldsymbol{R_0}) + \alpha \cdot \frac{\sum_{R_0 \in \mathrm{B}} \varphi^*(\boldsymbol{R}) \cdot \Delta\psi_{GD}(\boldsymbol{R}, \boldsymbol{R_0})}{\|\varphi(\boldsymbol{R})\|_\beta} \tag{34}$$

where $\Delta\psi_{GD}(\boldsymbol{R}, \boldsymbol{R_0})$ represents the gradient of the stochastic gradient descent method, α is the gradient-descent step size, B denotes the batch size of the probe positions, and β is chosen between 0 and 1 as normalization parameter[69]. As the error between calculated and estimated intensities increases along the gradient direction, it can be iteratively reduced by moving the current estimates in the negative gradient direction by a small step, α.

The probe can be initialized using an estimated set of aberrations and the probe-forming aperture, which can be derived from known microscope specifications such as the semi-convergence angle. A more accurate initialization can be achieved through a direct reference measurement of the vacuum probe. The initial object array is typically extended by up to half the extent of the probe and initialized as an array of ones[69]. The general workflow for a single iteration of the phase retrieval *via* gradient descent is summarized in Figure 4. For all probe positions, starting from the initial estimate of the object and probe, the real-space exit wave is calculated as a product of the two, relying on the POA (Equation (8)). The exit wave is propagated to the detector plane and updated based on the measured intensities. Subsequent back-propagation of the updated exit wave to real

space enables refinement of the probe and object functions using the stochastic gradient descent update functions during each iteration.

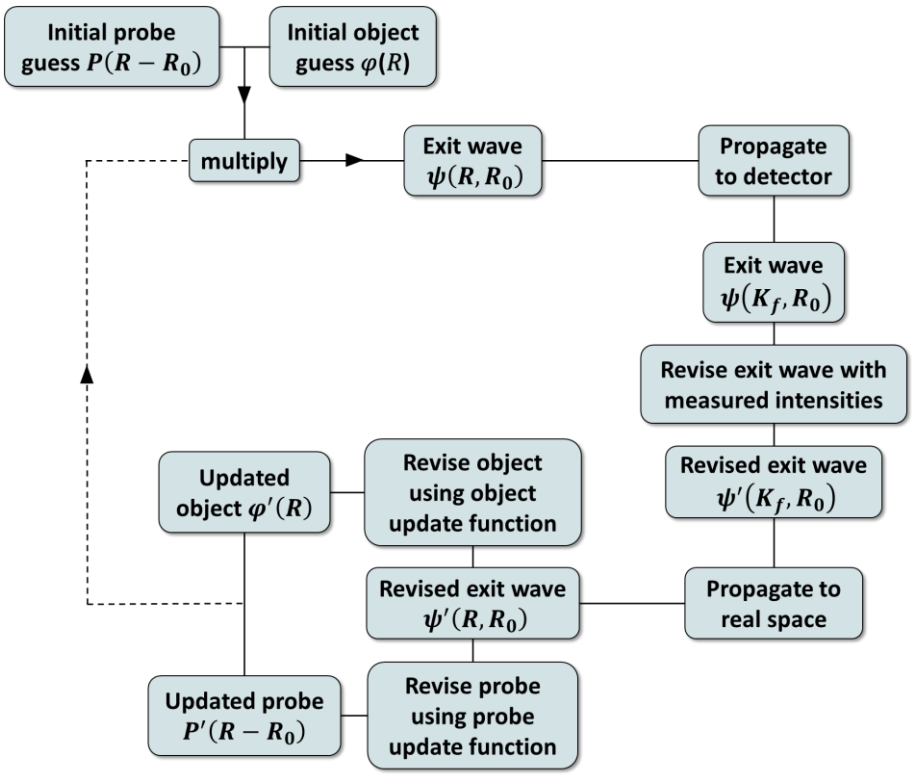

Figure 4. The flowchart illustrates the iteration of the gradient-descent iterative ptychographic phase reconstruction. One iteration of the algorithm involves processing individual diffraction patterns utilized to refine the estimates of the object and the probe. Typically, iterations are carried out until the error between the measured and calculated diffraction patterns falls below a predefined threshold.

1.2.4.1 Mixed-state electron ptychography

All the phase reconstruction algorithms described thus far assume coherent illumination, which is generally sufficient when in-focus illumination and a high-coherent field-emission gun are used or when not less than nanometer spatial resolution is targeted[103]. However, in practice, reconstructions and the information transfer from the sample in 4D STEM experiments to the detector are often influenced by the imaging system. Temporal and spatial incoherence cannot be neglected and a single pure-state coherent probe illumination is never achieved in real experiments. As a result of a partially coherent illumination, a single-slice reconstruction injects partial coherence information into the reconstruction, degrading its quality[104-106]. It has been shown that representing the probe as a linear combination of pure quantum states (*i.e.*, a mixed state) provides a model that better captures partial coherence and allows for higher-quality reconstructions. Instead of assuming a single coherent probe illumination, several incoherent probes can be propagated independently to the detector, where the measured diffraction pattern represents a superposition of their

contributions[94,103]. For mixed-state reconstructions, the forward operator is thus modified to incorporate l orthogonal probe functions $\{P^{(l)}\}$, and all subsequent iteration steps are adjusted accordingly[69].

$$\psi^{(l)}(\boldsymbol{R}, \boldsymbol{R_0}) = P^{(l)}(\boldsymbol{R} - \boldsymbol{R_0}) \cdot \varphi(\boldsymbol{R}) \tag{35}$$

$$J(\boldsymbol{R_0}, \boldsymbol{K_f}) = \sum_{l} \left| FT\left[\psi^{(l)}(\boldsymbol{R}, \boldsymbol{R_0})\right] \right|^2 \tag{36}$$

The versatility and robustness of mixed-state electron ptychography make it suitable for a wide range of applications. This approach enables large-field-of-view, high-resolution imaging, which is essential for characterizing both the overall morphology and the local atomic structure of complex nanostructures[107]. While iterative phase reconstructions can be applied to reconstruct the phase from both in-focus and defocused 4D STEM datasets, choosing the latter allows for faster and more stable acquisition of the diffraction patterns with sufficient overlap. This is of major importance, since it helps to mitigate slow detector readouts, large dataset sizes, and instabilities in the imaging system. Its high-contrast, high-precision, and low-dose imaging capabilities facilitate the investigation of atomic-scale dynamics involving light elements. The use of a large-area probe further enhances efficiency by enabling larger scan steps, reducing the number of diffraction patterns required, and thereby reducing computational demands for data reconstruction and analysis[108].

1.2.4.2 Multi-slice electron ptychography

The phase reconstruction algorithms introduced all rely on the POA or the WPOA, *i.e.*, a straightforward multiplication of the probe function and the specimen transmission function describes the interaction between the sample and the beam. This assumption serves as a useful approximation for thin and weakly scattering specimens but it becomes inadequate for thicker or strongly scattering samples[109,110]. In such cases, the illumination profile varies significantly with increasing depth due to the effects of dynamical scattering and free-space propagation. If the probe shape undergoes significant changes during propagation within the sample, the probe-sample interaction can no longer be accurately described by a single plane approximation, and a full multi-slice calculation is required in the phase retrieval process after a critical thickness is reached. Changes in the probe shape arise from both free-space propagation and scattering by the sample. The thickness limit T can be expressed as:

$$T = 1.3 \cdot \frac{\lambda}{\alpha_{max}^2} \tag{37}$$

where α_{max} is the maximum scattering angle of the diffraction pattern, and λ is the electron wavelength[103,111]. For the typical scattering angle deployed in the experiments conducted in this work of ~20 mrad and an acceleration voltage of 200 kV, this results in a thickness limit of approximately 6 nm, which is achievable for various samples. However, it was not possible for the samples investigated in this work, as described later. Additionally, for samples containing heavy elements, where a single atom can induce significant phase shifts and in fact affect the amplitude of the electron wave as well, the probe shape may be altered considerably by just a few atoms. Consequently, the multiplicative assumption of the beam-sample interaction breaks down, resulting in an even stricter thickness limit. Recent approaches to address the multiple scattering problem in thicker samples or those containing heavier elements include the use of multi-slice ptychography[112-114]. The py4DSTEM multi-slice ptychographic algorithm approximates the object as a stack of *n* slices, each on its own thin enough to satisfy the multiplicative assumption, resulting in a modified forward propagator for *n* slices that alternates between transmission and propagation steps. These and all subsequent steps within one iteration are adjusted accordingly[69].

$$\psi^{(n)}(\boldsymbol{R},\boldsymbol{R_0}) = p^{(n)}(\boldsymbol{R}-\boldsymbol{R_0}) \cdot \varphi^{(n)}(\boldsymbol{R}) \tag{38}$$

where

$$p^{(1)}(\boldsymbol{R}-\boldsymbol{R_0}) = P(\boldsymbol{R}-\boldsymbol{R_0}) \tag{39}$$

and

$$p^{(n)}(\boldsymbol{R}-\boldsymbol{R_0}) = \mathrm{Prop}_{\Delta z_{n-1}}\left[\psi^{(n-1)}(\boldsymbol{R},\boldsymbol{R_0})\right] \tag{40}$$

with $p^{(n)}(\boldsymbol{R}-\boldsymbol{R_0})$ and $\varphi^{(n)}(\boldsymbol{R})$ being the probe and specimen transmission functions at slice *n* and Δz_n refers to the thickness between the slices *n* and *n+1*.

The multi-slice algorithm has proven particularly effective for reconstructing the phase of thicker samples and was therefore used in this work. When employing the multi-slice algorithm for data acquisition, it is important to account for the fact that the probe changes its size in real space as it propagates through free space with increasing thickness. To prevent wrapping artifacts in the reconstruction, it is essential to ensure an adequately sized probe box in real space. Additionally, data should be acquired with a high dose to ensure a good signal-to-noise ratio for capturing depth information. Since iterative phase reconstructions do not necessarily converge uniquely, various regularizations can be applied to help reduce the dimensionality of the available solution space[69].

1.2.5 What makes a good 4D STEM dataset for electron ptychography?

The following section is based on my personal experience with acquiring in-focus or defocused 4D STEM datasets using the probe-C_S-corrected JEOL ARM200F microscope equipped with a MerlinEM Medipix3 camera. It serves as a guide for capturing high-quality datasets to enable successful phase reconstructions. Since microscopes and material systems vary, there cannot be a

universal procedure. However, certain key aspects should always be considered before and during dataset acquisition to optimize the outcome, as a well-recorded initial dataset significantly improves the chances of a successful phase reconstruction. Several experimental parameters must be considered during 4D STEM data acquisition, such as defocus, scan step size in real space, convergence angle, maximum scattering angle, and the number of detector pixels. Thus, it is the author's hope that the following provides a helpful overview and offers practical guidance for setting key experimental parameters to achieve optimal results.

In this study, non-iterative Single-Sideband phase reconstruction was used to extract phase information from in-focus 4D STEM datasets, while iterative phase reconstruction was applied to defocused 4D STEM datasets. Consequently, references to in-focus dataset acquisition relate to optimizing data collection for Single-Sideband reconstruction, whereas defocused dataset acquisition pertains to optimization for iterative phase reconstructions. Although iterative reconstruction can also be applied to in-focus datasets, this approach was not pursued in the present study.

1.2.5.1 Probe step size

For in-focus data acquisition, the primary consideration is ensuring that all spatial frequencies within the diffraction limit are adequately represented. The probe step size must be selected in accordance with the Nyquist-Shannon sampling theorem to capture the maximum possible resolution[115]. For a given aperture defined by the semi-convergence angle α and an electron wavelength λ, the maximum allowable distance between adjacent probe positions, ΔR_0, required to capture the highest theoretically attainable spatial frequency, is given by:

$$\Delta R_0 = \frac{\lambda}{4\alpha} \tag{41}$$

Although various reconstruction algorithms offer the possibility to correct residual aberrations within the dataset[116], it is advantageous to align the microscope optimally beforehand to minimize the influence of lens aberrations and to use appropriate apertures for dose fractionation. In this study, all datasets were acquired using a 30 µm condenser aperture, which corresponds to a probe semi-convergence angle of 20.4 mrad. Consequently, the required step size to achieve the diffraction limit for the 30 µm condenser aperture is 0.3073 Å or less. Larger step sizes lead to undersampling, which induces aliasing effects, resulting in periodic artifacts in the phase reconstructions. Conversely, oversampling with smaller step sizes does not improve resolution or image quality for in-focus datasets, but has no negative effects beyond an increased electron dose[117,118]. Therefore, the in-focus datasets presented in this thesis are all slightly oversampled with step sizes smaller than 0.3073 Å to ensure no aliasing effects in the reconstructions. In general, the

optimal step size can be enlarged by using lower acceleration voltages (which increase the electron wavelength) or smaller apertures. However, using smaller apertures in turn limits the achievable resolution[7]. Lower acceleration voltages introduce stronger temporal incoherence effects and increase the influence of lens aberrations, which can degrade the overall data quality[119]. With a well-optimized initial microscope alignment, it was possible to avoid the computationally intensive step for correcting residual aberrations in the SSB reconstructions of this study.

Defocused iterative ptychography relies on overlapping probe positions to provide redundant information for object reconstruction. As a result, the quality of the reconstruction is strongly affected by the extent of this overlap[108,120]. However, there is no single measure to define the actual overlap, as experimental factors and probe aberrations also play a role. The degree of probe overlap in a 4D STEM experiment is influenced by the defocus, the real-space scan step size, and the chosen semi-convergence angle (20.4 mrad in this study), which also determines the range of spatial frequencies that are efficiently transferred. If the probe overlap is insufficient, it can be increased in two ways: by reducing the scan step size, which enhances redundancy but either increases dataset size or limits the field of view, or by increasing the defocus. However, at one point the probe no longer fits within the real-space probe box, leading to wrap-around artifacts[69]. This can be remedied by using more detector pixels. Based on experimental studies, a minimum overlap of more than 40% is required for stable, high-quality reconstructions[108].

It is also essential to account for the practical limitations of both the microscope and the specimen. For instance, while the iterative phase reconstructions discussed earlier can offer some level of probe-position refinement, substantial scan distortion will significantly reduce the reconstruction quality. As a result, the number of probe positions in a scan should be carefully chosen by considering factors such as stability, magnification, and detector speed. In this study, adequate probe overlap was ensured by selecting a sufficiently small step size (~0.8–1.5 Å) for a 70×140 grid of probe positions. The stability of the specimen holder in the goniometer and the sample's resistance to beam damage allowed for the use of this step size while the MerlinEM Medipix3 detector acquired defocused datasets in 12-bit mode with a frame time of 1ms.

1.2.5.2 Detector sampling considerations

The resolution of the detector plane is governed by the angular range of the individual pixels and can be adjusted by altering the effective magnification factor between the image and detector plane. This magnification—often referred to by the name of its optical counterpart, the camera length, and therefore also measured in (virtual) length—determines how finely the BF disk is sampled, from which phase information is extracted in SSB ptychography. Yang *et al.* found that an array as small as 16×16 pixels suffices to achieve the highest signal-to-noise ratio, with no significant benefit from

increasing the number of pixels. Utilizing a smaller detector array, such as 16×16 pixels, enhances the speed of readout and data acquisition, which leads to faster data collection with a reduced electron dose. However, their analysis did not account for the impact of residual aberrations, suggesting that under more realistic conditions, a larger number of pixels could still be advantageous[83].

These considerations are particularly important for fast and efficient data acquisition, especially when working with materials that are sensitive to electron beam damage. However, for the samples investigated in this thesis, such stringent sampling criteria were not essential, as the oxides demonstrated fair robustness toward high electron doses. Therefore, 4D STEM datasets were collected using the full 256×256 pixel detector area. The camera length was adjusted so that the BF disk of the 30 µm aperture was sampled by 105×105 pixels, ensuring sufficient detector plane coverage. This approach allowed for the recording of both BF and DF electrons, enabling virtual imaging through appropriate masking of 4D STEM data.

As mentioned before, poor sampling in reciprocal space, which can also arise from factors such as binning or a reduced number of detector pixels, can be compensated for by denser real-space sampling through adjustments of the probe step size[121]. However, to achieve faster scanning, mitigate scanning artifacts, and reduce sample drift, this study adopted an alternative strategy. Despite the numerous advantages provided by DECs and the wide range of techniques they enable—including virtual imaging, orientation and strain mapping, and phase-contrast imaging—one remaining limitation is the slow scanning speed compared to standard STEM detectors. At lower scanning speeds, scan distortions, sample drift, and instabilities in the microscope alignment become more pronounced. In turn, the frame rate of DECs can be significantly increased through hardware binning, windowing, or by reducing the detector's dynamic range[61,122]. In this study, the latter approach was implemented for in-focus acquisition by adjusting the counting depth of the MerlinEM Medipix3 detector to 1-bit, meaning that each detector pixel could register only a binary signal (1 or 0)—a single event—per frame. This optimization reduced the frame time to 50 µs, enabling faster data acquisition. Due to this high acquisition speed in combination with the long camera length and a moderate beam intensity, oversaturation of the BF disk at each scan position was avoided despite the reduced dynamic range. The results show that a high dynamic range—such as that offered by a 12-bit counting mode, which comes at the expense of acquisition speed—is not always essential for obtaining high-quality data, particularly in low-dose to medium-dose imaging conditions with fast data acquisition speeds.

In iterative ptychography, constraints are introduced during data acquisition to ultimately control numerical accuracy, computational cost, and reconstruction resolution. During acquisition, the reciprocal pixel size ΔK_f defines the real-space extent of the probe. This means that the probe-

forming aperture and camera length should be selected such that the real-space probe extent ('probe box'), $e = 1/\Delta K_f$, is sufficiently large to fit the probe without wrap-around artifacts. To avoid these artifacts, it is further necessary that the number of detector pixels, which determines the size of the array used to store the moving-window probe, is set to an amount that the array is large enough to fit the defocused probe. This is particularly important when imaging thicker samples, as the probe practically expands with increasing sample depth[69].

In general, all scattering angles with sufficient counts should be included in the acquired diffraction patterns. Detectors with a small dynamic range are often restricted to the BF disk in this regard. But for detectors with a large dynamic range, collecting electrons scattered to higher angles allows for super-resolution reconstructions, *i.e.*, resolution beyond the aperture-induced diffraction limit. In this work, only the BF disk signals were used for reconstructions.

Since the detector and a ptychographic reconstruction act as a virtual lens, the achieved resolution for iterative reconstructions of defocused datasets depends more on the maximum resolvable scattering angles in the diffraction pattern—largely influenced by the detector pixel size—than on the real-space step size or the focal size of the microscope optics[69].

1.2.5.3 Finding the optimum (de)focus

The effectiveness of SSB electron ptychography is typically maximized when the probe is focused at the midplane of the sample. In this configuration, the phase contributions from the defocus at sample slices above and below the central plane effectively cancel each other out. This cancellation helps to prevent contrast reversals, particularly in cases where dynamical scattering effects are not excessively strong[123,124]. This consideration is particularly important when the microscope is initially aligned using conventional detectors before switching to the 4D STEM camera. In conventional imaging modes, for ABF imaging, the highest image quality is achieved by focusing on the top sample surface, while in ADF mode, optimal contrast is typically obtained by focusing on the bottom sample surface[125]. Depending on the sample thickness, this difference in optimal focus can significantly impact the reconstruction results.

For defocused 4D STEM data acquisition aimed at iterative phase reconstructions, the amount of defocus that can be employed is constrained by the number of pixels in the detector and the selected semi-convergence angle[69]. Figure 5(a) shows an exemplary probe, with experimental settings similar to those used in this work. As previously mentioned, the real-space probe extent $e = 1/\Delta K_f$ must be sufficiently large to fit the probe without inducing wrap-around artifacts, as shown in Figure 5(a). If the probe is excessively defocused (Figure 5(c)), it barely fits within the real-space probe box, constrained by the number and size of the detector pixels and this leads to wrap-around artifacts

during reconstruction. Furthermore, when recording diffraction data, it is important that the detector can sample the diffraction intensities adequately to capture the specimen features in the ronchigram, as shown in Figure 5(b). This imposes additional constraints on the maximum allowable defocus value; with excessive defocus, specimen features are not resolved sufficiently in the ronchigram, as visible in Figure 5(d) for a diffraction pattern with a larger defocus compared to the one shown in Figure 5(b).

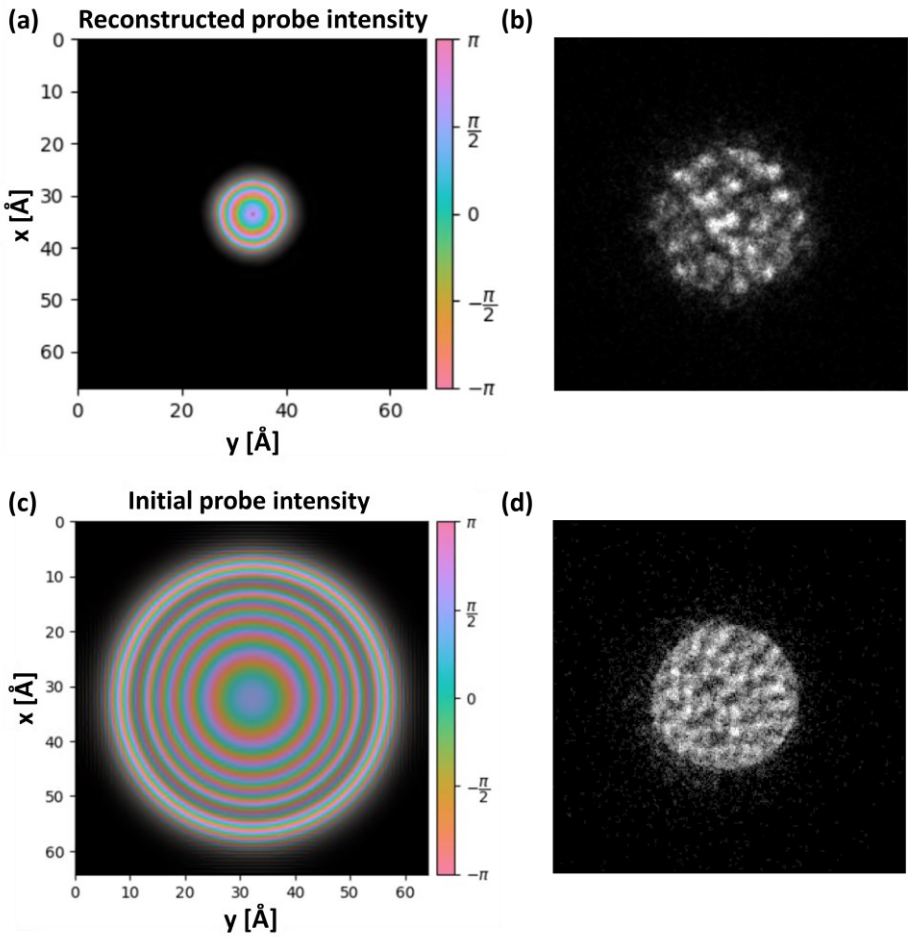

Figure 5. (a) Real-space intensity distribution of the electron probe used for typical 4D STEM data acquisition in this study. (b) Example diffraction pattern resulting from the interaction between the sample and the slightly defocused probe shown in (a). (c) Simulated probe with large overfocus, leading to wrap-around artifacts in the reconstruction. (d) Example diffraction pattern from a dataset acquired with a more defocused probe, showing reduced resolution of sample features in the ronchigram, compared to (b).

1.2.5.4 Hyper-parameter tuning for iterative phase reconstructions

To successfully perform an iterative ptychographic reconstruction of experimental data, it is essential to precisely know certain parameters employed during the experiment, including the scan step size, the reciprocal pixel size of the diffraction patterns, and the real-space/reciprocal-space rotation angle. The latter arises due to the helical path that accelerated electrons take along the

optical axis, as well as the orientation of the detector in the STEM column relative to the beam raster grid, which means that there is typically a rotational offset between the real-space/reciprocal-space coordinate systems. This real-space/reciprocal-space rotation angle must be accounted for in the reconstruction to ensure that the diffraction patterns are correctly interpreted in terms of their position in real space.

The gradient of the electrostatic potential is expected to be a conservative vector field, which allows for the determination of the real-space/reciprocal-space rotation by minimizing the curl or maximizing the divergence of the vectorial center-of-mass (CoM) of the virtual image as a function of a rotational offset[70,126]. This approach introduces a 180° ambiguity in the relative rotation, which can be resolved by ensuring that the phase shift remains positive across the sample, except for vacuum regions[69,70]. In the standard configuration of the JEOL ARM200F microscope with the MerlinEM Medipix3 detector, without any additional scan rotation being applied, this rotation angle is 134°for a 200 kV acceleration voltage.

Other parameters, such as defocus and other aberrations, are refined during the iterative reconstruction process; however, having a more accurate initial estimate can still improve convergence. In addition, reconstruction parameters, including iteration step size, batch size, and regularization strengths, also influence the quality of the final reconstruction.

To determine the optimal values for both experimental and reconstruction parameters, an optimizer based on the Bayesian optimization (BO) algorithm with Gaussian processes (GP) was implemented into the py4DSTEM software package used for the iterative reconstructions in this work. BO-GP is commonly employed for tuning hyperparameters in machine learning tasks[127-129]. The BO-GP algorithm models the function to be minimized as a combination of Gaussian processes and selects evaluation points by balancing the exploration of unsampled regions in the parameter space with the exploitation of local minima within the GP model[69].

Finally, experimental data may be influenced by various sources of artifacts, which are often not considered in ptychographic models. These include source incoherence, post-specimen aberrations introduced by the beam traveling through the spectrometer, and dead detector pixels. To mitigate these effects, strategies such as reducing the beam current to minimize incoherence, properly aligning the spectrometer, and utilizing dark current references are essential, depending on the severity of the issues. Furthermore, preprocessing techniques like weighted binning for dead pixels, as well as hot- and cold-pixel filtering and gain correction, can significantly enhance data quality. As mentioned before, a vacuum scan to obtain a suitable initial probe function is invaluable for every defocused ptychographic experiment[69].

1.2.6 Center-of-mass imaging

Although center-of-mass (CoM) or first-moment imaging was only used to determine the real-space/reciprocal-space rotation angle within the scope of ptychographic phase reconstructions in this work, it remains a key phase contrast imaging technique and was already utilized prior to the development of pixelated electron detectors. Therefore, it is suitable to include a brief description of this technique here as well.

When an electron beam interacts with the electrostatic potential of a sample, the CoM of the beam's momentum distribution undergoes a shift. The nature of this CoM shift depends on the probe characteristics and the sample features and can be used to reconstruct the sample's electrostatic potential[130]. Atomic-scale features typically result in a redistribution of intensity within the BF disk, whereas long-range, slowly varying fields induce near-rigid shifts of the entire disk. Or, to describe it in other words, high spatial frequency information about short-range potentials is encoded in the intensity distribution of the BF disk, while low spatial frequency information about long-range potentials is captured in the uniform displacement of the disk[130]. These phenomena have been known for a longer time now and have already been utilized by deducing the change in CoM in material systems through DPC using segmented detectors in STEM, as previously mentioned (Figure 2)[59,131-133].

In 4D STEM, the distribution of the electron intensity is recorded at each probe position, allowing to retrieve the electron wave phase from integrating the signal of a pixelated detector with a CoM response function. The CoM shift signal can be understood as the gradient of the local projected potential, cross-correlated with the intensity distribution of the incoming beam at a given probe position, assuming a POA with the 3D potential simplified to a 2D projected potential[130]. 4D STEM CoM measurements rely on the same principle as segmented detector DPC measurements, but can be seen as an improvement over the latter due to the better resolution of the detector used. For historical reasons, although both are essentially DPC measurements, we refer to DPC imaging when segmented detectors are used and to CoM imaging when the more finely pixelated detector is used[69]. Both DPC and CoM images are formed by using an anti-symmetric weighting function over the detector, *i.e.*, DPC uses +1 and –1 over the opposing detector halves, and CoM uses the coordinate of momentum space, such that any asymmetry in the diffraction pattern leads to a difference signal[130].

DPC/CoM phase reconstructions are straightforward and computationally inexpensive compared to other phase-contrast techniques. However, DPC reconstructions only solve for the phase of the sample and cannot deconvolve the probe's wave function. Therefore, any aberrations in the probe, including defocus, will affect the transfer of information in the reconstruction, and we cannot

reconstruct atomically-resolved images from a defocused 4D STEM dataset. Additionally, the reconstruction pixel size is limited by the real-space step size of the probe, with the absolute resolution limit determined by the semi-convergence angle. Beyond phase contrast imaging, DPC and CoM imaging are techniques sensitive to electric and magnetic fields, enabling the mapping of internal fields, polarization distributions, and charge accumulation or depletion at the nanoscale[69,134-136].

1.3 Oxides, oxide heterostructures, and interfaces

Fundamental physics research typically focuses on explaining thus far unconventional phenomena observed in material systems. As materials scientists, physicists, and chemists, we are eager to leverage these physical phenomena and unique material properties to facilitate their practical applications in real-world devices. A class of materials that offers immense versatility in functional applications is oxides. Many metals are capable of forming a wide variety of oxide compounds. The complex interplay and competition among charge, spin, structure, and orbital degrees of freedom has led, and still promises to lead to the discovery of exotic phenomena. These discoveries further advance fundamental science and engineering, enabling new application domains, as illustrated in Figure 6, which include superconductors, energy storage, catalysis, and electronic devices. Among the diverse range of functional oxides, 3*d* and 4*d* transition metal oxides show highly diverse properties. These materials include both metals and insulators, with some showing metal-insulator transitions characterized by drastic changes in conductivity[137]. Many of them are magnetic—in fact nearly all strong magnets belong to this group—and they also include superconductors with the highest critical temperatures[138].

The variety of phenomena in these materials is due to the fact that their electrons can either be localized on ions or delocalized, becoming itinerant[139]. As one progresses from the 3*d* to the 4*d* and 5*d* series, the general trend is a reduction in the correlation of *d*-electrons. The 4*d* and, particularly, the 5*d* electrons are more spatially extended compared to 3*d* electrons, leading to increased covalency with surrounding ions and a broader bandwidth. At the same time, the effective Hubbard repulsion energy and Hund's rule energy decrease[139]. In contrast, for these heavier elements, the relativistic spin-orbit interactions become increasingly significant, strongly influencing the properties of 4*d* and especially 5*d* systems. Combined with structural degrees of freedom, 4*d* transition metal compounds exhibit distinct electronic, structural, and bonding properties compared to their 3*d* counterparts and tend to have more delocalized electrons, leading to metallic or itinerant magnetic behavior[139].

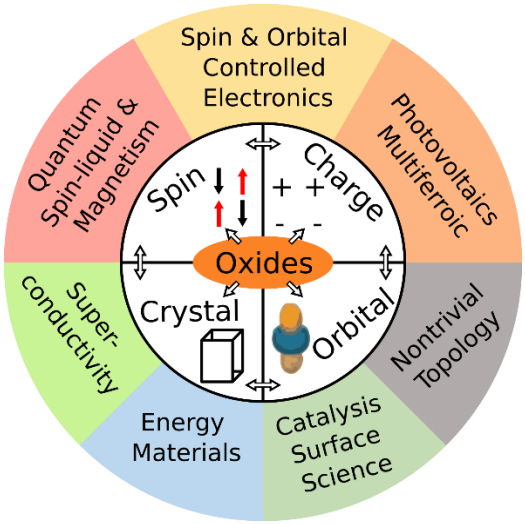

Figure 6. Schematic of degrees of freedom in oxides to tune material properties for the application as functional materials in various fields.

The enhanced spin-orbit coupling in 4*d* systems influences their electronic and magnetic properties, giving rise to phenomena such as unconventional superconductivity in Sr_2RuO_4 and itinerant ferromagnetism in $SrRuO_3$. Additionally, the stronger covalent bonding between 4*d* metals and ligands induces unique structural distortions, suppressed Jahn-Teller effects, and enhanced metal-ligand hybridization. Mixed-valence states and charge ordering, as observed in $NaRu_2O_4$, further add to the exotic electronic phases that emerge in these systems, and orbital and bond ordering may facilitate superconductivity in A_2RuO_4 (A = Sr, Ca) ruthenates. The ability of Ru to adapt distinct oxidation states from 0 to +8, with Ru^{3+} and Ru^{4+} being the most common in oxides, depends on both electronic and structural degrees of freedom. This adaptability enables the synthesis of mixed-valence ruthenates that exhibit temperature-dependent structural, electronic, and magnetic transitions[140-146].

Despite the remarkable diversity of properties, fundamental questions about the electronic structure of 4*d* transition metal oxides—particularly ruthenates—remain unresolved. This is due to the comparable magnitudes of several key parameters, including Hund's coupling, spin-orbit coupling, and exchange interactions, whose interplay is not yet fully understood[139]. Before phenomenological models can be established, extensive experimental investigations are necessary to explain observed phenomena. TEM is a particularly powerful tool for studying structure-property correlations in these materials. The second chapter of this thesis highlights the capabilities of TEM in revealing such rare phenomena in 4*d* transition metals, exemplified by the atomic-scale observation of an unconventional structural transition in the mixed-valence compound $NaRu_2O_4$, probed at elevated temperatures.

Once a material exhibiting intriguing electronic or structural behavior is discovered, it can be integrated into devices, often as a thin film or in combination with another material in a heterostructure, to create novel functionalities. Oxide heterostructures provide a powerful platform for engineering novel electronic phases by precisely tuning interfacial interactions, such as strain, charge transfer, and orbital hybridization. They consist of layers of different oxide materials, stacked with precise control to form sharp interfaces. These structures exploit the diverse and highly adjustable properties of oxides, including superconductivity, magnetism, ferroelectricity, and ionic conductivity[147].

By combining materials with complementary functionalities, oxide heterostructures can exhibit emergent properties not present in their individual components[148]. Heterostructure interfaces frequently determine the overall functionality and performance of devices[149,150]. By tuning the various degrees of freedom at oxide interfaces, novel and exotic materials can be precisely engineered, as illustrated in Figure 6. For example, interfaces between certain oxides can host a two-dimensional electron gas (2DEG) with high mobility or generate novel quantum states driven by interfacial coupling effects[151,152]. Heterostructures are widely used in transistors, diodes, and quantum wells to improve charge carrier mobility, reduce power loss, or for bandgap engineering in high-efficiency LEDs and lasers. Magnetic heterostructures enable spin-based data storage and processing, and are crucial for studying proximity effects and designing superconducting quantum interference devices (SQUIDs). Thin-film heterostructures enhance surface activity for sensors and catalysts. In photovoltaics and thermoelectrics, heterostructures optimize charge separation and energy conversion efficiency. As can be seen, the ability to engineer new functionalities renders oxide heterostructures valuable for both fundamental research and technological applications[149,152-154].

Delafossites (ABO_2) represent a particularly intriguing class of materials within the oxides, exhibiting remarkable transport, electronic, and structural properties. Their unique layered structure—composed of triangularly coordinated *A*-site cations (*A* = Cu, Pd, Ag, Pt) and edge-sharing BO_6 octahedra (*B* = Sc, Cr, Co, Fe, Rh)—induces significant anisotropy and enables a broad range of tunable functionalities[155,156]. Metallic delafossites such as $PdCoO_2$ and $PtCoO_2$ demonstrate exceptionally high in-plane conductivity, comparable to that of elemental metals, whereas others, like $CuCrO_2$, serve as some of the few transparent *p*-type conductors[157-160].

Beyond their intrinsic properties, delafossites are particularly promising for heterostructure engineering. Their atomically smooth layers and weak interlayer coupling provide an optimal platform for interfacial design, where strain, charge transfer, and orbital hybridization can be precisely controlled. The integration of delafossites into heterostructures allows for the exploration of new emergent phenomena while bridging the gap between the properties of single crystals and

their practical implementation into devices. This makes them a compelling system for both fundamental research and advanced technological applications[155,156]. The third and fourth chapters of this thesis focus on the interfacial engineering of delafossite thin films, aiming to harness the unique properties of single crystals for real-world device applications. In this context, STEM—with an emphasis on advanced imaging techniques such as electron ptychography, combined with spectroscopy, and imaging—serves as a powerful tool to investigate the nucleation mechanisms of various delafossites on different substrates. A thorough understanding of these growth mechanisms is essential for the successful fabrication of high-quality, phase-pure epitaxial films for device integration.

1.3.1 Fabrication of oxide heterostructures *via* PVD

Regardless of the growth mechanism, precise manufacturing techniques are essential for controlling layer thickness, composition, and interface quality in the fabrication of oxide heterostructures. Physical vapor deposition (PVD) methods are widely used for producing heterostructures and thin films by transferring material from a solid or liquid source to a substrate in a vacuum or controlled environment. These techniques rely on physical processes such as evaporation, sputtering, or ablation to vaporize the material, which then condenses onto a substrate to form a heterostructure. The versatility of PVD techniques enables the deposition of a wide range of materials, including metals, oxides, nitrides, and complex compounds.

Pulsed laser deposition (PLD) is a technique that involves the ablation of a source material from a stoichiometric target in a vacuum chamber using ultrashort laser pulses. The material is vaporized from the target as a plasma plume containing a variety of energetic entities, including atoms, molecules, electrons, ions, clusters, particulates, and molten globules. The vaporized material then deposits onto a substrate as a thin film, ideally maintaining the same composition as the source material, since during a short laser pulse, the different volatilities of the constituents can be neglected[161-163]. The dynamics of the plasma, *i.e.*, the spatial distribution of the plume, depend on the background pressure in the PLD chamber. In a high vacuum, the plume remains narrow and forward-directed, with little scattering from background gases. For intermediate background pressures, high-energy ions separate from less energetic species, and at high background pressures, resulting from the introduction of a reactive background gas like oxygen, the plume exhibits a diffusion-like expansion, with increased scattering due to the mass of the background gas[164,165]. Most importantly, an increase in background gas concentration, *i.e.*, higher chamber pressure, slows down the highly energetic species in the plume[166].

During the deposition process, high-energy species ablated from the target bombard the substrate surface and may potentially cause damage through sputtering of surface atoms or initiate defect

formation in the film. The sputtered substrate species and emitted target particles create a collision region that serves as a nucleation source and the key is tuning laser fluence, background pressure, and target-to-substrate distance to optimize energy levels[167]. If the condensation rate is high enough, thermal equilibrium is established on the substrate surface, supporting film growth. In general, each laser pulse results in a large supersaturation on the substrate compared to other physical deposition techniques with a more continuous flux of arriving species. In PLD, growth can occur in three modes:

(i) step-flow growth, where atoms diffuse to step edges on miscut substrates;
(ii) layer-by-layer growth, where islands nucleate, coalesce, and form smooth layers;
(iii) 3D growth, where islands stack atop each other, creating a rough surface[168].

Molecular beam epitaxy (MBE) is a technique that involves the assembly of films from individual elements or atomic/molecular beams, allowing for the precise construction of arbitrary compounds on suitably heated substrates in a high-vacuum environment. In contrast to PLD, the target materials are contained in precisely heated cells (commonly heated by electron beams) with a small opening, known as Knudsen cells. Shutters placed in front of the cells enable precise control of the molecular beams. The stoichiometry of the films is determined by the substrate temperature and the flux of the individual component species reaching the growing film. Typically, the films nucleate as small islands that coalesce into continuous atomically thin layers or *via* step-flow growth on miscut substrates. The ability to independently control the flux of each component in MBE allows for precise stoichiometric control, with the quality of the grown material being highly sensitive to the presence of impurity atoms[169].

MBE offers two distinct operational modes: shutter-controlled layer-by-layer growth or co-deposition of the materials. In shutter-controlled growth, the material flux from the Knudsen cells is controlled by the shutters, which intermittently open and close to enable the sequential deposition of each layer of the film. By alternating the exposure of the substrate to the atomic beams, this mode facilitates the fabrication of complex heterostructures, where atomic-scale control of each layer's growth is critical. During co-deposition, two or more atomic or molecular beams of different elements are simultaneously directed onto the substrate, allowing for the absorption-controlled growth of multi-element films with precisely controlled stoichiometry[170,171]. For the growth of oxides and multi-component oxides in particular, a molecular beam of oxidant is employed. The maximum pressure of the oxidant depends on the MBE geometry, the element to be oxidized, and the oxidant species used (*e.g.*, oxygen, ozone, or plasma sources)[150].

In addition to these two well-established methods for thin-film production, as well as other techniques such as sputtering and arc plasma deposition, a new method that combines the

advantages of MBE and PLD has recently emerged: thermal laser epitaxy (TLE). In TLE, laser beams located outside the vacuum chamber heat both the substrate and the sources. The chamber design enables a short working distance (<10 cm), maximizing the efficiency of the source. The composition of the background atmosphere and chamber pressure is constrained only by the condition that the mean free path of the evaporated species needs to exceed the source-substrate distance. The local laser heating facilitates the evaporation of solid elements from self-supported targets, eliminating the need for crucibles[172-174].

As a well-established technique for growing oxide heterostructures, MBE was the primary method used to grow ABO_2 delafossite thin films on various substrates in this thesis. The films were grown using both shutter-controlled growth and co-deposition within a high vacuum deposition environment, free from highly energetic species. While the choice of methodology is crucial in determining the structural integrity, stoichiometry, and bulk properties of the films, the resulting interfaces between different materials display varying degrees of coherence. The degree of lattice fit between the film and substrate significantly influences the interfaces, affecting the properties and performance of the heterostructure. Consequently, it is essential to select substrates that are appropriate for the desired application.

1.3.2 Coherent, semi-coherent, and incoherent interfaces

Interphase boundaries in solids can be classified into three categories based on their atomic structure: coherent, semi-coherent, and incoherent. Coherent interfaces form when the atomic lattices of the two adjoining phases align, maintaining a continuous lattice structure across the boundary. This results in minimal misfit strain and strong interfacial bonding, rendering them highly stable, as shown in Figure 7(a). When the lattice parameters of the two paired materials A and B slightly differ, coherence is maintained through elastic strain. The magnitude of the coherency strains and the resulting coherence stress depends on the lattice misfit between the two lattices and can be calculated as:

$$\delta_{Mismatch} = \frac{d_B - d_A}{d_A} \tag{42}$$

where d_A and d_B are the lattice parameters of material A and material B, which match at the interface[175]. As a result, for negative values of $\delta_{Mismatch}$, *i.e.*, $d_B < d_A$, material B is under tensile strain when forming an interface and for positive values of $\delta_{Mismatch}$, *i.e.*, $d_B > d_A$, material B is under compressive strain when the materials form an interface[176,177]. If the misfit between the two materials exceeds a critical value, it becomes energetically favorable for the system to incorporate misfit dislocations at the interface to compensate for the lattice mismatch instead of inducing elastic strain.

Semi-coherent interfaces develop and feature a partially aligned lattice with periodic dislocations, as shown in Figure 7(b). These dislocations relieve the strain but introduce localized distortions, striking a balance between stability and adaptability. Semi-coherent interfaces lack seamless structural connectivity, resulting in a disrupted interface that may significantly influence the heterostructure properties. The degree of incoherence strongly depends on the mismatch, but also correlates with the film thickness. Very thin films may grow completely coherent; however, as the film exceeds a critical thickness and elastic strain energy increases, the interface will become semi-coherent. A measure for the theoretical density of misfit dislocations, ρ_{theo}, that form at a heterointerface is given as:

$$\rho_{\text{theo}} = \frac{\delta_{Mismatch}}{b} \tag{43}$$

where b is the Burgers vector value of a misfit dislocation[178]. With the introduction of misfit dislocations, the interface exhibits nearly perfect matching, except for regions around the dislocation cores, where the structure is significantly distorted and the lattice planes become discontinuous.

Incoherent interfaces arise when the atomic arrangements of the two phases are entirely mismatched, resulting in a lack of crystallographic alignment. Such interfaces exhibit minimal structural continuity, leading to weaker bonding and higher elastic strain energy compared to coherent and semi-coherent interfaces, as shown in Figure 7(c)[176,177].

These classifications of heterostructure interfaces highlight the interplay between atomic alignment, strain accommodation, and stability at interphase boundaries, which must be considered when fabricating heterostructures, as interfacial properties significantly influence the overall heterostructure properties.

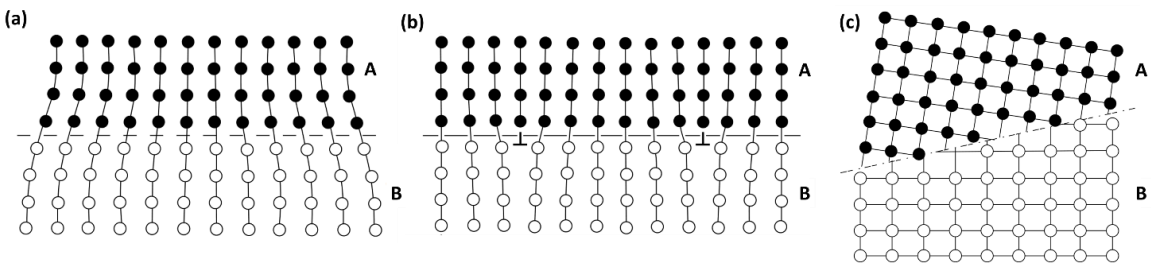

Figure 7. (a) Coherent interface with elastic mismatch strain stabilizing the heterostructure interface. (b) Semi-coherent interface with misfit dislocations relieving strain and stabilizing the heterostructure. (c) Incoherent interface. Adopted with permission[177], © 2009 by Taylor & Francis Group, LLC.

1.3.3 Analysis of misfit dislocations and strain in TEM: GPA and phase lock-in technique

To investigate the nature of heterostructure interfaces and epitaxial films, (S)TEM imaging provides a powerful tool for visualizing the atomic structure and strain distribution at interphase boundaries. Several methods are available, including direct imaging, diffraction, holography, and Fourier analysis of high-resolution images, which resolve the atomic structure to examine the strain field associated with heterostructure interfaces[179]. STEM enables direct imaging of atomic columns, and since HAADF STEM image contrast depends on the atomic number, HAADF STEM allows direct real-space tracking of atomic positions with picometer precision. However, strain analysis from real-space atom tracking can be computationally demanding and—even with high-quality data—challenging over large fields of view, as the materials may possess multiple coexisting structural order parameters, complicating the disentangling of lattice distortions and their interplay[180].

Fourier-based methods provide an alternative for efficiently analyzing structural information and separating orders with different periodicities, without requiring isolated atomic columns or such high signal-to-noise ratio data. The most prominent Fourier-based technique is geometric phase analysis (GPA), a powerful method for processing S(TEM) micrographs to generate phase-field and strain maps. The GPA algorithm reconstructs a displacement field from a micrograph by applying Fourier filtering centered on two non-collinear Bragg vectors. The resulting phase image reflects the local deviation of a chosen set of lattice planes relative to a reference lattice, while the strain field is derived from the lattice displacement field in a principal direction. Notably, the term "phase" in GPA refers to the phase, related to the position of image contrast maxima, and is not to be confused with the phase of the electron wave function that is reconstructed in ptychography[181,182]. STEM imaging, unlike HRTEM, can introduce artificial fringe distortions during image acquisition, with "flyback" errors along the fast scan direction being a significant artifact that must be considered for strain analyses from STEM images[183,184].

The phase lock-in analysis developed by Goodge *et al.* extends traditional GPA to Fourier components that encode periodic modulations of the crystal lattice, such as superlattice or secondary frequency peaks, as well as defects, such as misfit dislocations. This enables the extraction of the behavior of multiple different order parameters within the same image. Based on the principles of lock-in processing, the phase lock-in method is related to GPA, except that the phase demodulation step is performed in real space rather than reciprocal space. Conceptually, phase lock-in analysis yields qualitatively identical results to GPA and was used in the scope of this thesis due to the straightforward implementation in Python, provided by Goodge *et al.*, for data analysis of STEM images[185].

2 Direct evidence of anomalous Peierls transition induced charge density wave order at room temperature in metallic $NaRu_2O_4$

At the Max Planck Institute for Solid State Research, we mainly conduct fundamental physics research and frequently observe phenomena in oxide compounds that cannot be explained using established models. For the investigation of quantum materials, understanding anomalous behavior under charge degrees of freedom through bond formation is of fundamental importance. This study conducts the atomic-scale observation of an unconventional phase transition in the mixed-valence oxide $NaRu_2O_4$, contributing to the understanding of emergent phenomena in strongly correlated systems consisting of heavy 4*d* transition metals. Through this understanding, the atomistic origin of the interplay of the concepts of bond shortening (dimerization) and charge ordering at room temperature within metallic single-crystalline $NaRu_2O_4$ can be unveiled.

The transmission electron microscopy techniques utilized here allow to probe the lattice order of $NaRu_2O_4$ as a function of temperature and provide direct microscopic evidence of an anomalous Peierls-type transition. This transition is associated by a pronounced dimerization of Ru chains, resulting in a distinctive twofold superstructure along the *b*-axis below the critical transition temperature of ~535 K, coinciding with a charge order. *In-situ* heating experiments confirm the reversibility of this first-order phase transition, and periodic lattice-displacement maps depict atomic-scale displacements linked to dimerization.

The following text and figures in this chapter are adopted from this publication[186]:

Anna Scheid, Isha, Arvind K. Yogi, Masahiko Isobe, Birgit Bußmann, Tobias Heil, and Peter A. van Aken. Direct evidence of anomalous Peierls transition-induced charge density wave order at room temperature in metallic $NaRu_2O_4$, *Microscopy and Microanalysis*, Volume 31, Issue 1, ozae129, February 2025, https://doi.org/10.1093/mam/ozae129[186].

Contributions to this publication:

Anna Scheid, Arvind K. Yogi and Masahiko Isobe conceived the project. Anna Scheid wrote the initial manuscript and performed the TEM data acquisition and TEM data analysis. Isha synthesized the $NaRu_2O_4$ crystals under the supervision of Arvind K. Yogi and Birgit Bußmann contributed to TEM sample preparation. Arvind K. Yogi performed the resistivity measurements. Tobias Heil assisted with TEM data evaluation. Tobias Heil and Peter A. van Aken supervised this project and provided valuable input on data analysis. All co-authors revised the manuscript.

2.1 Introduction

Ruthenium-based 4*d* transition metal compounds (TMCs) have been widely studied in the realm of quantum materials and strongly correlated electron systems, attracting significant interest due to their nuanced spin-orbit coupling (SOC), which strikes a delicate balance between being neither excessively weak nor overwhelmingly dominant when compared to the Coulomb interaction U[187]. This complex interplay gives rise to a highly diverse spectrum of distinct electronic, structural, and bonding properties within the heavy 4*d* transition metal ruthenates, compared to their 3*d* counterparts, primarily due to the larger spatial extent of 4*d* orbitals, reduced electron-electron correlations, and stronger spin-orbit coupling. The 4*d* and especially the 5*d* orbitals are more spatially extended than 3*d* orbitals, leading to increased overlap with neighboring orbitals. This promotes stronger covalency with the surrounding ions and larger bandwidths. While 3*d* transition metals often display strong electron localization, leading to Mott-insulator behavior and pronounced magnetic ordering, 4*d* transition metals tend to have more delocalized electrons, resulting in metallic or itinerant magnetic behavior[139]. For these heavier elements, the relativistic spin-orbit interaction becomes more and more important and can determine electronic and magnetic properties, contributing to phenomena such as metal-insulator transitions, unconventional superconductivity, orbital ordering, and high-temperature ferromagnetism[188-192].

In ruthenate systems, the interplay between localized and itinerant electrons, combined with the orbital degrees of freedom, significantly enhances the diversity of electronic and magnetic properties, including temperature-dependent magnetic phase transitions and charge ordering (CO)[193,194]. A CO transition is typically accompanied by a metal-to-insulator transition, where the charge-ordered phase is insulating and the disordered phase is metallic. The CO state usually represents the low-temperature phase of a material that undergoes a symmetry-breaking transition, resulting in inequivalent ionic sites in different charge states. CO is commonly observed in mixed-valence or electron-/hole-doped materials, where elements can exist in multiple valence states. Above the transition temperature, the material typically adopts a single crystallographic metal site with an averaged valence state[195].

Strong correlations at low temperatures also depend on the material's electronic structure, which can be influenced by non-trivial topologies and symmetries. For instance, one-dimensional (1D) lattices with tunnel geometries can develop structural instabilities below the critical temperature (T_C), enhancing electron-phonon interactions and promoting a Peierls transition[196]. This transition results in a periodic modulation of the electronic charge density, forming a charge density wave (CDW), while the lattice distortion opens a gap at the Fermi level in the electronic band structure. While Mott-Hubbard physics successfully explain such metal-to-insulator transitions in 3*d*

transition metals[139], limited research has been conducted on this phenomenon in 4*d* transition metal oxides like ruthenates, especially in mixed-valence Na-Ru-O systems[140,141].

In the preceding study upon which this work is based, an unconventional first-order metal-to-metal transition with emergent CO was identified in $NaRu_2O_4$ at an elevated temperature of T_C = 535 K[141]. While the high-temperature (HT) phase is consistent with the orthorhombic *Pnma* (#62) space group, room-temperature (RT) single-crystal X-ray diffraction (SC-XRD) data reveal superlattice peaks, which differ from the structure previously reported by Darriet *et al.* and Regan *et al.*[197,198]. These earlier works, using $CaFe_2O_4$ as a structural prototype, refined the crystal structure of $NaRu_2O_4$ within the orthorhombic *Pnma* (#62) space group, and determined the lattice parameters as a = 9.2737(4) Å, b = 2.8215(1) Å, and c = 11.1701(5) Å by SC-XRD and powder neutron diffraction[197,198]. In addition, magnetic susceptibility measurements confirmed temperature-independent paramagnetism[198].

In contrast to the earlier observations by Darriet *et al*. and Regan *et al*., modern instrumentation has enabled the detection of weak $\mathbf{q} = (0, ½, 0)$ superlattice reflections emerging below 535 K, providing clear evidence of broken symmetry and lattice distortions. Yogi *et al*. used CBED patterns and confirmed a monoclinic $P112_1/a$ symmetry (#14) for the RT phase, a subgroup of the originally reported *Pnma* symmetry[141]. Structural analysis revealed significant dimerization along the crystallographic *b*-axis during the transition from the high-temperature (*Pnma*) phase to the low-temperature phase, leading to a doubling of the unit cell. All XRD reflections were well indexed by a monoclinic $\boldsymbol{a_0} \times 2\boldsymbol{b_0} \times \boldsymbol{c_0}$ cell with a primitive lattice of a = 9.273(6) Å, b = 5.643(3) Å, and c = 11.17(7) Å.

The relatively short bond length of approximately 2.6 Å in the dimers, which is smaller than that in metallic Ru, suggests direct metal-metal bonding and indicates the presence of a bond-centered CDW. Additionally, the nonequivalence of Ru sites during the transition suggests a site-centered CO. Interestingly, $NaRu_2O_4$ retained metallic behavior across the entire observed temperature range, albeit with a noticeable hysteresis in resistivity at the transition temperature[141]. It appears that the Ru 4*d* bands exhibit a delicate balance between correlations, the Coulomb interaction, and bandwidth, with the orbital degrees of freedom and mixed valence of Ru allowing the presence of both site- and bond-centered COs[199].

This coexistence of COs makes $NaRu_2O_4$ a rare example of CO phenomena in metallic systems, which are seldom observed in such materials[200]. For instance, in doped and intercalated $IrTe_2$ compounds, the interplay of electron correlations and modest spin-orbit coupling of 5*d* Ir electrons—comparable to that of 4*d* Ru electrons—gives rise to a variety of intriguing phenomena. These include uncompensated thermal hysteresis in the transition behavior, multiple CO states

while maintaining metallicity, anionic polymer bond breaking, dimerization, and charge fluctuations[200-203]. As there remains an ongoing debate in the literature regarding whether these phenomena involve orbital-driven Peierls transitions, extensive experimental investigations are crucial for establishing robust phenomenological models[140,141]. Thus, a more comprehensive understanding of the structural and electronic reconfigurations in the $NaRu_2O_4$ system as a function of temperature promises to advance our knowledge of quantum materials and correlated electron systems, paving the way for potential applications and innovations.

Improving on the large-scale XRD investigation of the previous work, this study focuses on examining the atomic lattice reconstruction in the metallic $NaRu_2O_4$ system, using SAED and *in-situ* STEM. The achievable spatial resolution of these techniques enables the investigation of local structural dynamics as a function of temperature, which X-ray studies, averaging properties over a wide specimen area, cannot reveal. Picometer-scale periodic lattice displacement (PLD) maps reveal the orbital-driven dimerization (Peierls-type distortion) along the crystallographic *b*-axis for different zone axes below the critical transition temperature. This study provides the first direct, atomically-resolved microscopic evidence for a quasi-one-dimensional Peierls-type symmetry-breaking phase transition at room temperature in $NaRu_2O_4$, which induces a unidirectional, commensurate CDW within the material.

2.2 Materials and methods

2.2.1 Sample preparation

Polycrystalline $NaRu_2O_4$ samples were synthesized by solid-state reaction of preheated RuO_2 (99.999%, Aldich) and Na_2CO_3 (99.999%, Aldich) under an Ar gas environment at 1123 K for 90 h with several intermediate grinding and pelletizing steps. High-quality single crystals of $NaRu_2O_4$ were then grown from this polycrystalline powder *via* a modified self-flux vapor transport reaction under flowing Ar gas (ultra-pure 99.999%). Long needle-shaped high-quality single crystals with a broad size distribution up to $1 \times 0.1 \times 0.1$ mm^3 were obtained from the final products. Phase purity was checked using a Bruker D8 Discover diffractometer with a Cu-Kα source, which shows no impurity peaks. To confirm the stoichiometry of the samples, an elemental analysis was performed using a COXI EM-30 scanning electron microscope equipped with a Bruker QUANTAX 70 energy-dispersive X-ray system. Electrical resistivity (ρ) measurements were performed using a home-built system equipped with a furnace (300 to 590 K) and a pulsed-tube cryostat (down to 3 K, Oxford). Electrical resistance was measured in the four-point geometry on a static sample holder with contacts to a large single-crystal needle made with silver paint and 10 μm gold wire. The current was applied perpendicular to the single crystal length, *i.e.*, the crystallographic *b*-axis.

2.2.2 TEM investigations

Different TEM specimens of the $NaRu_2O_4$ crystals were prepared. Some were prepared by drop-casting the crystals dispersed in ethanol onto lacey carbon-supported copper grids. Since the elongated structure of the crystals prevents direct imaging along the crystallographic *b*-axis, another batch of crystals was embedded in Epofix resin (Struers GmbH). They were then microtomed using a diamond knife (Diatome GmbH) and an EM UC6 ultramicrotome (Leica GmbH).

STEM investigations were performed using a JEOL ARM200F equipped with a cold field-emission gun and a probe C_S corrector (DCOR, CEOS GmbH). The measurements were performed at ambient temperature with an acceleration voltage of 200 kV. In order to improve the signal-to-noise ratio, reduce scanning artifacts, and address sample drift effects, the STEM images were generated from multi-frame acquisitions using high scanning speeds of 2-3 µs/pixel dwell time each, and applying post-acquisition cross-correlation using the built-in spatial alignment function in Gatan Digital Micrograph. In addition, a fixed rotation of the scan window with respect to the atomic lattice was implemented to avoid superposition of lattice peaks in the Fourier transform with features associated with scan artifacts. For the acquisition of the HAADF STEM images, a 30 µm condenser aperture was used to form an electron probe with an effective semi-convergence angle of 20.4 mrad, combined with a 3 mm BF aperture and a beam stopper for the ABF images. With a camera length of 6 cm for the simultaneously acquired HAADF and ABF images in Figure 8, this setup results in an effective semi-collection angle of 75-310 mrad and 11-23 mrad, respectively, using the JEOL STEM detectors. For the remaining HAADF STEM images, the Gatan annular STEM detector was used with a camera length of 2 cm, providing an effective semi-collection angle of 83-205 mrad.

The EELS data were acquired using a Gatan GIF Quantum ERS imaging filter with a 5 mm entrance aperture and a 1.5 cm camera length, resulting in a semi-collection angle of 111 mrad. Principal component analysis (PCA) was employed to improve the signal-to-noise ratio, and 15 principal components were used for accurate elemental mapping[204].

For 4D STEM data acquisition, a MerlinEM Medipix3 detector from Quantum Detectors was used with a camera length of 40 cm and a probe semi-convergence angle of 20.4 mrad. The detector was operated in 1-bit mode, which allowed effective detection of one electron per detector pixel in a single frame, with a fast pixel dwell time of 25 µs, corresponding to a frame rate of 40000 fps. The ptychographic reconstructions were performed for a 4D STEM dataset containing 400x400 scan positions with a pixel step size of 0.0121 nm, using ptychoSTEM, an open-source MATLAB script repository available on GitLab[83,84,116].

The SAED experiments were performed on a JEOL ARM200F equipped with a cold field-emission gun and an image C_S corrector (CetCOR, CEOS GmbH), operating at an acceleration voltage of 200 kV. A 20 µm selected area aperture resulting in an effective area radius of 120 nm was used for SAED pattern acquisition. The resulting SAED patterns were extensively simulated using the ReciPro software, as originally introduced by Seto *et al*[205].

A Gatan heating holder of model No. 652 was used for the *in-situ* heating experiments. This heating holder is equipped with a double-tilt system and a hexring sample support mechanism. The setup allows achieving temperatures of up to 1273 K, necessary for accurate and reliable high-temperature experiments. During both the heating and cooling experiments, temperature ramps were maintained at a constant rate of 20 K/min, ensuring controlled and gradual temperature changes to capture the dynamic behavior of the material under investigation.

2.3 Results and discussion

2.3.1 Microscopic structural investigation of $NaRu_2O_4$ along the *b*-axis

The RT phase of $NaRu_2O_4$ crystallizes in a monoclinic structure within the space group $P112_1/a$, with the lattice parameters a = 9.273(6) Å, b = 5.643(3) Å, and c = 11.17(7) Å. Its crystal structure is distinctive, particularly along the crystallographic *b*-axis. In the plane perpendicular to this axis, spatial voids are formed by edge-sharing double RuO_6 octahedra, which are interconnected with neighboring chains *via* corner oxygen atoms. Along the *b*-axis, these double chains form a two-legged zigzag ladder, creating a hollow-channel geometry, a feature commonly observed in various $CaFe_2O_4$-type lattices[206-209]. These pseudo-triangular channels accommodate the alkali ions, making the material promising for applications in Na-ion batteries and other ion transport-based technologies[210]. Figure 8(a) shows simultaneously acquired HAADF and ABF STEM images, revealing the atomic structure along the [010] zone axis.

Although the elongated rod shape of the crystals typically restricts access to this zone axis for drop-cast samples, ultramicrotomy-based TEM sample preparation allowed for imaging of the channel structure along the *b*-axis. The HAADF and ABF STEM images provide two-dimensional (2D) projection images of atomic column positions with sub-angstrom resolution[57]. While the HAADF image primarily emphasizes the heavier Ru atoms by collecting high-angle scattered electrons, the ABF image distinctly reveals sodium ions situated in the central cavity of edge- and corner-sharing RuO_6 octahedra. This distinction is due to the fact that only low-angle scattered electrons are detected, allowing the imaging of lighter ionic species[56,57]. The superposition with the structural model shows a high degree of agreement. In addition, EELS elemental maps were obtained from

the same sample area, and the isolation of signals from characteristic energy-loss edges (Na K, Ru $M_{5,4}$, and O K), shown in Figure 8(b), confirms the elemental distribution within the structure.

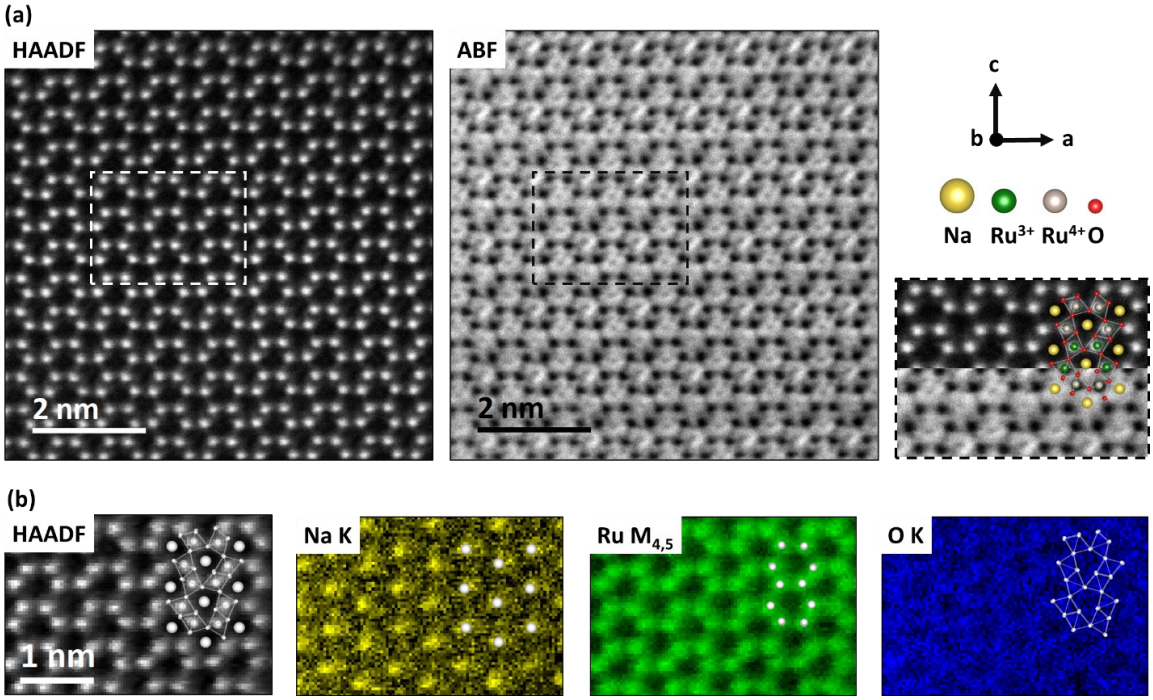

Figure 8. Representation of the hollow channel geometry of RT $NaRu_2O_4$ along the crystallographic *b*-axis. (a) Simultaneously acquired HAADF and ABF STEM images showing the tunnel structure. The inset shows the atomic arrangement, with the structural model superimposed. The ABF image shows the presence of Na^+ ions in the central cavity of the edge- and corner-sharing RuO_6 octahedra. (b) EELS elemental mapping over the identical sample area confirms the elemental distribution, as the atomic positions match their corresponding positions in the structural model (shown with white overlay). Due to the projection of alternating Ru^{3+} and Ru^{4+} atomic columns along the *b*-axis, they cannot be distinguished from the EELS signal. Reprinted under the terms of a CC-BY license. © 2025 The authors[186].

To provide a more comprehensive overview of the unique structure of $NaRu_2O_4$, Figure 9 shows RT STEM HAADF images along different zone axes, directly accessible from drop-cast $NaRuO_2$ crystals on lacey carbon TEM support grids. The HAADF-STEM images reveal the heavy Ru columns (overlaid for each orientation), and since the structure involving Na and O columns is more complex, for clarity, a structural model is displayed alongside each image to illustrate the Na and O columns along the respective axes.

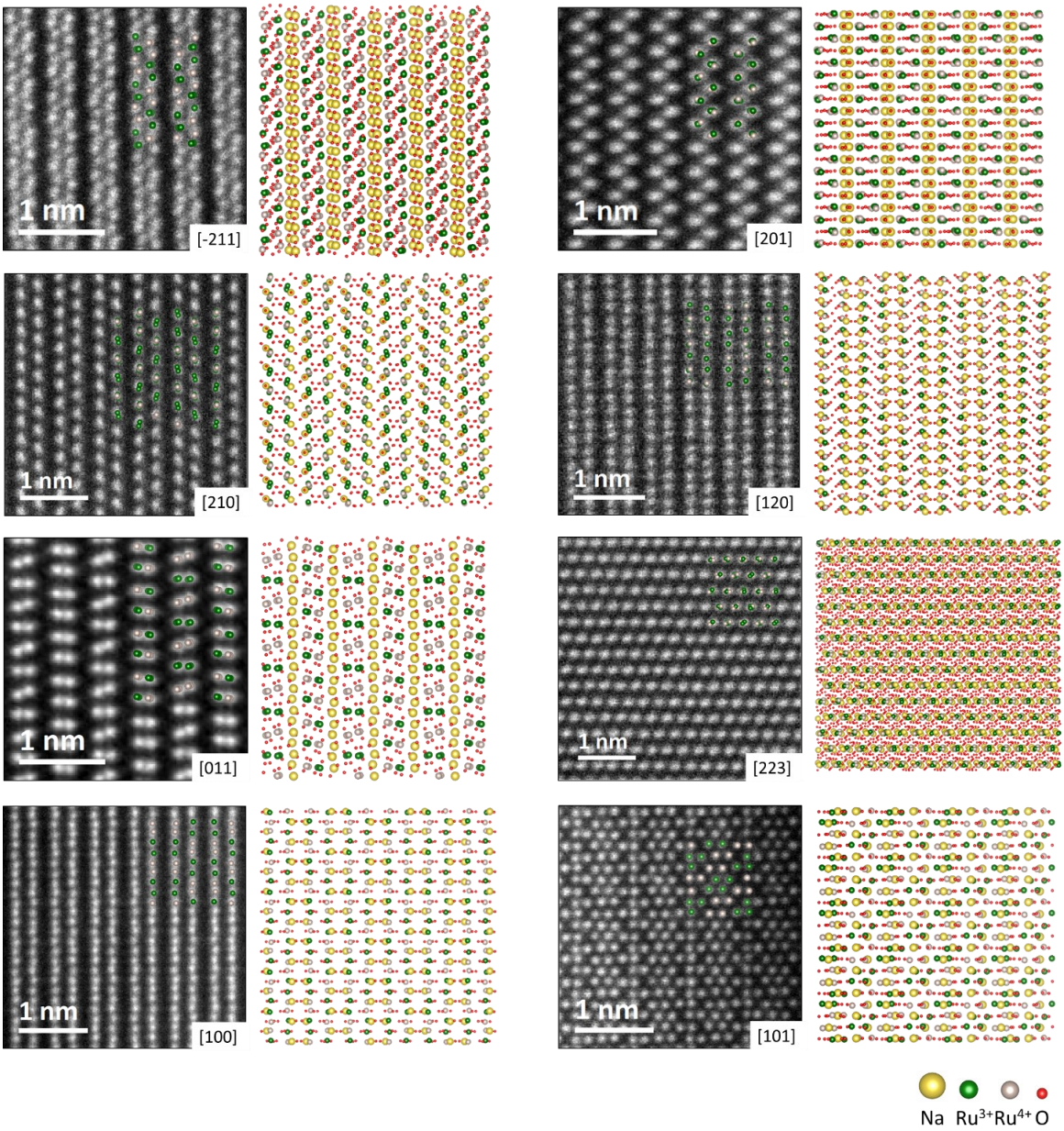

Figure 9. HAADF STEM images of RT $NaRu_2O_4$ along various zone axes. The HAADF images show contrast only for the heavy Ru atomic columns, while the Na and O columns are not visible. Each image is overlaid with the structural model along the respective zone axis, including only the Ru columns. The structural models, showing all atomic species, are displayed on the right of each STEM image. Reprinted under the terms of a CC-BY license. © 2025 The authors[186].

2.3.2 Electronic transport measurements

Due to the unusual tunnel structure of $NaRu_2O_4$ with edge- and corner-sharing RuO_6 octahedra, the material exhibits intriguing bulk electronic properties. Since the electron or hole scattering plays an important role in metallic $NaRu_2O_4$, the transport properties become crucial to understand the origin of the unconventional lattice distortion observed at elevated temperatures[141]. Figure 10(a) shows the electrical resistivity ρ of a single crystal of $NaRu_2O_4$ in the temperature range of

300 K ≤ T ≤ 590 K for both heating and cooling cycles. The experiment reveals that the system remains metallic with a resistivity in the order of a few $\mu\Omega$-cm throughout the entire temperature range. Notably, a hysteresis in electrical resistivity was observed in the heating and cooling cycles, indicating a first-order phase transition at T_C = 535 K.

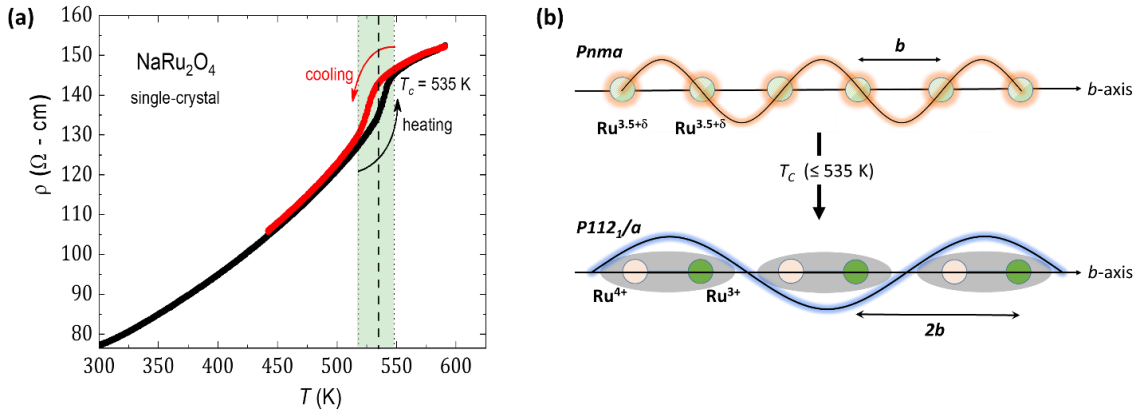

Figure 10. Temperature-dependent resistivity for $NaRu_2O_4$ in both heating and cooling modes between 590 K and 300 K[141]. The resistivity hysteresis, associated with a first-order phase transition, is indicated by the dotted line, the critical transition temperature of T_C = 535 K is highlighted by the vertical, black dashed line. (b) One-dimensional (1D) Ru chain along the *b*-axis tunnel structure. Above T_C, all atoms are equally spaced with the lattice constant b = 2.82(15) Å and the space group *Pnma*. Below T_C, the periodicity doubles to $2b$ = 5.643(3) Å with a symmetry-breaking transition to the $P112_1/a$ space group and the Ru-Ru bonds are shortened, as shown in the lower chain. This process leads to Ru^{4+}-Ru^{3+} dimerization along the *b*-axis. The physical consequence of such 1D electronic behavior is well defined as a Peierls-type phase transition in condensed-matter physics and leads to the formation of Ru dimers, highlighted in gray at the bottom. Reprinted under the terms of a CC-BY license. © 2025 The authors[186].

According to the preceding study, the **q** = (0, ½, 0) superlattice reflections persist up to a temperature of T_C = 535 K[141]. Beyond this temperature, the superlattice peaks undergo significant suppression. In the HT phase, the two independent Ru sites, Ru_1 and Ru_2, are equidistant with an interatomic distance of 2.82(15) Å. Upon cooling the material, the transition from orthorhombic *Pnma* to monoclinic $P112_1/a$, along with dimerization in the Ru chains, results in a doubling of the unit cell along the *b*-direction, according to the model shown in Figure 10(b). Simultaneously, the Ru sites become inequivalent ($Ru_{1A,B}$ and $Ru_{2A,B}$). Yogi *et al.* employed the bond valence sum (BVS) method and density functional theory with the local spin density approximation (LSDA and LSDA+U) to elucidate the charge pattern for the LT crystal phase[17]. In the HT phase, all Ru ions exist in the average 3.5+ valence state, whereas in the LT phase, a distinction between Ru^{3+} (Ru_{1A} and Ru_{2A}) and Ru^{4+} (Ru_{1B} and Ru_{2B}) states emerges. Consequently, in addition to bond order, a site-centered CO is also present in the metallic system at RT.

It is possible to study valence changes or different valences of atoms by EELS. However, the Ru $M_{5,4}$ edges, used for EELS elemental mapping in Figure 8, do not exhibit suitable "white lines" for valence state analysis. The Ru $L_{3,2}$ EELS edges, located at high energy losses (L_3 = 2838 eV and L_2 = 2967 eV), would provide suitable white lines for valence state determination[211]. Unfortunately, achieving a sufficient signal-to-noise ratio at these energy losses with the available microscope setup requires an electron dose that exceeds the material's critical threshold for structural stability. These edges could be accessed with newer counting detectors featuring low noise floors, as well as microscopes and spectrometers optimized for high-energy losses[212-215]. In addition, stripe-scanning techniques could be employed to fractionate the dose across multiple columns, followed by post-acquisition summation[216].

2.3.3 *In-situ* heating experiments

In-situ heating STEM experiments were conducted to examine the reversible structural transformation of $NaRu_2O_4$. The sample was gradually heated to temperatures slightly above the expected transition point and subsequently cooled back to room temperature. Since significant structural degradation was observed beyond 600 K, higher temperatures were avoided. HAADF STEM images, acquired along the [100] zone axis, are shown in Figure 11. The corresponding Fourier transform amplitudes, shown in the insets, reveal Bragg peaks associated with the crystalline lattice. The in-plane wave vector amplitude of q = ½ reciprocal lattice units, observed for the superlattice peaks, indicates the emergence of a twofold superstructure. Importantly, the commensurate **q** = (0, ½, 0) superlattice peaks, which are characteristic of dimerization, vanish in the HT phase and reappear upon cooling to the LT phase.

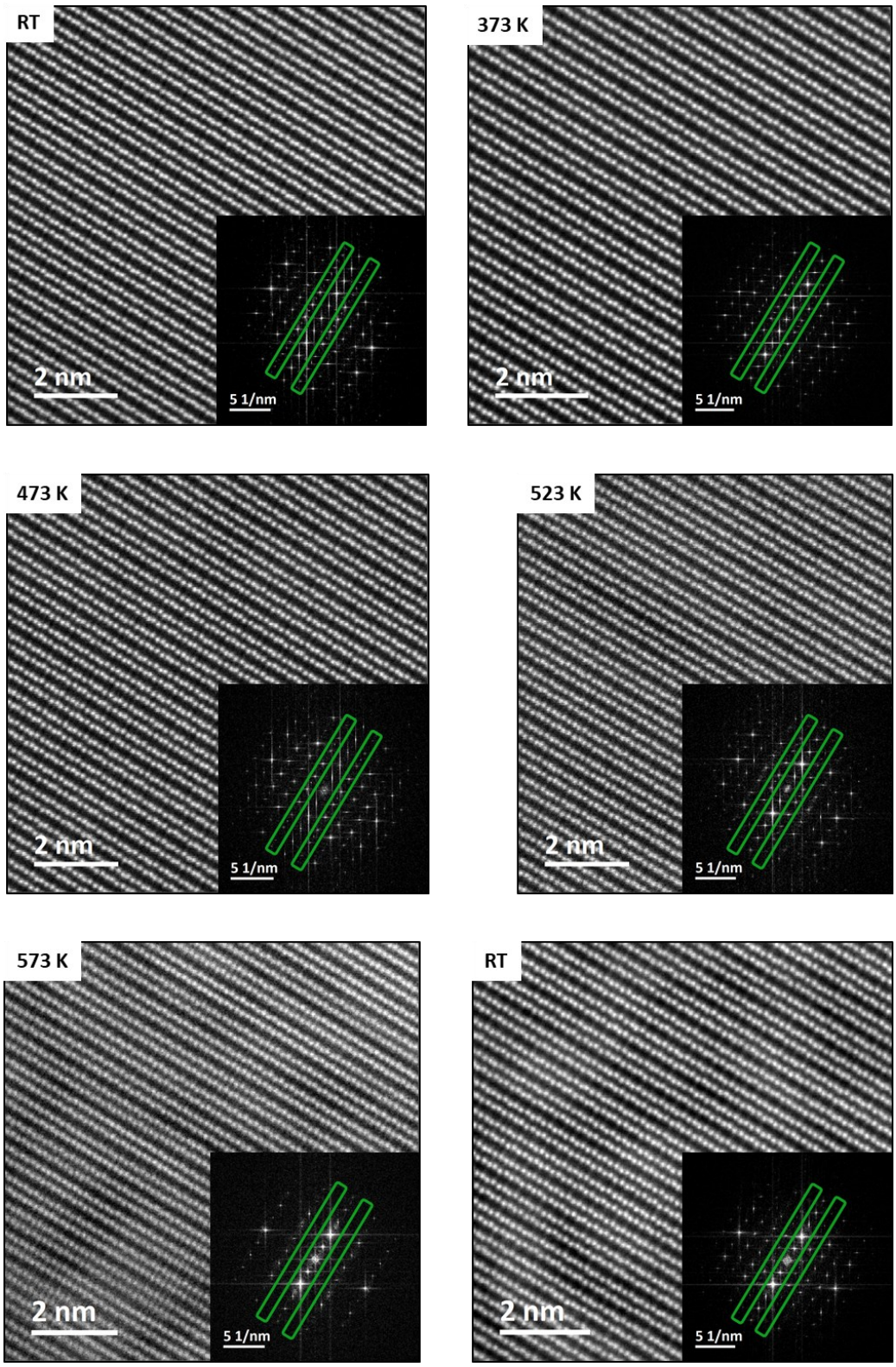

Figure 11. *In-situ* atomic-resolution HAADF STEM images of $NaRu_2O_4$ along the crystallographic [100] zone axis. The insets show the Fourier transform of each image. For temperatures below the critical temperature of 535 K, the (0, ½, 0) superlattice peaks are clearly visible (the regions with first-order superlattice peaks are outlined in green). Above the critical temperature, the structure transforms to the HT-*Pnma* phase and the superlattice peaks disappear. Upon cooling to room temperature, the peaks reappear and the structure transforms back to the LT-$P112_1/a$ phase. Adopted under the terms of a CC-BY license. © 2025 The authors[186].

In addition, *in-situ* SAED imaging was performed on a [100]-oriented single crystal to analyze the temperature-dependent structural evolution. The SAED patterns in Figure 12 further validate the displacive lattice modulations of the Ru sites at lower temperatures, leading to the observed doubling of the unit cell. With increasing temperature, the intensity of the superlattice reflections gradually diminishes until they vanish at the critical temperature T_C, followed by their reappearance upon cooling. These observations indicate an enhancement in bond-order strength and electronic correlations well below T_C. As an alternative to the SAED measurements conducted in this work, advanced STEM diffraction techniques could offer further insights into the temperature-dependent structural evolution. For instance, dimerization along the [010] direction could be probed from the [100] or [101] zone axis through the emergence of a higher-order Laue zone, which provides 3D structural information, as commonly observed in other modulated systems[217-219]. For microscopes equipped with a 4D STEM detector and the capability to perform precession or nanobeam diffraction, techniques such as 4D STEM nanobeam diffraction or 4D STEM precession diffraction could be utilized to track the emergence and disappearance of [0, ½, 0] superlattice spots. These approaches offer the advantage of reducing image distortions arising from instrument instabilities while also minimizing electron-beam exposure during *in-situ* experiments, providing a viable alternative to conventional SAED[220].

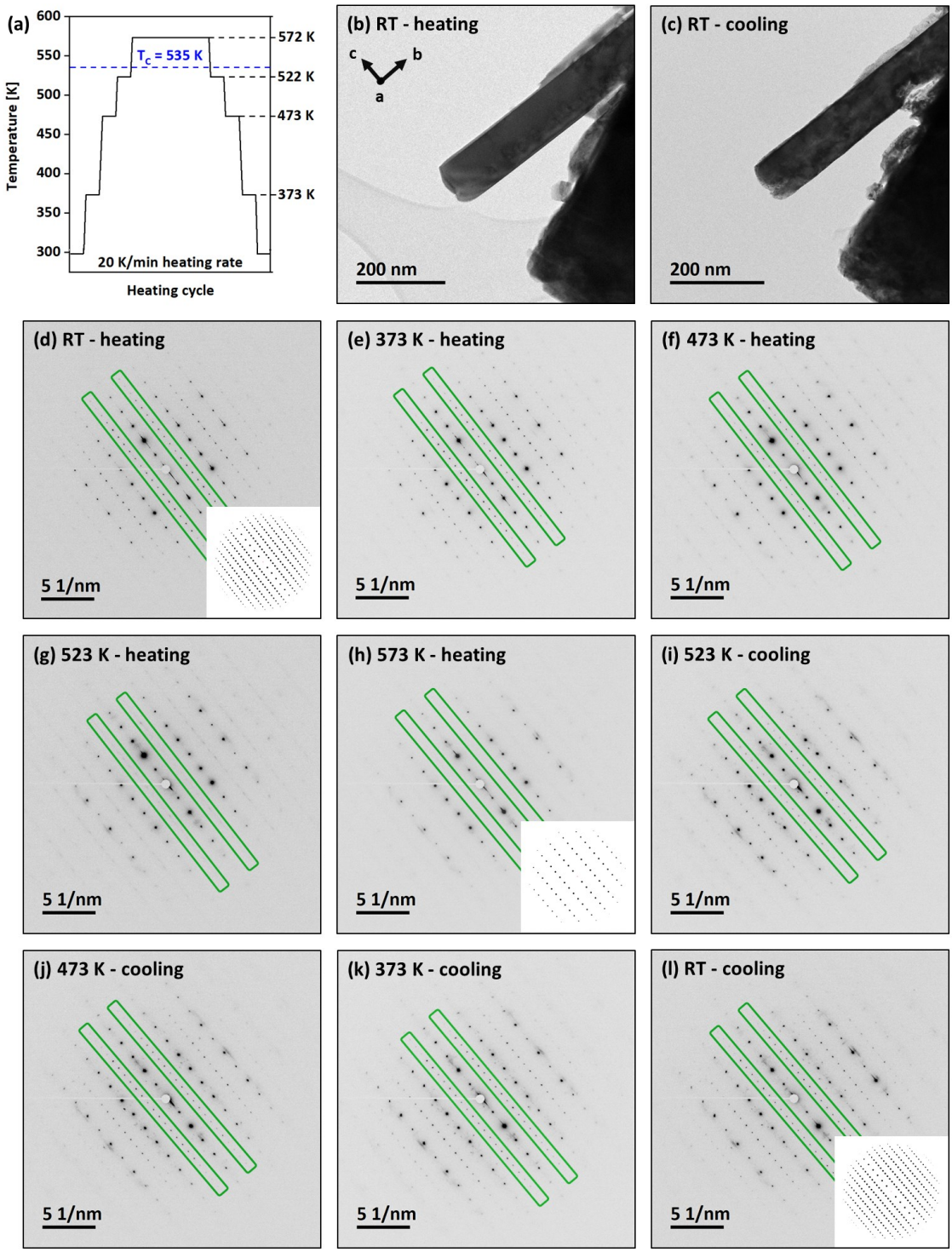

Figure 12. *In-situ* SAED of $NaRu_2O_4$, oriented along the [100] zone axis. (a) Temperature profile of the heating cycle. (b) TEM image of the [100] oriented crystal before the start of the heating experiment. (c) TEM image of the [100] oriented crystal after cooling back to RT. (d)-(l) SAED patterns taken at different temperatures (the areas with first-order superlattice peaks are outlined in green). Above the critical temperature, the superlattice peaks disappear and reappear when the sample is cooled below T_C. The insets in (d), (h), and (l) show simulated SAED patterns for the respective phases (LT-$P112_1/a$ phase for (d) and (b) and HT-*Pnma* phase for (h)). In addition, the TEM image in (c) and irregular spots in the SAED patterns indicate some degree of structural damage. Reprinted under the terms of a CC-BY license. © 2025 The authors[186].

The SAED measurements conducted in this study are sufficient to capture the structural transformation and confirm the reversibility of the transition, which induces CDW modulations. These modulations are attributed to the formation of distinct molecular Ru^{4+}-Ru^{3+} dimers. A straightforward explanation of the apparent CDW modulations in $NaRu_2O_4$ is given by the concept of the orbital-driven Peierls transition, which can open a gap at the Fermi level due to symmetry breaking, as schematically shown in Figure 13(a)[196]. This interpretation suggests that the CDW state arises due to electron-phonon interactions within the $NaRu_2O_4$ single crystal.

The Ru-Ru dimerization-induced lattice distortion modifies the energy band structure by creating a gap at the Fermi surface, leading to a first-order phase transition. This transition is characterized by a pronounced hysteresis and a slight decrease in conductivity exclusively at T_C, while below this temperature, the material remains a good metallic conductor. The presence of a CDW order in the metallic state of $NaRu_2O_4$ is attributed to multi-orbital effects. Within the molecular orbital framework, the dimer and diagonal bonds between dimers along the zigzag ladder structure in the *b*-direction give rise to Z-type charge and bond order clusters, as illustrated in Figure 13(b). However, the diagonal bond is not strong enough to drive the system into an insulating state, allowing it to retain metallic conductivity below T_C[141].

In addition, the lattice distortions accompanying dimerization can induce periodic modulations in the electron density. This type of symmetry breaking aligns with a Peierls-type transition, as observed in in the $NaRu_2O_4$ single crystal. Typically, Peierls transitions emerge in 1D metallic systems at low temperatures due to dimerization[196]. This study identifies a Peierls-type transition in a 3D solid with embedded 1D substructures. The crystal structure of $NaRu_2O_4$ exhibits two key 1D motives: (1) 1D tunnels and (2) legs of quasi-1D zigzag ladders, collectively form an interconnected 1D tunnel network within the lattice. This transition bears similarity to the Peierls-type transition reported in the $K_2Cr_8O_{16}$ hollandite tunnel system, where dimerization occurs within four 2x2 octahedral 1D chimneys. However, unlike $K_2Cr_8O_{16}$, where the transition drives the system from a metallic to an insulating state, $NaRu_2O_4$ remains metallic below the critical transition temperature[221]. Furthermore, while Peierls transitions in 1D metals typically occur at low temperatures, in $NaRu_2O_4$, the transition is observed at elevated temperatures, with the ordered state persisting at room temperature[196]. Given these distinct characteristics, the Peierls-type transition in $NaRu_2O_4$ is classified as “anomalous”.

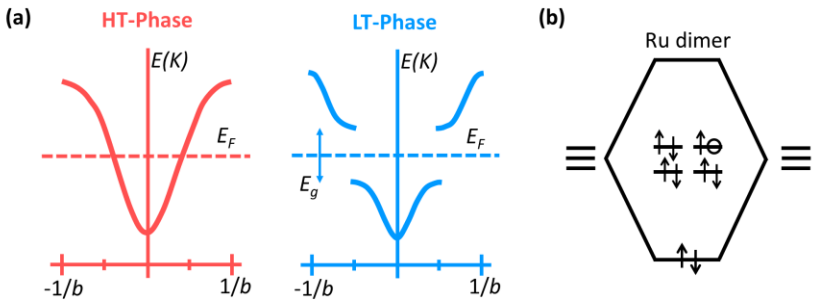

Figure 13. (a) Schematic of a Peierls transition from the HT phase (left) to the LT phase (right), accompanied by the opening of a gap in the electronic spectrum *E(K)*. The distance between lattice sites in the uniform chain is *b*. (b) Unique molecular orbitals formed by Ru^{4+}-Ru^{3+} dimerization in the Z-type charge and bond order system. Reprinted under the terms of a CC-BY license. © 2025 The authors[186].

Figure 14(a) shows a temperature series of atomic-resolution HAADF STEM images of $NaRu_2O_4$ along the [100] direction, all captured from the same region of interest. From RT up to 523 K, the four independent Ru sites remain clearly distinguishable. However, beyond the critical transition temperature at 573 K, this distinction is lost, and the unit cell size along the *b*-direction contracts by ½ due to the disappearance of dimerization. Interestingly, the HAADF image obtained after cooling the sample back to RT confirms the reversibility of the first-order transformation.

To correlate the STEM observations with the structural models of the two phases established by Yogi *et al.*, the dimer bond length along the *b*-axis was determined from the full field-of-view images in Figure 11 for each temperature. In the LT-$P112_1/a$ phase, the dimers $Ru_{1A,B}$ and $Ru_{2A,B}$ remain distinguishable. The structural models in Figure 14(b) emphasize the relevant lattice spacings for each phase. Specifically, the dimer and interdimer bond lengths for $Ru_{1A,B}$ are indicated by solid arrows, with theoretical bond lengths of 2.6013 Å and 3.0348 Å, respectively. Notably, the dimer bond length is significantly shorter than the actual metal-metal bond length for Ru[222]. For the $Ru_{2A,B}$ dimer, the theoretical bond lengths of 2.6115 Å and 3.0242 Å for the dimer and interdimer, respectively, are indicated by dashed arrows. As a result, a clear difference in the interatomic distance *d* between adjacent Ru_{1A}-Ru_{1B} and Ru_{2A}-Ru_{2B} columns is expected due to the pronounced dimerization.

Above the critical temperature, when dimerization disappears, the bond lengths of the dimer and interdimer should converge to the theoretical equal value of d_{theo} = 2.82(15) Å (shown by the blue arrows in Figure 14(b)). To quantify the interatomic distances from the full field-of-view HAADF images, atomic positions were determined using the 2D Gaussian fitting algorithm Atomap[223]. Initially, the algorithm identifies the positions of all atomic columns of interest by locating the most intense local features, separated by a minimum distance. It then refines these positions using the center of mass within a circular region at the current position, where the radius is set to 40 % of the

nearest-neighbor distance. For the refined positions, the algorithm fits the atomic columns with a 2D elliptical Gaussian function[223]. The accuracy of the peak-finding algorithm was evaluated using a reference $SrTiO_3$ sample: From an HAADF STEM image, acquired with similar STEM imaging conditions as the other measurements of this study, an average distance of d = 390.7 pm (d_{theo} = 390.5 pm) with a standard deviation of σ = 2.7 pm was calculated from the distances between 870 neighboring Sr columns. This demonstrates picometer-level accuracy for the Atomap algorithm, comparable to other algorithms based on 2D Gaussian fitting[180,224-226].

The measured bond lengths in Figure 14(b) demonstrate that the experimental lattice spacings are consistent with those of the structural models for both the HT and LT phases. The *in-situ* heating experiment confirms the presence of bond order and strong dimerization below the critical temperature, which vanishes at temperatures above T_C in $NaRu_2O_4$. At temperatures above the transition temperature, slight structural damage becomes evident through uneven contrast across the Ru columns in the atomic-resolution images in Figure 11. These regions contain degradation products that manifest as additional, irregular spots in the diffraction patterns shown in Figure 12. Notably, no amorphous background is observed in the SAED patterns at elevated temperatures or after the phase transition. This suggests that the structural damage results from the combined effects of electron-beam irradiation and high temperatures. Similar sample degradation has been previously reported by Yogi *et al.* in *in-situ* XRD measurements following prolonged irradiation[141]. Additionally, it is well established that continuous electron-beam irradiation accelerates structural degradation[227].

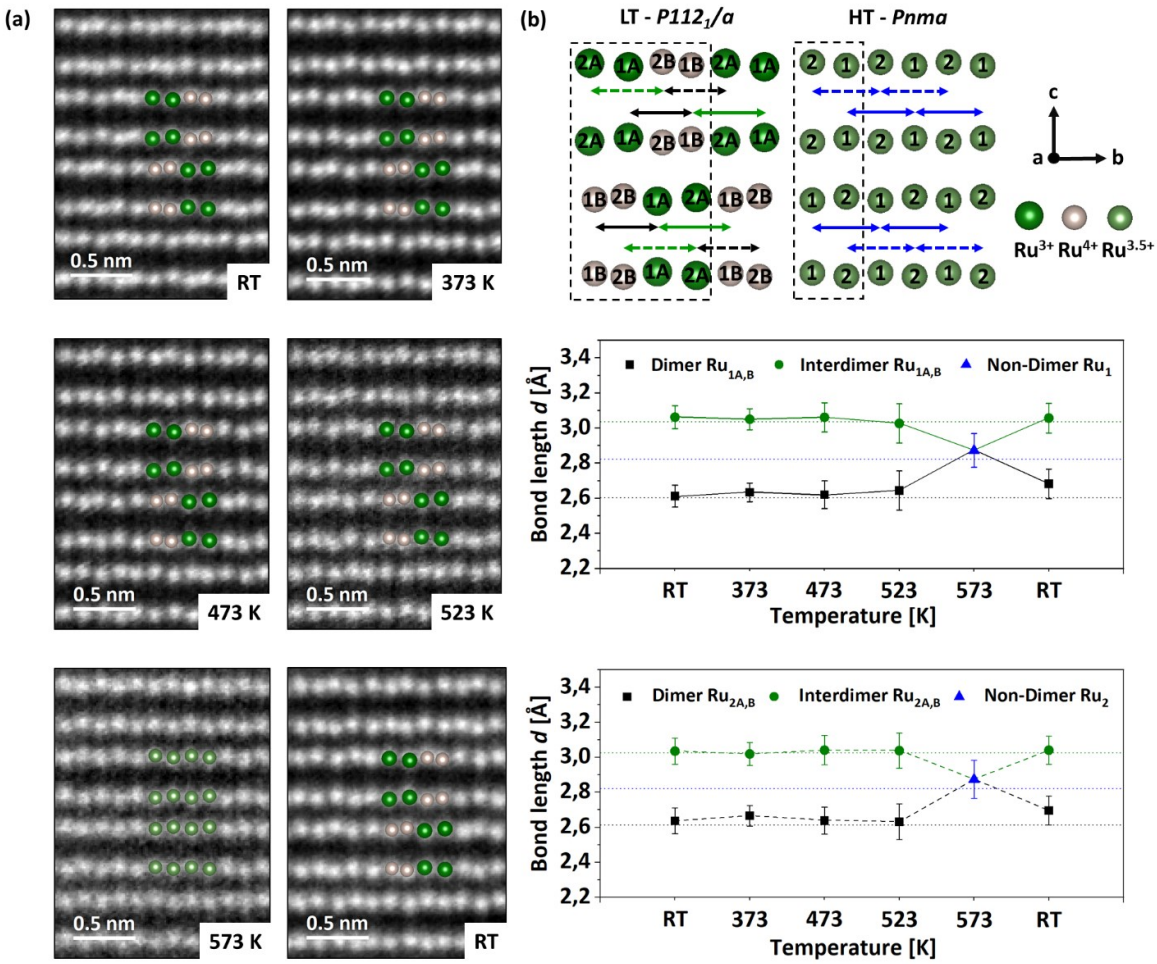

Figure 14. (a) *In-situ* atomic-resolution HAADF STEM images of $NaRu_2O_4$ along the crystallographic [100] zone axis with the structural model superimposed for each temperature. (b) Display of the structural models for the LT-*P112₁/a* phase (RT to 523 K), which shows four independent Ru sites (dimer $Ru_{1A,B}$ and dimer $Ru_{2A,B}$), and the HT-*Pnma* phase (573 K), which shows two distinct Ru sites (Ru_1 and Ru_2). The dashed black boxes indicate the respective unit cells. The dimer bond length and interdimer bond length, elucidated as a function of temperature, were derived from the full field-of-view HAADF images in Figure 11. The solid arrows in the structural model indicate the corresponding lattice spacings for the $Ru_{1A,B}$ dimer, while the dashed arrows indicate the lattice spacings within and between the $Ru_{2A,B}$ dimers. The dotted lines in the plots represent the theoretical values derived from the structural models. Reprinted under the terms of a CC-BY license. © 2025 The authors[186].

2.3.4 Periodic lattice displacement mapping

To further examine the local atomic displacements during the phase transition, PLD maps were constructed by extracting displacement vectors for each atomic site from the HAADF images shown in Figure 15. To do so, a reference lattice is essential for a comprehensive visualization of the atomic displacement that leads to the doubling of the unit cell along the *b*-direction. However, due to temporal instability in the TEM sample holder, thermal expansion of the sample during the heating process, and resulting sample drift, it was not feasible to obtain precise images of the atomic

structure at identical locations in both the HT and LT phases. Consequently, direct determination of the local atomic displacement was not possible. Instead, to visualize the displacement during dimerization, a synthetic HT phase was derived from the LT data following an approach similar to that used by Savitzky *et al*[180]. A reference HT image was created by removing all satellite peaks from the Fourier transform of the HAADF images of the LT phase. The superlattice peaks were damped to the background level in the amplitude of the Fourier transform while preserving the phase. An inverse Fourier transform was then applied to generate the reference lattice, which lacked any components associated with q = ½ reciprocal lattice units.

Following this approach the atomic positions from HAADF images of the LT phase were calculated using Gaussian peak fitting[223]. The difference between the fitted atom positions of the reference lattice and the LT phase was used to produce the PLD maps, shown at the bottom of Figure 15. However, it should be noted that while the reference lattice effectively removes superlattice reflections, it does not accurately represent the HT phase, as other factors, such as thermal expansion, were not considered. PLD maps were extracted for two different crystallographic zone axes, providing clear observation of the dimerization along the *b*-axis. The displacement pattern reveals the shortening of the Ru-Ru column distance within a dimer, accompanied by the elongation of the interdimer Ru-Ru distance.

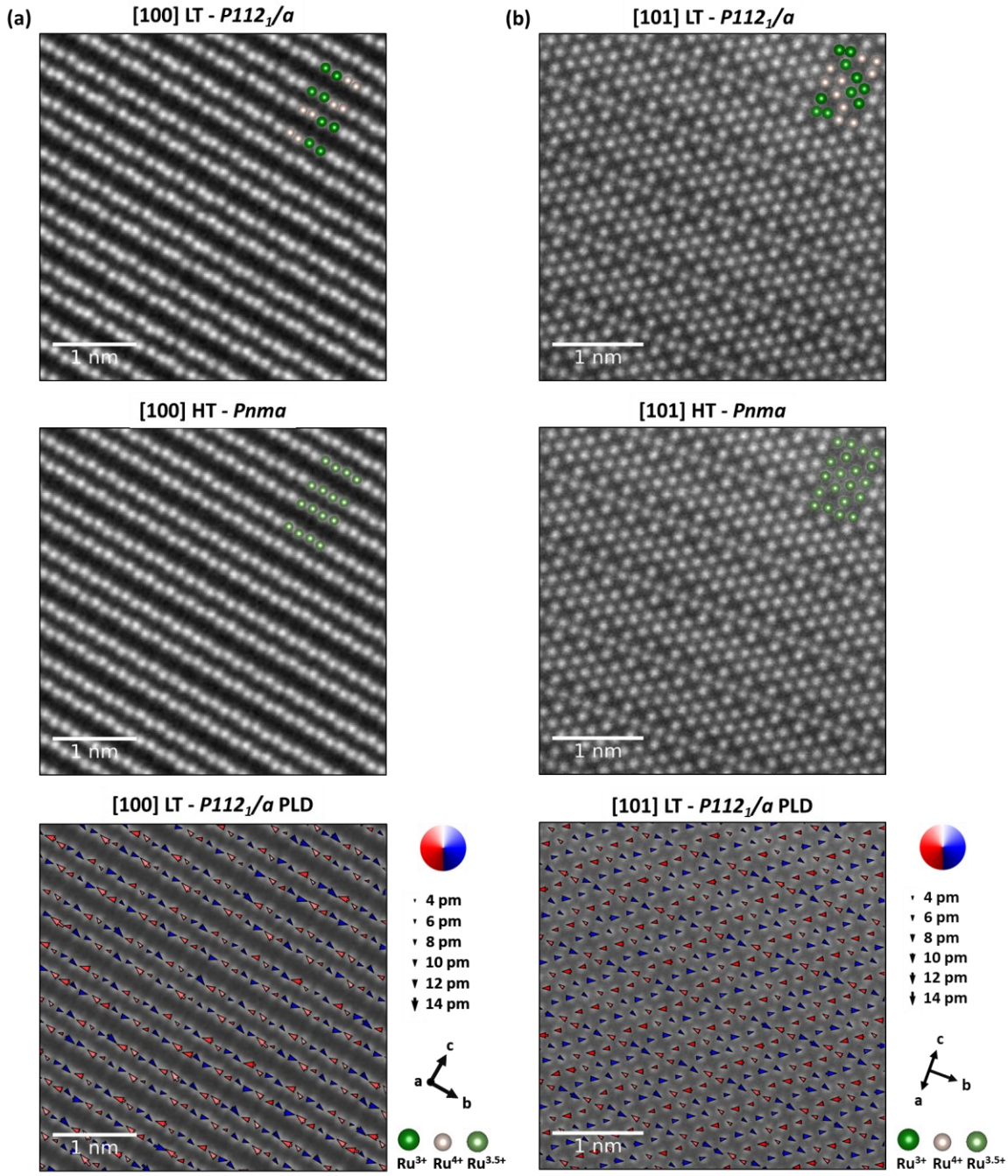

Figure 15. Visualization of picometer-scale periodic lattice displacements of Ru sites in $NaRu_2O_4$ oriented along the (a) [100] and (b) [101] zone axes. At the top, the HAADF images show the original LT-*P112₁/a* phase. In the middle are the synthetic HT-*Pnma* images derived from the original LT phase *via* Fourier processing. At the bottom, the arrows in the PLD maps indicate the ionic displacement, calculated as the difference in atomic positions between the (synthetic) HT and LT phases. The arrows indicate the displacement at each atomic lattice site, with their length representing the displacement amplitude and their color representing the polarization vector angle (the direction of the displacement). Adopted under the terms of a CC-BY license. © 2025 The authors[186].

Figure 16 further illustrates the HAADF images used in Figure 15, with an overlay of the fitted atomic column positions and the difference image between the HT and LT phases for both zone

axes. The enlarged insets in Figure 16 demonstrate the picometer precision achieved by the Gaussian peak fitting algorithm[223].

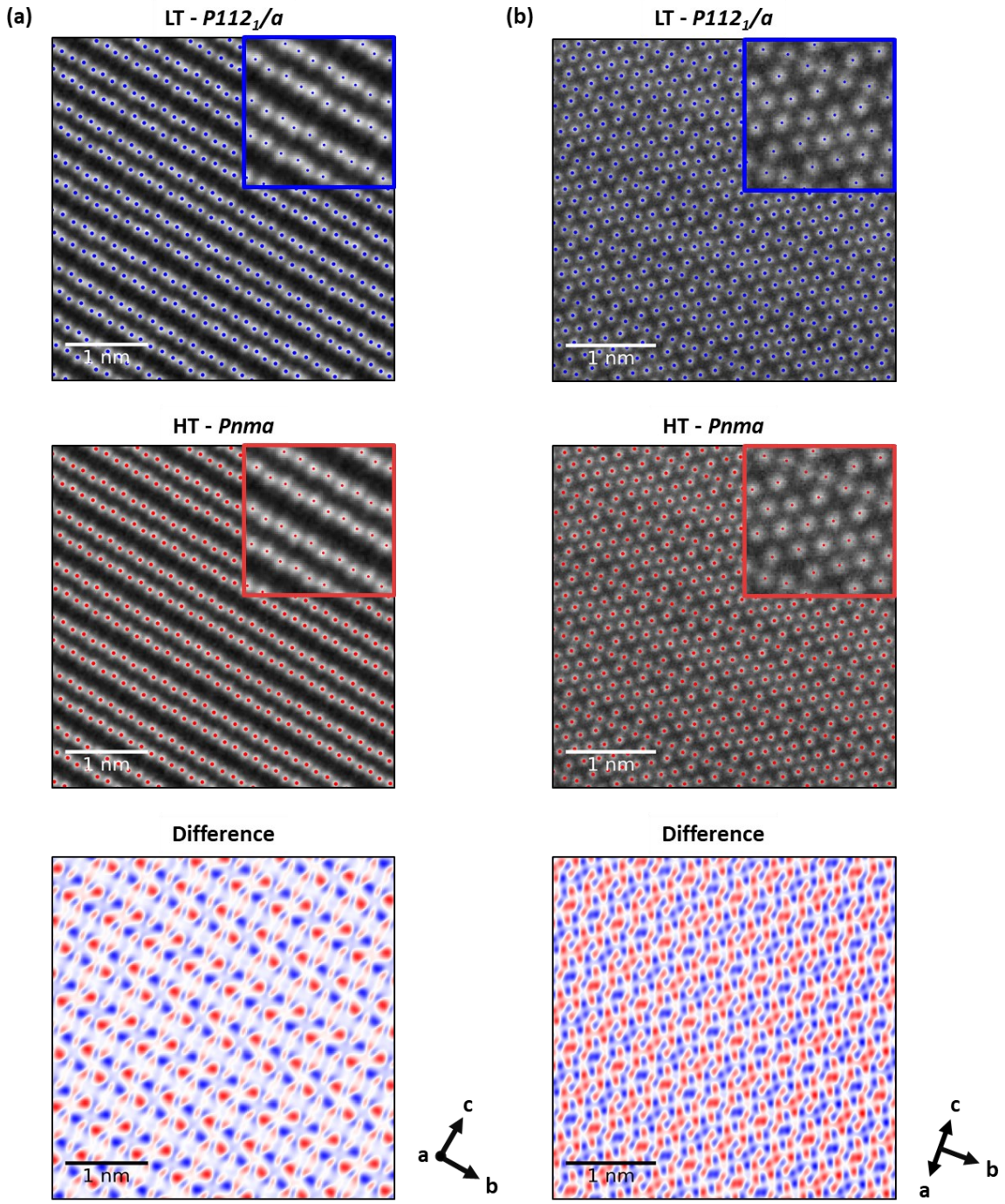

Figure 16. Gaussian peak fitting of Ru atomic columns along the (a) [100] and (b) [101] zone axis. The HAADF images at the top show the original LT-$P112_1/a$ phase from which the synthetic HT-*Pnma* images shown in the middle were derived by Fourier processing. The insets demonstrate the accurate peak positioning of the Atomap algorithm[49]. The difference images at the bottom were calculated from the synthetic HT and the original LT phases and thus represent relevant lattice modulations for the two zone axes. Adopted under the terms of a CC-BY license. © 2025 The authors[186].

To investigate the lattice displacement in the LT phase, it would have been valuable to explore the corresponding displacements of O and Na. Unfortunately, due to their low atomic weight, these elements are not visible in the HAADF images shown in Figure 15, necessitating the use of advanced STEM imaging techniques to visualize the light elements. An attempt to utilize 4D STEM for this purpose is shown in Figure 17, which presents STEM images along the [100] zone axis. The virtual (a) ABF and (b) low-angle annular dark-field (LAADF) images were generated from a 4D STEM dataset by masking the diffraction patterns with the ABF and LAADF detector geometries for each probe position. Despite the low contrast of the light elements in both the LAADF and ABF images, the object phase was reconstructed using the SSB method (Figure 17(c))[83,84,116]. This approach reveals the overlapping O and Na atomic columns adjacent to the Ru columns, consistent with the overlaid structural model. However, due to the overlap of the Na and O atomic columns along the projection direction, it remains impossible to track the individual columns using Gaussian peak fitting. As a result, the displacement of these lighter elements could not be further investigated. Nevertheless, the possibility that the displacement of Na and O ions—particularly during dimerization—could influence the observed HAADF contrast and potentially affect the intensity of the Ru columns should not be ruled out. Even though Na and O contribute minimally to the HAADF contrast, their displacement may lead to slight deviations from the true Ru-column positions when fitting the atomic columns in the low-temperature phase.

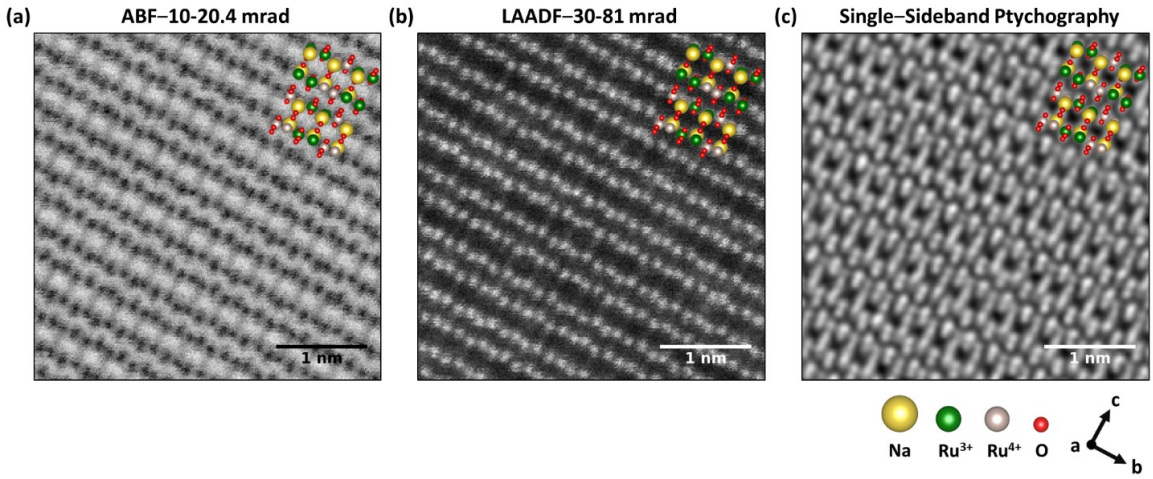

Figure 17. (a) Virtual ABF image, created by integrating the diffraction patterns from a 400x400 probe positions 4D STEM scan over an annular mask with inner- and outer radius of 10 and 20.4 mrad. (b) Virtual low-angle annular dark-field (LAADF) image, created by integrating the diffraction patterns over an annular mask with an inner- and outer radius of 30 and 81 mrad. (c) SSB ptychographic phase reconstruction showing high contrast for both light and heavy elements. Reprinted under the terms of a CC-BY license. © 2025 The authors[186].

The STEM study revealed strong periodic lattice displacements in the LT phase with significant ionic displacements within the pseudo-triangular tunnels of the $NaRu_2O_4$ single crystals. This displacement drives the dimerization of Ru^{3+} and Ru^{4+} (4*d* electrons) along the *b*-axis in the LT

phase ($P112_1/a$), while the HT phase (*Pnma*) exists above T_C = 535 K. The atomic-scale lattice reconstruction from SAED and STEM experiments provides direct evidence for the formation of bond order and an anomalous Peierls transition-induced CDW, despite the system remaining metallic. Notably, the material becomes even more metallic in the LT phase, though parts of the Fermi surface may be lost near the first-order phase transition (Figure 13(a)).

The symmetry breaking induced by dimerization results in a doubling of the unit cell along the *b*-axis, similar to conventional Peierls transitions. However, in contrast to traditional Peierls transitions, where electron condensation into CDWs typically occurs at temperatures far below room temperature, this transition is observed at higher temperatures.

2.4 Conclusions

This study presents direct atomic-resolution microscopic evidence of an anomalous Peierls transition that induces a unidirectional, commensurate charge density wave phase in $NaRu_2O_4$ single crystals at high temperatures (< 535 K). To investigate the structural dynamics and phase transition responses of $NaRu_2O_4$, both SAED and atomic-resolution STEM were employed. The results reveal two distinct phases, namely the LT-$P112_1/a$ and HT-*Pnma*, and provide insights into their structural characteristics, unraveling the formation of a twofold superstructure in the LT phase. *In-situ* heating experiments demonstrate the reversible nature of the first-order transition, where the material undergoes a transformation from orthorhombic to monoclinic symmetry, accompanied by dimerization in the Ru chains, resulting in a unit cell doubling along the *b*-direction. PLD maps further support these findings, illustrating atomic displacements associated with dimerization, thus confirming the existence of a bond order within the LT phase. The superstructure within the LT phase highlights the intricate interplay between charge and lattice degrees of freedom in $NaRu_2O_4$.

This work provides in-depth quantitative insights into the temperature-dependent structural and electronic behavior of the highly correlated metallic system $NaRu_2O_4$, revealing complex lattice and charge ordering phenomena at atomic resolution. This study underscores the powerful capabilities of transmission electron microscopy (TEM) in investigating atomic-scale transitions. Future studies focusing on the evolution of the electrical properties during this transition, such as additional Hall effect and magnetoresistance measurements, will provide a more comprehensive understanding of the material's electronic behavior and its structure-property relationships.

3 Unveiling the interfacial reconstruction mechanism enabling stable growth of the delafossite $PdCoO_2$ on Al_2O_3 and $LaAlO_3$

This chapter explores how fundamental physics research can facilitate the first steps in progressing from the discovery of a material system with unique properties to its integration into functional oxide devices. The study demonstrates how STEM can be employed to investigate interfacial phenomena that facilitate the stable growth of functional delafossites on a substrate. Delafossites, comprised of noble metal (A^+) and strongly correlated sublayers (BO_2^-), form intrinsic heterostructures with highly anisotropic properties. These properties (*e.g.*, $PtCoO_2$ boasts the highest conductivity per carrier of any known oxide material, while $PdCoO_2$ exhibits the longest electron mean free path among all metals[157-159,228]) hold significant potential for various applications in electronics and spintronics, but their exploitation hinges on the successful growth of high-quality thin films on suitable substrates.

Within this context, the unique lattice geometry of delafossites presents a significant challenge to thin-film fabrication, as different delafossite materials grow differently—even when deposited on the same substrate—ranging from successful epitaxy to complete growth suppression. These variations often lack a clear correlation with obvious factors like, for example, the lattice mismatch. In certain cases, unidentified stabilization mechanisms appear to enable growth, allowing these materials to form stable thin films or to serve as buffer layers for subsequent delafossite growth.

The STEM investigations, particularly electron ptychography combined with spectroscopy and conventional STEM imaging, reveal the presence of a secondary phase, forming at the substrate surface, which stabilizes $PdCoO_2$, grown *via* molecular beam epitaxy, on Al_2O_3 and $LaAlO_3$ substrates, a mechanism that differs significantly from the one observed for the Cu-based delafossites in the fourth chapter. The discovery of the secondary phase provides new insights into how $PdCoO_2$ thin films are stabilized at the interface, in a way that is clearly different from the usual strain-relief mechanisms seen in oxide heterostructures. Understanding the stabilization processes in delafossite thin films is an important step toward reliable growth for their application in electronic devices.

The following text and figures in this chapter were adopted from this publication[229]:

Scheid, A., Heil, T., Suyolcu, Y. E., Song, Q., Enderlein, N., Nono Tchiomo, A. P., Ngabonziza, P., Hansmann, P., Schlom, D. G. & van Aken, P. A. Unveiling the interfacial reconstruction mechanism enabling stable growth of the delafossite $PdCoO_2$ on Al_2O_3 and $LaAlO_3$. *ACS Applied Materials & Interfaces* 7, 14795–14802, April 2025, 10.1021/acsami.5c03536[229].

Contributions to this publication:

Anna Scheid and Y. Eren Suyolcu conceived the project. Anna Scheid wrote the initial manuscript and performed the STEM acquisition and STEM data analysis. Tobias Heil assisted with STEM data evaluation and discussion. Qi Song synthesized all delafossite thin films *via* MBE under the supervision of Darrell G. Schlom. Niklas Enderlein performed the density functional theory (DFT) calculations under the supervision of Philipp Hansmann. Tobias Heil and Peter A. van Aken supervised this project and provided valuable input on data analysis. All co-authors revised the manuscript.

As part of this project, contributions were made to the following publications:

- Investigation of surface reconstructions and electronic structure in delafossites, facilitated by the successful growth of these materials using $PdCoO_2$ buffer layers.

  Qi Song, Zhiren He, Brendan D. Faeth, Christopher T. Parzyck, **Anna Scheid**, Chad J. Mowers, Yufan Feng, Qing Xu, Sonia Hasko, Jisung Park, Matthew R. Barone, Y. Eren Suyolcu, Peter A. van Aken, Betül Pamuk, Craig J. Fennie, Phil D. C. King, Kyle M. Shen, and Darrell G. Schlom. Surface reconstructions and electronic structure of metallic delafossite thin films. *APL Materials* **12**, 081117 (2024). https://doi.org/10.1063/5.0217540[230].

- The growth of $PdCoO_2$ on Al_2O_3 *via* PLD for the study of magnetotransport properties in films patterned into Hall bar devices.

  Arnaud P. Nono Tchiomo, Anand Sharma, Sethulakshmi Sajeev, **Anna Scheid**, Peter A. van Aken, Takayuki Harada, and Prosper Ngabonziza. Magnetotransport properties in epitaxial films of metallic delafossite $PdCoO_2$: Effects of thickness and width variations in Hall bar devices. *Physical Review Materials* **9**, 055001 (2025). 10.1103/PhysRevMaterials.9.055001[231].

3.1 Introduction

Delafossites with a chemical composition of ABO_2, contain metallic ions in the formal oxidation state of A^+ and B^{3+}. The unique crystal structure of delafossites consists of alternating charged layers of A^+-ions sandwiched between planes of edge-sharing $[BO_2]^-$ octahedra, and the noble-metal A^+-ions are linearly coordinated to two oxygen-ions[232-234]. Delafossites exhibit distinct polymorph structures depending on the interlayer stacking. In the so-called *3R* polytype, the subsequent A^+-layers are stacked in the same direction, and the delafossite has trigonal symmetry with space group $R\bar{3}m$. For the *2H*-type structure, the two consecutive A^+ layers are stacked 180° rotated with respect to one another, and the structure is hexagonal with the space group $P6_3/mmc$[228,234].

Delafossite oxides display a variety of physical properties, depending on the *A*- and *B*-site cations. These include *p*-type or ambipolar semiconductivity (for *A* = Cu; *B* = Al, Cr, Fe, Ga, Y, In), photocatalytic activity ($AgGaO_2$), multiferroicity ($CuFeO_2$), and metallic conductivity ($PdCoO_2$, $PdCrO_2$, $PdRhO_2$, $PtCoO_2$, and $AgNiO_2$)[235-239]. The metallic delafossites $PdCoO_2$, $PdCrO_2$, $PdRhO_2$, and $PtCoO_2$, in which the *A*-site cations are responsible for metallic conductivity, crystallize in the *3R* polytype. In $AgNiO_2$, electrical conduction is associated with the *B*-site Ni with a complex valence state[155]. The metallic delafossites exhibit the highest observed in-plane conductivity among the oxides. For example, $PtCoO_2$ has the highest conductivity per carrier of any material and $PdCoO_2$ has the longest low-temperature mean free path of all known metals[157-159,228]. The room-temperature conductivity of $PdCoO_2$ is about four times higher than that of Pd metal itself and approaches that of pure elements, such as Cu, Ag, and Au[157,240].

The layered structure of insulating, strongly correlated transition-metal oxide layers and conductive triangularly coordinated Pd or Pt layers makes metallic delafossites intrinsic heterostructures with highly anisotropic properties and quasi-2D electrical conduction. The resistivity within the *ab*-plane of metallic delafossites is generally orders of magnitude lower than along the *c*-axis[228]. This remarkable conductivity is probably carried almost exclusively by the Pd/Pt 4*d*/5*d* orbitals[228,240]. The highly dispersive band corresponding to these states crosses the Fermi level and gives rise to a cylindrical Fermi surface, reflecting the quasi-2D electrons in the Pd/Pt layers[240].

In addition, delafossites are chemically stable up to temperatures of 800-925 °C, allowing for applications in the high-temperature regime[232].

Given the limited size of delafossite single crystals (typically a few millimeters) and the growing interest in their use for electronic and spintronic applications, as well as their potential in oxide heterostructures, researchers have produced metallic delafossite thin films using methods such as reactive sputtering, PLD, and MBE[155,156]. Unfortunately, to date, the electrical conductivity of these

thin films has not matched that of single crystals. Although delafossite thin films exhibit similar conductivity to their single crystal counterparts at room temperature, the low-temperature resistivity differs by orders of magnitude[159,241].

One of the most critical challenges in thin-film growth is the selection of an appropriate substrate. In general, the lattice mismatch between the delafossite film and the substrate can lead to strain-induced degradation of properties and defects that diminish film quality. Since delafossites possess trigonal crystal structures, they are commonly grown on the planes of substrates with threefold or sixfold symmetry, such as (001)-oriented sapphire (*c*-Al_2O_3) or (111) planes of cubic crystals[155,156]. Despite the relatively large lattice mismatch between metallic delafossites and substrates, for example, a mismatch of ~6% for $PdCrO_2$ on *c*-Al_2O_3, high-quality *c*-axis-oriented thin films can be grown[241-244]. It has been observed that some delafossites grow particularly well or poorly, regardless of the lattice mismatch between the substrate and the film[245]. Interestingly, some films with a greater mismatch seem to grow better than those with a smaller mismatch. Therefore, it seems that for certain delafossites, there exists an unknown mechanism that relieves the lattice mismatch strain at the interface, which the traditional concepts of coherent and semi-coherent interfaces cannot fully explain. A detailed understanding of the interfacial structure between the substrate and the epitaxial films is essential, with STEM techniques providing key insights into the atomic-scale configuration.

In this work, electron ptychography, EELS, and conventional STEM imaging reveal an atomic-scale reconstruction at the interface of $PdCoO_2$ grown on Al_2O_3(001) and $LaAlO_3(111)_{pc}$, where the subscript denotes pseudocubic indices, that facilitates epitaxial growth. This investigation reveals an unconventional growth mechanism driven by a complex interplay between Al and Co at the interface. These findings have significant implications for improving the stable growth of delafossite thin films.

3.2 Materials and methods

3.2.1 Sample preparation

Thin films of $PdCoO_2$ were synthesized on (001)-oriented sapphire (*c*-Al_2O_3), $(111)_{pc}$-oriented $LaAlO_3$, and (111)-oriented $SrTiO_3$ substrates using reactive oxide molecular beam epitaxy in a Veeco GEN10 MBE system. The substrates were heated to temperatures ranging from 500 °C to 580 °C, as measured by a thermocouple positioned close to, but not in direct contact with, the substrate heater. During deposition, a gas mixture consisting of approximately 80% ozone and 20% oxygen was introduced, with a background pressure ranging from 5×10^{-6} to 8.5×10^{-6} Torr. Shutter-controlled layer-by-layer thin-film growth of $PdCoO_2$ on Al_2O_3 was achieved by actuating the shutters of the MBE to supply monolayer doses of Pd and Co, following the sequence of atomic

layers along the *c*-axis of the $PdCoO_2$ crystal structure. $PdCoO_2$ films grown on $LaAlO_3$ and $SrTiO_3$ substrates were co-deposited by simultaneously exposing the substrate to Co, Pd, and ozone molecular beams under conditions where the excess Pd supplied desorbs as PdO (g). Once finished, the films were immediately cooled to 300 °C in the same ozone background pressure in which they were grown. Further details and growth parameter optimization are provided in a previous study[243].

Epitaxial films of $PdCoO_2$ were also deposited by PLD. These $PdCoO_2$ films were deposited on the (001)-oriented Al_2O_3 at a substrate temperature of 700 °C under an oxygen pressure of 0.1–0.15 Torr in the PLD chamber. To achieve a stoichiometric composition in the $PdCoO_2$ films, the PLD growth method of alternately ablating the $PdCoO_2$ and mixed-phase PdO_X targets was employed[246].

The thin-film structure was characterized after growth using a PANalytical Empyrean X-ray diffractometer with Cu $K\alpha_1$ radiation.

3.2.2 STEM specimen preparation

Electron-transparent specimens were prepared by diamond cutting and tripod wedge polishing. Afterward, a precision ion polishing system (PIPS II, Model 695) equipped with a liquid nitrogen cooling stage utilizing argon ions was employed for final thinning.

3.2.3 STEM investigations

STEM investigations were conducted using a JEOL ARM200F, which is equipped with a cold field emission gun and a probe C_S corrector (DCOR, CEOS GmbH). The measurements were conducted at ambient temperatures with an acceleration voltage of 200 kV. To enhance the signal-to-noise ratio, mitigate scan artifacts, and minimize sample drift effects, STEM images were generated from multi-frame acquisitions, using high scanning speeds (2-3 µs/pixel) and applying post-acquisition cross-correlation.

For spectroscopic measurements, EELS data were acquired with a Gatan GIF Quantum ERS imaging filter, using a 5 mm entrance aperture and a camera length of 1.5 cm, yielding a semi-collection angle of 111 mrad. Principal component analysis (PCA) was employed to enhance the signal-to-noise ratio, utilizing 15 principal components for accurate elemental mapping[247].

For comprehensive 4D STEM data acquisition, a MerlinEM Medipix3 detector by Quantum Detectors was utilized, with the microscope camera length set to 80 cm and the probe semi-convergence angle set to 20.4 mrad. The detector was operated in 1-bit mode, enabling optimal detection of one electron per pixel in a single frame with a rapid pixel dwell time of 50 µs, corresponding to a frame rate of 20000 fps. Ptychographic reconstructions in this chapter were

performed using ptychoSTEM, an open-source MATLAB script repository available on GitLab[83,84,116].

The sample thickness was estimated by comparing simulated position-averaged convergent beam electron diffraction (PACBED) patterns with experimental PACBEDs extracted from the 4D STEM datasets, which were acquired in the same sample region as the EELS measurements. For the simulations, the *ab*TEM package was used. The semi-convergence angle and probe parameters were chosen in accordance with the experimental data. A total of 10 frozen phonon configurations were used for each simulation and a PACBED thickness series was calculated using multi-slice simulations[248].

3.2.4 Density functional theory calculations

Density functional theory (DFT) calculations were conducted using the Quantum ESPRESSO suite[249-251]. The calculations used optimized norm-conserving pseudopotentials with an energy cutoff of 120 Ry, and the exchange-correlation interaction was approximated by the Perdew-Burke-Ernzerhof functional (PBE)[252,253]. Brillouin zone integration was performed on a 6×3×1 electron momentum grid, ensuring an equal sampling density for the rectangular supercell with the in-plane lattice constants a=4.7606 Å and b=8.2456 Å. The out-of-plane lattice constant c was larger than 30 Å for all considered simulation cells, such that a single k-point along the k_z direction was sufficient. A Gaussian smearing of 0.02 Ry was applied, and the derived total energies were converged within the accuracy of 0.03 eV based on the chosen numerical parameters.

During the geometry optimizations, the mentioned in-plane lattice constants (which correspond to the experimental lattice spacing of Al_2O_3) were kept fixed, while the out-of-plane lattice constant (corresponding to the stacking direction) and the atomic positions were fully optimized. Different thicknesses of the Al_2O_3 compound in the simulation cells were tested, specifically 4, 6, and 8 Al layers. Upon optimizing these respective simulation cells with different thicknesses of Al_2O_3, the variation in the calculated interface energy was found to be less than 0.01 eV. This result indicates that a minimum of 6 Al layers in the pure, *i.e.*, unsubstituted Al_2O_3 are sufficient to achieve robust and reliable results.

3.3 Results and discussion

3.3.1 Structural characterization of the $PdCoO_2$ thin films

The $PdCoO_2$ thin films grown on Al_2O_3 and $LaAlO_3$ substrates exhibit high structural quality, as evidenced by the X-ray diffraction (XRD) patterns, the reflection high-energy electron diffraction (RHEED) spots, as well as the low-magnification HAADF STEM images shown in Figure 18.

Besides the substrate reflections, only the *00l* reflections corresponding to the bulk crystal structure of $PdCoO_2$ were detected, confirming that the films are *c*-axis-oriented, epitaxial, and phase-pure. In particular, the presence of Laue oscillations around the XRD reflections of the $PdCoO_2$ films grown on Al_2O_3 indicates that these films have well-defined thicknesses, smooth surfaces, and a straight film-substrate interface.

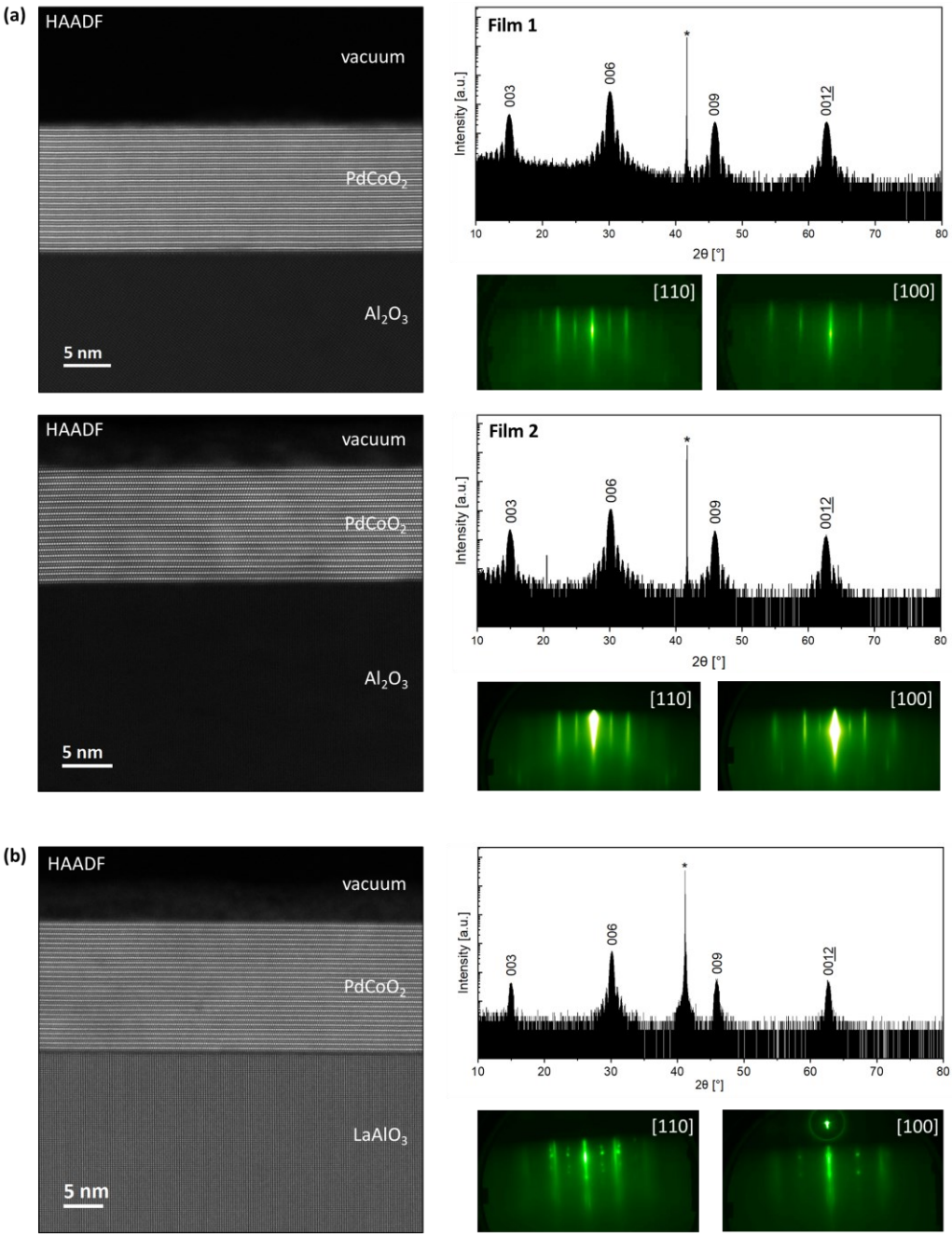

Figure 18. (a) STEM HAADF images, X-ray diffraction, and *in-situ* RHEED patterns, of two $PdCoO_2$ thin films grown on an Al_2O_3 substrate. The Laue oscillations observed for the $PdCoO_2$ peaks indicate an abrupt and smooth film-substrate interface, which is also visible in the STEM images. (b) STEM HAADF, X-ray diffraction, and *in-situ* RHEED patterns of a $PdCoO_2$ thin film grown on $LaAlO_3$. Asterisks (∗) denote substrate reflections. Adopted under the terms of a CC-BY license. © 2025 The authors[229].

Figure 19 shows HAADF STEM images of the $PdCoO_2$ thin films along the [210] and [010] orientations on both substrates. Delafossites grow with a 30° rotation relative to the Al_2O_3 substrate orientation due to the lattice geometry, and therefore, the orientation noted in the STEM images consistently indicates the film, but not the substrate. In HAADF images, the contrast is proportional to the atomic number. Thus, the Al and O atoms are either not or only very weakly visible, whereas the heavy La and Pd atomic columns appear the brightest, followed by the slightly lighter Co species. Along the [210] orientation, the oxygen octahedra lie in projection, and discrete octahedral orientations cannot be distinguished.

The STEM cross-section images along the [010] orientation of the films reveal domains with different orientations of the CoO_6 octahedra in subsequent layers of the films on both substrates, indicated by ticks in the insets. The stacking faults and twins observed in the thin films occur because both configurations appear energetically equally favorable during growth[254]. These defects are likely the main reason for the lower residual resistivity ratio of thin films compared to bulk crystals[156]. The in-plane rotational twins are present in all epitaxial delafossite thin films, grown on non-delafossite *c*-axis oriented substrates, studied to date and are visible in the XRD measurements of the films (Figure 18)[242,254,255]. In addition to the twins, which can be avoided using high-miscut substrates, individual defects are occasionally observed, such as steps on substrate terraces or point defects[254]. However, the films do not contain any impurity phases, such as PdO_X or Co_3O_4, which often occur under improper growth conditions[241,256].

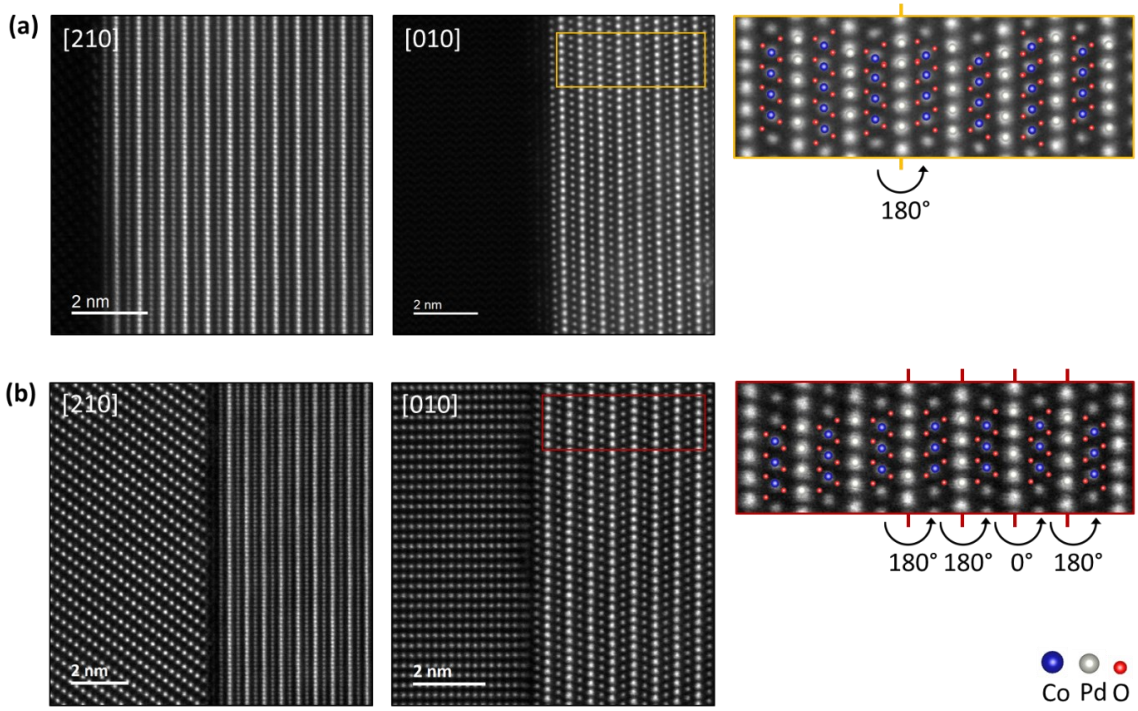

Figure 19. HAADF STEM images of $PdCoO_2$ thin films (right) on (a) Al_2O_3 and (b) $LaAlO_3$ for two structural orientations of the films. For stable growth, the growth is always initiated with a $[CoO]^-$-layer. The insets in the [010] images reveal domains with opposing orientations of the CoO_6 octahedra in subsequent $[CoO]^-$-layers, and highlight stacking faults (0° swap) and twin domains (180° swap) in the films. Adopted under the terms of a CC-BY license. © 2025 The authors[229].

3.3.2 Structural characterization of the $PdCoO_2/Al_2O_3$ and $PdCoO_2/LaAlO_3$ interfaces

For a more detailed analysis of the atomic structure at the interface, HAADF imaging, which primarily detects electrons scattered at high angles, does not provide sufficient contrast for visualizing light elements. Therefore, imaging techniques optimized for visualizing O and Al are required. One of the most effective methods for visualizing light elements is ABF imaging[56]. Here, the annular detector captures electrons only from the outer region of the BF disk, where the contribution of beam interactions with light elements is reduced due to channeling effects. This results in low image intensities at the atomic column locations[257].

Figure 20 shows simultaneously acquired STEM HAADF and ABF images of the thin-film interface along two zone axes for $PdCoO_2$ films grown on Al_2O_3 (Figure 20(a) and (b)) and $LaAlO_3$ (Figure 20(c) and (d)). While the HAADF imaging only provides strong contrast for the heavier atomic species, in the simultaneously captured ABF images, the light elements are clearly revealed. Figure 20(b) and (d) distinctly show the orientation of the CoO_6 octahedra, which is mirrored in the fourth (Figure 20(b)) and fifth (Figure 20(d)) layers due to their equivalent growth probability.

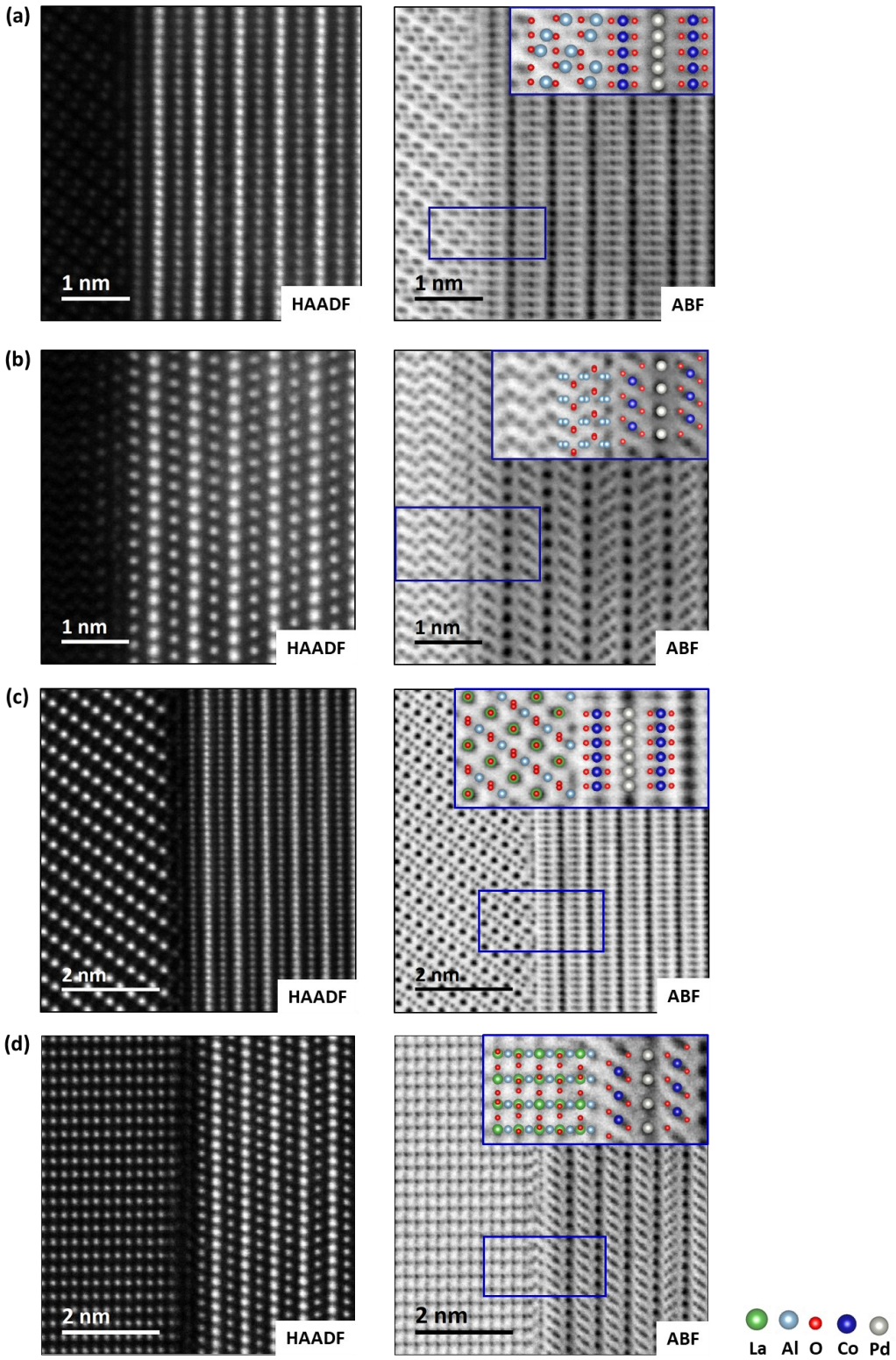

Figure 20. Simultaneously acquired HAADF STEM and ABF STEM images of the $Al_2O_3/PdCoO_2$ interface for the (a) [210] and (b) [010] zone axes and the $LaAlO_3/PdCoO_2$ interface for the (c) [210] and (d) [010] zone axes. While the HAADF STEM images show strong contrast primarily for the heavy elements Pd, Co, and La, the ABF images clearly reveal the O and Al atoms. The insets in the ABF images show an overlay with the structural models of the substrates and thin films with unmatched atomic contrast at the interface within the substrates. Adopted under the terms of a CC-BY license. © 2025 The authors[229].

The STEM images further demonstrate that, in all cases, the film growth is initiated with a $[CoO]^-$ layer. The MBE synthesis has shown that, if one attempts to initiate growth with a Pd^+ layer, the films do not grow stably and tend to decompose completely[241]. This observation underscores the critical role of initiating growth with Co under an ozone background pressure to stabilize the delafossites on the substrate.

To assess the stability of different interface configurations, DFT calculations were performed using the Quantum ESPRESSO suite for the $PdCoO_2/Al_2O_3$ interfaces[249-251]. The interface can be understood best through a shared structural feature in the oxygen network. Both structures coincide at the interface *via* oxygen triangles (yellow triangles in Figure 21(a)), which serve as covalent bonding bridges between the two materials. For the DFT interface simulations, rectangular in-plane supercells of both materials were constructed, ensuring that each contained the same number of oxygen triangles. The unit cell vectors $(\vec{a}_S, \vec{b}_S)$ were defined as linear combinations of the primitive cell vectors $(\vec{a}_P, \vec{b}_P)$. For $PdCoO_2$, the chosen supercell was spanned by $\vec{a}_S = 2\vec{a}_P + \vec{b}_P$ & $\vec{b}_S = 3\vec{b}_P$, and for Al_2O_3, by $\vec{a}_S = \vec{a}_P$ & $\vec{b}_S = \vec{a}_P + 2\vec{b}_P$, respectively. As highlighted in Figure 21(a), the rectangular cells contain two oxygen triangles along the short, and three oxygen triangles along the long side of the rectangle, respectively. Given that Al_2O_3 forms the substrate of the actual samples, the in-plane lattice parameters of the rectangular simulation cells were fixed to the experimentally determined lattice constant of Al_2O_3. Consequently, the lattice spacing of $PdCoO_2$, which is 2.98% larger than that of Al_2O_3, was slightly compressed relative to its bulk value. Since DFT calculations require periodic boundary conditions, the constructed unit cells effectively form a stacked, alternating structure with two identical interfaces per unit cell, as shown at the bottom of Figure 21(b). A structural optimization step was performed, in which the lattice constant along the interface normal vector and the atomic positions of all atoms in the unit cell were fully relaxed.

To estimate the stability of different interface configurations, the total energy of the (optimized) interface was compared to that of its two constituents (see Figure 21(b) - note that the factor two (2Δ) in the equation indicates that there are two identical interfaces in the simulation cell)[258,259]. The latter was determined through two separate self-consistent field (SCF) calculations from the deconstructed unit cell, without any additional geometry optimization. As the oxygen layer at the interface is shared by both components (Al_2O_3 and $PdCoO_2$), two different approaches were considered when defining the isolated constituents from the full simulation cell for the calculation of the interface energy (according to the scheme in Figure 21(b)): either ascribing the oxygen layer to belong to Al_2O_3 or to $PdCoO_2$. The resulting interface energies were computed by both means, and the energetic differences between the various interfaces are represented in the form of matrices in Figure 21(c). The table on the left corresponds to the oxygen layer being assigned to Al_2O_3, while the table on the right represents the case where it is assigned to $PdCoO_2$.

When the O-layer is ascribed to Al_2O_3, *i.e.*, when the interface energy is defined as the binding energy between the shared O-layer and the Co- or Pd-layer, respectively, it is found that the Co-interface is significantly more stable (by 4.0 eV per unit cell area of ~40 Å^2). This is consistent with the bonding characteristics of Co and Pd. Specifically, Pd forms covalent bonds with only two oxygen atoms, with a bond angle of 180°, whereas Co bonds with six oxygen atoms to form an octahedron (see Figure 21(b)). As a result, the Co-interface contains three times as many Co-O bonds as the Pd-interface has Pd-O bonds, leading to a higher binding energy. In contrast, in the Pd-interface, each oxygen atom in the shared O-layer is bonded to only one Pd atom, while in the Co-interface, each oxygen atom is bonded to three Co atoms. Thus, the shared O-layer in the Pd-interface exhibits a higher demand for electrons from the Al-layer, as the Pd-interface donates less electron density to the shared O-layer compared to the Co-interface. Consequently, the shared O-layer in the Pd-interface is more strongly bonded to the first Al-layer of Al_2O_3 than in the Co-interface. This is confirmed by the binding energies calculated from ascribing the shared O-layer to the delafossite. This can be seen as the direct consequence of the Co-interface exhibiting greater stability than the Pd-interface in terms of their bonding strength to the shared O-layer.

As is frequently observed in oxide heterostructures, chemical intermixing at the interface could contribute to the stabilization of the films on the substrate[260-262]. Alternatively, vacancies or interstitial sites within the substrate may be occupied during growth, further stabilizing the films[263,264]. Therefore, moving on from the Co-interface, the energetic feasibility of substituting Co-atoms into the first Al layer (adjacent to the interface) of Al_2O_3 was examined. Different cases of 50% Co-substitution (affecting two of the four Al-atoms per Al-layer) and the 100% case were tested. The calculated binding energies, listed in the tables in Figure 21(c), display a clear trend: the 0% substitution (*i.e.*, 100% Al) is the most stable, the 100% Co-substitution (*i.e.*, 100% Co) is the least stable, and the three tested cases of 50% Co-substitution fall in between these extremes. Although Co substitution is not inherently energetically favorable, it is also not exceptionally unfavorable for the 50% substitution cases, suggesting that a smaller percentage of Co-substitution could statistically occur in experiment. This is particularly plausible because the substrate surface does not achieve a perfectly Al-terminated surface, despite pretreatment, and surface roughness likely results in numerous Al-vacancies[265].

Furthermore, a detailed examination of the insets in the ABF images in Figure 20 reveals atomic columns at the interface that do not align with the structural model of the substrate and the film along both orientations for the two different substrates. The unmatched atomic columns are located within the top layers of the substrates, while the films themselves align perfectly with the initial CoO_6 octahedral layers. No structural defects, such as misfit dislocations, are observed within the first layer of the films.

To follow up on this observation of unmatched atomic columns within the substrate, interfaces where Co was incorporated into the stoichiometrically induced Al vacancies in Al_2O_3 were explored *via* DFT, as the unmatched atomic columns in the insets of Figure 20(a) seem to imply. Under the condition that the lattice spacing of the Al_2O_3 substrate was constrained during all geometry optimizations, the additional Co within the Al_2O_3 led to a seemingly unphysical enhancement of the bonding distance between the Co-interface and the oxygen connected to the Co-inserted Al-layer of the Al_2O_3. Hence, this bond enhancement along the *c*-direction happens in response to the in-plane compression introduced by the additional Co in the Al_2O_3, indicating that the insertion of Co is not energetically favorable without reconstructions.

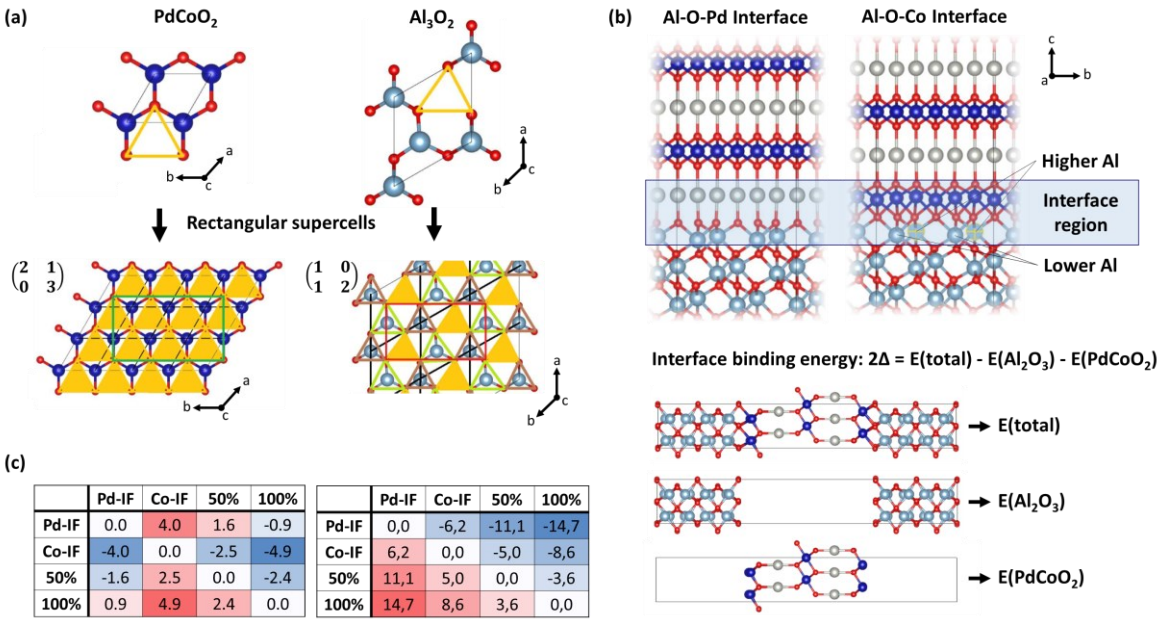

	Pd-IF	Co-IF	50%	100%
Pd-IF	0.0	4.0	1.6	-0.9
Co-IF	-4.0	0.0	-2.5	-4.9
50%	-1.6	2.5	0.0	-2.4
100%	0.9	4.9	2.4	0.0

	Pd-IF	Co-IF	50%	100%
Pd-IF	0,0	-6,2	-11,1	-14,7
Co-IF	6,2	0,0	-5,0	-8,6
50%	11,1	5,0	0,0	-3,6
100%	14,7	8,6	3,6	0,0

Figure 21. (a) Oxygen layers exhibiting a triangular (highlighted) in-plane arrangement, a shared structural feature between $PdCoO_2$ and Al_2O_3. The top panel displays the primitive hexagonal unit cells of the two interfaced compounds, while the bottom panel shows the specific rectangular supercells utilized for the interface simulations. (b) Top panel: Side views of the Pd- and Co-interface simulation geometries. The interface region separating the two compounds is highlighted with transparent blue. Co-substituted Al-sites are highlighted as 'Higher Al' and 'Lower Al' depending on their *c*-axis position. The interface binding energy is calculated as the difference between the total energy of the (optimized) interface and that of its two constituents. (c) Differences in calculated interface energies (per unit cell area of ~40 $Å^2$) between the (in order) Pd-, Co-, 50% Co-substituted, and 100% Co-substituted interfaces. For 50% Co-substitution, various substitution patterns were tested and averaged in the table for simplicity, as all were energetically positioned between the extreme cases of 0% and 100%. The differences are represented as an antisymmetric matrix, where a negative matrix element (i, j) indicates that the i-interface (row index) is more stable than the j-interface (column index). Matrix elements are color-coded: negative values are shown in blue, positive values in red, with a smooth interpolation between the extreme values. Zero values (on the diagonal) are represented in white. The table on the left corresponds to the calculation of interface energies with the shared oxygen layer attributed to the Al_2O_3, and the table on the right to the delafossite ($PdCoO_2$) constituent of the simulation cell, respectively. Adopted under the terms of a CC-BY license. © 2025 The authors[229].

Therefore, the unmatched atomic columns observed in the ABF images in Figure 20 suggest a complete atomic reconstruction at the interface between the substrates and the films. Although an increased contrast in the HAADF images has been noted in previous studies of $PdCoO_2$ thin films on Al_2O_3, the appearance of such an interfacial phase within the substrate surface has not been observed for $PdCoO_2$ thin films before and may be critical for enabling the stable epitaxial growth of the films[242,245].

3.3.3 Chemical analysis of the $PdCoO_2/Al_2O_3$ and $PdCoO_2/LaAlO_3$ interfaces

To characterize the chemical nature of the phase associated with the unmatched atomic columns, EELS was performed across the interfaces. Previous studies have demonstrated that reliable interpretations of interface structures can be achieved only under very thin specimen conditions[266,267]. Specifically, for samples thinner than approximately 20 nm, misinterpretations due to thickness effects, and complex propagation phenomena, such as beam broadening, cross-talk, and de-channeling, can be avoided. Therefore, a thin sample area of the specimen was selected to facilitate atomic-scale quantification of the interface structure. The thickness was estimated as 8.3 nm for the $PdCoO_2/Al_2O_3$ interface and 11.4 nm for the $PdCoO_2/LaAlO_3$ interface, based on multi-slice simulations of position-averaged convergent beam electron diffraction (PACBED) patterns using the *ab*TEM algorithm and a comparison to measured PACBEDs from a 4D STEM scan in the same sample area, shown in Figure 22[248].

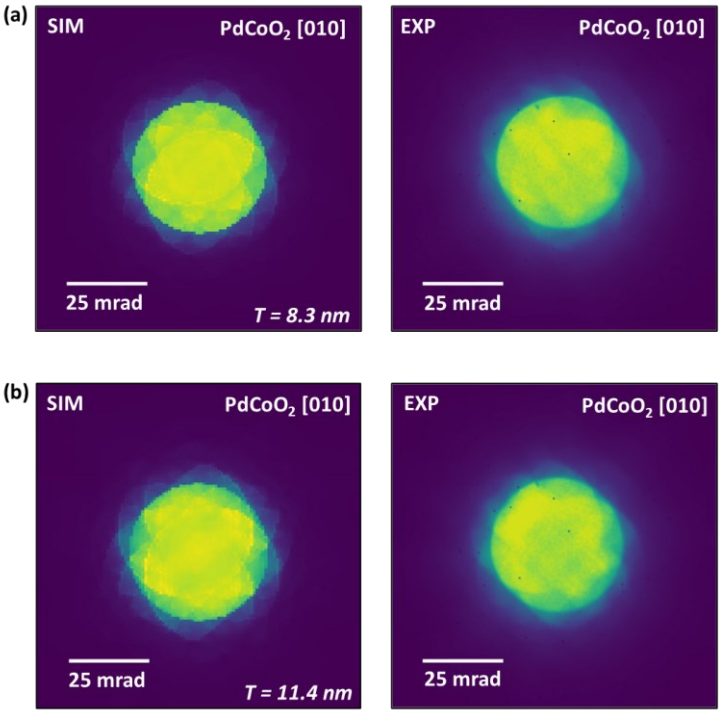

Figure 22. Simulated (SIM) and experimental (EXP) PACBEDs for the [010] orientations of $PdCoO_2$ from 4D STEM scans across the (a) $PdCoO_2/Al_2O_3$ and (b) $PdCoO_2/LaAlO_3$ interface. Adopted under the terms of a CC-BY license. © 2025 The authors[229].

The isolation of the signals from characteristic energy-loss edges enables a detailed analysis of the elemental distribution at the interface. Figure 23(a) and (c) show the extracted signals from the characteristic energy-loss edges of O (O K edge), Al (Al K edge), Co (Co $L_{3,2}$ edge), La (La $M_{5,4}$ edge), and Pd (Pd $M_{5,4}$). The white arrows indicate the physical boundary between each substrate and thin film. The EELS elemental maps confirm that the films initiate with a layer of $[CoO]^-$, followed by the first layer of Pd^+ ions. While the Pd signal is well-defined, some Co signal remains detectable within the surface layers of the substrates.

In the Co $L_{3,2}$ edge elemental maps in Figure 23(a) and (c), the line spectra extracted in Figure 23(b) and (d) for the Co $L_{3,2}$ edge and the corresponding O K edge are indicated by numbered arrows. The graphs show that a cobalt signal extends up to the second layer of the substrates. Notably, a distinct shift of the edge towards lower energies, along with a change in the L_3/L_2 edge ratio, occurs at the interface between the substrate and the film, between line signals 4 and 3. This shift, coupled with the alteration in the edge ratio, indicates a reduction in the Co valence compared to the Co^{3+} state in the films. Beyond the first $[CoO]^-$ layer, the shape and energy loss of the edges remain constant. The O K line signal 1 shows the typical shape of an O K edge in Al_2O_3 and $LaAlO_3$, respectively, while the O K edges extracted from signals 7 and 6 within the films exhibit the characteristic signature of the octahedrally coordinated oxygens in $PdCoO_2$.

Previous studies on interface reconstructions in delafossites with different *A* and *B* ions ($CuCrO_2/Al_2O_3$) identified a stabilizing reconstruction at the interface, forming a monolayer-thick $CuCr_{1-x}Al_xO_2$ alloy. In fact, a strong reduction in the Cr $L_{3,2}$ edge signal was observed, without a chemical shift or change in the edge ratio across the interface. This suggests that the interface reconstruction in $PdCoO_2$ is of a fundamentally different nature[245]. The EELS data implies that, in addition to chemical intermixing at the interface, the secondary phase at the interface contains cobalt in a lower oxidation state compared to the bulk film.

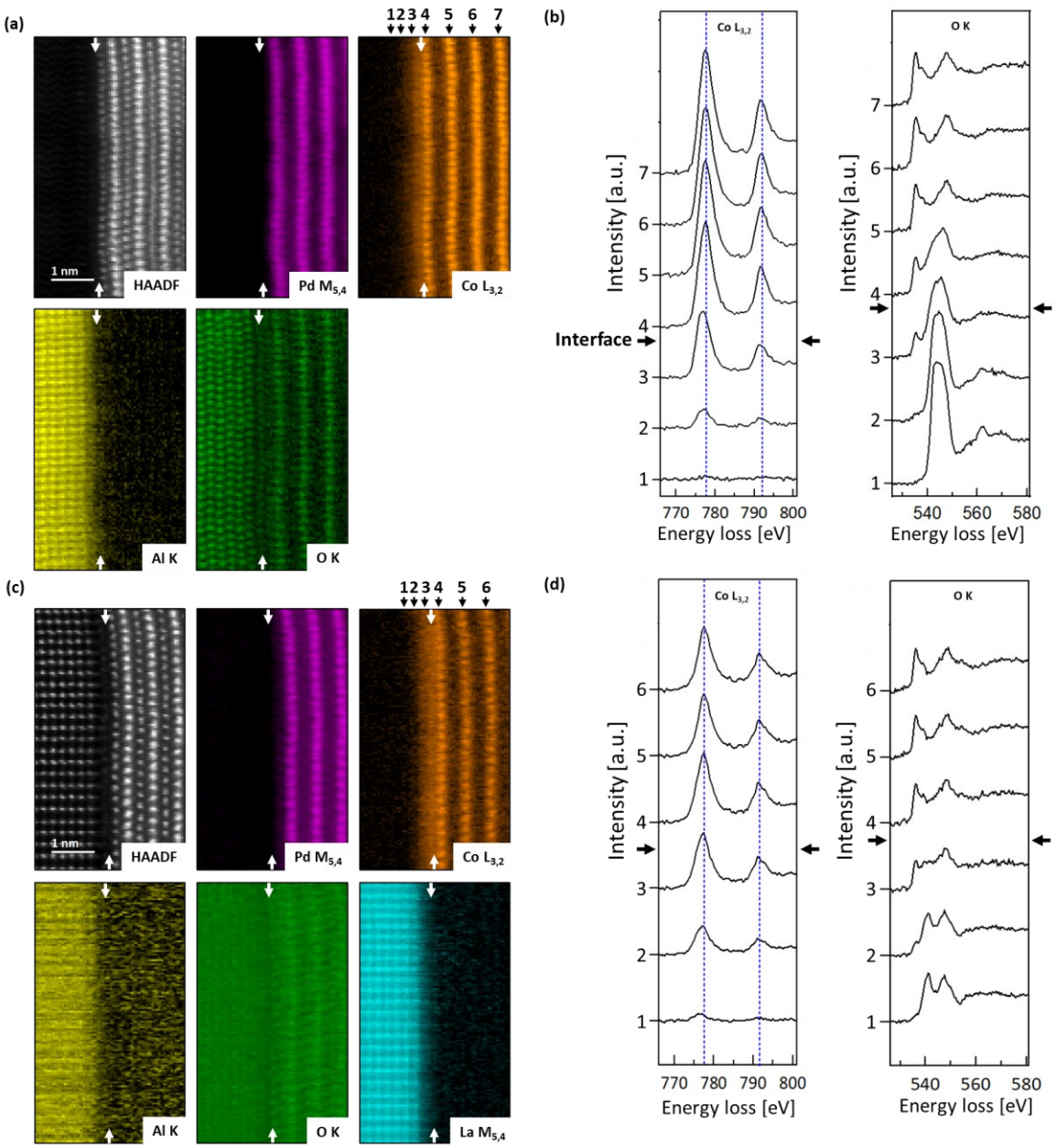

Figure 23. EELS elemental mapping of the (a) $PdCoO_2/Al_2O_3$ and (c) $PdCoO_2/LaAlO_3$ interface, obtained by extracting the indicated edge signals from a 2D spectrum image along the [010] zone axis. The films are initiated with a layer of $[CoO]^-$ and the elemental maps indicate chemical intermixing at the interface between the substrate and the film, while the sharp Pd signal shows that the Pd layer is not involved in the interfacial reconstruction. The O K edge elemental maps include a minor Pd signal due to overlapping of the respective edges in the EELS spectrum. The white arrows indicate the physical interface between substrate and film. (b) and (d) show the Co $L_{3,2}$ and O K edge signals, extracted along the numbered arrows indicated in (a) and (c). A strong Co signal is detectable up to two layers deep in both substrates, and a shift of the edge towards lower energy loss is observed, in combination with a change in the L_3/L_2 edge ratio. The O K edge shows features of the bulk materials far away from the interface and a mixed signal at the interface. Adopted under the terms of a CC-BY license. © 2025 The authors[229].

3.3.4 Electron ptychography of the $PdCoO_2/Al_2O_3$ and $PdCoO_2/LaAlO_3$ interfaces

For a comprehensive, large-scale structural analysis of the interfacial phase, advanced imaging techniques that offer strong contrast for light elements (O and Al) across extensive fields of view, are essential. In STEM, phase-related imaging methods are commonly used to achieve high contrast for both light and heavy elements simultaneously. Compared to conventional HRTEM phase contrast imaging, direct focused probe scanning techniques with post acquisition SSB and WDD reconstructions provide a simpler contrast transfer function (CTF). These methods do not require aberrations to generate contrast and can avoid zero crossings, thereby simplifying the imaging process and interpretation significantly.

By scanning the convergent electron beam across the sample, 4D STEM datasets were acquired by collecting a 256×256 pixel binary diffraction pattern for each probe position during the 2D scan. The binary mode of the MerlinEM Medipix3 camera enabled rapid acquisition at 20000 frames per second. The presence of the sample, particularly a very thin one (WPOA), induces a significant phase shift in the incoming electron wave, even for light elements, thereby facilitating effective imaging of the interfacial reconstruction involving Al and O[85]. Since a direct measurement of the exit-wave phase is not possible, and only intensities can be recorded, reconstruction techniques are required to back-calculate the phase from diffraction patterns obtained during the 2D raster scan. Each diffraction pattern provides critical information about both the amplitude and phase of the transmitted electron wave. To solve the phase problem for in-focus 4D STEM diffraction patterns, SSB ptychography is employed. The interference patterns between the central and diffracted beams carry the relative phase information of transmitted and scattered electrons, which is crucial for reconstructing the sample's transmission function. By extracting the interference regions (referred to as double-overlap regions) between the central and scattered beams for each spatial frequency, high signal-to-noise phase images of the structure are obtained. A detailed explanation of the SSB reconstruction algorithm can be found in the introduction of this thesis or in previous works[84,85].

Figure 24(a) illustrates the SSB reconstruction of an in-focus 4D STEM dataset for the $PdCoO_2/Al_2O_3$ interface. At the bottom, the Al_2O_3 substrate is shown and the delafossite thin film is shown at the top, initiating with a $[CoO]^-$ octahedral layer, followed by the Pd^+ layer. Since the film grows 30° rotated relative to the substrate orientation, only the film is viewed along the [010] zone axis. In the second $[CoO]^-$ layer, the CoO_6 octahedra are mirrored compared to the first layer in the film, forming a twin domain, which can arise due to the equivalent energetic stability of the two orientations. At the interface, the atomic reconstruction in the substrate surface is clearly visible, characterized by periodically repeating features occurring at regular intervals, indicated by white ticks. Figure 24(b) shows a higher magnification view of one such feature, revealing three distinct structural regions within each repeating unit, as highlighted in the insets. Given that a TEM

image represents a 2D projection of a 3D structure, certain regions can be attributed to a single orientation of CoO, while others correspond to its 180° rotated counterpart. In addition, specific regions require a superposition of both models, incorporating a 180° inversion of the octahedral orientation. Figure 24(c) shows the result of the SSB reconstruction of an in-focus 4D STEM dataset for the $PdCoO_2/LaAlO_3$ interface for the [010] film orientation. Here, the atomic reconstruction in the substrate surface is evident, with repeating features marked by white ticks, similar to the $PdCoO_2/Al_2O_3$ interface. However, in this case, the periodicity is higher, as $PdCoO_2$ has a greater lattice mismatch on $LaAlO_3$ (-9.06%) compared to Al_2O_3 (+2.9%). The insets in Figure 24(c) further indicate the existence of regions with a single CoO orientation, regions with a 180° inversion of the octahedral orientation, and regions requiring a superposition of both configurations. Notably, a comparable interfacial reconstruction is observed in both systems, despite their differing lattice parameter relationships. In the case of $PdCoO_2/Al_2O_3$, where $d_{film}>d_{substrate}$, the film initially experiences compressive strain during growth. Conversely, for $PdCoO_2/LaAlO_3$, where $d_{film}<d_{substrate}$, the film grows under initial tensile strain.

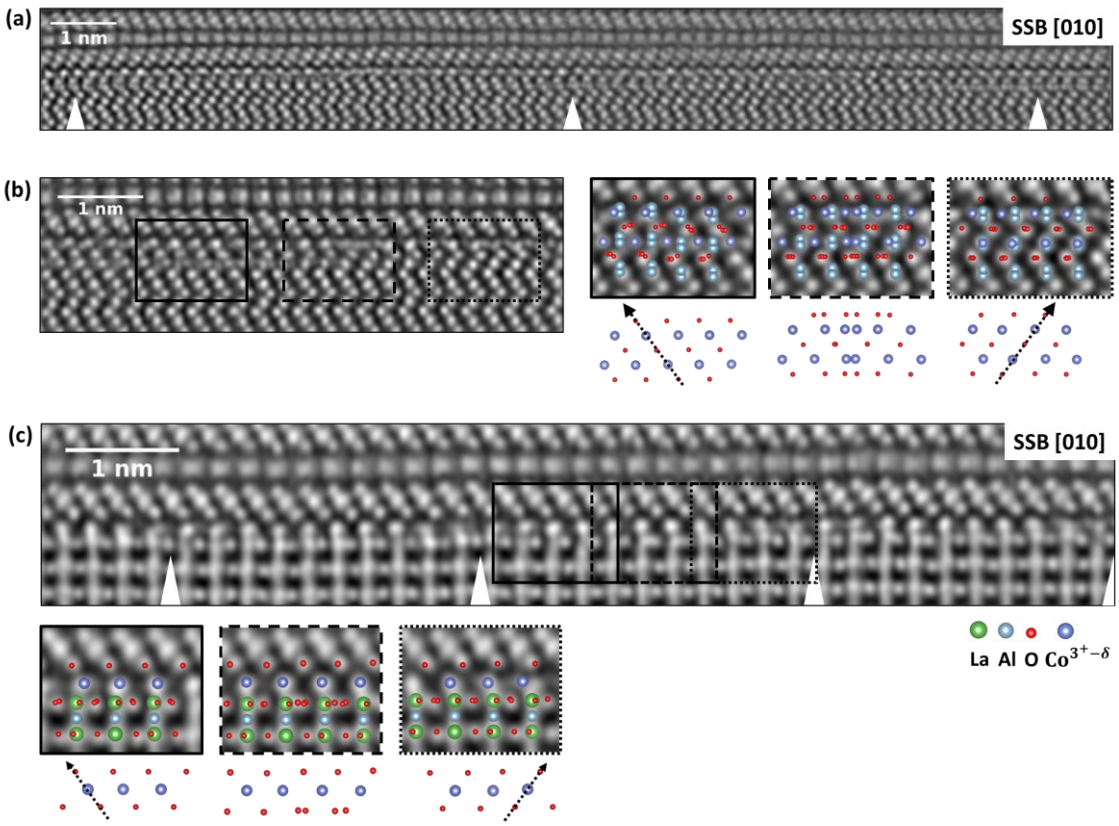

Figure 24. (a) SSB ptychographic phase reconstruction from a 4D STEM dataset with 800×90 probe positions acquired across the $PdCoO_2/Al_2O_3$ interface. Repeating features in the substrate surface are indicated by white ticks. (b) High-magnification SSB phase reconstruction of the interface revealing the presence of subdomains, indicated by black boxes, with two opposing octahedral orientations of the CoO phase. (c) SSB phase reconstruction from a 4D STEM dataset with 600×100 probe positions acquired across the $PdCoO_2/LaAlO_3$ interface. The insets reveal subdomains with two opposing octahedral orientations of the CoO phase. Adopted under the terms of a CC-BY license. © 2025 The authors[229].

In thin-film epitaxy, the lattice mismatch describes the relationship between the crystalline lattice parameters at the film-substrate interface and is a key factor in epitaxial thin-film growth. It is defined as the relative difference between the relaxed lattice parameters of the film and the substrate. According to the model proposed by Frank and van der Merwe, the lattice mismatch is given by Equation (42)[175]. However, for delafossite thin films that grow with a 30° in-plane rotation relative to the substrate, as shown in Figure 25, the in-plane lattice parameter of the film (2.83 Å) must be adjusted by a factor of $\cos(30°) \cdot 2$ at the interface. The lattice mismatches for the systems examined in this work are listed in Table 1.

Table 1. Lattice mismatch calculations for the $PdCoO_2/Al_2O_3$, $PdCoO_2/LaAlO_3$, and $PdCoO_2/SrTiO_3$ interfaces using Equation (42)[175]. Adopted under the terms of a CC-BY license. © 2025 The authors[229].

	$PdCoO_2/Al_2O_3(001)$	$PdCoO_2/LaAlO_3(111)_{pc}$	$PdCoO_2/SrTiO_3(111)_{pc}$
d_{film} [Å]	4.90	4.90	4.90
$d_{substrate}$ [Å]	4.76	5.39	5.51
$\delta_{Mismatch}$	+2.98 %	-9.06 %	-11.04 %

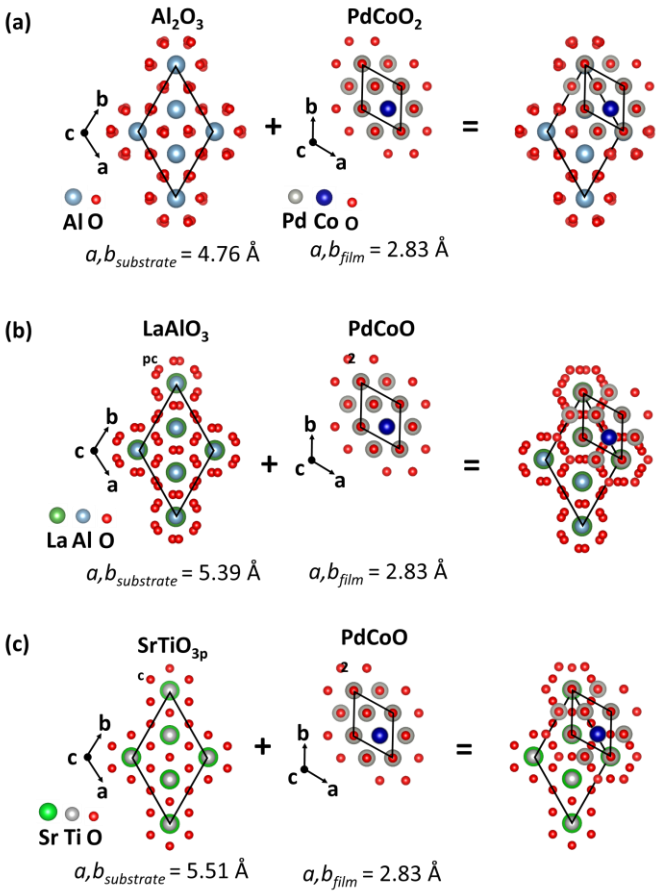

Figure 25. Orientation relationship between the (a) Al_2O_3, (b) $LaAlO_3$, and (c) $SrTiO_3$ substrates and the $PdCoO_2$ thin film with a 30° rotated growth of the film on the substrate. Lattice parameters are given for the indicated solid unit cells. Adopted under the terms of a CC-BY license. © 2025 The authors[229].

To determine the driving force behind the observed octahedral distortion, reconstructions were performed along the [210] orientation of the films, where the octahedra are projected in a manner that prevents differentiation between opposing orientations. Figure 26 shows 4D STEM phase reconstructions of the (a) $PdCoO_2/Al_2O_3$ interface and (b) $PdCoO_2/LaAlO_3$ interface. In both cases, a lattice modulation was analyzed using the phase lock-in method developed by Goodge *et al.*, mentioned in the introduction chapter of this thesis[185]. Through this approach, the amplitude and phase field of a lattice peak associated with the film structure—highlighted by the yellow spot in the Fourier transform insets—were extracted. Within the interfacial phase, defects are evident, which manifest in a discontinuity in the modulation amplitude and a phase singularity (2π wrap-around of the phase) in the phase field. Notably, the higher periodicity of the $LaAlO_3$ interfacial reconstruction results in a higher number of such defects within the field of view. These defects are likely the reason for the octahedral distortion at the interface and compensate the mismatch strain.

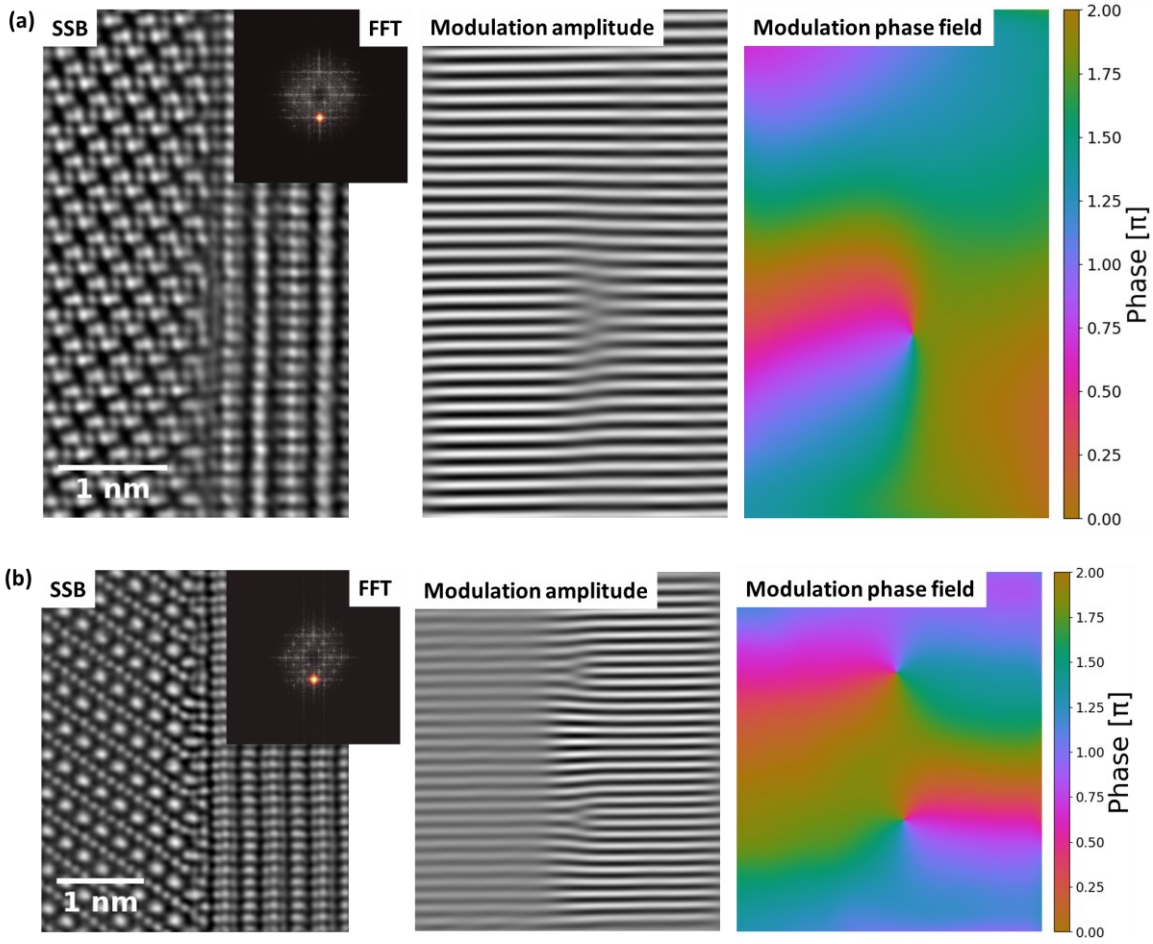

Figure 26. Phase lock-in lattice-modulation analysis from SSB phase reconstructions along the [210] orientation of $PdCoO_2$ on (a) Al_2O_3 and (b) $LaAlO_3$. Extracted modulation amplitude and phase field from the fast Fourier-transformed image reveal the presence of defects in the interfacial phase. Adopted under the terms of a CC-BY license. © 2025 The authors[229].

Integrating these findings provides a comprehensive understanding of the interfacial reconstruction mechanism that stabilizes $PdCoO_2$ thin films on Al_2O_3 and $LaAlO_3$ substrates. The observation of repeating structural features suggests the formation of a thin CoO secondary phase within the substrate surface during film growth. In bulk CoO, cobalt adopts a 2^+ valence state, whereas in $PdCoO_2$, cobalt is in a 3^+ state. The presence of cobalt within the upper substrate layers, as confirmed by EELS elemental mapping for both substrates, combined with fine-structure analyses indicating a reduction in Co valence across the interface, strongly supports the formation of a structurally distorted CoO phase at the interface. This interpretation is further reinforced by the overlaid atomic models on the phase reconstructions.

The incorporation of CoO within the substrate surface offers an alternative perspective on the mechanism of lattice mismatch accommodation at the interface, diverging from conventional models of strain relaxation in oxide heterostructures. Typically, at coherent interfaces, the lattice misfit is minimal and is accommodated through the elastic deformation of adjacent lattices, resulting in a near-perfect atomic alignment at the interface. In contrast, semi-coherent interfaces, which exhibit moderate lattice misfit, compensate for the mismatch by forming a periodic array of interfacial misfit dislocations. At incoherent interfaces, where the lattice misfit is substantial, the adjacent crystals on either side of the interface retain their intrinsic lattice structures and are rigidly stacked, inhibiting the formation of interfacial misfit dislocations. The formation of a distinct phase of the film material within the substrate does not conform to these standard strain relaxation mechanisms[268].

However, similar secondary phase formations have been observed in various heterojunction systems. For example, van der Waals interfacial reconstructions between transition metal dichalcogenides (TMDs) and gold have been reported, involving the emergence of a metastable AuS_4 phase at the interface[269]. Likewise, the reconstruction of the polar interface between hexagonal $LuFeO_3$ and intergrown Fe_3O_4 nanolayers follows a unique structural rearrangement that stabilizes the nanolayered ferrite, a process recognized as a universal mechanism for the stabilization of polar surfaces[270]. In another case of a 2DEG at the $TiO_2/LaAlO_3$ interface, the presence oxygen vacancies in anatase TiO_2 facilitates the formation of an additional alloy layer, $TiAlO_4$, through interface-driven processes. STEM investigations have provided direct evidence of this extra layer in the early stages of TiO_2 growth on $LaAlO_3$[263]. Similarly, CaO films grown on Mo(001) are stabilized by Mo diffusion from the substrate into the film, where Mo substitutes approximately 25% of the Ca ions, forming a rocksalt-type $CaMoO_4$ structure that enables the growth of extended, defect-free oxide patches[271].

Generally, interface reaction mechanisms involving topotactic transformations have been explored as a less common pathway for epitaxial systems to accommodate lattice misfit at reactive spinel

interfaces[272]. These findings highlight that interfacial reconstructions and the emergence of secondary phases are not merely incidental to growth, but fundamental processes that can drive material stabilization and transformation, often giving rise to new structural and electronic properties.

The crystal structure of metallic delafossites features a stacking of alternating charged layers along the *c*-axis. In thin films, this arrangement—comprising alternating positively charged $[A]^+$ and negatively charged $[BO_2]^-$ layers—leads to a net dipole moment within each unit cell. Based on Tasker's classification of ionic surfaces, this configuration corresponds to a type 3 polar surface[273]. To avoid a diverging electrostatic potential, either the surface or the interface of the ABO_2 film must undergo some form of electronic or structural reconstruction[155]. Although numerous surface reconstructions have been reported in delafossites and delafossite thin films—commonly revealed via angle-resolved photoemission spectroscopy (ARPES)—not all terminations with $[A]^+$ or $[BO_2]^-$ layers show such reconstructions. This indicates that different mechanisms may exist to compensate for the polar surface charge in these materials[230,243,274-276]. The interfacial reconstruction observed in this chapter may thus not only contribute to the epitaxial stabilization but also compensate for the polar surface charge.

The necessity of a CoO phase at the $PdCoO_2/Al_2O_3$ and $PdCoO_2/LaAlO_3$ interfaces is further supported by the observation that films completely decompose and do not nucleate when the growth is initiated with a Pd layer, as confirmed by DFT calculations, which demonstrate an energetically more stable $Al_2O_3/[CoO]^-$ interface than an Al_2O_3/Pd^+ interface (see Figure 21). DFT calculations were also performed with an additional CoO layer at the interface, effectively forming a Co bilayer in the CoO(111) configuration. However, due to a 10% in-plane compression relative to bulk CoO(111) for the ideal (unreconstructed) interface on Al_2O_3, geometry optimization of this extra CoO layer led to unphysically large out-of-plane bond elongations, similar to the case with Co incorporation into Al_2O_3. These results indicate that a secondary CoO phase at the interface cannot remain in its ideal form without reconstruction, as confirmed by STEM observations. Using DFT to exploratively model the reconstructions observed by STEM, without a clear candidate, is unfortunately computationally unfeasible due to the excessive size of the required supercells.

In addition to Al_2O_3 and $LaAlO_3$, an attempt was made to grow $PdCoO_2$ thin films on (111) $SrTiO_3$ substrates *via* MBE. Although the lattice mismatch for $SrTiO_3$ (-11.04%) is similar to that of $LaAlO_3$ (-9.06%), the structural analysis (Figure 27) reveals significant decomposition of the film, with stable growth being unattainable. In the few regions where the film does grow (highlighted in the blue inset in Figure 27), it exhibits a 60° rotation relative to the substrate, rather than the energetically favored 30° rotation observed for films on Al_2O_3 or $LaAlO_3$ (green frame in Figure 27). This suggests that the complex interplay between Al in the Al_2O_3 and $LaAlO_3$ substrates and

Co at the interface plays a crucial role in stabilizing the interfacial phase, and thus enables successful film growth. In contrast, this stabilization mechanism does not occur with $SrTiO_3$ as the substrate.

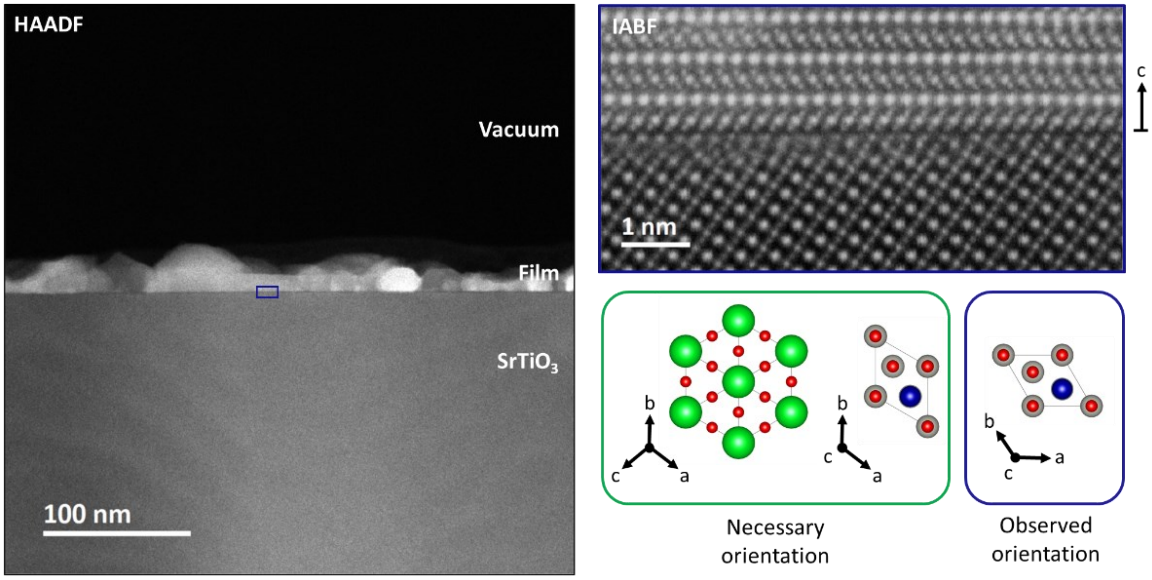

Figure 27. HAADF STEM image of a decomposed $PdCoO_2$ thin film grown on a (111) $SrTiO_3$ substrate. The blue inset highlights an area without decomposition, revealing a $PdCoO_2$ thin film grown with 60° rotation instead of 30° rotation on the substrate in the inverted ABF (IABF) image. The green frame shows the film orientation relative to the (111) $SrTiO_3$ substrate for stable growth and the blue frame shows the actually observed orientation along the *c*-axis of the film. Adopted under the terms of a CC-BY license. © 2025 The authors[229].

To exclude the influence of the growth mode on the formation of the interfacial phase, $PdCoO_2$ films on Al_2O_3 were synthesized using PLD. As shown by the SSB phase reconstructions for two zone axes and the structural models at the interface in Figure 28 and Figure 29, the interfacial phase is present in the substrate surface regardless of the fabrication method chosen. The reconstructions provide strong contrast for all elements and reveal the presence of the periodically repeating features in the substrate surface layer.

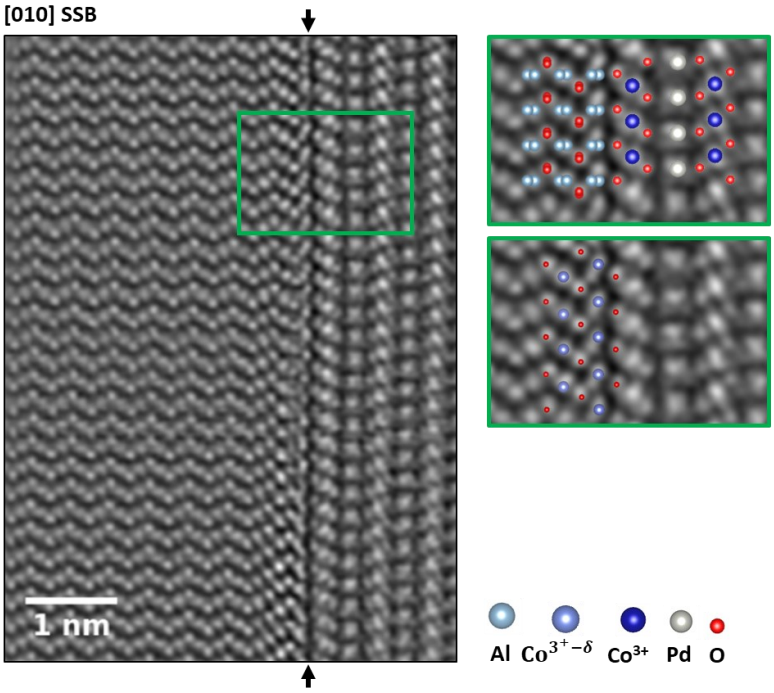

Figure 28. SSB ptychographic phase reconstruction from a 4D STEM dataset acquired across the $PdCoO_2/Al_2O_3$ interface of a PLD grown thin film along the [010] film orientation. The black arrows indicate the physical interface between the substrate and film. The insets show structural model overlays with the film and substrate models and the interfacial phase along the respective [010] zone axes. Adopted under the terms of a CC-BY license. © 2025 The authors[229].

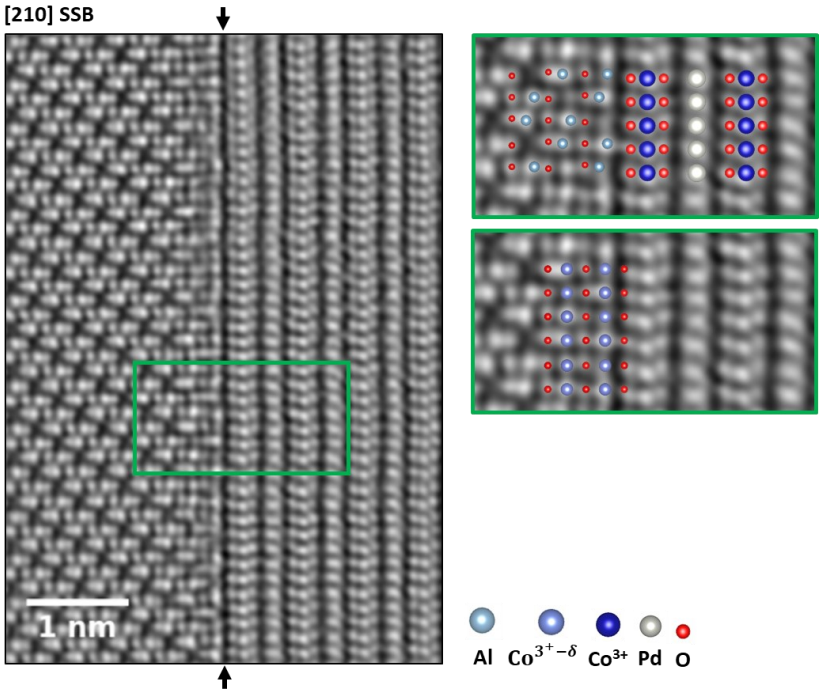

Figure 29. SSB ptychographic phase reconstruction from a 4D STEM dataset acquired across the $PdCoO_2/Al_2O_3$ interface of a PLD grown thin film along the [210] film orientation. The black arrows indicate the physical interface between the substrate and film. The insets show structural model overlays with the film and substrate models and the interfacial phase along the respective [210] zone axes. Adopted under the terms of a CC-BY license. © 2025 The authors[229].

With a comprehensive understanding of the growth mechanism and stabilization of $PdCoO_2$ epitaxial films on Al_2O_3 and $LaAlO_3$ substrates, a method has been developed to enable the stable growth of films that would otherwise be unstable on Al_2O_3. This method involves the initial nucleation of a few-unit-cell-thick buffer layer of high-quality $PdCoO_2$ under optimized growth conditions[230]. Additionally, studies on delafossites with varying *A* and *B* cations have shown that a stable delafossite buffer layer, such as $CuCrO_2$, can effectively support the epitaxial growth of other delafossite materials, including $PdCrO_2$[242,245].

3.4 Conclusions

A distinct atomic reconstruction at the interface between oxide MBE-grown $PdCoO_2$ thin films and Al-containing substrates Al_2O_3 and $LaAlO_3$ has been identified. This reconstruction is characterized by additional atomic columns within the substrate's surface layers, suggesting the formation of an ultra-thin secondary phase. Comprehensive STEM analyses, including the ptychographic phase reconstructions combined with EELS elemental mapping, reveal the presence of a CoO phase at the interface, modulating periodically within the substrate. In this phase, cobalt exists in a lower valence state ($Co^{3^+-\delta}$) compared to the Co^{3+} state in $PdCoO_2$. Observations of unstable $PdCoO_2$ growth, when initiated with a Pd^+ layer, further emphasize the critical role of the interfacial phase in enabling epitaxy. These results highlight the complex interplay between the film and the substrate during growth, where atomic-scale defects and valence changes at the interface significantly influence the structural properties of the thin films. Consequently, a deeper understanding of these phenomena is crucial for refining growth processes and provides a promising strategy for the synthesis of stable delafossite thin films using high-quality $PdCoO_2$ buffer layers.

4 Atomic-scale mechanisms of nucleation and stabilization in $CuCrO_2$ and $CuFeO_2$ delafossite thin films on Al_2O_3

Based on the findings of the previous section, the next logical step is to compare the interfacial reconstructions observed for $PdCoO_2$ with those of delafossites containing different *A* and *B* cations, grown on the same substrates. It has been found that Cu-based delafossites, specifically $CuCrO_2$ and $CuFeO_2$, also display a stable growth on Al_2O_3 and can therefore be used, among other applications, as buffer layers for the deposition of other delafossites that do not grow epitaxially on their own. The aim of the investigations in this chapter was to assess whether the unconventional film stabilization mechanism identified for Pd-based delafossites is a material-specific phenomenon or whether similar mechanisms apply more generally to delafossite thin films. Here, a combination of 4D STEM phase reconstructions *via* iterative electron ptychography, spectroscopy, and conventional STEM imaging reveals detailed insights into the nucleation mechanism for the stable growth of Cu-based delafossites on Al_2O_3 using $CuCrO_2$ and $CuFeO_2$ films grown *via* MBE as examples. The stabilization mechanism for these Cu-based delafossites differs significantly from the interfacial reconstruction observed for $PdCoO_2$. Here, the combination of a misfit dislocation network at the interface and monolayer-deep chemical intermixing relieves the lattice mismatch strain at the interface.

The following text and figures in this chapter are adopted from this publication[277]:

Scheid, A., Song, Q., Ribet, S. M., Ophus, C., Suyolcu, Y. E., Schlom, D. G., Heil, T., van Aken, P. A.: Atomic-scale mechanisms of nucleation and stabilization in $CuCrO_2$ and $CuFeO_2$ delafossite thin films on Al_2O_3. *Advanced Materials Interfaces* 12, 2500218, May 2025, 10.1002/admi.202500218[277].

Contributions to this manuscript:

Anna Scheid conceived the project. Anna Scheid wrote the initial manuscript and performed the TEM data acquisition and TEM data analysis. Stephanie M. Ribet taught Anna Scheid the methodology for analyzing defocused 4D STEM datasets, under the supervision of Colin Ophus during a three week stay of Anna Scheid at the Lawrence Berkeley National Laboratory. Both, Stephanie M. Ribet and Colin Ophus made valuable contributions to the discussions. Qi Song synthesized the delafossite thin films *via* MBE under the supervision of Darrell G. Schlom. Tobias Heil assisted with TEM data evaluation and analysis. Y. Eren Suyolcu assisted with project coordination. Tobias Heil and Peter A. van Aken supervised this project and provided valuable input on data analysis and discussions. All co-authors revised the manuscript.

4.1 Introduction

Cu-based delafossites, such as $CuCrO_2$ and $CuFeO_2$, are *p*-type semiconductors and considered promising candidates for transparent conducting oxides (TCOs), with potential applications in various devices, including solar cells and spintronic systems[160,278]. Both $CuCrO_2$ and $CuFeO_2$ adopt the *3R*-type delafossite structure, with lattice parameters of a=2.976 Å, b=2.976 Å, c=17.110 Å for $CuCrO_2$, and a=3.033 Å, b=3.033 Å, c=17.161 Å for $CuFeO_2$[279,280]. $CuCrO_2$ exhibits antiferromagnetic ordering below 24 K, while $CuFeO_2$ orders antiferromagnetically below 11.2 K, with its magnetic properties being tunable through *B*-site doping[280-286]. Both compounds exhibit strong coupling between magnetic and structural properties, which paves the way for multiferroelectricity[287]. Due to its frustrated triangular lattice, $CuCrO_2$ becomes ferroelectric below its Néel temperature without applying external magnetic fields or doping at the Cr^{3+} sites, in contrast to $CuFeO_2$. The quasi-2D magnetic behavior makes $CuCrO_2$ especially promising for spintronic applications[288]. $CuCrO_2$ and $CuFeO_2$ thin films can form layered thin-film structures and heterojunctions, which are crucial for their integration into functional devices. Therefore, these materials provide a platform for investigating quantum confinement effects, interface engineering, and strain-induced modifications of electronic and magnetic properties[289,290].

The fabrication of high-quality thin films of $CuCrO_2$ and $CuFeO_2$ poses several challenges though, primarily due to improper growth conditions and the significant lattice mismatch with commonly used substrates such as Al_2O_3, which often leads to the formation of impurity phases, defects, and twin domains[241,254,291]. Given the lattice parameters $a(CuCrO_2)$ = 2.97 Å, $a(CuFeO_2)$ = 3.03 Å, and $a(Al_2O_3)$ = 4.76 Å, the calculated lattice mismatches are 8.25 % for $CuCrO_2/Al_2O_3$ and 10.33 % for $CuFeO_2/Al_2O_3$ (using Equation (42)) with a 30° rotated film growth analogous to the Pd-based delafossites of the third chapter, as described by Sun *et al.*[241]. Since the structural and electronic properties of thin films are strongly influenced by the nature of the film-substrate interface, optimizing growth conditions to achieve smooth, high-quality films while managing strain and minimizing defects is of fundamental importance[155,156,292]. $CuCrO_2$ delafossites may be employed as isostructural substrates or buffer layers due to their high resistivity and minimal lattice mismatch with Pd-based delafossites[242].

Surprisingly, Cu-based delafossites can be fabricated as thin films with high crystallinity, similar to $PdCoO_2$ thin films, despite the large lattice mismatch on Al_2O_3[241,245,254,290,293,294]. However, the underlying stabilization mechanisms for $CuCrO_2$ and $CuFeO_2$ films remain unexplored, and existing models based on Pd-based delafossites fail to fully explain their growth behavior[295].

The previous chapter examined the film growth of $PdCoO_2$ on Al_2O_3 and $LaAlO_3$, which is facilitated by the formation of an interfacial phase, comprising a CoO secondary phase embedded

within the substrate. This mechanism leads to significantly more stable films compared to other commonly used substrates for delafossites, such as $SrTiO_3(111)$[155,156]. This deviates from the conventional understanding of a semi-coherent heterostructure interface, which is characterized by partial lattice matching, accompanied by the potential formation of misfit dislocations to relieve mismatch strain. While a dislocation network induces localized defects, the general structural integrity of the film is preserved[268]. The findings of the previous chapter indicated that, for the successful epitaxial growth of other delafossites, it is advantageous to first deposit a $PdCoO_2$ buffer layer on Al_2O_3 before growing additional delafossite layers, if direct film growth is either not feasible or leads to a high defect density. The structural and chemical compatibility provided by a buffer layer can introduce homogeneous and stable nucleation with delafossite symmetry, which cannot be achieved from direct nucleation for certain delafossites. Close lattice matching between the buffer layer and a delafossite substrate facilitates epitaxial alignment and reduces interfacial strain[230].

Since $CuCrO_2$ and $CuFeO_2$ delafossite thin films can grow epitaxially on Al_2O_3 despite exceptionally high mismatch strains of 8.25 % and 10.33 %, respectively, it is of interest to explore whether a stabilization mechanism similar to that observed for $PdCoO_2$ delafossites is at play and to assess the implications for the use of $CuCrO_2$ as buffer layers[245,290,296]. A study by Ok *et al.* explored the interfacial stabilization of $CuCrO_2$ on Al_2O_3, reporting that the nucleation of a thermodynamically stable, atomically thin $CuCr_{1-X}Al_XO_2$ interfacial layer is crucial for the epitaxy of $CuCrO_2$ delafossites on Al_2O_3 substrates[245]. However, this study primarily focused on the chemical composition of the interface rather than investigating its atomic reconstruction with high-resolution imaging techniques. Based on DFT calculations, the authors proposed that the formation of the interfacial alloy is responsible for the stable growth of delafossite films *via* pulsed laser epitaxy (PLE)[245].

Through a combination of STEM techniques involving HAADF imaging, ABF imaging, EELS, and iterative multi-slice phase reconstructions from defocused 4D STEM datasets, it will be shown in this chapter that, in addition to the formation of this interfacial layer, an atomic reconstruction occurs at the interface, which further stabilizes the film on the substrate. Specifically, chemical intermixing and the formation of a misfit dislocation network at the semi-coherent interface stabilize the Cu-based delafossites on Al_2O_3. The misfit dislocations at the interface cause periodic distortions in the BO_6 octahedra within the first layer of the films. Notably, this stabilization mechanism for the Cu-based delafossites differs significantly from the mechanism that stabilizes $PdCoO_2$ films.

4.2 Materials and methods

4.2.1 Sample preparation

$CuCrO_2$ and $CuFeO_2$ films were synthesized *via* MBE using a Veeco Gen10 system on (001)-oriented Al_2O_3 substrates. The substrates were heated to 830 °C, with the temperature monitored by a thermocouple positioned near the substrate heater. Cu, Cr, and Fe were evaporated from MBE effusion cells, each set to deliver a flux of approximately $1 \cdot 10^{13}$ atoms cm^2s^{-1}, as measured by a quartz crystal microbalance. This initial flux calibration was further refined by measuring the thickness of a CuO calibration film grown on a (100)-oriented MgO substrate using X-ray reflectivity (XRR)[297]. Cr_2O_3 and Fe_2O_3 calibration films were grown on (001)-oriented Al_2O_3 substrates and similarly characterized by XRR. For the growth of $CuCrO_2$ films, the deposition atmosphere consisted of a mixture of approximately 80% ozone and 20% oxygen at a background pressure of $1 \cdot 10^{-6}$ Torr. $CuFeO_2$ films were grown in an atmosphere with a background pressure of $5 \cdot 10^{-7}$ Torr, utilizing a gas mixture of 5% ozone and 95% oxygen. The shutters for Cu and Cr (or Fe) were controlled to introduce monolayer doses of these elements in a sequential manner, following the atomic layer arrangement along the *c*-axis of the crystal structure of $CuCrO_2$ (or $CuFeO_2$). The structure was characterized by a Panalytical Empyrean X-ray diffractometer utilizing Cu $K\alpha_1$ radiation.

4.2.2 STEM specimen preparation

The preparation of electron-transparent specimens included diamond cutting and tripod wedge polishing. Afterwards, a precision ion polishing system (Gatan PIPS II, Model 695), equipped with a liquid nitrogen cooling stage and using ionized argon, was employed for final thinning.

4.2.3 STEM investigations

STEM investigations were conducted using a JEOL ARM200F, which is equipped with a cold field-emission gun and a probe C_S corrector (DCOR, CEOS GmbH). The measurements were executed at ambient temperatures with an acceleration voltage of 200 kV and a probe semi-convergence angle of 20.4 mrad. To enhance the signal-to-noise ratio, mitigate scan artifacts, and minimize sample drift effects, STEM images were generated from multi-frame acquisitions, using high scanning speeds (~3 µs/pixel dwell time) and applying post-acquisition cross-correlation.

For spectroscopic measurements, EELS data were acquired with a Gatan GIF Quantum ERS imaging filter, with a 5 mm entrance aperture yielding a semi-collection angle of 111 mrad at the used camera length of 1.5 cm. PCA was employed to enhance the signal-to-noise ratio, utilizing 15

principal components for accurate elemental mapping, while the line scan signals were extracted from the raw data[247].

For comprehensive 4D STEM data acquisition, a MerlinEM Medipix3 detector by Quantum Detectors was utilized, with the microscope camera length set to 80 cm and the probe semi-convergence angle to 20.4 mrad. The detector was operated in 12-bit mode and each dataset was acquired with 70×140 probe positions, with a probe position dwell time of 1 ms and a defocus of ~20-30 nm. Ptychographic reconstructions were performed using the iterative multi-slice and mixed-state electron ptychography algorithms implemented in py4DSTEM, an open-source Python repository available on GitHub[69,70].

The sample thickness was estimated by comparing simulated PACBED patterns with experimental PACBEDs extracted from the 4D STEM datasets, which were acquired in the same sample region as the EELS measurements. For the simulations, the *ab*TEM package was used, with the simulation parameters in accordance with the experimental setup[248].

4.3 Results and discussion

4.3.1 Structural characterization of the $CuCrO_2$ and $CuFeO_2$ thin films

Thin films of $CuCrO_2$ and $CuFeO_2$ were synthesized on Al_2O_3 substrates *via* MBE in a Veeco GEN10 MBE system. Lower-magnification STEM images of the thin films, along with X-ray diffraction θ-2θ scans and RHEED patterns acquired after deposition, are shown in Figure 30. These data confirm the epitaxy and phase purity of the films.

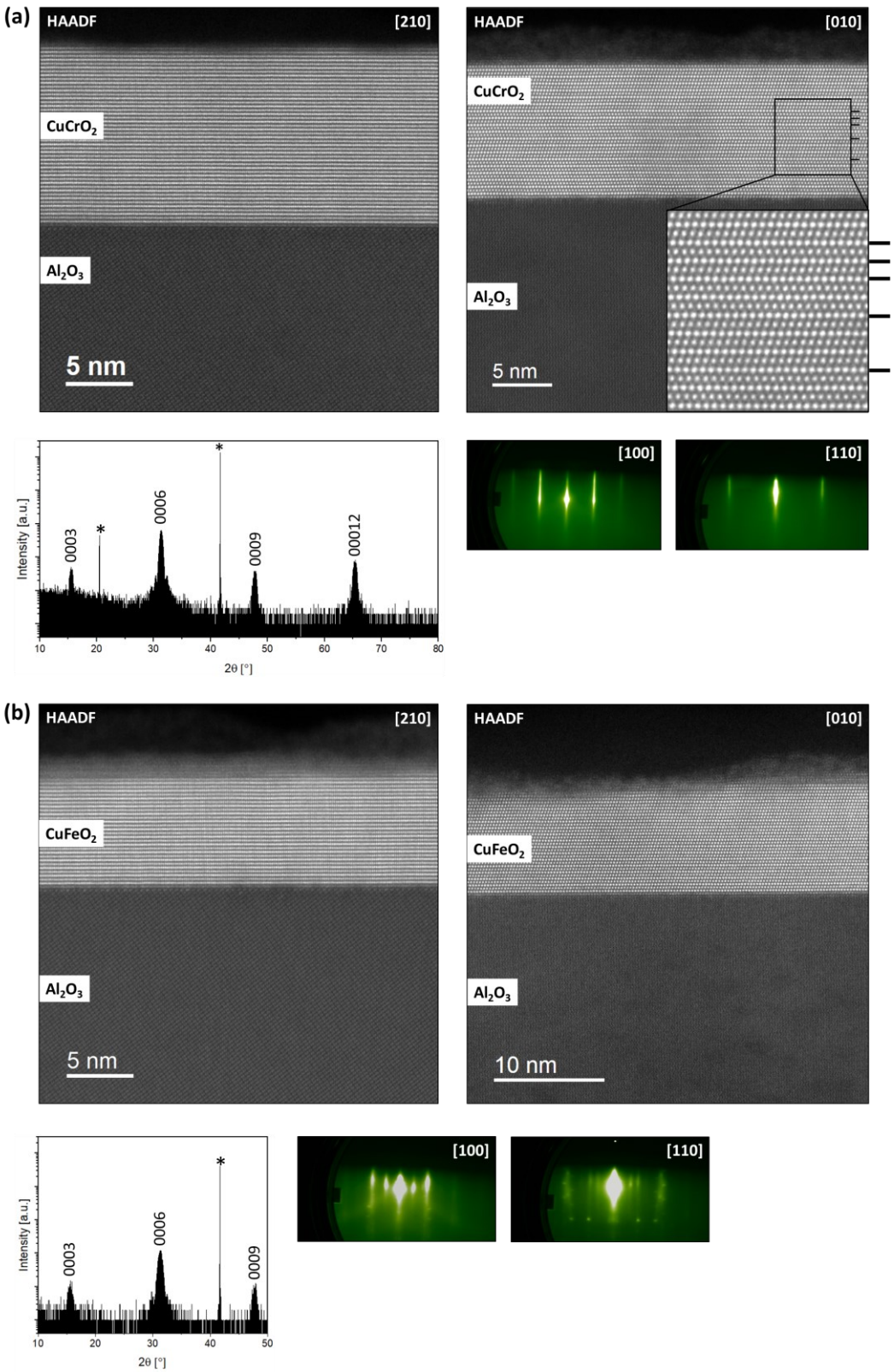

Figure 30. Low-magnification HAADF STEM images, *in-situ* RHEED patterns, and X-ray diffraction data of (a) $CuCrO_2/Al_2O_3$ and (b) $CuFeO_2/Al_2O_3$ along different zone axes of the films. For $CuCrO_2$, twin domains are observed in the [010] zone axis image, as indicated by the ticks in the magnified inset, whereas a single domain is present for $CuFeO_2$. Minor surface damage from sample preparation is visible on the $CuFeO_2$ sample. Asterisks (∗) in the X-ray diffraction patterns denote substrate reflections. Adopted under the terms of a CC-BY license. © 2025 The authors[277].

HAADF and ABF STEM images of the $CuCrO_2/Al_2O_3$ and $CuFeO_2/Al_2O_3$ interfaces, captured along two different zone axes, are shown in Figure 31 and Figure 32. The light elements, Al and O, which are often difficult to discern at the higher scattering angles in HAADF images, become more visible at the lower scattering angles in ABF images. Due to their lattice symmetry, delafossites grow on Al_2O_3 substrates with a 30° rotation, and the probability of film growth with either +30° or –30° orientation is equally high[156,291]. As a result, for the same substrate orientation, two distinct film orientations can be observed for the same orientation of the substrate in Figure 31(b) and Figure 32(b), the [010] orientation of $CuCrO_2$ and the $[0\bar{1}0]$ orientation of $CuFeO_2$. Therefore, the noted orientation indices consistently indicate the orientation of the film in the following sections, not that of the substrate.

The magnified cutouts of the ABF images with the structural model overlays show the oxygen octahedra for the [010] and $[0\bar{1}0]$ zone axes (Figure 31(b) and Figure 32(b)) and the projection of the atoms along the [210] zone axis (Figure 31(a) and Figure 32(a)), where the octahedral orientations are not distinguishable. Consequently, twins or stacking faults in delafossites are unperceivable along the latter zone axis. It should be noted that twinning and stacking faults are common crystal defects in delafossite films and result from the energetically equivalent growth of the films in two structural orientations, which are 180° in-plane rotated relative to each other[155,291]. Here, for the [010] and $[0\bar{1}0]$ zone axes, only a single domain is visible in the ABF images in Figure 31(b) and Figure 32(b), with no observed stacking faults or twinning in this region. However, the twins and stacking faults are visible in the inset in the lower-magnification image for the [010] zone axis in Figure 30 and marked by ticks.

The film growth is initiated with a layer of $[CrO_2]^-$ and $[FeO_2]^-$, respectively, as it has been observed that neither Pd-based films nor Cu-based films form a crystalline film when growth initiation is attempted with Cu^+ or Pd^+ layers[229,243,245,295]. Upon closer inspection of the interface, it becomes evident that the contrast in the HAADF images for both the substrate and the film deviates in the initial layer compared to subsequent layers. While a lower contrast is observed for the initial $[CrO_2]^-$ layer in the film, an increase in contrast is visible for the surface layers of the substrate compared to the subsequent layers of both film and substrate. The ABF images particularly highlight an apparent distortion of the oxygen octahedra in the initial $[CrO_2]^-$ and $[FeO_2]^-$ layers for the [010] and $[0\bar{1}0]$ orientation.

Here, the observations differ significantly from those in the previously studied $PdCoO_2$ thin films[229,295]: no reduction in contrast was observed in the first layer of $[CoO_2]^-$, nor was there any distortion of the oxygen octahedra within this layer. The observations from conventional STEM imaging support the hypothesis of Ok *et al*. that during nucleation, at the interface, Cr or Fe ions substitute Al ions, respectively[245]. However, findings from advanced STEM imaging, along with

the observation that stable film growth occurs only when initiated with a $[CoO_2]^-$ or $[FeO_2]^-$ layer, suggest that a structural reconstruction in the first layer is essential for enabling epitaxial growth.

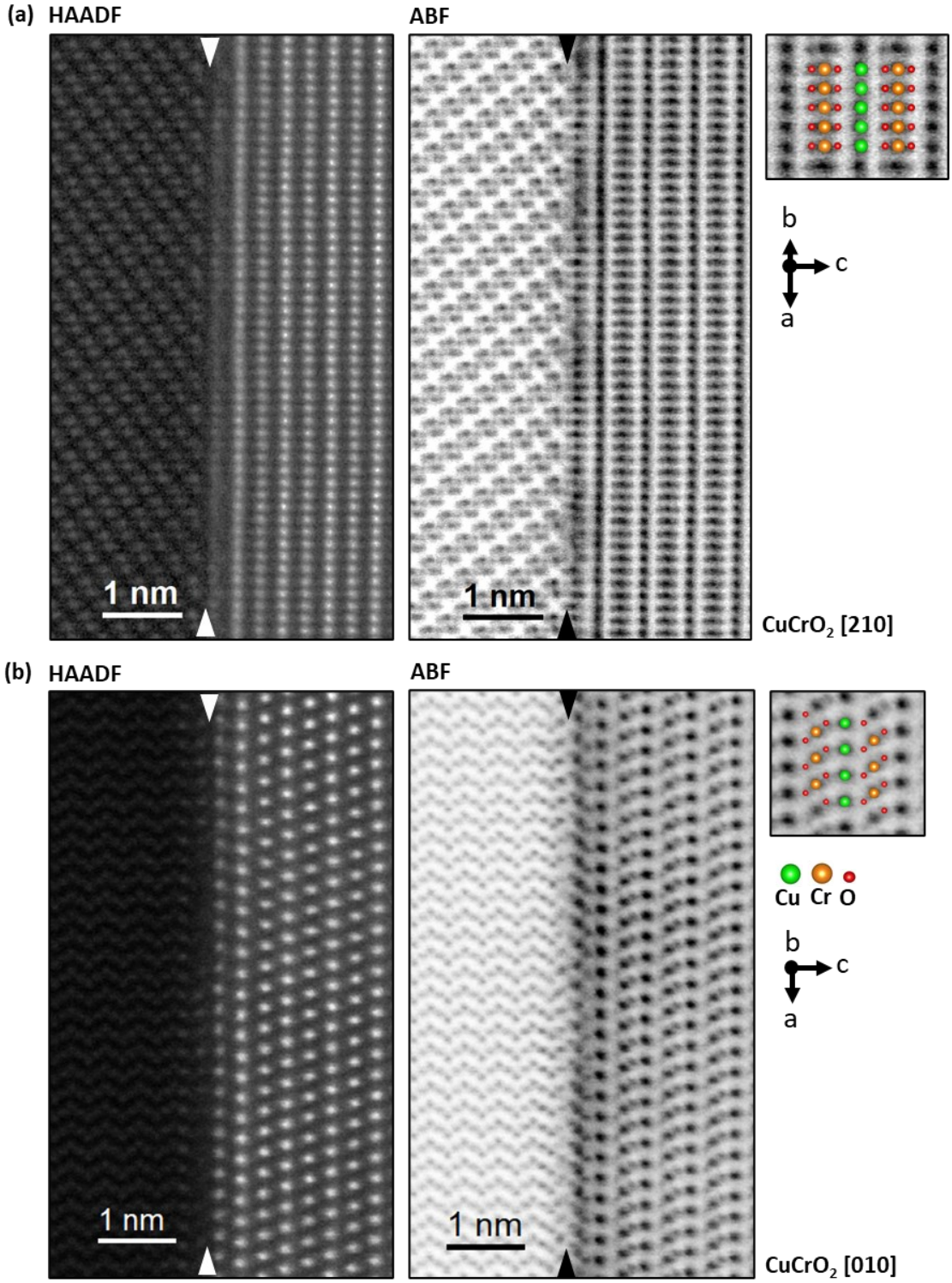

Figure 31. HAADF and ABF STEM images of the $CuCrO_2/Al_2O_3$ interface along the (a) [210] and (b) [010] zone axes. The cutouts of the ABF images show an overlay of the structural model of the film, indicating the orientation of the oxygen octahedra along the (a) [210] and (b) [010] zone axes. Black and white ticks indicate the physical interface in each image. Adopted under the terms of a CC-BY license. © 2025 The authors[277].

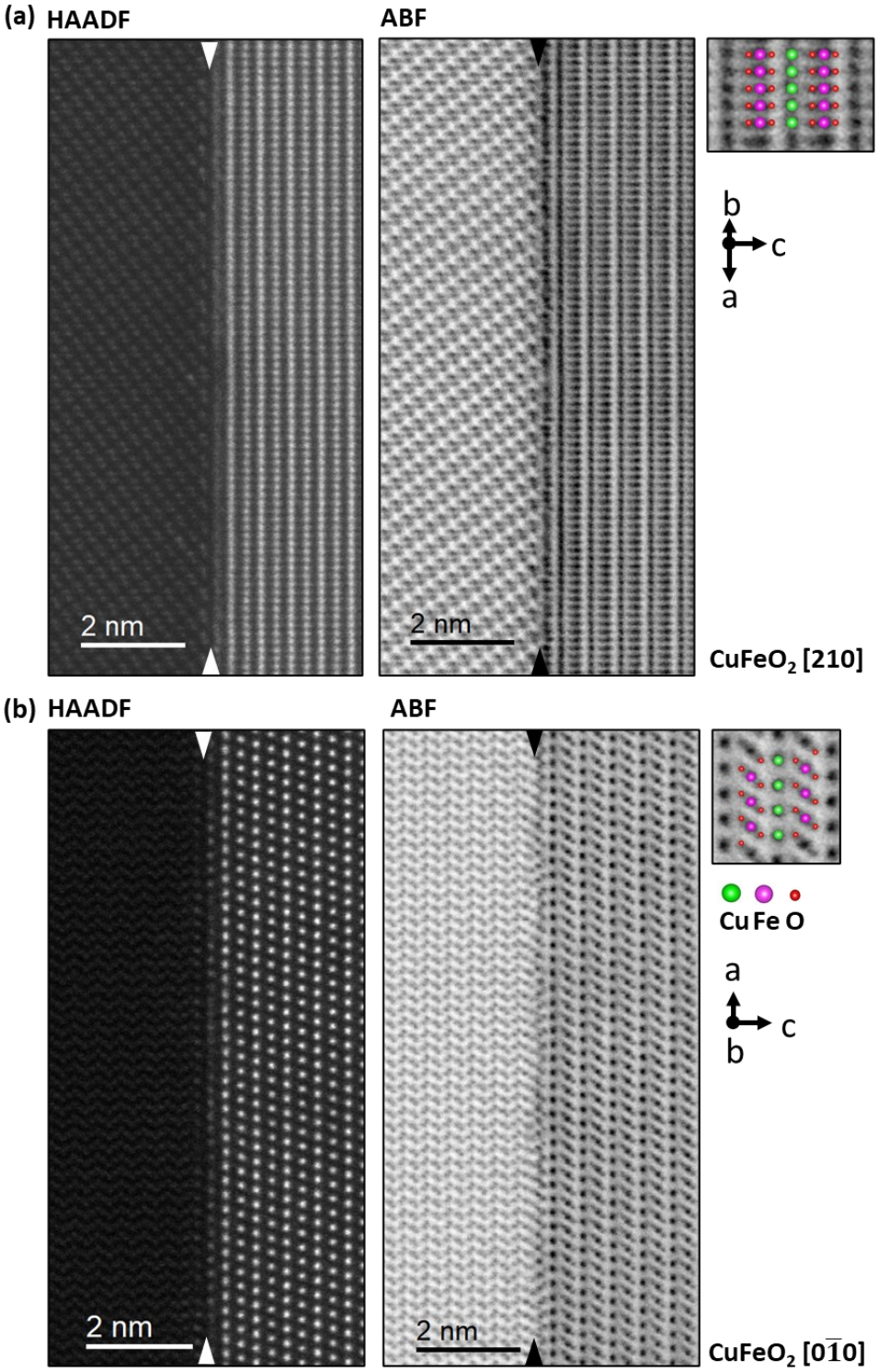

Figure 32. HAADF and ABF STEM images of the $CuFeO_2/Al_2O_3$ interface along the (a) [210] and (b) [0$\bar{1}$0] zone axes. The cutouts of the ABF images show an overlay of the structural model of the film, indicating the orientation of the oxygen octahedra along the (a) [210] and (b) [0$\bar{1}$0] zone axes. Black and white ticks indicate the physical interface in each image. Adopted under the terms of a CC-BY license. © 2025 The authors[277].

4.3.2 Lattice modulation analysis of the $CuCrO_2$ and $CuFeO_2$ thin films

From the HAADF and ABF STEM images along the two zone axes shown in Figure 31 and Figure 32, periodic contrast variations at the interface are evident. To characterize these variations more precisely, the order parameter at the interface was analyzed. Specifically, a coarse-grained phase field, $\phi(r)$, was extracted from the fast Fourier transform (FFT) of an inverted ABF (IABF) image along the [210] orientation of both films. This phase field is associated with a lattice modulation of the substrate as the reference, as the microscopic picture of the lattice modulations may be correlated to phase information of defects at the interface. Variations in the phase field, which reflect deviations from ideal long-range modulations, were extracted using the phase lock-in technique developed by Goodge *et al.*[185]. A lattice modulation of the Al_2O_3 substrate was selected in each case, indicated by a yellow spot in the FFT inset in Figure 33(a) and Figure 34(a). The extracted modulation amplitude (Figure 33(b) and Figure 34(b)) reveals the presence of periodic lattice defects at the interface within the initial layer of the delafossite thin films.

Using a $\boldsymbol{k}$-vector along the same direction as the Burgers vector $\boldsymbol{b}$ of the dislocation defect, a phase winding around 2π at the dislocation core is observed (Figure 33(c) Figure 34(c)). These periodically occurring misfit dislocations alleviate the mismatch strain resulting from the differences in lattice parameters between the substrate and the film at the interface. Additionally, a strain analysis shown in Figure 33(d, e) and Figure 34(d, e), reveals the stress distribution around the dislocation cores. The measured strain of the films relative to the substrate aligns with the calculated mismatch strains from the lattice parameters, which are +8.25 % and +10.33 % for $CuCrO_2$ and $CuFeO_2$ on Al_2O_3, respectively.

From multiple STEM HAADF and ABF images, the average spacing of the misfit dislocations was determined for both films with an average dislocation density of 0.50 ± 0.04 dislocations/nm for the $CuCrO_2$ thin film and a dislocation density of 0.68 ± 0.06 dislocations/nm for the $CuFeO_2$ thin film. The theoretical misfit dislocation density ρ_{theo} necessary to relieve the mismatch strain between the lattices at the interface can be calculated using Equation (43). With a Burgers vector value of b = 1.488 Å for $CuCrO_2$ and 1.516 Å for $CuFeO_2$ and the mismatch strain $\delta_{Mismatch}$ = 8.25 % for the $CuCrO_2/Al_2O_3$ and $\delta_{Mismatch}$ = 10.33 % for the $CuFeO_2/Al_2O_3$ interface, theoretical dislocation densities of 0.554 dislocations/nm and 0.681 dislocations/nm, respectively, are obtained. The measured dislocation densities are in good agreement with the predicted values, although slightly fewer dislocations appear to be necessary for $CuCrO_2$. These discrepancies indicate that additional mechanisms may be involved in the film stabilization on the substrate.

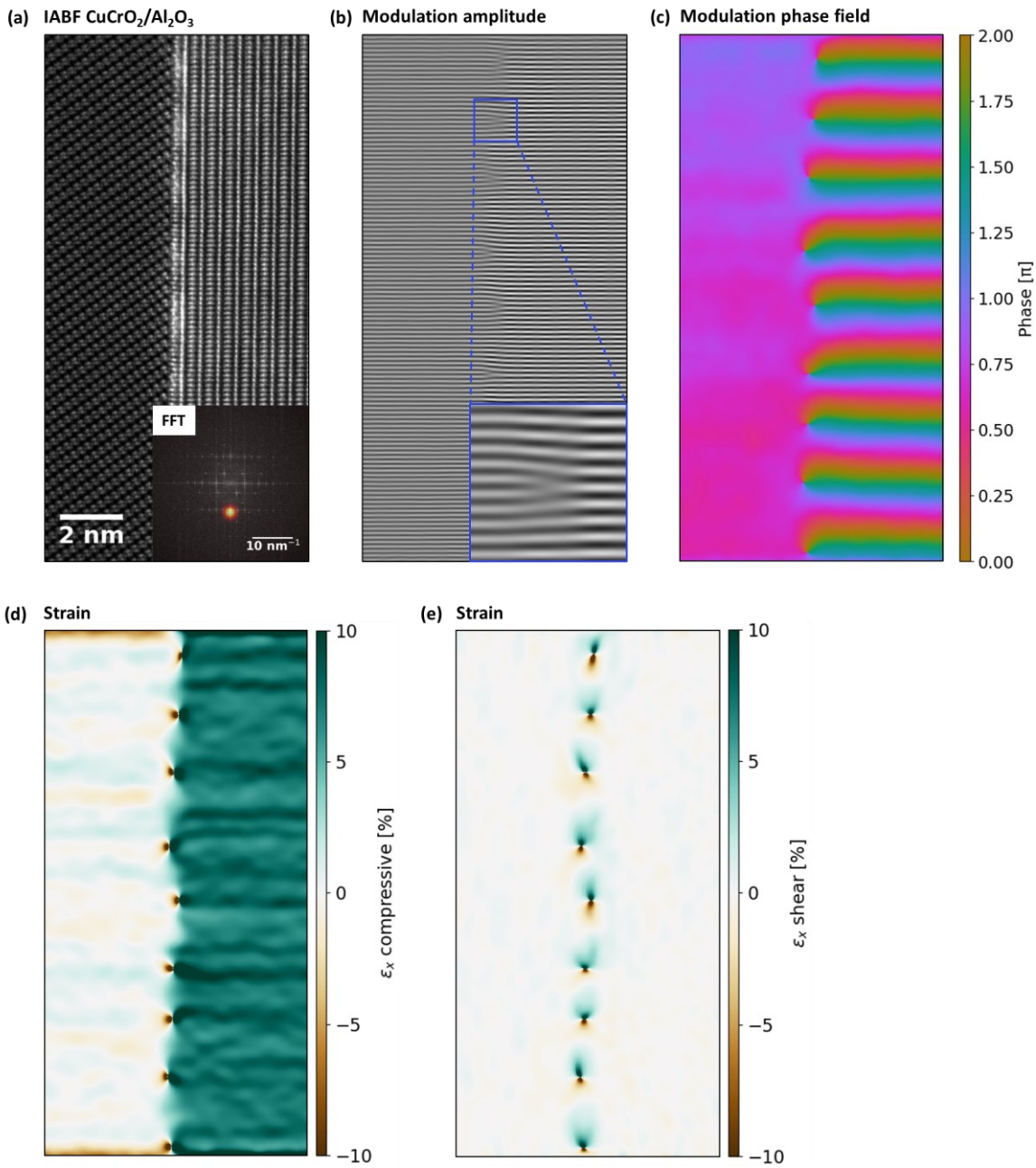

Figure 33. Phase lock-in analysis of the $CuCrO_2/Al_2O_3$ interface along the [210] orientation. (a) IABF image of the interface and the Fourier transform of the entire field of view. The yellow points in the FFT indicate the lattice modulation selected for analysis. The extracted amplitude (b) and phase field (c) of the lattice modulation highlight defects at the interface corresponding to misfit dislocations, characterized by a discontinuity in amplitude modulation and a 2π phase wrap-around. The strain analysis in (d) and (e) highlights the strain distribution around the dislocations. Adopted under the terms of a CC-BY license. © 2025 The authors[277].

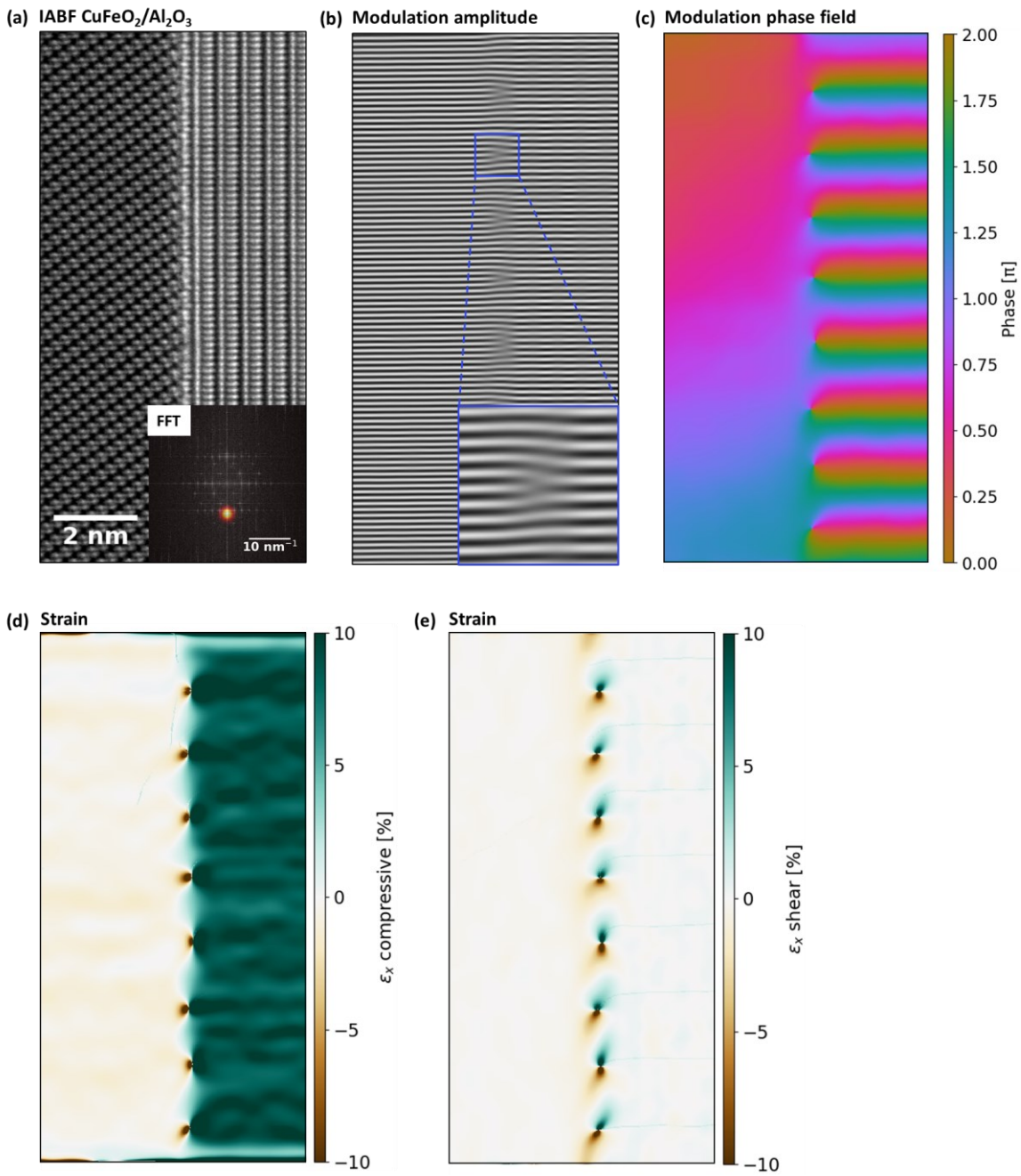

Figure 34. Phase lock-in analysis of the $CuFeO_2/Al_2O_3$ interface along the [210] orientation. (a) IABF image of the interface and the Fourier transform of the entire field of view. The yellow points in the FFT indicate the lattice modulation selected for analysis. The extracted amplitude (b) and phase field (c) of the lattice modulation highlight defects at the interface corresponding to misfit dislocations, characterized by a discontinuity in amplitude modulation and a 2π phase wrap-around. The strain analysis in (d) and (e) highlights the strain distribution around the dislocations. Adopted under the terms of a CC-BY license. © 2025 The authors[277].

4.3.3 Electron ptychography of the $CuFeO_2/Al_2O_3$ and $CuFeO_2/Al_2O_3$ interfaces

Due to the insufficient resolution of conventional STEM imaging techniques for precise atomic-level imaging of the reconstruction at the interface, advanced imaging methods that are capable of

providing strong contrast for both light and heavy elements are necessary. In TEM, electron wave phase imaging methods (not to be confused with the FFT phase investigation discussed earlier) are particularly suitable for this purpose, as significant changes in the phase of the electron wave interacting with the sample occur even for light elements[298]. Unfortunately, STEM electron detectors can only detect intensities, *i.e.*, the squared modulus of the electron exit wave, resulting in the loss of sample-specific phase information during the experiment. Direct phase contrast imaging techniques, including Zernike phase contrast microscopy (PCM) and DPC, address this issue by transforming phase variations at the object plane into intensity variations at the imaging plane[299,300].

In contrast, post-processing phase retrieval techniques, such as electron ptychography, recover the object wave function from previously acquired diffraction intensities at each probe position[69]. The corresponding imaging mode is often referred to as 4D STEM, due to the acquisition of a 2D real-space scan with a 2D diffraction pattern for each probe position[38]. Several theoretical algorithms have been proposed for this computational imaging method. These algorithms can generally be categorized into two classes as described in the first chapter of this thesis: (1) direct inversion algorithms, such as the WDD and SSB; and (2) iterative algorithms, such as gradient descent or parallel projection methods with relaxed sampling conditions compared to non-iterative algorithms[38].

Iterative ptychographic algorithms offer the advantage of overcoming resolution limitations caused by residual aberrations and enabling super-resolution imaging[301]. Additionally, these algorithms allow for dose fractionation and faster acquisition speeds by increasing probe overlap and information redundancy *via* the acquisition of 4D STEM datasets with a defocused probe[103,302]. Non-iterative reconstructions are limited to very thin materials, as they approximate the interaction of the beam with the sample as a simple product of the sample function and the object transmission function with the probe-sample interaction only affecting the phase of the electron wave. This WPOA approximation is not valid for thicker samples where multiple scattering occurs. Iterative reconstructions, on the other hand, offer the possibility to embed multi-slice algorithms, and thus enable a more realistic reconstruction for samples with a finite thickness, and may additionally offer the possibility to achieve depth-dependent information[109,303].

In this chapter, gradient descent iterative multi-slice and mixed-state ptychography is employed to obtain high-resolution, high-contrast images of the misfit dislocation structure at the $CuCrO_2/Al_2O_3$ and $CuFeO_2/Al_2O_3$ interfaces along two zone axes. 4D STEM datasets containing diffraction patterns from 70×140 probe positions at the interface between the substrate and film were acquired, and iterative phase reconstructions were performed using the open-source Python package

py4DSTEM. A detailed description of the algorithm can be found in the first chapter and the work of Varnavides *et al.*[69].

The initial probe calibration parameters were obtained through BO refinement. The scattering potential was initially assumed to be empty, and the probe was initialized using an aperture derived from a 4D vacuum scan acquired immediately after dataset acquisition. The object and probe were jointly reconstructed using a batched stochastic gradient descent algorithm. In Fourier space, the probe amplitude was constrained, while the phase was smoothed by fitting a Zernike-like aberration surface expansion. The object was constrained to be a positive potential object, meaning that the amplitude was fixed to unity at each iteration. Convergence was typically achieved within 40 iterations, and additional reconstruction parameters are provided in Table 2 below. Final images of the structure were obtained by averaging the inner slices of the multi-slice reconstructions.

Table 2. Reconstruction parameters for iterative ptychographic reconstructions. Adopted under the terms of a CC-BY license. © 2025 The authors[277].

	$CuCrO_2/Al_2O_3$ [210]	**$CuCrO_2/Al_2O_3$ [0$\bar{1}$0]**	**$CuFeO_2/Al_2O_3$ [210]**	**$CuFeO_2/Al_2O_3$ [010]**
Mode	Multi-slice ptychography	Mixed-state ptychography	Mixed-state ptychography	Mixed-state ptychography
Number of probes	1	2	3	3
Iterations	100	150	50	100
Number of slices	20	20	15	15
Slice thickness [nm]	1	1.5	1.5	1.5
Number of averaged inner slices	10	7	7	7

Subsections of the reconstructed phase images from the 4D STEM datasets, for two orientations of $CuCrO_2$ and $CuFeO_2$, are shown in Figure 35 and Figure 36.

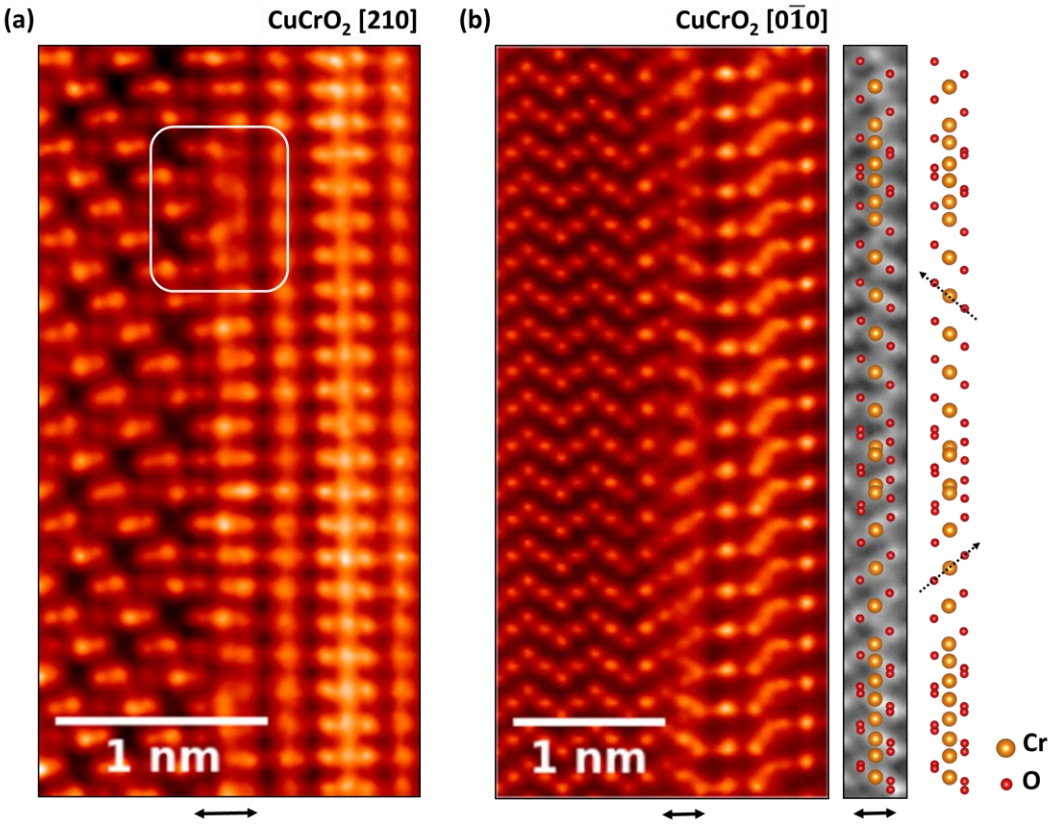

Figure 35. Atomic-resolution multi-slice 4D STEM phase reconstructions of the $CuCrO_2/Al_2O_3$ interface along the (a) [210] and (b) [0$\bar{1}$0] zone axes of the film. The misfit dislocations at the interface, one of which is highlighted by the solid box, alleviate the mismatch strain between substrate and film and cause an in-plane rotational distortion of the CrO_6 octahedra around the misfit dislocation cores (b). The interfacial layer involving the atomic reconstruction at the interface is indicated by black arrows. Adopted under the terms of a CC-BY license. © 2025 The authors[277].

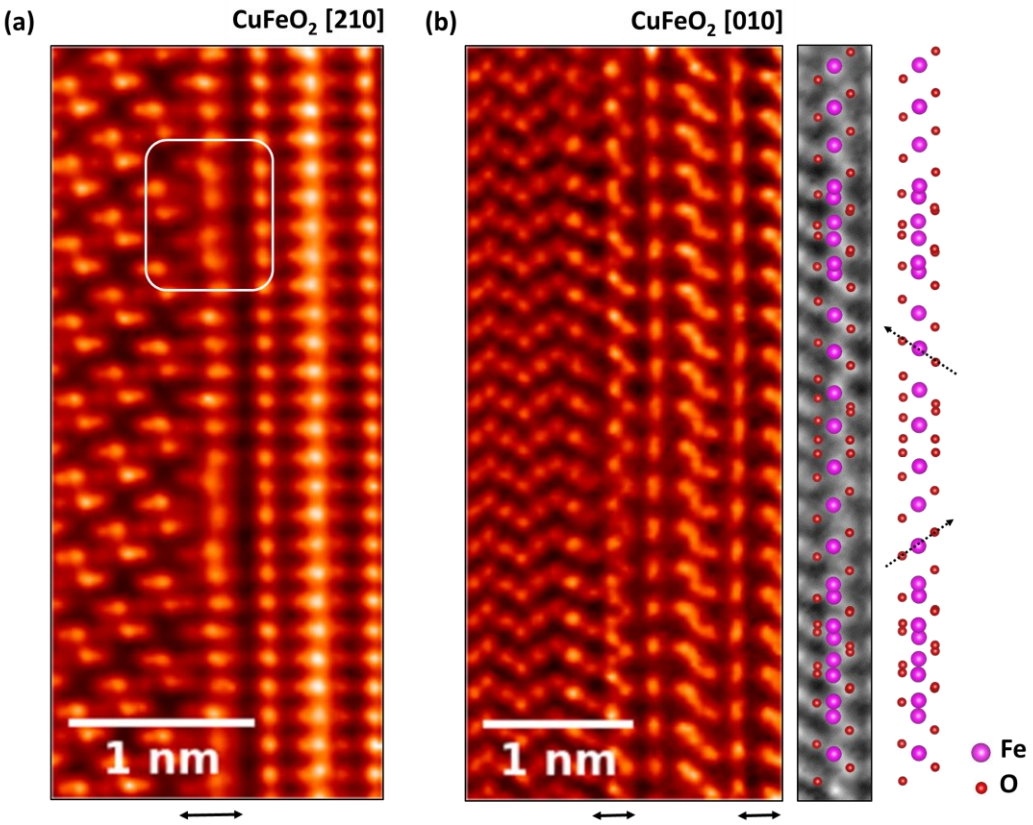

Figure 36. Atomic-resolution multi-slice 4D STEM phase reconstructions of the $CuFeO_2/Al_2O_3$ interface along the (a) [210] and (b) [010] zone axes of the film. The misfit dislocations at the interface, one of which is highlighted by the solid box, alleviate the mismatch strain between substrate and film and cause an in-plane rotational distortion of the FeO_6 octahedra around the misfit dislocation cores (b). The interfacial layer involving the atomic reconstruction at the interface is indicated by black arrows. Adopted under the terms of a CC-BY license. © 2025 The authors[277].

The full field-of-view phase images of the interface reconstructions are shown in Figure 37. The phase reconstructions feature strong contrast for both the light and heavy elements, uncovering the atomic structure of the misfit dislocations along the [210] orientation. A missing Co-O/Fe-O half-plane distorts the lattice at the misfit dislocation core, alleviating the mismatch strain as indicated by the solid boxes in Figure 35 and Figure 36. Due to the greater lattice mismatch for $CuFeO_2$, a higher density of misfit dislocations compared to $CuCrO_2$ can be identified, in accordance to the phase lock-in analysis and misfit dislocation density measurements. The missing half plane results in a pronounced, periodic distortion of the oxygen octahedra structure within the interface layer, as evident from the phase reconstructions along the $[0\bar{1}0]$ and [010] orientations. The oxygen-octahedra distortions, resembling a swapping between two opposing orientations around the misfit dislocation core, are limited to the very first $[CrO_2]^-$ and $[FeO_2]^-$ layer indicated by the black arrows in Figure 35, Figure 36, and Figure 37.

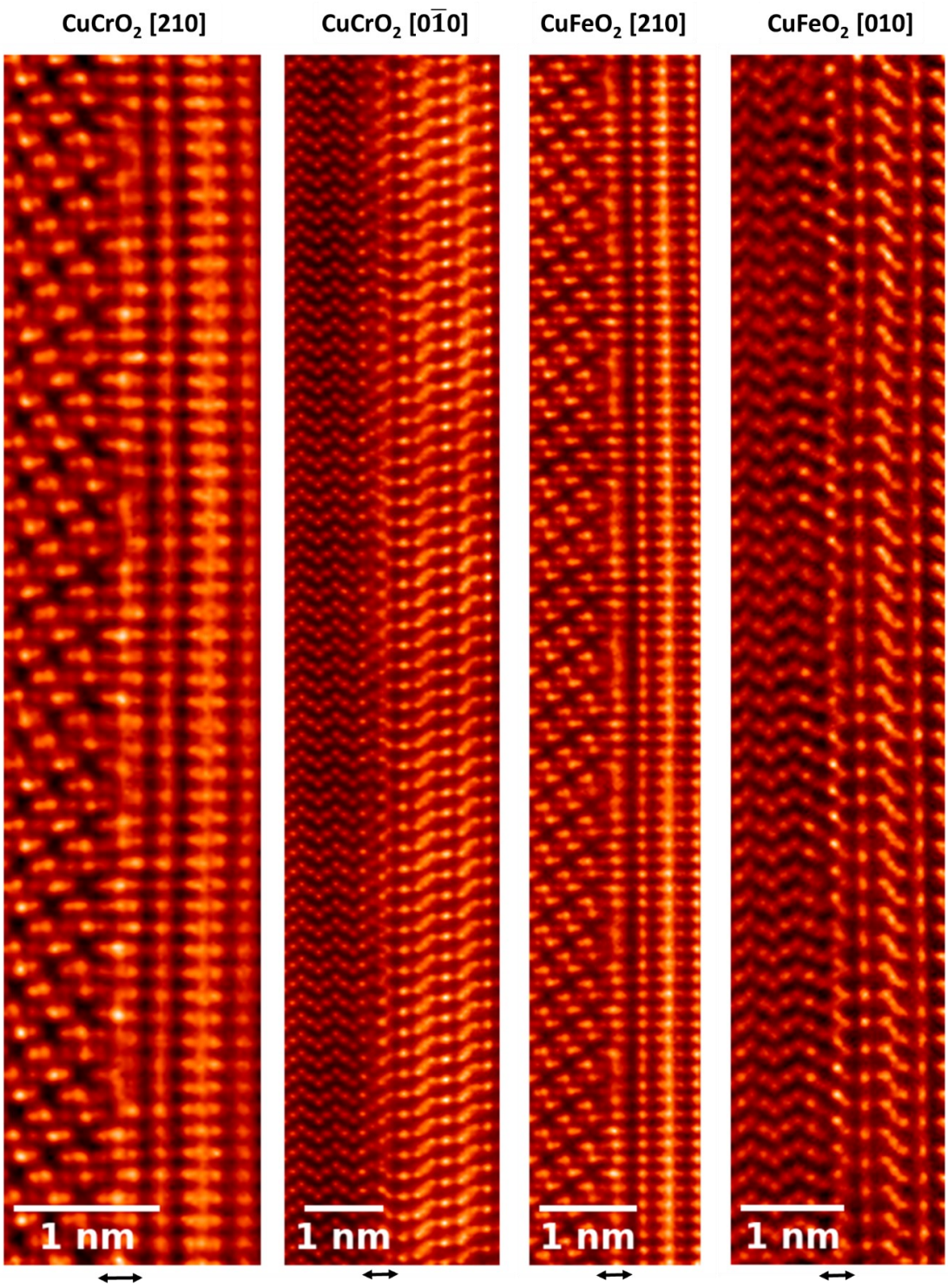

Figure 37. Full field of view images of the 4D STEM phase reconstructions along two different zone axes for $CuCrO_2$ and $CuFeO_2$ with the Al_2O_3 substrate on the left and the films on the right. The interfacial layer involving the atomic reconstruction at the interface is indicated by black arrows. Adopted under the terms of a CC-BY license. © 2025 The authors[277].

For the phase reconstructions in this chapter, thickness series simulations of PACBEDs were performed using the *ab*TEM algorithm, and the approximate thickness of the samples was determined through mean squared error (MSE) calculations between the simulated PACBEDs and

the real PACBED for each measurement[248]. The semi-convergence angle and probe parameters were chosen in accordance with the experimental data. A total of 10 frozen phonon configurations were used for each simulation and a PACBED thickness series was calculated using multi-slice simulations. Figure 38 shows the experimental PACBEDs from the phase reconstructions shown in Figure 37 and the corresponding PACBED simulation with the lowest MSE. The thickness estimations confirm that multi-slice algorithms provide more accurate phase reconstructions compared to single-slice reconstructions.

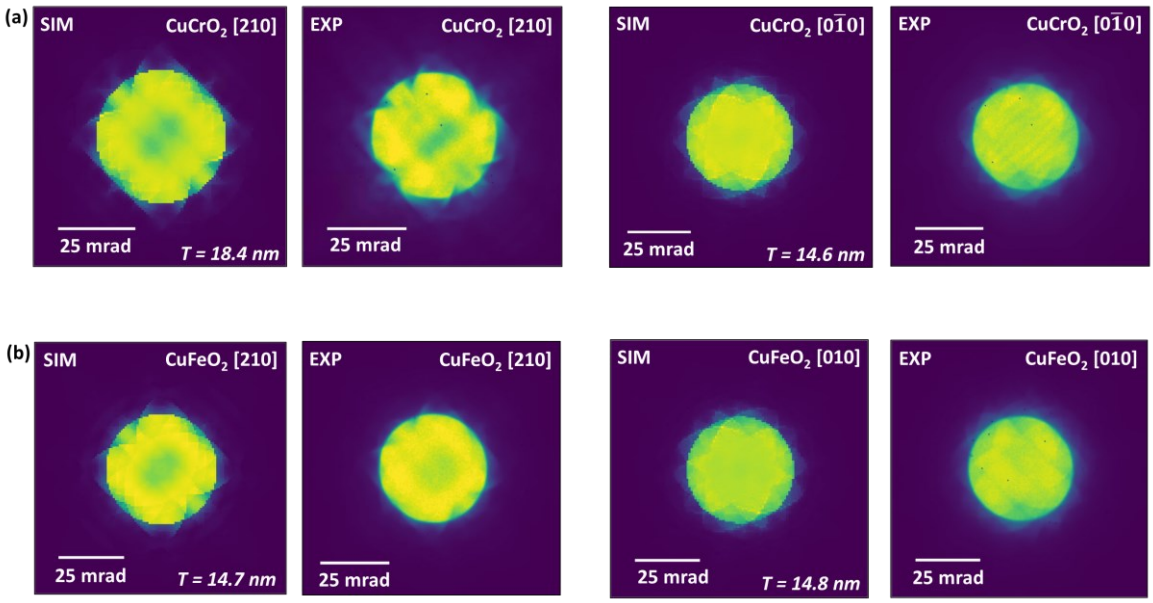

Figure 38. Simulated (SIM) and experimental (EXP) PACBEDs for the [210] and [010]/[0$\bar{1}$0] zone axes of (a) $CuCrO_2$ and (b) $CuFeO_2$. Adopted under the terms of a CC-BY license. © 2025 The authors[277].

4.3.4 Chemical analysis of the $CuFeO_2/Al_2O_3$ and the $CuFeO_2/Al_2O_3$ interfaces

To gain deeper insights into the chemical characteristics of the interface, EELS spectra imaging was performed along the same interface areas in [010]/[0$\bar{1}$0] orientations of $CuCrO_2$ and $CuFeO_2$ as the 4D STEM datasets. Prior research has indicated that accurate interpretation of EELS measurements at interfaces is achievable only when the sample is sufficiently thin, ideally thinner than ~20 nm[266,267]. Otherwise, complex propagation effects, including beam-broadening, cross-talk, and de-channeling, may lead to misinterpretations. Consequently, the measurements were conducted on the thinnest regions of the sample to facilitate atomic-scale quantification of the interface structure. The isolation of the signal from characteristic energy-loss edges allows a comprehensive analysis of the elemental distribution at the interface.

Figure 39 shows the extracted signal from the characteristic energy-loss edges of O (O K edge), Al (Al K edge), Cr (Cr $L_{3,2}$ edge), Fe (Fe $L_{3,2}$ edge), and Cu (Cu $L_{3,2}$) for the $CuCrO_2/Al_2O_3$ and $CuFeO_2/Al_2O_3$ interface. The white ticks indicate the physical boundary between substrate and film.

The EELS elemental maps for both films confirm that the films grow on the substrate with an initial layer of $[CrO_2]^-$ and $[FeO_2]^-$, respectively, followed by the first layer of Cu^+ ions. While the Cu signal is well defined for all layers in the films, a strong difference in the extracted Cr and Fe signals between the very first and subsequent $[CrO_2]^-$ and $[FeO_2]^-$ layers is observed. A substantially reduced Cr and Fe signal in the first layer of the films is visible, and a significant Cr and Fe signal on the substrate side of the physical boundary is present. This suggests the occurrence of chemical intermixing at the interface and the formation of an interfacial phase, similar to the observations of Ok *et al.*[245]. The EELS signal of the *B*-cations fully recovers starting from the second layer within the films. This indicates that the intermixing is limited to the first monolayer of the film and is in agreement with the observations from STEM imaging, which suggest a reconstruction at the interface restricted to the topmost layer only.

Besides the elemental maps, Figure 39 shows layer-resolved integrated EELS spectra of the *B*-cation $L_{3,2}$ edges and the O K edges across the interfaces. The atomic layer corresponding to each spectrum is denoted in the elemental maps of the *B*-cations. The extracted line spectra confirm that the *B*-cation signal extends up to two monolayers deep into the substrate and the consistent energy-loss value and $L_{3,2}$ edge ratio proves the preservation of a 3^+ oxidation state of Cr and Fe across the interface. This differs significantly from $PdCoO_2$ thin films, discussed in the previous chapter, where the Co signal intensity at the first layer of the film remains the same as in the subsequent layers[229,295]. Additionally, a distinct change in the Co $L_{3,2}$ edge ratios and energy loss was observed for the Co signal within the substrate, suggesting a change in the valence state from 3^+ to lower valences. Meanwhile, for the Cu-based delafossites, no Cu $L_{2,3}$ edge signal was detected on the substrate side, verifying that Al atoms were intermixed with the *B*-site atoms and not Cu atoms, comparable to the Pd signal in the $PdCoO_2$ delafossite films. The O K edge signal across the interface shows the characteristic features of bulk $CuCrO_2$, $CuFeO_2$, and Al_2O_3 at the monolayer forming the interface, similar to what was observed by Ok *et al.*[245]. The EELS analysis indicates the formation of an atomically thin monolayer of $CuCr_{1-X}Al_XO_2$ alloy at the interface.

Combining this result with the insights gained from the phase reconstructions and the strain analysis, the growing process of $CuCrO_2$ can be retraced as follows, with $CuFeO_2$ showing a similar behavior: At the initial nucleation stage, Cr atoms penetrate the subsurface layers of the Al_2O_3 substrate, while Al atoms diffuse away to the surface in exchange. These free Al atoms then stabilize the nucleation of $CuCrO_2$ delafossite thin films at the surface. Without these Al atoms, Cr_2O_3 would become the most stable phase during nucleation, hindering the formation of the delafossite phase[245]. The main mechanism for strain relief at this stage is the formation of misfit dislocations, which cause significant distortions of the oxygen octahedra in the initial layer of the film but do not affect the subsequent layers. Finally, the homogeneous and stable nucleation, facilitated by the delafossite

symmetry of $CuCr_{1-X}Al_XO_2$, promotes the high-quality growth of $CuCrO_2$ thin films. Here, a distinct stabilization mechanism compared to Pd-based delafossites is observed; nevertheless, stable growth is still achieved, suggesting that Cu-based delafossites are suitable as buffer layers on Al_2O_3 substrates.

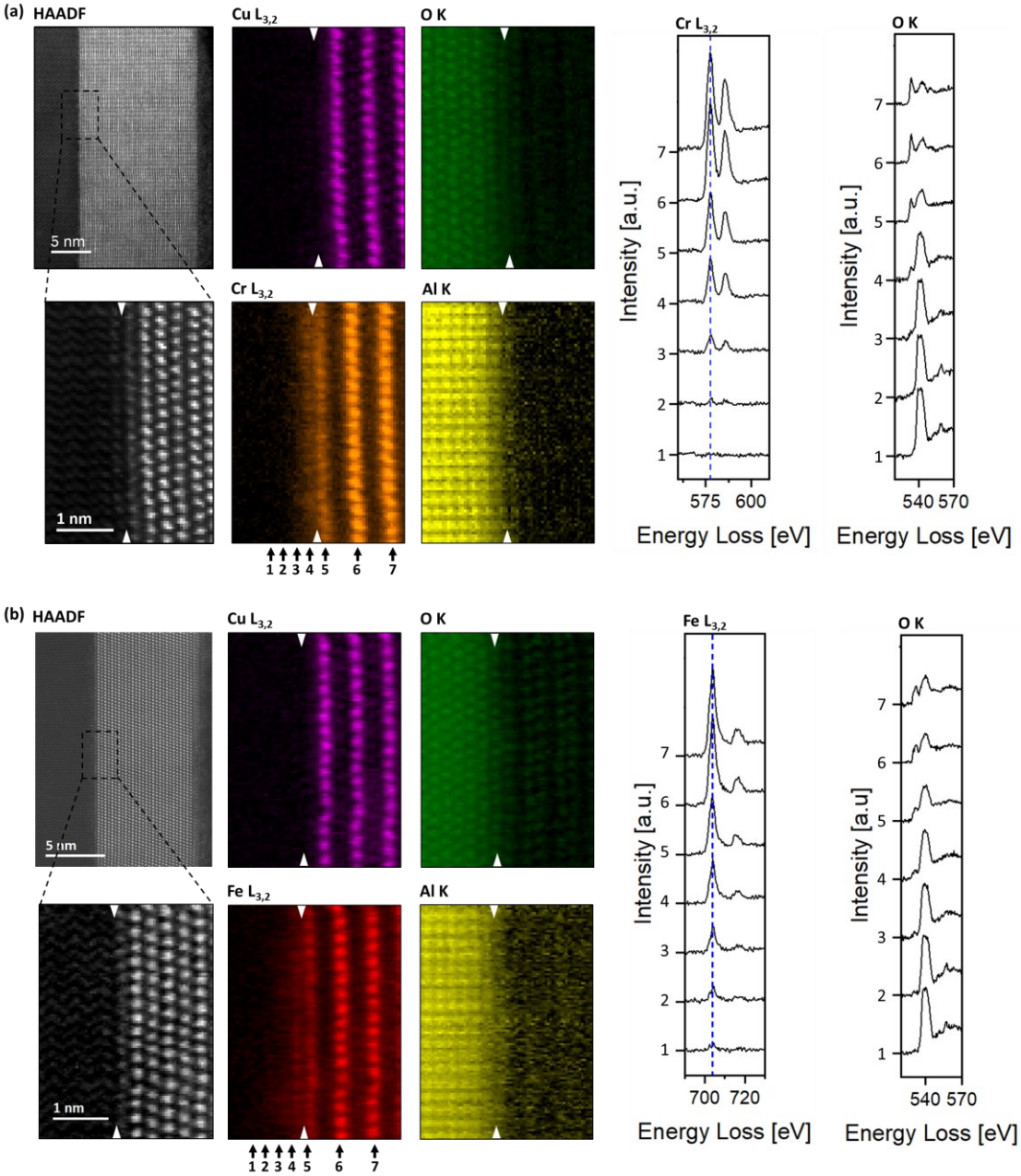

Figure 39. EELS elemental mapping and extracted edge spectra of (a) the $CuCrO_2/Al_2O_3$ and (b) the $CuFeO_2/Al_2O_3$ interfaces. A 2D spectrum image was acquired across the interfaces, as shown in the insets on the left. The elemental maps in (a) and (b) show extracted signals from the characteristic energy-loss edges of O (O K edge), Al (Al K edge), Cr (Cr $L_{3,2}$ edge), Fe (Fe $L_{3,2}$ edge), and Cu (Cu $L_{3,2}$). The white ticks indicate the physical interface between the substrate and film. For $CuCrO_2$ (a) and $CuFeO_2$ (b), the $L_{3,2}$ edge signals and the O K edges are shown on the right. Each numbered signal was extracted along the numbered arrows shown in the Cr/Fe elemental maps on the left. Adopted under the terms of a CC-BY license. © 2025 The authors[277].

4.4 Conclusions

In this chapter, the atomic reconstruction at the interface between thin films of $CuCrO_2$/$CuFeO_2$ delafossites and Al_2O_3 substrates was investigated by utilizing advanced STEM methods. The observations shed light on the mechanism behind the unusually stable growth of these two delafossites on the Al_2O_3 substrate using MBE, despite their significant lattice mismatches. Strain analysis at the interface based on the phase lock-in method reveals the presence of a misfit-dislocation network that relieves the mismatch strain between the substrate and films. Iterative phase reconstructions uncover the atomic structure of the misfit dislocations and the resulting lattice distortions at the interface. EELS elemental mapping and spectral analysis reveal additional chemical intermixing at the interface, which stabilizes the films on the substrate during the initial steps of nucleation. With all these findings combined, the initial growth process of the Cu-based delafossites can be retraced and it is possible to explain how the lattice mismatches are compensated. While these mechanisms differ significantly from the observations for Pd-based delafossites, $CuCrO_2$ and $CuFeO_2$ grow stably on Al_2O_3 as well, demonstrating their suitability as buffer layers for other delafossites that otherwise would not.

5 Summary

This thesis highlighted the potential of S(TEM) to explore the structural and interfacial characteristics of 3*d* and 4*d* transition metal oxides and thin films at the atomic scale. While the first part focuses on applying (S)TEM to the investigation of unusual physical phenomena, in particular the first order metal-to-metal phase transition in mixed-valence $NaRu_2O_4$ crystals at elevated temperatures, in the second and third part, STEM is employed to examine different stabilization mechanisms of delafossite thin films on various substrates, providing an explanation for their surprisingly stable growth.

In the first part of the thesis, an unconventional structural transition in the mixed-valence 4*d* transition metal oxide $NaRu_2O_4$ was observed. Tracking the transition from the high-temperature *Pnma* to the low-temperature $P112_1/a$ structure using a combination of direct imaging and diffraction techniques, allowed to image the dimerization in the quasi-one-dimensional Ru-chains along the crystallographic *b*-axis of the crystals. Interestingly, the material stays metallic over the whole temperature range, contradicting the commonly observed metal-insulator transitions in mixed-valence 3*d* transition metal oxides. The clear structural signatures, accessible transition temperature, and reversible nature of the phase change make $NaRu_2O_4$ well suited for comparative studies.

Looking ahead, several paths emerge that could further advance the understanding of the structural transition in $NaRu_2O_4$ and place it in the broader framework of correlated transition metal oxides. The rare coexistence of metallic conductivity, charge ordering, and lattice dimerization in a single material suggests that $NaRu_2O_4$ may represent a model system for exploring coupled electronic and structural instabilities in mixed-valence ruthenates. In particular, advanced theoretical calculations could provide insights into the remaining question of how metallic conductivity can coexist with charge ordering and dimerization in the 4*d* transition metal ruthenate. By comparing dimerized and non-dimerized configurations, such calculations can help determine the energetically favored phases and clarify how charge distribution and band structure evolve across the transition. Future research could also focus on related systems, such as $Na_{2.7}Ru_4O_9$, which exhibits an unconventional CO at room temperature while retaining metallicity with two successive phase transitions and emergent superlattice reflections[140]. Further studies may therefore benefit from extending the atomic-scale investigation to these structurally and electronically related systems. Furthermore, systematic chemical substitution at the Na or Ru sites may offer a route to tune the structural and electronic instabilities and map out phase boundaries. In addition, future advances in phase reconstruction techniques and depth-sensitive imaging methods may eventually enable direct insight into the role of Na and O in the phase transition and associated dimerization in $NaRu_2O_4$.

The second and third part of the thesis examined the stabilization mechanisms governing the epitaxial growth of delafossite thin films. Despite their unique lattice geometries and significant mismatch with common substrates, $PdCoO_2$, $CuCrO_2$, and $CuFeO_2$ exhibit distinct interfacial stabilization mechanisms. For $PdCoO_2$ thin films grown *via* MBE on Al_2O_3 and $LaAlO_3$, the combination of 4D STEM electron ptychography, EELS investigations, and conventional imaging allows to reveal the formation of a CoO secondary interfacial phase, which facilitates epitaxy by modulating the substrate structure. Interestingly, this stabilization mechanism differs from the common picture of a misfit-dislocation network stabilizing semi-coherent thin-film interfaces. The importance of the secondary phase is further underscored by the instability of $PdCoO_2$ when film nucleation is attempted with a Pd^+ layer. It turns out that for Cu-based delafossites ($CuCrO_2$ and $CuFeO_2$) on Al_2O_3, the stabilization mechanism differs significantly. Phase lock-in strain analysis performed on STEM images, together with iterative phase reconstructions uncover a misfit dislocation network at the interface, which relieves mismatch strain and enables stable film growth. STEM-EELS elemental mapping confirms monolayer-deep chemical intermixing besides the reconstruction, which plays a crucial role in early-stage nucleation.

These findings paint a comprehensive picture of how interfacial atomic reconstructions and strain relaxation strategies influence delafossite thin films. The observed differences in the stabilization mechanisms of various delafossites on the same substrate naturally raise the question of how other delafossites, with different *A* and *B* cations, behave at the interface. Investigating these systems in the future could provide further insights into the fundamental mechanisms governing their epitaxial growth. In addition, the potential role of the interfacial reconstruction in modulating or compensating for the polar surface charge—arising from the alternating charged layers along the *c*-axis in delafossite structures—deserves further investigation. The possibility that such reconstructions help neutralize built-in electrostatic potentials opens up new questions about the coupling between interface and surface phenomena. Combining atomic-resolution interface analysis with surface-sensitive techniques like ARPES will be essential to explore this interplay. Moreover, based on the successfully stabilized thin films, growth parameters can now be optimized to achieve defect-free buffer layers and phase-pure thin films. This is particularly relevant for delafossites that do not grow directly on certain substrates, as the findings demonstrate that a stable buffer layer can facilitate the integration of otherwise incompatible delafossite thin films. Finally, future studies should examine to what extent the stabilization pathways influence functional properties of the heterostructures, such as conductivity and carrier mobility, and how they can be tuned through growth parameters or substrate selection to enable the reliable integration of delafossites into oxide-based electronic devices. Continued advancements in thin-film deposition techniques and the results of this work contribute to the growing understanding of how delafossite thin films can be reliably synthesized and integrated into functional heterostructures.

Ultimately, the continuous improvement of STEM techniques holds great promise for advancing the understanding of structural phenomena in complex materials. While hardware improvements continuously enhance both STEM data acquisition and processing—particularly when it comes to large 4D STEM datasets—the increasing versatility and the possibility for combining different techniques open new avenues for structural characterization. Innovative approaches, born from these novel possibilities, such as the integration of joint ptychography and tomography, bring us closer to achieving a full 3D atomic-scale characterization of materials with transmission electron microscopy[107]. Their realization represents a significant step forward in the endeavor to comprehend interfacial phenomena, where precise structural insights at the atomic level are crucial for understanding and optimizing functional materials properties.

6 References

1 Knoll, M. & Ruska, E. Das Elektronenmikroskop. *Zeitschrift für Physik* **78**, 318-339 (1932). 10.1007/bf01342199

2 Urban, K. W., Barthel, J., Houben, L., Jia, C.-L., Jin, L., Lentzen, M., Mi, S.-B., Thust, A. & Tillmann, K. Progress in atomic-resolution aberration corrected conventional transmission electron microscopy (CTEM). *Progress in Materials Science* **133**, 101037 (2023). 10.1016/j.pmatsci.2022.101037

3 Ruska, E. The development of the electron microscope and of electron microscopy (Nobel lecture). *Angewandte Chemie, International Edition in English* **26**, 595–605 (1987). 10.1002/anie.198705953

4 Li, J., Johnson, G., Zhang, S. & Su, D. In situ transmission electron microscopy for energy applications. *Joule* **3**, 4-8 (2019). 10.1016/j.joule.2018.12.007

5 Mast, J., Verleysen, E., Hodoroaba, V. D. & Kaegi, R. Characterization of nanomaterials by transmission electron microscopy: Measurement procedures. In *Micro Nano Technol*, 29-48 (2020). 10.1016/B978-0-12-814182-3.00004-3

6 Franken, L. E., Grünewald, K., Boekema, E. J. & Stuart, M. C. A. A technical introduction to transmission electron microscopy for soft-matter: Imaging, possibilities, choices, and technical developments. *Small* **16**, e1906198 (2020). 10.1002/smll.201906198

7 Rayleigh. Investigations in optics, with special reference to the spectroscope. *The London, Edinburgh, and Dublin Philosophical Magazine and Journal of Science* **8**, 261-274 (1879). 10.1080/14786447908639684

8 Hetherington, C. Aberration correction for TEM. *Materials Today* **7**, 50-55 (2004). 10.1016/s1369-7021(04)00571-1

9 Tsuno, K. Resolution limit of a transmission electron microscope with an uncorrected conventional magnetic objective lens. *Ultramicroscopy* **50**, 245–253 (1993). 10.1016/0304-3991(93)90193-2

10 Reimer, L. & Kohl, H. Transmission electron microscopy: Physics of image formation. 5th Edition. *Springer* (2008).

11 Orloff, J. Survey of electron sources for high-resolution microscopy. *Ultramicroscopy* **28**, 88–97 (1989). 10.1016/0304-3991(89)90278-7

12 Postek, M. T. & Joy, D. C. Submicrometer microelectronics dimensional metrology: scanning electron microscopy. *Journal of Research of the National Bureau of Standards* **92**, 205-228 (1987). 10.6028/jres.092.018

13 Fowler, R. H. & Nordheim, L. Electron emission in intense electric fields. *Proceedings of the Royal Society of London. Series A. Mathematical and Physical Sciences* **119**, 173–181 (1928). 10.1098/rspa.1928.0091

14 Crewe, A. V., Wall, J. & Welter, L. M. A high-resolution scanning transmission electron microscope. *Journal of Applied Physics* **39**, 5861–5868 (1968). 10.1063/1.1656079

15 Williams, D. B. & Carter, C. B. Transmission electron microscopy: A textbook for materials science. *Springer US* (2009). 10.1007/978-0-387-76501-3

16 Lorentz, H. A. Versuch einer Theorie der electrischen und optischen Erscheinungen in bewegten Körpern. *E. J. Brill* (1895).

17 Egerton, R. F. Physical principles of electron microscopy. *Springer International Publishing* (2016). 10.1007/978-3-319-39877-8

18 Scherzer, O. Über einige Fehler von Elektronenlinsen. *Zeitschrift für Physik* **101**, 593–603 (1936). 10.1007/bf01349606

19 Rose, H. Historical aspects of aberration correction. *Journal of Electron Microscopy* **58**, 77–85 (2009). 10.1093/jmicro/dfp012

20 Bleloch, A. & Lupini, A. Imaging at the picoscale. *Materials Today* **7**, 42–48 (2004). 10.1016/s1369-7021(04)00570-x

21 Nellist, P. D. Scanning transmission electron microscopy. In *Science of microscopy* (eds. Peter W. Hawkes & John C. H. Spence), *Springer New York*, 65–132 (2007). 10.1007/978-0-387-49762-4_2

22 Rodenburg, J. M. & Bates, R. H. T. The theory of super-resolution electron microscopy via Wigner-distribution deconvolution. *Philosophical Transactions of the Royal Society of London. Series A: Physical and Engineering Sciences* **339**, 521–553 (1992). 10.1098/rsta.1992.0050

23 Scherzer, O. The theoretical resolution limit of the electron microscope. *Journal of Applied Physics* **20**, 20–29 (1949). 10.1063/1.1698233

24 Scherzer, O. Sphärische und chromatische Korrektur von Elektronen-Linsen. *Optik* **2**, 114-132 (1947).

25 Rose, H. Correction of aberrations, a promising means for improving the spatial and energy resolution of energy-filtering electron microscopes. *Ultramicroscopy* **56**, 11–25 (1994). 10.1016/0304-3991(94)90142-2

26 Krivanek, O. L., Nellist, P. D., Dellby, N., Murfitt, M. F. & Szilagyi, Z. Towards sub-0.5 A electron beams. *Ultramicroscopy* **96**, 229–237 (2003). 10.1016/s0304-3991(03)00090-1

27 Urban, K., Kabius, B., Haider, M. & Rose, H. A way to higher resolution: spherical-aberration correction in a 200 kV transmission electron microscope. *Journal of Electron Microscopy* **48**, 821–826 (1999). 10.1093/oxfordjournals.jmicro.a023753

28 Erni, R., Rossell, M. D., Kisielowski, C. & Dahmen, U. Atomic-resolution imaging with a sub-50-pm electron probe. *Physical Review Letters* **102**, 096101 (2009). 10.1103/PhysRevLett.102.096101

29 Kisielowski, C., Freitag, B., Bischoff, M., van Lin, H., Lazar, S., Knippels, G., Tiemeijer, P., van der Stam, M., Harrach, S. v., Stekelenburg, M., Haider, M., Uhlemann, S., Müller, H., Hartel, P., Kabius, B., Miller, D., Petrov, I., Olson, E. A., Donchev, T., Kenik, E. A., Lupini, A. R., Bentley, J., Pennycook, S. J., Anderson, I. M., Minor, A. M., Schmid, A. K., Duden, T., Radmilovic, V., Ramasse, Q. M., Watanabe, M., Erni, R., Stach, E. A., Denes, P. & Dahmen, U. Detection of single atoms and buried defects in three dimensions by aberration-corrected electron microscope with 0.5-A information limit. *Microscopy and Microanalysis: the Official Journal of Microscopy Society of America, Microbeam Analysis Society, Microscopical Society of Canada* **14**, 469–477 (2008). 10.1017/s1431927608080902

30 Hosokawa, F., Sawada, H., Kondo, Y., Takayanagi, K. & Suenaga, K. Development of Cs and Cc correctors for transmission electron microscopy. *Microscopy* **62**, 23–41 (2013). 10.1093/jmicro/dfs134

31 Linck, M., Hartel, P., Uhlemann, S., Kahl, F., Müller, H., Zach, J., Haider, M., Niestadt, M., Bischoff, M., Biskupek, J., Lee, Z., Lehnert, T., Börrnert, F., Rose, H. & Kaiser, U. Chromatic aberration correction for atomic resolution TEM imaging from 20 to 80 kV. *Physical Review Letters* **117**, 076101 (2016). 10.1103/PhysRevLett.117.076101-

32 Fultz, B. & Howe, J. M. Diffraction contrast in TEM images. In *Transmission electron microscopy and diffractometry of materials* (eds. Brent Fultz & James M. Howe), *Springer Berlin Heidelberg*, 339–422 (2001). 10.1007/978-3-662-04516-9_7

33 Bendersky, L. A. & Gayle, F. W. Electron diffraction using transmission electron microscopy. *Journal of Research of the National Institute of Standards and Technology* **106**, 997–1012 (2001). 10.6028/jres.106.051

34 de Graef, M. Introduction to conventional transmission electron microscopy. *Cambridge University Press* (2003). 10.1017/cbo9780511615092

35 Tanaka, M. Convergent-beam electron diffraction. In *Electron crystallography* (eds. Douglas L. Dorset, Sven Hovmöller, & Xiaodong Zou), *Springer Netherlands*, 77–113 (1997). 10.1007/978-94-015-8971-0_7

36 Goodhew, P. General introduction to transmission electron microscopy (TEM). In *Aberration-corrected analytical transmission electron microscopy* (ed. Rik Brydson), *Wiley*, 1–19 (2011). 10.1002/9781119978848.ch1

37 Nellist, P. D. The principles of STEM imaging. In *Scanning transmission electron microscopy* (eds. Stephen J. Pennycook & Peter D. Nellist), *Springer New York*, 91–115 (2011). 10.1007/978-1-4419-7200-2_2

38 Ophus, C. Four-dimensional scanning transmission electron microscopy (4D-STEM): From scanning nanodiffraction to ptychography and beyond. *Microscopy and Microanalysis: The Official Journal of Microscopy Society of America, Microbeam Analysis Society, Microscopical Society of Canada* **25**, 563–582 (2019). 10.1017/s1431927619000497

39 Egerton, R. F. Electron energy-loss spectroscopy in the electron microscope. *Springer US* (2011). 10.1007/978-1-4419-9583-4

40 Kohl, H. & Rose, H. Theory of image formation by inelastically scattered electrons in the electron microscope. In *Advances in electronics and electron physics Volume 65*, *Elsevier*, 173–227 (1985). 10.1016/s0065-2539(08)60878-1

41 Verbeeck, J., van Dyck, D. & van Tendeloo, G. Energy-filtered transmission electron microscopy: an overview. *Spectrochimica Acta Part B: Atomic Spectroscopy* **59**, 1529–1534 (2004). 10.1016/j.sab.2004.03.020

42 Egerton, R. F. Electron energy-loss spectroscopy in the TEM. *Reports on Progress in Physics* **72**, 016502 (2009). 10.1088/0034-4885/72/1/016502

43 Browning, N. D. & Pennycook, S. J. Atomic-resolution electron energy-loss spectroscopy in the scanning transmission electron microscope. *Journal of Microscopy* **180**, 230–237 (1995). 10.1111/j.1365-2818.1995.tb03682.x

44 Klie, R. F., Arslan, I. & Browning, N. D. Atomic resolution electron energy-loss spectroscopy. *Journal of Electron Spectroscopy and Related Phenomena* **143**, 105–115 (2005). 10.1016/j.elspec.2004.05.009

45 Muller, D. A., Tzou, Y., Raj, R. & Silcox, J. Mapping sp^2 and sp^3 states of carbon at sub-nanometre spatial resolution. *Nature* **366**, 725–727 (1993). 10.1038/366725a0

46 Pearson, D. H., Fultz, B. & Ahn, C. C. Measurements of 3d state occupancy in transition metals using electron energy loss spectrometry. *Applied Physics Letters* **53**, 1405–1407 (1988). 10.1063/1.100457

47 Pearson, D. H., Ahn, C. C. & Fultz, B. White lines and d-electron occupancies for the 3d and 4d transition metals. *Physical Review. B, Condensed Matter* **47**, 8471–8478 (1993). 10.1103/PhysRevB.47.8471

48 Frati, F., Hunault, M. O. J. Y. & Groot, F. M. F. d. Oxygen K-edge X-ray absorption spectra. *Chemical Reviews* **120**, 4056–4110 (2020). 10.1021/acs.chemrev.9b00439

49 van Aken, P. A. & Liebscher, B. Quantification of ferrous/ferric ratios in minerals: new evaluation schemes of Fe L23 electron energy-loss near-edge spectra. *Physics and Chemistry of Minerals* **29**, 188–200 (2002). 10.1007/s00269-001-0222-6

50 Shindo, D. & Oikawa, T. Energy dispersive X-ray spectroscopy. In *Analytical electron microscopy for materials science* (eds. Daisuke Shindo & Tetsuo Oikawa), *Springer Japan*, 81–102 (2002). 10.1007/978-4-431-66988-3_4

51 Hofmann, S. Quantitative analysis (data evaluation). In *Auger- and X-Ray photoelectron spectroscopy in materials science* (ed. Siegfried Hofmann), *Springer Berlin Heidelberg*, 77–204 (2013). 10.1007/978-3-642-27381-0_4

52 Müllejans, H. & Bruley, J. Electron energy-loss spectroscopy (EELS): Comparison with X-ray analysis. *Le Journal de Physique IV* **03**, 2083-2092 (1993). 10.1051/jp4:19937332

53 Chattarji, R. F. The theory of Auger transitions. *Academic Press, London* (1976).

54 Fan, G. Y. & Ellisman, M. H. High-sensitivity lens-coupled slow-scan CCD camera for transmission electron microscopy. *Ultramicroscopy* **52**, 21–29 (1993). 10.1016/0304-3991(93)90019-t

55 Ruijter, W. J. d. Imaging properties and applications of slow-scan charge-coupled device cameras suitable for electron microscopy. *Micron* **26**, 247–275 (1995). 10.1016/0968-4328(95)00054-8

56 Okunishi, E., Ishikawa, I., Sawada, H., Hosokawa, F., Hori, M. & Kondo, Y. Visualization of light elements at ultrahigh resolution by STEM annular bright field microscopy. *Microscopy and Microanalysis: The Official Journal of Microscopy Society of America, Microbeam Analysis Society, Microscopical Society of Canada* **15**, 164–165 (2009). 10.1017/s1431927609093891

57 Okunishi, E., Sawada, H. & Kondo, Y. Experimental study of annular bright field (ABF) imaging using aberration-corrected scanning transmission electron microscopy (STEM). *Micron* **43**, 538–544 (2012). 10.1016/j.micron.2011.10.007

58 Haider, M., Epstein, A., Jarron, P. & Boulin, C. A versatile, software configurable multichannel STEM detector for angle-resolved imaging. *Ultramicroscopy* **54**, 41–59 (1994). 10.1016/0304-3991(94)90091-4

59 Shibata, N., Findlay, S. D., Kohno, Y., Sawada, H., Kondo, Y. & Ikuhara, Y. Differential phase-contrast microscopy at atomic resolution. *Nature Physics* **8**, 611–615 (2012). 10.1038/nphys2337

60 Wu, M., Stroppa, D. G., Pelz, P. & Spiecker, E. Using a fast hybrid pixel detector for dose-efficient diffraction imaging beam-sensitive organic molecular thin films. *Journal of Physics: Materials* **6**, 045008 (2023). 10.1088/2515-7639/acf524

61 Ryll, H., Simson, M., Hartmann, R., Holl, P., Huth, M., Ihle, S., Kondo, Y., Kotula, P., Liebel, A., Müller-Caspary, K., Rosenauer, A., Sagawa, R., Schmidt, J., Soltau, H. & Strüder, L. A pnCCD-based, fast direct single electron imaging camera for TEM and STEM. *Journal of Instrumentation* **11**, P04006 (2016). 10.1088/1748-0221/11/04/p04006

62 Tate, M. W., Purohit, P., Chamberlain, D., Nguyen, K. X., Hovden, R., Chang, C. S., Deb, P., Turgut, E., Heron, J. T., Schlom, D. G., Ralph, D. C., Fuchs, G. D., Shanks, K. S., Philipp, H. T., Muller, D. A. & Gruner, S. M. High dynamic range pixel array detector for scanning transmission electron microscopy. *Microscopy and Microanalysis: The Official Journal of Microscopy Society of America, Microbeam Analysis Society, Microscopical Society of Canada* **22**, 237–249 (2016). 10.1017/s1431927615015664

63 Ballabriga, R., Alozy, J., Blaj, G., Campbell, M., Fiederle, M., Frojdh, E., Heijne, E. H. M., Llopart, X., Pichotka, M., Procz, S., Tlustos, L. & Wong, W. The Medipix3RX: A high resolution, zero dead-time pixel detector readout chip allowing spectroscopic imaging. *Journal of Instrumentation* **8**, C02016-C02016 (2013). 10.1088/1748-0221/8/02/c02016

64 Ansari, R., Beuville, E., Borer, K., Cenci, P., Clark, A. G., Federspiel, A., Gildemeister, O., Gössling, C., Hara, K., Heijne, E. H. M., Jarron, P., Lariccia, P., Lisowski, B., Munday, D. J., Pal, T., Parker, M. A., Redaelli, N., Scampoli, P., Simak, V., Singh, S. L., Vallon-Hulth, T. & Wells, P. S. The silicon detectors in the UA2 experiment. *Nuclear Instruments and Methods in Physics Research Section A: Accelerators, Spectrometers, Detectors and Associated Equipment* **279**, 388–395 (1989). 10.1016/0168-9002(89)91111-x

65 Ercan, A., Tate, M. W. & Gruner, S. M. Analog pixel array detectors. *Journal of Synchrotron Radiation* **13**, 110–119 (2006). 10.1107/s0909049505028529

66 Caswell, T. A., Ercius, P., Tate, M. W., Ercan, A., Gruner, S. M. & Muller, D. A. A high-speed area detector for novel imaging techniques in a scanning transmission electron microscope. *Ultramicroscopy* **109**, 304–311 (2009). 10.1016/j.ultramic.2008.11.023

67 Clabbers, M. T. B., Martynowycz, M. W., Hattne, J., Nannenga, B. L. & Gonen, T. Electron-counting MicroED data with the K2 and K3 direct electron detectors. *Journal of Structural Biology* **214**, 107886 (2022). 10.1016/j.jsb.2022.107886

68 McMullan, G., Turchetta, R. & Faruqi, A. R. Single event imaging for electron microscopy using MAPS detectors. *Journal of Instrumentation* **6**, C04001 (2011). 10.1088/1748-0221/6/04/c04001

69 Varnavides, G., Ribet, S. M., Zeltmann, S. E., Yu, Y., Savitzky, B. H., Byrne, D. O., Allen, F. I., Dravid, V. P., Scott, M. C. & Ophus, C. Iterative phase retrieval algorithms for scanning transmission electron microscopy, 25 (2023). arXiv:2309.05250

70 Savitzky, B. H., Zeltmann, S. E., Hughes, L. A., Brown, H. G., Zhao, S., Pelz, P. M., Pekin, T. C., Barnard, E. S., Donohue, J., Rangel DaCosta, L., Kennedy, E., Xie, Y., Janish, M. T., Schneider, M. M., Herring, P., Gopal, C., Anapolsky, A., Dhall, R., Bustillo, K. C., Ercius, P., Scott, M. C., Ciston, J., Minor, A. M. & Ophus, C. py4DSTEM: A software package for four-dimensional scanning transmission electron microscopy data analysis. *Microscopy and Microanalysis: The Official Journal of Microscopy Society of America, Microbeam Analysis Society, Microscopical Society of Canada* **27**, 712–743 (2021). 10.1017/s1431927621000477

71 Bethe, H. Theorie der Beugung von Elektronen an Kristallen. *Annalen der Physik* **392**, 55–129 (1928). 10.1002/andp.19283921704

72 Tanaka, N. Cowley's theory for TEM and STEM imaging. In *Electron nano-imaging* (ed. Nobuo Tanaka), *Springer Japan*, 267–271 (2024). 10.1007/978-4-431-56940-4_19

73 Krivanek, O. L., Dellby, N. & Lupini, A. R. Towards sub-Å electron beams. *Ultramicroscopy* **78**, 1–11 (1999). 10.1016/s0304-3991(99)00013-3

74 Rodenburg, J. M. Ptychography and related diffractive imaging methods. In *Advances in imaging and electron physics* (ed. Hawkes), *Elsevier*, 87–184 (2008). 10.1016/s1076-5670(07)00003-1

75 Kirkland, A. I. & Meyer, R. R. "Indirect" high-resolution transmission electron microscopy: aberration measurement and wavefunction reconstruction. *Microscopy and Microanalysis: The Official Journal of Microscopy Society of America, Microbeam Analysis Society, Microscopical Society of Canada* **10**, 401–413 (2004). 10.1017/s1431927604040437

76 Kirkland, E. J. Advanced computing in electron microscopy. *Springer US* (2010). 10.1007/978-1-4419-6533-2

77 Hoppe, W. Beugung im inhomogenen Primärstrahlwellenfeld. I. Prinzip einer Phasenmessung von Elektronenbeungungsinterferenzen. *Acta Crystallographica Section A* **25**, 495–501 (1969). 10.1107/s0567739469001045

78 Boehme, T. K. & Bracewell, R. The Fourier transform and its applications. *The American Mathematical Monthly* **73**, 685 (1966). 10.2307/2314845

79 Rodenburg, J. M., McCallum, B. C. & Nellist, P. D. Experimental tests on double-resolution coherent imaging via STEM. *Ultramicroscopy* **48**, 304–314 (1993). 10.1016/0304-3991(93)90105-7

80 Robert, H. L. L., Leidl, M. L., Müller-Caspary, K. & Verbeeck, J. Benchmarking analytical electron ptychography methods for the low-dose imaging of beam-sensitive materials (2025). 10.48550/arXiv.2501.08874

81 Nellist, P. D. & Rodenburg, J. M. Electron ptychography. I. experimental demonstration beyond the conventional resolution limits. *Acta Crystallographica Section A Foundations of Crystallography* **54**, 49–60 (1998). 10.1107/s0108767397010490

82 Yang, H., MacLaren, I., Jones, L., Martinez, G. T., Simson, M., Huth, M., Ryll, H., Soltau, H., Sagawa, R., Kondo, Y., Ophus, C., Ercius, P., Jin, L., Kovács, A. & Nellist, P. D. Electron ptychographic phase imaging of light elements in crystalline materials using Wigner distribution deconvolution. *Ultramicroscopy* **180**, 173–179 (2017). 10.1016/j.ultramic.2017.02.006

83 Yang, H., Pennycook, T. J. & Nellist, P. D. Efficient phase contrast imaging in STEM using a pixelated detector. Part II: optimisation of imaging conditions. *Ultramicroscopy* **151**, 232–239 (2015). 10.1016/j.ultramic.2014.10.013

84 Pennycook, T. J., Lupini, A. R., Yang, H., Murfitt, M. F., Jones, L. & Nellist, P. D. Efficient phase contrast imaging in STEM using a pixelated detector. Part 1: experimental demonstration at atomic resolution. *Ultramicroscopy* **151**, 160–167 (2015). 10.1016/j.ultramic.2014.09.013

85 O'Leary, C. M., Martinez, G. T., Liberti, E., Humphry, M. J., Kirkland, A. I. & Nellist, P. D. Contrast transfer and noise considerations in focused-probe electron ptychography. *Ultramicroscopy* **221**, 113189 (2021). 10.1016/j.ultramic.2020.113189

86 Yang, C., Qian, J., Schirotzek, A., Maia, F. & Marchesini, S. Iterative algorithms for ptychographic phase retrieval (2011). 10.48550/arXiv.1105.5628

87 Yan, H. Ptychographic phase retrieval by proximal algorithms. *New Journal of Physics* **22**, 023035 (2020). 10.1088/1367-2630/ab704e

88 Guizar-Sicairos, M. & Fienup, J. R. Phase retrieval with transverse translation diversity: a nonlinear optimization approach. *Optics Express* **16**, 7264–7278 (2008). 10.1364/oe.16.007264

89 Godard, P., Allain, M., Chamard, V. & Rodenburg, J. Noise models for low counting rate coherent diffraction imaging. *Optics express* **20**, 25914–25934 (2012). 10.1364/oe.20.025914

90 Bian, L., Suo, J., Chung, J., Ou, X., Yang, C., Chen, F. & Dai, Q. Fourier ptychographic reconstruction using Poisson maximum likelihood and truncated Wirtinger gradient. *Scientific Reports* **6**, 27384 (2016). 10.1038/srep27384

91 Odstrčil, M., Menzel, A. & Guizar-Sicairos, M. Iterative least-squares solver for generalized maximum-likelihood ptychography. *Optics Express* **26**, 3108–3123 (2018). 10.1364/oe.26.003108

92 Fienup, J. R. Phase retrieval algorithms: a comparison. *Applied Optics* **21**, 2758–2769 (1982). 10.1364/ao.21.002758

93 Rodenburg, J. M. & Faulkner, H. M. L. A phase retrieval algorithm for shifting illumination. *Applied Physics Letters* **85**, 4795–4797 (2004). 10.1063/1.1823034

94 Thibault, P. & Menzel, A. Reconstructing state mixtures from diffraction measurements. *Nature* **494**, 68–71 (2013). 10.1038/nature11806

95 Maiden, A., Johnson, D. & Li, P. Further improvements to the ptychographical iterative engine. *Optica* **4**, 736-742 (2017). 10.1364/optica.4.000736

96 Maiden, A. M. & Rodenburg, J. M. An improved ptychographical phase retrieval algorithm for diffractive imaging. *Ultramicroscopy* **109**, 1256–1262 (2009). 10.1016/j.ultramic.2009.05.012

97 Ruder, S. An overview of gradient descent optimization algorithms (2016). arXiv:1609.04747

98 Melnyk, O. Convergence properties of gradient methods for blind ptychography, 39 (2023). arXiv.2306.08750

99 Konijnenberg, A. P., Coene, W. M. J. & Urbach, H. P. Model-independent noise-robust extension of ptychography. *Optics Express* **26**, 5857–5874 (2018). 10.1364/oe.26.005857

100 Thibault, P. & Guizar-Sicairos, M. Maximum-likelihood refinement for coherent diffractive imaging. *New Journal of Physics* **14**, 063004 (2012). 10.1088/1367-2630/14/6/063004

101 Yeh, L.-H., Dong, J., Zhong, J., Tian, L., Chen, M., Tang, G., Soltanolkotabi, M. & Waller, L. Experimental robustness of Fourier ptychography phase retrieval algorithms. *Optics Express* **23**, 33214–33240 (2015). 10.1364/oe.23.033214

102 Leidl, M. L., Diederichs, B., Sachse, C. & Müller-Caspary, K. Influence of loss function and electron dose on ptychography of 2D materials using the Wirtinger flow. *Micron* **185**, 103688 (2024). 10.1016/j.micron.2024.103688

103 Chen, Z., Odstrcil, M., Jiang, Y., Han, Y., Chiu, M.-H., Li, L.-J. & Muller, D. A. Mixed-state electron ptychography enables sub-angstrom resolution imaging with picometer precision at low dose. *Nature Communications* **11**, 2994 (2020). 10.1038/s41467-020-16688-6

104 Dwyer, C., Erni, R. & Etheridge, J. Measurement of effective source distribution and its importance for quantitative interpretation of STEM images. *Ultramicroscopy* **110**, 952–957 (2010). 10.1016/j.ultramic.2010.01.007

105 Cao, S., Kok, P., Li, P., Maiden, A. M. & Rodenburg, J. M. Modal decomposition of a propagating matter wave via electron ptychography (2016). 10.48550/arXiv.1611.09622

106 Nellist, P. D. & Rodenburg, J. M. Beyond the conventional information limit: the relevant coherence function. *Ultramicroscopy* **54**, 61–74 (1994). 10.1016/0304-3991(94)90092-2

107 Pelz, P. M., Griffin, S. M., Stonemeyer, S., Popple, D., DeVyldere, H., Ercius, P., Zettl, A., Scott, M. C. & Ophus, C. Solving complex nanostructures with ptychographic atomic electron tomography. *Nature Communications* **14**, 7906 (2023). 10.1038/s41467-023-43634-z

108 Moshtaghpour, A. & Kirkland, A. I. On overlap ratio in defocused electron ptychography (2025). 10.48550/arXiv.2502.00762

109 Gao, S., Wang, P., Zhang, F., Martinez, G. T., Nellist, P. D., Pan, X. & Kirkland, A. I. Electron ptychographic microscopy for three-dimensional imaging. *Nature Communications* **8**, 163 (2017). 10.1038/s41467-017-00150-1

110 Clark, L., Martinez, G. T., O'Leary, C. M., Yang, H., Ding, Z., Petersen, T. C., Findlay, S. D. & Nellist, P. D. The effect of dynamical scattering on single-plane phase retrieval in electron ptychography. *Microscopy and Microanalysis: The Official Journal of Microscopy Society of America, Microbeam Analysis Society, Microscopical Society of Canada* **29**, 384–394 (2023). 10.1093/micmic/ozac022

111 Tsai, E. H. R., Usov, I., Diaz, A., Menzel, A. & Guizar-Sicairos, M. X-ray ptychography with extended depth of field. *Optics Express* **24**, 29089–29108 (2016). 10.1364/oe.24.029089

112 Romanov, A., Cho, M. G., Scott, M. C. & Pelz, P. Multi-slice electron ptychographic tomography for three-dimensional phase-contrast microscopy beyond the depth of focus limits. *Journal of Physics: Materials* **8**, 015005 (2025). 10.1088/2515-7639/ad9ad2

113 Ribet, S. M., Varnavides, G., Pedroso, C. C. S., Cohen, B. E., Ercius, P., Scott, M. C. & Ophus, C. Uncovering the three-dimensional structure of upconverting core–shell nanoparticles with multislice electron ptychography. *Applied Physics Letters* **124** (2024). 10.1063/5.0206814

114 Yoon, D., Shao, Y.-T., Yang, Y., Ren, D., Abruña, H. D. & Muller, D. A. Imaging Li vacancies in a Li-ion battery cathode material by depth sectioning multi-slice electron ptychographic reconstructions. *Microscopy and Microanalysis: The Official Journal of Microscopy Society of America, Microbeam Analysis Society, Microscopical Society of Canada* **29**, 1263–1264 (2023). 10.1093/micmic/ozad067.647

115 Shannon, C. E. A mathematical theory of communication. *Bell System Technical Journal* **27**, 379–423 (1948). 10.1002/j.1538-7305.1948.tb01338.x

116 Yang, H., Rutte, R. N., Jones, L., Simson, M., Sagawa, R., Ryll, H., Huth, M., Pennycook, T. J., Green, M. L. H., Soltau, H., Kondo, Y., Davis, B. G. & Nellist, P. D. Simultaneous atomic-resolution electron ptychography and Z-contrast imaging of light and heavy elements in complex nanostructures. *Nature Communications* **7**, 12532 (2016). 10.1038/ncomms12532

117 O'Leary, C. The development and applications of STEM ptychography using direct electron detectors. PhD thesis, *University of Oxford* (2020).

118 Wolberg, G. Sampling, reconstruction, and antialiasing. In *The computer science and engineering handbook* (ed. Allen B. Tucker), *{CRC} Press*, 1270-1299 (1997).

119 Oxley, M. P. & Dyck, O. E. The importance of temporal and spatial incoherence in quantitative interpretation of 4D-STEM. *Ultramicroscopy* **215**, 113015 (2020). 10.1016/j.ultramic.2020.113015

120 Bunk, O., Dierolf, M., Kynde, S., Johnson, I., Marti, O. & Pfeiffer, F. Influence of the overlap parameter on the convergence of the ptychographical iterative engine. *Ultramicroscopy* **108**, 481–487 (2008). 10.1016/j.ultramic.2007.08.003

121 Batey, D. J., Edo, T. B., Rau, C., Wagner, U., Pešić, Z. D., Waigh, T. A. & Rodenburg, J. M. Reciprocal-space up-sampling from real-space oversampling in x-ray ptychography. *Physical Review A* **89**, 043812 (2014). 10.1103/PhysRevA.89.043812

122 O'Leary, C. M., Allen, C. S., Huang, C., Kim, J. S., Liberti, E., Nellist, P. D. & Kirkland, A. I. Phase reconstruction using fast binary 4D STEM data. *Applied Physics Letters* **116** (2020). 10.1063/1.5143213

123 Gao, C., Hofer, C. & Pennycook, T. J. On central focusing for contrast optimization in direct electron ptychography of thick samples. *Ultramicroscopy* **256**, 113879 (2024). 10.1016/j.ultramic.2023.113879

124 Gao, C., Hofer, C., Jannis, D., Béché, A., Verbeeck, J. & Pennycook, T. J. Overcoming contrast reversals in focused probe ptychography of thick materials: An optimal pipeline for efficiently determining local atomic structure in materials science. *Applied Physics Letters* **121**, 101037 (2022). 10.1063/5.0101895

125 Lee, S., Oshima, Y., Hosono, E., Zhou, H. & Takayanagi, K. Reversible contrast in focus series of annular bright field images of a crystalline $LiMn_2O_4$ nanowire. *Ultramicroscopy* **125**, 43–48 (2013). 10.1016/j.ultramic.2012.09.011

126 Zachman, M. J., Yang, Z., Du, Y. & Chi, M. Robust atomic-resolution imaging of lithium in battery materials by Center-of-Mass scanning transmission electron microscopy. *ACS Nano* **16**, 1358–1367 (2022). 10.1021/acsnano.1c09374

127 Bergstra, J., Bardenet, R., Bengio, Y. & Kégl, B. Algorithms for hyper-parameter optimization. In *Advances in neural information processing systems* (eds. J. Shawe-Taylor, R. Zemel, P. Bartlett, F. Pereira, & K. Q. Weinberger), *Curran Associates, Inc*, (2011).

128 Cao, M. C., Chen, Z., Jiang, Y. & Han, Y. Automatic parameter selection for electron ptychography via Bayesian optimization. *Scientific reports* **12**, 12284 (2022). 10.1038/s41598-022-16041-5

129 Pelz, P. M., Qiu, W. X., Bücker, R., Kassier, G. & Miller, R. J. D. Low-dose cryo electron ptychography via non-convex Bayesian optimization. *Scientific Reports* **7**, 9883 (2017). 10.1038/s41598-017-07488-y

130 Cao, M. C., Han, Y., Chen, Z., Jiang, Y., Nguyen, K. X., Turgut, E., Fuchs, G. D. & Muller, D. A. Theory and practice of electron diffraction from single atoms and extended objects using an EMPAD. *Microscopy* **67**, 150-161 (2018). 10.1093/jmicro/dfx123

131 Dekkers, N. H. & de Lang, H. Differential phase contrast in a STEM. *Optik* **41**, 452-456 (1974).

132 Shibata, N., Kohno, Y., Findlay, S. D., Sawada, H., Kondo, Y. & Ikuhara, Y. New area detector for atomic-resolution scanning transmission electron microscopy. *Journal of Electron Microscopy* **59**, 473–479 (2010). 10.1093/jmicro/dfq014

133 Seki, T., Ikuhara, Y. & Shibata, N. Toward quantitative electromagnetic field imaging by differential-phase-contrast scanning transmission electron microscopy. *Microscopy* **70**, 148–160 (2021). 10.1093/jmicro/dfaa065

134 Müller, K., Krause, F. F., Béché, A., Schowalter, M., Galioit, V., Löffler, S., Verbeeck, J., Zweck, J., Schattschneider, P. & Rosenauer, A. Atomic electric fields revealed by a quantum mechanical approach to electron picodiffraction. *Nature Communications* **5**, 5653 (2014). 10.1038/ncomms6653

135 Lubk, A. & Zweck, J. Differential phase contrast: An integral perspective. *Physical Review A* **91**, 023805 (2015). 10.1103/PhysRevA.91.023805

136 Toyama, S., Seki, T., Kohno, Y., Murakami, Y. O., Ikuhara, Y. & Shibata, N. Nanoscale electromagnetic field imaging by advanced differential phase-contrast STEM. *Nature Reviews Electrical Engineering* **2**, 27–41 (2025). 10.1038/s44287-024-00117-7

137 Imada, M., Fujimori, A. & Tokura, Y. Metal-insulator transitions. *Reviews of Modern Physics* **70**, 1039–1263 (1998). 10.1103/RevModPhys.70.1039

138 Dagotto, E. High temperature superconductors: A review. In *Recent progress in many-body theories* (eds. E. Schachinger, H. Mitter, & H. Sormann), *Springer US*, 319–374 (1995). 10.1007/978-1-4615-1937-9_30

139 Khomskii, D. Transition metal compounds. *Cambridge University Press* (2014). 10.1017/cbo9781139096782

140 Yogi, A., Sathish, C. I., Sim, H., Coak, M. J., Noda, Y. & Park, J.-G. Symmetry breaking and unconventional charge ordering in single crystal $Na_{2.7}Ru_4O_9$. *Physical Review B* **98**, 085113 (2018). 10.1103/PhysRevB.98.085113

141 Yogi, A. K., Yaresko, A., Sathish, C. I., Sim, H., Morikawa, D., Nuss, J., Tsuda, K., Noda, Y., Khomskii, D. I. & Park, J.-G. Coexisting Z-type charge and bond order in metallic $NaRu_2O_4$. *Communications Materials* **3**, 9 (2022). 10.1038/s43246-022-00224-8

142 Stitzer, K. E., Smith, M. D., Gemmill, W. R. & zur Loye, H.-C. Novel mixed-valent (V/VI) triple perovskite ruthenates: observation of a complex low-temperature structural and magnetic transition. *Journal of the American Chemical Society* **124**, 13877–13885 (2002). 10.1021/ja0271781

143 Marques, C. A., Rhodes, L. C., Fittipaldi, R., Granata, V., Yim, C. M., Buzio, R., Gerbi, A., Vecchione, A., Rost, A. W. & Wahl, P. Magnetic-field tunable intertwined checkerboard charge order and nematicity in the surface layer of Sr_2RuO_4. *Advanced Materials* **33**, e2100593 (2021). 10.1002/adma.202100593

144 Allred, J. M., Wang, L. M., Khalifah, P. & Cava, R. J. $Na_{27}Ru_{14}O_{48}$: A new mixed-valence sodium ruthenate with magnetic heptameric plaquettes. *Journal of Solid State Chemistry* **184**, 44–51 (2011). 10.1016/j.jssc.2010.10.016

145 Ng, K. K. & Sigrist, M. The role of spin-orbit coupling for the superconducting state in Sr_2RuO_4. *Europhysics Letters* **49**, 473–479 (2000). 10.1209/epl/i2000-00173-x

146 Ahn, K.-H., Marmodoro, A., Hejtmánek, J., Jirák, Z. & Knížek, K. Role of spin-orbit coupling in canted ferromagnetism and spin-wave dynamics of $SrRuO_3$. *Physical Review B* **105**, 245107 (2022). 10.1103/PhysRevB.105.245107

147 Singh, A., Sikarwar, S., Verma, A. & Chandra Yadav, B. The recent development of metal oxide heterostructures based gas sensor, their future opportunities and challenges: A review. *Sensors and Actuators A: Physical* **332**, 113127 (2021). 10.1016/j.sna.2021.113127

148 Hwang, H. Y., Iwasa, Y., Kawasaki, M., Keimer, B., Nagaosa, N. & Tokura, Y. Emergent phenomena at oxide interfaces. *Nature Materials* **11**, 103–113 (2012). 10.1038/nmat3223

149 Mannhart, J. & Schlom, D. G. Oxide interfaces--an opportunity for electronics. *Science (New York, N.Y.)* **327**, 1607–1611 (2010). 10.1126/science.1181862

150 Schlom, D. G. Perspective: Oxide molecular-beam epitaxy rocks! *APL Materials* **3**, 062403 (2015). 10.1063/1.4919763

151 Chen, S., Ren, C. & Liang, S. Spintronics phenomena of two-dimensional electron gas at oxide interfaces. *Advanced Devices & Instrumentation* **4** (2023). 10.34133/adi.0024

152 Coll, M., Fontcuberta, J., Althammer, M., Bibes, M., Boschker, H., Calleja, A., Cheng, G., Cuoco, M., Dittmann, R., Dkhil, B., El Baggari, I., Fanciulli, M., Fina, I., Fortunato, E., Frontera, C., Fujita, S., Garcia, V., Goennenwein, S. T. B., Granqvist, C.-G., Grollier, J., Gross, R., Hagfeldt, A., Herranz, G., Hono, K., Houwman, E., Huijben, M., Kalaboukhov, A., Keeble, D. J., Koster, G., Kourkoutis, L. F., Levy, J., Lira-Cantu, M., MacManus-Driscoll, J. L., Mannhart, J., Martins, R., Menzel, S., Mikolajick, T., Napari, M., Nguyen, M. D., Niklasson, G., Paillard, C., Panigrahi, S., Rijnders, G., Sánchez, F., Sanchis, P., Sanna, S., Schlom, D. G., Schroeder, U., Shen, K. M., Siemon, A., Spreitzer, M., Sukegawa, H., Tamayo, R., van den Brink, J., Pryds, N. & Granozio, F. M. Towards oxide electronics: a roadmap. *Applied Surface Science* **482**, 1–93 (2019). 10.1016/j.apsusc.2019.03.312

153 Zappa, D., Galstyan, V., Kaur, N., Munasinghe Arachchige, H. M. M., Sisman, O. & Comini, E. Metal oxide -based heterostructures for gas sensors- A review. *Analytica Chimica Acta* **1039**, 1–23 (2018). 10.1016/j.aca.2018.09.020

154 Alferov, Z. I. Nobel Lecture: The double heterostructure concept and its applications in physics, electronics, and technology. *Reviews of Modern Physics* **73**, 767–782 (2001). 10.1103/RevModPhys.73.767

155 Harada, T. Thin-film growth and application prospects of metallic delafossites. *Materials Today Advances* **11**, 100146 (2021). 10.1016/j.mtadv.2021.100146

156 Harada, T. & Okada, Y. Metallic delafossite thin films for unique device applications. *APL Materials* **10**, 070902 (2022). 10.1063/5.0097269

157 Hicks, C. W., Gibbs, A. S., Mackenzie, A. P., Takatsu, H., Maeno, Y. & Yelland, E. A. Quantum oscillations and high carrier mobility in the delafossite $PdCoO_2$. *Physical Review Letters* **109**, 116401 (2012). 10.1103/PhysRevLett.109.116401

158 Kushwaha, P., Sunko, V., Moll, P. J. W., Bawden, L., Riley, J. M., Nandi, N., Rosner, H., Schmidt, M. P., Arnold, F., Hassinger, E., Kim, T. K., Hoesch, M., Mackenzie, A. P. & King, P. D. C. Nearly free electrons in a 5d delafossite oxide metal. *Science Advances* **1**, e1500692 (2015). 10.1126/sciadv.1500692

159 Zhang, Y., Tutt, F., Evans, G. N., Sharma, P., Haugstad, G., Kaiser, B., Ramberger, J., Bayliff, S., Tao, Y., Manno, M., Garcia-Barriocanal, J., Chaturvedi, V., Fernandes, R. M., Birol, T., Seyfried, W. E. & Leighton, C. Crystal-chemical origins of the ultrahigh conductivity of metallic delafossites. *Nature Communications* **15**, 1399 (2024). 10.1038/s41467-024-45239-6

160 Akin, S., Liu, Y., Dar, M. I., Zakeeruddin, S. M., Grätzel, M., Turan, S. & Sonmezoglu, S. Hydrothermally processed $CuCrO_2$ nanoparticles as an inorganic hole transporting material for low-cost perovskite solar cells with superior stability. *Journal of Materials Chemistry A* **6**, 20327–20337 (2018). 10.1039/c8ta07368f

161 F. Brech, L. C. Optical micromission stimulated by a ruby MASER. *Applied Spectroscopy* **16**, 59 (1962).

162 Smith, H. M. & Turner, A. F. Vacuum deposited thin films using a ruby laser. *Applied Optics* **4**, 147-148 (1965). 10.1364/ao.4.000147

163 Webb, C. E. & Jones, J. D. C. Handbook of laser technology and applications. Volume 1, Principles. *Routledge* (2019).

164 Schneider, C. W. & Lippert, T. PLD plasma plume analysis: a summary of the PSI contribution. *Applied Physics. A, Materials Science & Processing* **129**, 138 (2023). 10.1007/s00339-023-06408-4

165 Ojeda-G-P, A., Schneider, C. W., Lippert, T. & Wokaun, A. Pressure and temperature dependence of the laser-induced plasma plume dynamics. *Journal of Applied Physics* **120**, 225301 (2016). 10.1063/1.4971251

166 Shepelin, N. A., Tehrani, Z. P., Ohannessian, N., Schneider, C. W., Pergolesi, D. & Lippert, T. A practical guide to pulsed laser deposition. *Chemical Society Reviews* **52**, 2294–2321 (2023). 10.1039/d2cs00938b

167 Ogugua, S. N., Ntwaeaborwa, O. M. & Swart, H. C. Latest development on pulsed laser deposited thin films for advanced luminescence applications. *Coatings* **10**, 1078 (2020). 10.3390/coatings10111078

168 Ma, C. & Chen, C. Pulsed laser deposition for complex oxide thin film and nanostructure. In *Advanced nano deposition methods* (eds. Yuan Lin & Xin Chen), *Wiley*, 1–31 (2016). 10.1002/9783527696406.ch1

169 Arthur, J. R. Molecular beam epitaxy. *Surface Science* **500**, 189–217 (2002). 10.1016/s0039-6028(01)01525-4

170 Eckstein, J. N. & Bozovic, I. High-temperature superconducting multilayers and heterostructures grown by atomic layer-by-layer molecular beam epitaxy. *Annual Review of Materials Science* **25**, 679–709 (1995). 10.1146/annurev.ms.25.080195.003335

171 Gonser, U., Osgood, R. M., Panish, M. B., Sakaki, H., Lotsch, H. K. V., Herman, M. A. & Sitter, H. Molecular Beam Epitaxy. *Springer Berlin Heidelberg* (1996). 10.1007/978-3-642-80060-3

172 Smart, T. J., Mannhart, J. & Braun, W. Thermal laser evaporation of elements from across the periodic table. *Journal of Laser Applications* **33**, 022008 (2021). 10.2351/7.0000348

173 Kim, D. Y., Mannhart, J. & Braun, W. Thermal laser evaporation for the growth of oxide films. *APL Materials* **9**, 081105 (2021). 10.1063/5.0055237

174 Braun, W. & Mannhart, J. Film deposition by thermal laser evaporation. *AIP Advances* **9**, 085310 (2019). 10.1063/1.5111678

175 Frank, F. C. & van der Merve, J. H. One-dimensional dislocations. II. Misfitting monolayers and oriented overgrowth. *Proceedings of the Royal Society of London. Series A. Mathematical and Physical Sciences* **198**, 216–225 (1949). 10.1098/rspa.1949.0096

176 Smallman, R. E. & Ngan, A. H. W. Surfaces, grain boundaries and interfaces. In *Modern physical metallurgy*, *Elsevier*, 415–442 (2014). 10.1016/b978-0-08-098204-5.00010-9

177 Porter, D. A. & Easterling, K. E. Phase transformations in metals and alloys (revised reprint). *CRC Press* (2009). 10.1201/9781439883570

178 Matthews, J. Defects in epitaxial multilayers I. Misfit dislocations. *Journal of Crystal Growth* **27**, 118–125 (1974). 10.1016/0022-0248(74)90424-2

179 Cooper, D. & Rouviere, J. L. Strain measurement with nanometre resolution by transmission electron microscopy. *Advanced Materials Research* **996**, 3–7 (2014). 10.4028/www.scientific.net/AMR.996.3

180 Savitzky, B. H., El Baggari, I., Admasu, A. S., Kim, J., Cheong, S.-W., Hovden, R. & Kourkoutis, L. F. Bending and breaking of stripes in a charge ordered manganite. *Nature Communications* **8**, 1883 (2017). 10.1038/s41467-017-02156-1

181 Hÿtch, M. J., Putaux, J.-L. & Pénisson, J.-M. Measurement of the displacement field of dislocations to 0.03 A by electron microscopy. *Nature* **423**, 270–273 (2003). 10.1038/nature01638

182 Rouvière, J. L. & Sarigiannidou, E. Theoretical discussions on the geometrical phase analysis. *Ultramicroscopy* **106**, 1–17 (2005). 10.1016/j.ultramic.2005.06.001

183 Sanchez, A. M., Galindo, P. L., Kret, S., Falke, M., Beanland, R. & Goodhew, P. J. An approach to the systematic distortion correction in aberration-corrected HAADF images. *Journal of Microscopy* **221**, 1–7 (2006). 10.1111/j.1365-2818.2006.01533.x

184 Chung, J., Lian, G. & Rabenberg, L. Practical and reproducible mapping of strains in Si devices using geometric phase analysis of annular dark-field images from scanning transmission electron microscopy. *IEEE Electron Device Letters* **31**, 854–856 (2010). 10.1109/led.2010.2049562

185 Goodge, B. H., El Baggari, I., Hong, S. S., Wang, Z., Schlom, D. G., Hwang, H. Y. & Kourkoutis, L. F. Disentangling coexisting structural order through phase lock-in analysis of atomic-resolution STEM data. *Microscopy and Microanalysis: The Official Journal of Microscopy Society of America, Microbeam Analysis Society, Microscopical Society of Canada*, 1–8 (2022). 10.1017/s1431927622000125

186 Scheid, A., Isha, Yogi, A. K., Isobe, M., Bußmann, B., Heil, T. & van Aken, P. A. Direct evidence of anomalous peierls transition-induced charge density wave order at room temperature in metallic $NaRu_2O_4$. *Microscopy and microanalysis: The Official Journal of Microscopy Society of America, Microbeam Analysis Society, Microscopical Society of Canada* **31** (2025). 10.1093/mam/ozae129

187 Şaşıoğlu, E., Friedrich, C. & Blügel, S. Effective Coulomb interaction in transition metals from constrained random-phase approximation. *Physical Review B* **83**, 121101 (2011). 10.1103/PhysRevB.83.121101

188 Ali, Z., Saghayezhian, M., Wang, Z., O'Hara, A., Shin, D., Ge, W., Chan, Y. T., Zhu, Y., Wu, W., Pantelides, S. T. & Zhang, J. Emergent ferromagnetism and insulator-metal transition in δ-doped ultrathin ruthenates. *npj Quantum Materials* **7** (2022). 10.1038/s41535-022-00518-7

189 Huang, H.-L. & Jeng, H.-T. Orbital ordering and magnetism in layered Perovskite ruthenate Sr_2RuO_4. *Scientific Reports* **10**, 7089 (2020). 10.1038/s41598-020-63415-8

190 Liu, Y. & Mao, Z.-Q. Unconventional superconductivity in Sr_2RuO_4. *Physica C: Superconductivity and its Applications* **514**, 339–353 (2015). 10.1016/j.physc.2015.02.039

191 Malik, S. K., Kundaliya, D. C. & Kale, R. D. High temperature magnetic ordering in La_2RuO_5. *Solid State Communications* **135**, 166–169 (2005). 10.1016/j.ssc.2005.04.016

192 Yamamoto, A., A. Sharma, P., Okamoto, Y., Nakao, A., Aruga Katori, H., Niitaka, S., Hashizume, D. & Takagi, H. Metal–insulator transition in a pyrochlore-type ruthenium oxide, $Hg_2Ru_2O_7$. *Journal of the Physical Society of Japan* **76**, 043703 (2007). 10.1143/jpsj.76.043703

193 Baidya, S., Sarkar, S., Saha-Dasgupta, T. & Sarma, D. D. Interplay of localized and itinerant character of Ru ions: $Tl_2Ru_2O_7$ versus $Hg_2Ru_2O_7$. *Physical Review B* **86**, 125117 (2012). 10.1103/PhysRevB.86.125117

194 Streltsov, S., Mazin, I. I. & Foyevtsova, K. Localized itinerant electrons and unique magnetic properties of $SrRu_2O_6$. *Physical Review B* **92**, 134408 (2015). 10.1103/PhysRevB.92.134408

195 Attfield, J. P. Charge ordering in transition metal oxides. *Solid State Sciences* **8**, 861–867 (2006). 10.1016/j.solidstatesciences.2005.02.011

196 Peierls, R. E. Quantum theory of solids. *Clarendon Pres,s Oxford University Press* (2001).

197 Darriet, J. & Vidal, A. Les composés $NaRu_2O_4$ et $NaFeRuO_4$. Structure cristalline de $NaFeRuO_4$. *Bulletin de Minéralogie* **98**, 374–377 (1975). 10.3406/bulmi.1975.7020

198 Regan, K. A., Huang, Q., Lee, M., Ramirez, A. P. & Cava, R. J. Structure and magnetism of $NaRu_2O_4$ and $Na_{2.7}Ru_4O_9$. *Journal of Solid State Chemistry* **179**, 195–204 (2006). 10.1016/j.jssc.2005.10.016

199 Efremov, D. V., van den Brink, J. & Khomskii, D. I. Bond- versus site-centred ordering and possible ferroelectricity in manganites. *Nature Materials* **3**, 853–856 (2004). 10.1038/nmat1236

200 Ko, K.-T., Lee, H.-H., Kim, D.-H., Yang, J.-J., Cheong, S.-W., Eom, M. J., Kim, J. S., Gammag, R., Kim, K.-S., Kim, H.-S., Kim, T.-H., Yeom, H.-W., Koo, T.-Y., Kim, H.-D. & Park, J.-H. Charge-ordering cascade with spin-orbit Mott dimer states in metallic iridium ditelluride. *Nature Communications* **6**, 7342 (2015). 10.1038/ncomms8342

201 Fang, A. F., Xu, G., Dong, T., Zheng, P. & Wang, N. L. Structural phase transition in $IrTe_2$: a combined study of optical spectroscopy and band structure calculations. *Scientific Reports* **3**, 1153 (2013). 10.1038/srep01153

202 Ootsuki, D., Wakisaka, Y., Pyon, S., Kudo, K., Nohara, M., Arita, M., Anzai, H., Namatame, H., Taniguchi, M., Saini, N. L. & Mizokawa, T. Orbital degeneracy and Peierls instability in the triangular-lattice superconductor $Ir_{1-x}Pt_xTe_2$. *Physical Review B* **86**, 014519 (2012). 10.1103/PhysRevB.86.014519

203 Khomskii, D. I. & Mizokawa, T. Orbitally induced Peierls state in spinels. *Physical Review Letters* **94**, 156402 (2005). 10.1103/PhysRevLett.94.156402

204 Bosman, M., Watanabe, M., Alexander, D. T. L. & Keast, V. J. Mapping chemical and bonding information using multivariate analysis of electron energy-loss spectrum images. *Ultramicroscopy* **106**, 1024–1032 (2006). 10.1016/j.ultramic.2006.04.016

205 Seto, Y. & Ohtsuka, M. ReciPro : free and open-source multipurpose crystallographic software integrating a crystal model database and viewer, diffraction and microscopy simulators, and diffraction data analysis tools. *Journal of Applied Crystallography* **55**, 397–410 (2022). 10.1107/s1600576722000139

206 Akimoto, J., Awaka, J., Kijima, N., Takahashi, Y., Maruta, Y., Tokiwa, K. & Watanabe, T. High-pressure synthesis and crystal structure analysis of $NaMn_2O_4$ with the calcium ferrite-type structure. *Journal of Solid State Chemistry* **179**, 169–174 (2006). 10.1016/j.jssc.2005.10.020

207 Catti, M. High-pressure stability, structure and compressibility of Cmcm -$MgAl_2O_4$: an ab initio study. *Physics and Chemistry of Minerals* **28**, 729–736 (2001). 10.1007/s002690100190

208 Irifune, T., Naka, H., Sanehira, T., Inoue, T. & Funakoshi, K. In situ X-ray observations of phase transitions in $MgAl_2O_4$ spinel to 40 GPa using multianvil apparatus with sintered diamond anvils. *Physics and Chemistry of Minerals* **29**, 645–654 (2002). 10.1007/s00269-002-0275-1

209 Yamaura, K., Huang, Q., Moldovan, M., Young, D. P., Sato, A., Baba, Y., Nagai, T., Matsui, Y. & Takayama-Muromachi, E. High-pressure synthesis, crystal structure determination, and a Ca substitution study of the metallic rhodium oxide $NaRh_2O_4$. *Chemistry of Materials* **17**, 359–365 (2005). 10.1021/cm0483846

210 Jiao, S., Zhan, P. & Wang, J. $CaFe_2O_4$-type Structure $NaRu_2O_4$: a Novel Cathode Material for Li-ion Batteries. *International Journal of Electrochemical Science* **12**, 280–291 (2017). 10.20964/2017.01.52

211 MacLaren, I., Cummings, R. B., Gordon, F., Frutos-Myro, E., McFadzean, S., Brown, A. P. & Craven, A. J. Performing EELS at higher energy losses at both 80 and 200 kV. *Elsevier*, 299–355 (2019). 10.1016/bs.aiep.2019.02.001

212 MacLaren, I., Annand, K. J., Black, C. & Craven, A. J. EELS at very high energy losses. *Microscopy* **67**, 78-85 (2018). 10.1093/jmicro/dfx036

213 Plotkin-Swing, B., Corbin, G. J., Carlo, S. d., Dellby, N., Hoermann, C., Hoffman, M. V., Lovejoy, T. C., Meyer, C. E., Mittelberger, A., Pantelic, R., Piazza, L. & Krivanek, O. L. Hybrid pixel direct detector for electron energy loss spectroscopy. *Ultramicroscopy* **217**, 113067 (2020). 10.1016/j.ultramic.2020.113067

214 Hart, J. L., Lang, A. C., Li, Y., Shahrezaei, S., Alix-Williams, D. D., Falk, M. L., Mathaudhu, S. N., Frenkel, A. I. & Taheri, M. L. Revealing local order via high energy EELS. *Materials Today Nano* **21**, 100298 (2023). 10.1016/j.mtnano.2022.100298

215 Hart, J. L., Lang, A. C., Leff, A. C., Longo, P., Trevor, C., Twesten, R. D. & Taheri, M. L. Direct detection electron energy-loss spectroscopy: A method to push the limits of resolution and sensitivity. *Scientific Reports* **7**, 8243 (2017). 10.1038/s41598-017-07709-4

216 Heidelmann, M., Barthel, J. & Houben, L. StripeSTEM, a technique for the isochronous acquisition of high angle annular dark-field images and monolayer resolved electron energy loss spectra. *Ultramicroscopy* **109**, 1447–1452 (2009). 10.1016/j.ultramic.2009.07.007

217 Silinga, A., Allen, C. S., Barthel, J., Ophus, C. & MacLaren, I. Measurement of atomic modulation direction using the azimuthal variation of first-order Laue zone electron diffraction. *Microscopy and Microanalysis: The Official Journal of Microscopy ociety of America, Microbeam Analysis Society, Microscopical Society of Canada* **29**, 1682–1687 (2023). 10.1093/micmic/ozad089

218 Huang, F.-T., Gloter, A., Chu, M.-W., Chou, F. C., Shu, G. J., Liu, L.-K., Chen, C. H. & Colliex, C. Scanning transmission electron microscopy using selective high-order laue zones: three-dimensional atomic ordering in sodium cobaltate. *Physical Review Letters* **105**, 125502 (2010). 10.1103/PhysRevLett.105.125502

219 Nord, M., Barthel, J., Allen, C. S., McGrouther, D., Kirkland, A. I. & MacLaren, I. Atomic resolution HOLZ-STEM imaging of atom position modulation in oxide heterostructures. *Ultramicroscopy* **226**, 113296 (2021). 10.1016/j.ultramic.2021.113296

220 Bustillo, K. C., Zeltmann, S. E., Chen, M., Donohue, J., Ciston, J., Ophus, C. & Minor, A. M. 4D-STEM of beam-sensitive materials. *Accounts of Chemical Research* **54**, 2543–2551 (2021). 10.1021/acs.accounts.1c00073

221 Toriyama, T., Nakao, A., Yamaki, Y., Nakao, H., Murakami, Y., Hasegawa, K., Isobe, M., Ueda, Y., Ushakov, A. V., Khomskii, D. I., Streltsov, S. V., Konishi, T. & Ohta, Y. Peierls

mechanism of the metal-insulator transition in ferromagnetic hollandite $K_2Cr_8O_{16}$. *Physical Review Letters* **107**, 266402 (2011). 10.1103/PhysRevLett.107.266402

222 Pauling, L. Metal-metal bond lengths in complexes of transition metals. *Proceedings of the National Academy of Sciences of the United States of America* **73**, 4290–4293 (1976). 10.1073/pnas.73.12.4290

223 Nord, M., Vullum, P. E., MacLaren, I., Tybell, T. & Holmestad, R. Atomap: a new software tool for the automated analysis of atomic resolution images using two-dimensional Gaussian fitting. *Advanced Structural and Chemical Imaging* **3**, 9 (2017). 10.1186/s40679-017-0042-5

224 Mukherjee, D., Miao, L., Stone, G. & Alem, N. mpfit: a robust method for fitting atomic resolution images with multiple Gaussian peaks. *Advanced Structural and Chemical Imaging* **6** (2020). 10.1186/s40679-020-0068-y

225 Levin, B. D. A., Lawrence, E. L. & Crozier, P. A. Tracking the picoscale spatial motion of atomic columns during dynamic structural change. *Ultramicroscopy* **213**, 112978 (2020). 10.1016/j.ultramic.2020.112978

226 Miao, L., Chmielewski, A., Mukherjee, D. & Alem, N. Picometer-precision atomic position tracking through electron microscopy. *Journal of Visualized Experiments*, 62164 (2021). 10.3791/62164

227 Egerton, R. F., Li, P. & Malac, M. Radiation damage in the TEM and SEM. *Micron* **35**, 399–409 (2004). 10.1016/j.micron.2004.02.003

228 Mackenzie, A. P. The properties of ultrapure delafossite metals. *Reports on Progress in Physics* **80**, 032501 (2017). 10.1088/1361-6633/aa50e5

229 Scheid, A., Heil, T., Suyolcu, Y. E., Song, Q., Enderlein, N., Nono Tchiomo, A. P., Ngabonziza, P., Hansmann, P., Schlom, D. G. & van Aken, P. A. Unveiling the interfacial reconstruction mechanism enabling stable growth of the delafossite $PdCoO_2$ on Al_2O_3 and $LaAlO_3$. *ACS Applied Materials & Interfaces*, 14795–14802 (2025). 10.1021/acsami.5c03536

230 Song, Q., He, Z., Faeth, B. D., Parzyck, C. T., Scheid, A., Mowers, C. J., Feng, Y., Xu, Q., Hasko, S., Park, J., Barone, M. R., Suyolcu, Y. E., van Aken, P. A., Pamuk, B., Fennie, C. J., King, P. D. C., Shen, K. M. & Schlom, D. G. Surface reconstructions and electronic structure of metallic delafossite thin films. *APL Materials* **12**, 081117 (2024). 10.1063/5.0217540

231 Ngabonziza, P., Nono Tchiomo, A. P., Sharma, A., Sajeev, S., Scheid, A., van Aken, P. A. & Harada, T. Magnetotransport properties in epitaxial films of metallic delafossite $PdCoO_2$: Effects of thickness and width variations in Hall bar devices. *Physical Review Materials* **9**, 055001 (2025). 10.1103/PhysRevMaterials.9.055001

232 Shannon, R. D., Rogers, D. B., Prewitt, C. T. & Gillson, J. L. Chemistry of noble metal oxides. III. Electrical transport properties and crystal chemistry of ABO_2 compounds with the delafossite structure. *Inorganic Chemistry* **10**, 723–727 (1971). 10.1021/ic50098a013

233 Lechermann, F. From basic properties to the Mott design of correlated delafossites. *npj Computational Materials* **7**, 120 (2021). 10.1038/s41524-021-00586-6

234 Marquardt, M. A., Ashmore, N. A. & Cann, D. P. Crystal chemistry and electrical properties of the delafossite structure. *Thin Solid Films* **496**, 146–156 (2006). 10.1016/j.tsf.2005.08.316

235 Fang, M., He, H., Lu, B., Zhang, W., Zhao, B., Ye, Z. & Huang, J. Optical properties of p-type $CuAlO_2$ thin film grown by rf magnetron sputtering. *Applied Surface Science* **257**, 8330–8333 (2011). 10.1016/j.apsusc.2011.03.116

236 Yu, R.-S., Lee, Y.-F. & Lai, Y.-S. Synthesis and optoelectronic properties of $CuFeO_2$ semiconductor thin films. *ECS Journal of Solid State Science and Technology* **5**, 646-652 (2016). 10.1149/2.0091612jss

237 Kawazoe, H., Yasukawa, M., Hyodo, H., Kurita, M., Yanagi, H. & Hosono, H. P-type electrical conduction in transparent thin films of $CuAlO_2$. *Nature* **389**, 939–942 (1997). 10.1038/40087

238 Kimura, T., Lashley, J. C. & Ramirez, A. P. Inversion-symmetry breaking in the noncollinear magnetic phase of the triangular-lattice antiferromagnet $CuFeO_2$. *Physical Review B* **73**, 220401 (2006). 10.1103/PhysRevB.73.220401

239 Maruyama, Y., Irie, H. & Hashimoto, K. Visible light sensitive photocatalyst, delafossite structured alpha-$AgGaO_2$. *The Journal of Physical Chemistry B* **110**, 23274–23278 (2006). 10.1021/jp063406s

240 Eyert, V., Frésard, R. & Maignan, A. On the metallic conductivity of the delafossites $PdCoO_2$ and $PtCoO_2$. *Chemistry of Materials* **20**, 2370–2373 (2008). 10.1021/cm703404e

241 Sun, J., Barone, M. R., Chang, C. S., Holtz, M. E., Paik, H., Schubert, J., Muller, D. A. & Schlom, D. G. Growth of $PdCoO_2$ by ozone-assisted molecular-beam epitaxy. *APL Materials* **7**, 121112 (2019). 10.1063/1.5130627

242 Ok, J. M., Brahlek, M., Choi, W. S., Roccapriore, K. M., Chisholm, M. F., Kim, S., Sohn, C., Skoropata, E., Yoon, S., Kim, J. S. & Lee, H. N. Pulsed-laser epitaxy of metallic delafossite $PdCrO_2$ films. *APL Materials* **8**, 051104 (2020). 10.1063/1.5144743

243 Song, Q., Sun, J., Parzyck, C. T., Miao, L., Xu, Q., Hensling, F. V. E., Barone, M. R., Hu, C., Kim, J., Faeth, B. D., Paik, H., King, P. D. C., Shen, K. M. & Schlom, D. G. Growth of $PdCoO_2$ films with controlled termination by molecular-beam epitaxy and determination of their electronic structure by angle-resolved photoemission spectroscopy. *APL Materials* **10**, 091113 (2022). 10.1063/5.0101837

244 Brahlek, M., Rimal, G., Ok, J. M., Mukherjee, D., Mazza, A. R., Lu, Q., Lee, H. N., Ward, T. Z., Unocic, R. R., Eres, G. & Oh, S. Growth of metallic delafossite $PdCoO_2$ by molecular beam epitaxy. *Physical Review Materials* **3**, 093401 (2019). 10.1103/PhysRevMaterials.3.093401

245 Ok, J. M., Yoon, S., Lupini, A. R., Ganesh, P., Chisholm, M. F. & Lee, H. N. Interfacial stabilization for epitaxial $CuCrO_2$ delafossites. *Scientific Reports* **10**, 11375 (2020). 10.1038/s41598-020-68275-w

246 Harada, T., Fujiwara, K. & Tsukazaki, A. Highly conductive $PdCoO_2$ ultrathin films for transparent electrodes. *APL Materials* **6**, 046107 (2018). 10.1063/1.5027579

247 Cueva, P., Hovden, R., Mundy, J. A., Xin, H. L. & Muller, D. A. Data processing for atomic resolution electron energy loss spectroscopy. *Microscopy and Microanalysis: The Official Journal of Microscopy Society of America, Microbeam Analysis Society, Microscopical Society of Canada* **18**, 667–675 (2012). 10.1017/s1431927612000244

248 Madsen, J. & Susi, T. The abTEM code: transmission electron microscopy from first principles. *Open Research Europe* **1**, 24 (2021). 10.12688/openreseurope.13015.2

249 Giannozzi, P., Baroni, S., Bonini, N., Calandra, M., Car, R., Cavazzoni, C., Ceresoli, D., Chiarotti, G. L., Cococcioni, M., Dabo, I., Dal Corso, A., Gironcoli, S. d., Fabris, S., Fratesi, G., Gebauer, R., Gerstmann, U., Gougoussis, C., Kokalj, A., Lazzeri, M., Martin-Samos, L., Marzari, N., Mauri, F., Mazzarello, R., Paolini, S., Pasquarello, A., Paulatto, L., Sbraccia, C., Scandolo, S., Sclauzero, G., Seitsonen, A. P., Smogunov, A., Umari, P. & Wentzcovitch, R. M. QUANTUM ESPRESSO: a modular and open-source software project for quantum simulations of materials. *Journal of Physics. Condensed Matter: an Institute of Physics Journal* **21**, 395502 (2009). 10.1088/0953-8984/21/39/395502

250 Giannozzi, P., Andreussi, O., Brumme, T., Bunau, O., Buongiorno Nardelli, M., Calandra, M., Car, R., Cavazzoni, C., Ceresoli, D., Cococcioni, M., Colonna, N., Carnimeo, I., Dal Corso, A., Gironcoli, S. d., Delugas, P., DiStasio, R. A., Ferretti, A., Floris, A., Fratesi, G., Fugallo, G., Gebauer, R., Gerstmann, U., Giustino, F., Gorni, T., Jia, J., Kawamura, M., Ko, H.-Y., Kokalj, A., Küçükbenli, E., Lazzeri, M., Marsili, M., Marzari, N., Mauri, F., Nguyen, N. L., Nguyen, H.-V., Otero-de-la-Roza, A., Paulatto, L., Poncé, S., Rocca, D., Sabatini, R., Santra, B., Schlipf, M., Seitsonen, A. P., Smogunov, A., Timrov, I., Thonhauser, T., Umari, P., Vast, N., Wu, X. & Baroni, S. Advanced capabilities for materials modelling with Quantum ESPRESSO. *Journal of Physics. Condensed Matter: an Institute of Physics Journal* **29**, 465901 (2017). 10.1088/1361-648X/aa8f79

251 Giannozzi, P., Baseggio, O., Bonfà, P., Brunato, D., Car, R., Carnimeo, I., Cavazzoni, C., Gironcoli, S. d., Delugas, P., Ferrari Ruffino, F., Ferretti, A., Marzari, N., Timrov, I., Urru, A. & Baroni, S. Quantum ESPRESSO toward the exascale. *The Journal of Chemical Physics* **152**, 154105 (2020). 10.1063/5.0005082

252 Hamann, D. R. Optimized norm-conserving Vanderbilt pseudopotentials. *Physical Review B* **88**, 085117 (2013). 10.1103/PhysRevB.88.085117

253 van Setten, M. J., Giantomassi, M., Bousquet, E., Verstraete, M. J., Hamann, D. R., Gonze, X. & Rignanese, G.-M. The PseudoDojo: Training and grading a 85 element optimized norm-conserving pseudopotential table. *Computer Physics Communications* **226**, 39–54 (2018). 10.1016/j.cpc.2018.01.012

254 Ok, J. M., Yoon, S., Lupini, A. R., Ganesh, P., Huon, A., Chisholm, M. F. & Lee, H. N. Twin-domain formation in epitaxial triangular lattice delafossites. *ACS Applied Materials & Interfaces* **13**, 22059–22064 (2021). 10.1021/acsami.1c04169

255 Harada, T., Bredol, P., Inoue, H., Ito, S., Mannhart, J. & Tsukazaki, A. Determination of the phase coherence length of $PdCoO_2$ nanostructures by conductance fluctuation analysis. *Physical Review B* **103**, 045123 (2021). 10.1103/PhysRevB.103.045123

256 Harada, T., Nagai, T., Oishi, M. & Masahiro, Y. Sputter-grown c-axis-oriented $PdCoO_2$ thin films. *Journal of Applied Physics* **133**, 085302 (2023). 10.1063/5.0136749

257 Findlay, S. D., Shibata, N., Sawada, H., Okunishi, E., Kondo, Y. & Ikuhara, Y. Dynamics of annular bright field imaging in scanning transmission electron microscopy. *Ultramicroscopy* **110**, 903–923 (2010). 10.1016/j.ultramic.2010.04.004

258 Welch, E. W., Jung, Y.-K., Walsh, A., Scolfaro, L. & Zakhidov, A. A density functional theory study on the interface stability between $CsPbBr_3$ and CuI. *AIP Advances* **10**, 085023 (2020). 10.1063/5.0018925

259 Jung, Y.-K., Butler, K. T. & Walsh, A. Halide perovskite heteroepitaxy: bond formation and carrier confinement at the PbS–$CsPbBr_3$ interface. *The Journal of Physical Chemistry C* **121**, 27351–27356 (2017). 10.1021/acs.jpcc.7b10000

260 Baiutti, F., Christiani, G. & Logvenov, G. Towards precise defect control in layered oxide structures by using oxide molecular beam epitaxy. *Beilstein Journal of Nanotechnology* **5**, 596–602 (2014). 10.3762/bjnano.5.70

261 Lei, Q., Golalikhani, M., Davidson, B. A., Liu, G., Schlom, D. G., Qiao, Q., Zhu, Y., Chandrasena, R. U., Yang, W., Gray, A. X., Arenholz, E., Farrar, A. K., Tenne, D. A., Hu, M., Guo, J., Singh, R. K. & Xi, X. Constructing oxide interfaces and heterostructures by atomic layer-by-layer laser molecular beam epitaxy. *npj Quantum Materials* **2**, 10 (2017). 10.1038/s41535-017-0015-x

262 Willmott, P. R., Pauli, S. A., Herger, R., Schlepütz, C. M., Martoccia, D., Patterson, B. D., Delley, B., Clarke, R., Kumah, D., Cionca, C. & Yacoby, Y. Structural basis for the conducting interface between $LaAlO_3$ and $SrTiO_3$. *Physical Review Letters* **99**, 155502 (2007). 10.1103/PhysRevLett.99.155502

263 Islam, M., Rajak, P., Knez, D., Chaluvadi, S. K., Orgiani, P., Rossi, G., Dražić, G. & Ciancio, R. HAADF STEM and ab initio calculations investigation of anatase TiO_2/$LaAlO_3$ heterointerface. *Applied Sciences* **12**, 1489 (2022). 10.3390/app12031489

264 Sayle, D. C., Sayle, T. X., Parker, S. C., Catlow, C. R. & Harding, J. H. Effect of defects on the stability of heteroepitaxial ceramic interfaces studied by computer simulation. *Physical Review. B, Condensed Matter* **50**, 14498–14505 (1994). 10.1103/PhysRevB.50.14498

265 Su, C.-Y., Menghini, M., Smets, T., Dillemans, L., Lieten, R. & Locquet, J. P. Influence of the surface pretreatment on the electrical properties of MgO and Al_2O_3 Gate stacks grown by MBE. *IOP Conference Series: Materials Science and Engineering* **41**, 012010 (2012). 10.1088/1757-899x/41/1/012010

266 Lu, P., Xiong, J., van Benthem, M. & Jia, Q. Atomic-scale chemical quantification of oxide interfaces using energy-dispersive X-ray spectroscopy. *Applied Physics Letters* **102**, 173111 (2013). 10.1063/1.4804184

267 Spurgeon, S. R., Du, Y. & Chambers, S. A. Measurement error in atomic-scale scanning transmission electron microscopy-energy-dispersive X-ray spectroscopy (STEM-EDS) mapping of a model oxide interface. *Microscopy and Microanalysis: The Official Journal of Microscopy Society of America, Microbeam Analysis Society, Microscopical Society of Canada* **23**, 513–517 (2017). 10.1017/s1431927617000368

268 Uberuaga, B. P., Dholabhai, P. P., Pilania, G. & Chen, A. Semicoherent oxide heterointerfaces: Structure, properties, and implications. *APL Materials* **7**, 100904 (2019). 10.1063/1.5121027

269 Luo, R., Xu, W. W., Zhang, Y., Wang, Z., Wang, X., Gao, Y., Liu, P. & Chen, M. Van der Waals interfacial reconstruction in monolayer transition-metal dichalcogenides and gold heterojunctions. *Nature Communications* **11**, 1011 (2020). 10.1038/s41467-020-14753-8

270 Akbashev, A. R., Roddatis, V. V., Vasiliev, A. L., Lopatin, S., Amelichev, V. A. & Kaul, A. R. Reconstruction of the polar interface between hexagonal $LuFeO_3$ and intergrown Fe_3O_4 nanolayers. *Scientific Reports* **2**, 672 (2012). 10.1038/srep00672

271 Shao, X., Nilius, N., Myrach, P., Freund, H.-J., Martinez, U., Prada, S., Giordano, L. & Pacchioni, G. Strain-induced formation of ultrathin mixed-oxide films. *Physical Review B* **83**, 245407 (2011). 10.1103/PhysRevB.83.245407

272 Sieber, H., Hess, D. & Werner, P. Misfit accommodation mechanisms at moving reaction fronts during topotaxial spinel-forming thin-film solid-state reactions: A high-resolution transmission electron microscopy study of five spinels of different misfits. *Philosophical Magazine A* **75**, 889–908 (1997). 10.1080/01418619708214000

273 Tasker, P. W. The stability of ionic crystal surfaces. *Journal of Physics C: Solid State Physics* **12**, 4977–4984 (1979). 10.1088/0022-3719/12/22/036

274 Noh, H.-J., Jeong, J., Jeong, J., Cho, E.-J., Kim, S. B., Kim, K., Min, B. I. & Kim, H.-D. Anisotropic electric conductivity of delafossite $PdCoO_2$ studied by angle-resolved photoemission spectroscopy. *Physical Review Letters* **102**, 256404 (2009). 10.1103/PhysRevLett.102.256404

275 Mazzola, F., Sunko, V., Khim, S., Rosner, H., Kushwaha, P., Clark, O. J., Bawden, L., Marković, I., Kim, T. K., Hoesch, M., Mackenzie, A. P. & King, P. D. C. Itinerant ferromagnetism of the Pd-terminated polar surface of $PdCoO_2$. *Proceedings of the National Academy of Sciences of the United States of America* **115**, 12956–12960 (2018). 10.1073/pnas.1811873115

276 Sunko, V., Rosner, H., Kushwaha, P., Khim, S., Mazzola, F., Bawden, L., Clark, O. J., Riley, J. M., Kasinathan, D., Haverkort, M. W., Kim, T. K., Hoesch, M., Fujii, J., Vobornik, I., Mackenzie, A. P. & King, P. D. C. Maximal Rashba-like spin splitting via kinetic-energy-coupled inversion-symmetry breaking. *Nature* **549**, 492–496 (2017). 10.1038/nature23898

277 Scheid, A., Song, Q., Ribet, S. M., Ophus, C., Suyolcu, Y. E., Schlom, D. G., Heil, T. & van Aken, P. A. Atomic-scale mechanisms of nucleation and stabilization in $CuCrO_2$ and $CuFeO_2$ delafossite thin films on Al_2O_3. *Advanced Materials Interfaces* **12**, 2500218 (2025). 10.1002/admi.202500218

278 Deng, Z., Fang, X., Wu, S., Zhao, Y., Dong, W., Shao, J. & Wang, S. Structure and optoelectronic properties of Mg-doped $CuFeO_2$ thin films prepared by sol–gel method. *Journal of Alloys and Compounds* **577**, 658–662 (2013). 10.1016/j.jallcom.2013.06.155

279 Sukeshini, A. Physicochemical characterization of $CuFeO_2$ and lithium intercalation. *Solid State Ionics* **128**, 33–41 (2000). 10.1016/s0167-2738(00)00274-5

280 Poienar, M., Damay, F., Martin, C., Hardy, V., Maignan, A. & André, G. Structural and magnetic properties of $CuCr_{1-x}Mg_xO_2$ by neutron powder diffraction. *Physical Review B* **79**, 14412 (2009). 10.1103/PhysRevB.79.014412

281 Maouhoubi, A., Ouzaroual, L., Toual, Y., Mouchou, S., Mezzat, F., Azouaoui, A., Ez-Zahraouy, H., Hourmatallah, A., Bouslykhane, K. & Benzakour, N. Structural, electronic and magnetic properties of the $CuFeO_2$ multiferroic compound. *Arabian Journal of Chemistry* **17**, 105437 (2024). 10.1016/j.arabjc.2023.105437

282 Ye, F., Dai, H., Peng, K., Li, T., Chen, J., Chen, Z. & Li, N. Effect of Mn doping on the microstructure and magnetic properties of $CuFeO_2$ ceramics. *Journal of Advanced Ceramics* **9**, 444–453 (2020). 10.1007/s40145-020-0387-4

283 Kadowaki, H., Kikuchi, H. & Ajiro, Y. Neutron powder diffraction study of the two-dimensional triangular lattice antiferromagnet $CuCrO_2$. *Journal of Physics: Condensed Matter* **2**, 4485–4493 (1990). 10.1088/0953-8984/2/19/014

284 Poienar, M., Hardy, V., Kundys, B., Singh, K., Maignan, A., Damay, F. & Martin, C. Revisiting the properties of delafossite $CuCrO_2$: A single crystal study. *Journal of Solid State Chemistry* **185**, 56–61 (2012). 10.1016/j.jssc.2011.10.047

285 Seki, S., Onose, Y. & Tokura, Y. Spin-driven ferroelectricity in triangular lattice antiferromagnets $ACrO_2$ (A=Cu, Ag, Li, or Na). *Physical Review Letters* **101**, 067204 (2008). 10.1103/PhysRevLett.101.067204

286 Collins, M. F. & Petrenko, O. A. Review/Synthèse: Triangular antiferromagnets. *Canadian Journal of Physics* **75**, 605–655 (1997). 10.1139/p97-007

287 Aktas, O., Truong, K. D., Otani, T., Balakrishnan, G., Clouter, M. J., Kimura, T. & Quirion, G. Raman scattering study of delafossite magnetoelectric multiferroic compounds: $CuFeO_2$ and $CuCrO_2$. *Journal of Physics. Condensed Matter: an Institute of Physics Journal* **24**, 036003 (2012). 10.1088/0953-8984/24/3/036003

288 Albaalbaky, A., Kvashnin, Y., Ledue, D., Patte, R. & Frésard, R. Magnetoelectric properties of multiferroic $CuCrO_2$ studied by means of ab initio calculations and Monte Carlo simulations. *Physical Review B* **96**, 064431 (2017). 10.1103/PhysRevB.96.064431

289 Han, M. J., Duan, Z. H., Zhang, J. Z., Zhang, S., Li, Y. W., Hu, Z. G. & Chu, J. H. Electronic transition and electrical transport properties of delafossite $CuCr_{1-x}Mg_xO_2$ ($0 \leq x \leq 12\%$) films prepared by the sol-gel method: A composition dependence study. *Journal of Applied Physics* **114**, 163526 (2013). 10.1063/1.4827856

290 Shin, D., Foord, J. S., Egdell, R. G. & Walsh, A. Electronic structure of $CuCrO_2$ thin films grown on Al_2O_3(001) by oxygen plasma assisted molecular beam epitaxy. *Journal of Applied Physics* **112**, 113718 (2012). 10.1063/1.4768726

291 Chang, C. S., Sun, J., Khim, S., Mackenzie, A. P., Schlom, D. G. & Muller, D. A. Visualization of defects in single-crystal and thin-film $PdCoO_2$ using aberration-corrected scanning transmission electron microscopy. *Physical Review Materials* **6**, 093401 (2022). 10.1103/PhysRevMaterials.6.093401

292 Schlom, D. G., Chen, L. Q., Pan, X., Schmehl, A. & Zurbuchen, M. A. A thin film approach to engineering functionality into oxides. *Journal of the American Ceramic Society* **91**, 2429–2454 (2008). 10.1111/j.1551-2916.2008.02556.x

293 Tripathi, T. S. & Karppinen, M. Structural optical and electrical transport properties of ALD-fabricated $CuCrO_2$ Films. *Physics Procedia* **75**, 488–494 (2015). 10.1016/j.phpro.2015.12.061

294 Li, D., Fang, X., Deng, Z., Zhou, S., Tao, R., Dong, W., Wang, T., Zhao, Y., Meng, G. & Zhu, X. Electrical, optical and structural properties of CuCrO 2 films prepared by pulsed laser deposition. *Journal of Physics D: Applied Physics* **40**, 4910–4915 (2007). 10.1088/0022-3727/40/16/023

295 Scheid, A., Heil, T., Suyolcu, Y. E., Song, Q., Enderlein, N., Tchiomo, A. P. N., Ngabonziza, P., Hansmann, P., Schlom, D. G. & van Aken, P. A. Unveiling the interfacial reconstruction mechanism enabling stable growth of the delafossite $PdCoO_2$ on Al_2O_3 and $LaAlO_3$ (2025). arXiv:2502.13727

296 Li, S. Z., Liu, J., Wang, X. Z., Yan, B. W., Li, H. & Liu, J. M. Epitaxial growth of delafossite $CuFeO_2$ thin films by pulse laser deposition. *Physica B: Condensed Matter* **407**, 2412–2415 (2012). 10.1016/j.physb.2012.03.037

297 Sun, J., Parzyck, C. T., Lee, J. H., Brooks, C. M., Kourkoutis, L. F., Ke, X., Misra, R., Schubert, J., Hensling, F. V., Barone, M. R., Wang, Z., Holtz, M. E., Schreiber, N. J., Song, Q., Paik, H., Heeg, T., Muller, D. A., Shen, K. M. & Schlom, D. G. Canonical approach to cation flux calibration in oxide molecular-beam epitaxy. *Physical Review Materials* **6**, 033802 (2022). 10.1103/PhysRevMaterials.6.033802

298 Glaeser, R. M. Invited review article: Methods for imaging weak-phase objects in electron microscopy. *The Review of Scientific Instruments* **84**, 111101 (2013). 10.1063/1.4830355

299 Zernike, F. Phase contrast, a new method for the microscopic observation of transparent objects. *Physica* **9**, 686–698 (1942). 10.1016/s0031-8914(42)80035-x

300 Lazić, I., Bosch, E. G. T. & Lazar, S. Phase contrast STEM for thin samples: Integrated differential phase contrast. *Ultramicroscopy* **160**, 265–280 (2016). 10.1016/j.ultramic.2015.10.011

301 Humphry, M. J., Kraus, B., Hurst, A. C., Maiden, A. M. & Rodenburg, J. M. Ptychographic electron microscopy using high-angle dark-field scattering for sub-nanometre resolution imaging. *Nature Communications* **3**, 730 (2012). 10.1038/ncomms1733

302 Song, J., Allen, C. S., Gao, S., Huang, C., Sawada, H., Pan, X., Warner, J., Wang, P. & Kirkland, A. I. Atomic resolution defocused electron ptychography at low dose with a fast, direct electron detector. *Scientific Reports* **9**, 3919 (2019). 10.1038/s41598-019-40413-z

303 Chen, Z., Jiang, Y., Shao, Y.-T., Holtz, M. E., Odstrčil, M., Guizar-Sicairos, M., Hanke, I., Ganschow, S., Schlom, D. G. & Muller, D. A. Electron ptychography achieves atomic-resolution limits set by lattice vibrations (2021). 10.48550/arXiv.2101.00465